Infrared Field Measurements of Sea Surface Temperature: Analysis of Wake Signatures and Comparison of Skin Layer Models

by Christopher J. Zappa

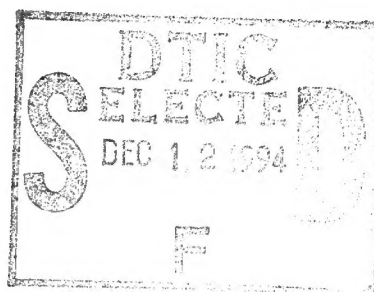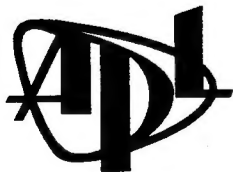Technical Report
APL-UW TR 9412
August 1994

19941205 076

Infrared Field Measurements of Sea Surface Temperature: Analysis of Wake Signatures and Comparison of Skin Layer Models

by Christopher J. Zappa

Technical Report
APL-UW TR 9412
August 1994

DTIC QUALITY INSPECTED 6

Applied Physics Laboratory   University of Washington
1013 NE 40th Street   Seattle, Washington 98105-6698

FOREWORD

This report is a slightly revised version of the thesis submitted in partial fulfillment of the requirements for the Master of Science in Engineering degree at the University of Washington in August 1994. Dr. Harry H. Yeh, Professor of Civil Engineering, was the chairperson of the supervisory committee.

ABSTRACT

Infrared field measurements of ocean skin temperature made aboard the R/P FLIP in January of 1992 approximately 400 nautical miles off the coast of San Diego are presented. An extensive literature review accompanies these measurements probing the fundamentals of air-sea interaction, electromagnetics, and free-surface flows. A thin layer at the air-sea interface, known as the ocean skin layer, transfers heat by molecular conduction. The skin layer is on the order of a millimeter and typically 0.1 to 0.5 °C cooler than the water just below for conditions of net heat flux from the ocean to the atmosphere. Two surface-piercing cables hanging from FLIP's port boom, each 1 cm in diameter, provided a disturbance of the skin layer mixing the warmer water from below up to the surface. Employing an infrared imager, we detected the temperature variations, tracked the signatures and quantified the spatial and thermal changes in time of these artificial disturbances, which were on the order of a meter. This unique method of visualizing turbulence at an air-water interface provides a direct measurement of the bulk-skin temperature difference, ΔT. The recovery rate of the skin layer was found to be directly related to the level, or strength, of the disruption under low wind speed conditions (≈ 2 m/s). At moderate wind speeds (≈ 7 m/s), both the natural (breaking waves) and artificial (wakes) disturbances recovered within 2 s compared to an extrapolated recovery time of up to ≈ 120 s under low wind speeds for the wake signatures. The difference is primarily a function of the net heat flux and sublayer thickness, which relate directly to the existing environmental conditions (e.g., turbulence intensity, sea state, wind speed). Previous reports of ≈ 10 to 12 s skin layer recovery times emphasize the significance of our results. Signatures of cool wakes and a transitional sequence from warm to cool wakes over the course of 15 minutes highlighted the small-scale spatial variability and non-uniform temperature profile. Narrow field-of-view radiometers were used to compute calibrated and reflection corrected time series of ΔT (referenced to 10 cm depth) over a 4 day period. A comparison of the existing ΔT models is presented using measured values of the net heat flux, wind speed, and ΔT. For the present dataset, longwave radiation dominated the regulation of net heat flux at night while the

iii

solar insolation dominated during the day. The ΔT models did not adequately predict the phenomenon of the daytime heat flux and skin layer development under low wind conditions. Notwithstanding, the models agree well with the measured ΔT at night under high wind speeds.

TABLE OF CONTENTS

LIST OF FIGURES

LIST OF TABLES

NOTATION

A	-	Dimensionless arbitrary constant
a	-	Absorptivity
α	-	Thermal diffusivity
a_c	-	Absorption coefficient
a_o	-	Wave amplitude
A_s	-	Surface area
a_s	-	Oceanic albedo
B	-	Dimensionless arbitrary constant
$\overline{B}$	-	Bowen ratio
b	-	Characteristic wake dimension
β	-	Dimensionless constant
b_ℓ	-	Width of the laminar wake
b_m	-	Maximum characteristic wake dimension
b_t	-	Width of the turbulent wake
c	-	Speed of light in free space
C_1	-	Coefficient for Hasse's model (Chapter 5)
C_1	-	Experimental value for $C_1 = 2\pi c^2 h$ (Chapter 3)
C_2	-	Coefficient for Hasse's model (Chapter 5)
C_2	-	Experimental value for $C_2 = hc/k_b$ (Chapter 3)
C_D	-	Resistance or drag coefficient
C_{dc}	-	Coefficient of drag for the cylinder
C_E	-	Transfer coefficient
C_H	-	Transfer coefficient
C_L	-	Lift coefficient
C_m	-	Coefficient of inertia for the cylinder
C_p	-	Phase velocity
c_{pa}	-	Specific heat of air
$C_{PRT\text{-}5}$	-	PRT-5 calibration constant
c_{pw}	-	Isobaric specific heat of water
C_{te}	-	Coefficient of thermal expansion
D	-	Diameter of cable, wire, or cylinder

δ	-	Boundary layer thickness
d	-	Depth of water
d_{eo}	-	E-folding, or effective optical, depth
δ_k	-	Thermal molecular conduction layer
δ_v	-	Viscous shear sublayer
$\delta_{v\sigma}$	-	Viscous sublayer accounting for surface tension
E	-	Energy associated with electromagnetic radiation
ε	-	Emissivity
ε_{dw}	-	Emissivity of water from Downing and Williams (1975)
ε_t	-	Energy flux per unit mass
ε_o	-	Permittivity constant
ε_{si}	-	Spectrally integrated ε_{dw}
$\bar{\varepsilon}_w$	-	Emissivity of water averaged over the local incidence angles
Φ	-	Flux or the time rate of electromagnetic energy
f	-	Functional variable
f	-	Optimized constant for Schluessel *et al.*'s model
F_D	-	Drag force
F_I	-	Inertial force
Φ_o	-	Scalar potential
F_o	-	Vortex shedding frequency
F_T	-	Total force
G	-	Arbitrary onstant
g	-	Acceleration due to gravity
γ	-	Experimentally determined heat transfer coefficient
h	-	Planck's constant
η	-	Similarity variable
H_o	-	Wave height
η_o	-	Surface elevation
I	-	Incident flux density (irradiance or incidence)
i	-	Index
I_{LW}	-	Longwave irradiance measured from the pyrgeometer
I_{so}	-	Solar radiation present at the top of the atmosphere
I_{SW}	-	Shortwave irradiance measured by the pyranometer
j	-	Optimized constant for Schluessel *et al.*'s model

K	-	von Kármán constant
k	-	Thermal conductivity
k_b	-	Boltzmann's constant
k_o	-	Wavenumber
L	-	Diffusion length
λ	-	Wavelength of electromagnetic radiation
ℓ	-	Mixing length
L_e	-	Latent heat of vaporization
ℓ_k	-	Kolmogorov length scale
L_{mo}	-	Monin-Obukhov length
L_o	-	Wavelength
λ_o	-	Experimentally determined proportionality constant
ℓ_o	-	Intermediate length scale
M	-	Exitent flux density (exitance or emittance)
$\mathbf{m}$	-	Number of standard atmospheric masses
$M_{b\lambda}$	-	Spectral exitance or emittance
$M_{o\lambda}$	-	Observed exitance
$M_{r\lambda}$	-	Background radiation reflected into sensor
N	-	Complex index of refraction
n	-	Experimental exponent (2.20) and Quantum number (3.3)
ν	-	Kinematic viscosity
n	-	Real part of index of refraction
ν_e	-	Eddy, virtual, or apparent viscosity (Chapter 4)
ν_e	-	Frequency of electromagnetic radiation (Chapter 3)
n_k	-	Imaginary part of N (extinction coefficient or absorption index)
Nu	-	Nusselt number
P	-	Pressure
p	-	Exponent
π	-	Pi
P_o	-	Pressure outside the turbulent wake
Pr	-	Prandtl number
q	-	Exponent
θ	-	Incidence, or zenith, angle
q_a	-	Actual specific humidity

Q_E	-	Latent (evaporative) heat flux
Q_G	-	Downwelling infrared heat flux from the clouds and sky
Q_H	-	Sensible heat flux
Q_{IR}	-	Infrared radiation emitted by the water surface
Θ_m	-	Momentum thickness
Q_{net}	-	Net heat flux
Q_S	-	Solar insolation
q_s	-	Saturated specifid humidity
R	-	Flux density per solid angle (radiance, sterance, or brightness)
ρ	-	Density
r	-	Reflectivity
Ra	-	Rayleigh number
ρ_a	-	Density of air
$\overline{\rho' w'}$	-	Vertical flux of density
R_b	-	Radiance of a blackbody with the same temperature as the ocean
r_d	-	Radial distance
Re	-	Reynolds number
Re_ℓ	-	Mixing length Reynolds number
Re_{ℓ_k}	-	Kolmogorov length Reynolds number
Re_{ℓ_o}	-	Intermediate length Reynolds number
Re_o	-	Reynolds number according to u_o
Re_w	-	Wave Reynolds number according to a_o, ω_o, and k_o
R_{hsky}	-	Radiance of the sky at the horizon only
Ri	-	Richardson number
R_{sea}	-	Radiance of a calm sea
R_{sky}	-	Radiance of a cloudless sky
ρ_w	-	Density of water
σ	-	Surface tension
σ_b	-	Stefan-Boltzmann constant
σ_r	-	Surface roughness
St	-	Strouhal number
σ_x	-	Standard deviation of the Gaussian temperature distribution
T	-	Temperature
τ	-	Shear stress

t	-	Time
t^*	-	Nondimensional timestep
T_a	-	Bulk temperature of air
τ_a	-	Atmospheric shear or wind stress
T_{amb}	-	Undisturbed skin layer temperature
T_b	-	Bulk water temperature
T_{cal}	-	Thermistor measured temperature in the calibration bath
τ_e	-	Transmissivity
τ_{es}	-	Transmittance of the atmosphere
T_{IR}	-	Temperature output from the PRT-5
$T_{IR\text{-}c}$	-	Corrected PRT-5 value
t_k	-	Kolmogorov time scale
T_{max}	-	Maximum temperature within the wake
T_o	-	Wave period {one instance as Brightness temperature in (3.32)}
T_r	-	Effective background temperature
τ_r	-	Reynolds stress tensor
T_s	-	Water surface temperature
T_{sky}	-	Measure of the sky temperature from the upward-looking KT-19
$T_{s_{max}}$	-	Maximum of temperature wave
$T_{s_{min}}$	-	Minimum of temperature wave
T_{sst}	-	Actual sea surface temperature measured by radiometer
τ_w	-	Surface shear stress in the water
τ_{wv}	-	Wave supporting stress
U	-	Flow speed
u	-	X-direction velocity
$\vec{u}$	-	Velocity field ($\vec{u} = (u,v,w)$)
u'	-	Xcomponent fluctuating turbulent velocity
U_{IO}	-	Wind speed measured at 10 m height above the sea surface
u_{*a}	-	Atmospheric friction velocity
u_{*w}	-	Friction velocity in the water
u'^*	-	Characteristic velocity for the mixing length scale
$u_k'^*$	-	Kolmogorov scale velocity
$u_o'^*$	-	Intermediate scale velocity
$\overline{u}_\ell$	-	Stokes' drift (time-averaged lagrangian velocity)

u_o	-	Horizontal orbital velocity
$\bar{u}_{sc}$	-	Average horizontal surface motion predicted from scanner
u_w	-	Wake velocity
v	-	Y-direction velocity
v'	-	Y-component fluctuating turbulent velocity
Ω	-	Solid Angle
w	-	Z-direction velocity
w'	-	Z-component fluctuating turbulent velocity
w_o	-	Vertical orbital velocity
$\bar{\omega}$	-	Vorticity field ($\bar{\omega} = \nabla \times \bar{u}$)
ω_o	-	Wave frequency
x	-	Space coordinate
ξ	-	Transverse component of vorticity (X-component)
x_m	-	Mean of the Gaussian temperature distribution
x_p	-	Pixel position
y	-	Space coordinate
ψ	-	Stream function used as similarity variable
y_p	-	Pixel position
z	-	Space coordinate
ζ	-	Z-component of vorticity
z_o	-	Roughness length
μ	-	Dynamic viscosity
μ_o	-	Permeability constant
ΔT	-	Bulk-skin temperature difference ($\Delta T = T_b - T_s$)
ΔT_{fg}	-	ΔT for Fedorov and Ginsburg's model
ΔT_{hd}	-	ΔT for Hasse's model
ΔT_s	-	ΔT for Saunders' model
$\Delta \tilde{T}_s$	-	Amplitude of temperature wave ($\Delta \tilde{T}_s = T_{s_{max}} - T_{s_{min}}$)
ΔT_{sc}	-	ΔT for Schluessel $et\ al.$'s model
ΔT_w	-	Temperature difference across the wake ($\Delta T_w = T_{max} - T_{amb}$)

ACKNOWLEDGMENTS

I would like to express the deepest of gratitude to my co-advisors Dr. Andrew T. Jessup and Professor Harry H. Yeh for their ceaseless effort in teaching, guiding, and providing valuable insight which aided in the completion of my Masters research and in the preparation of this Thesis. I would also like to thank Professor Ronald E. Nece for his participation on my committee and helpful input. I am grateful for the assistance of Dr. Serhad Ataktürk and Ralph Monis from the Atmospheric Sciences Department. A special thanks to Jim Turner for his support and for the numerous stimulating conversations. Finally, Katell Guellec deserves sincere appreciation for her continuing and boundless support which drove me to persist in my endeavors.

CHAPTER 1

Introduction

One of the most significant oceanographic applications of satellite remote sensing is the mapping of sea surface temperature using infrared radiometry. Sea surface temperature plays an important role in regulating the fluxes of gas, heat, and momentum at the air-sea interface, which all drive global climate changes and weather patterns. Following the diurnal cycle of the sun, the ocean typically heats up during the day and cools off during the night. The flux of heat associated with the diurnal cycle will establish a temperature gradient near the ocean surface according to the laws of conduction. The direction and magnitude of the heat flux determine whether the sea surface is cooler or warmer than the underlying bulk water. Therefore, sea surface temperature provides a direct link to the net heat flux across the air-sea interface.

On the open ocean, the surface is typically a few tenths of a degree Celsius cooler than the underlying bulk water a few millimeters or centimeters below. This phenomenon develops as a result of a net upward heat flux. Assuming vertical motions are suppressed at the free-surface, the heat flux must be transferred by molecular conduction. Molecular conduction allows for large temperature differences over relatively small distances. Hence, most of the heat is transferred across a thin boundary, or skin, layer at the surface. A cool skin layer regularly exists at night and throughout most of the day and is on the order of a millimeter. Observations suggest typical temperature differences between 0.1 and 0.5 °C. Occasionally, with a slight zephyr and strong insolation, the skin layer may become warmer than the underlying water.

The role of the skin layer in regulating the transfer of heat is of great interest to oceanographers. Studying the flux of heat across the air-sea interface requires the measurement of the bulk-skin temperature difference, ΔT. While the bulk temperature at depths of 10 cm or greater is relatively simple to monitor, the measurement of the temperature within

the skin layer using contact thermistors is quite difficult. In order to overcome this difficulty, investigators have typically employed narrow field-of-view infrared radiometers which provide a spatially-averaged point measurement of the electromagnetic radiation from depths of less than 100 μm of water. The amount of radiation sensed by the radiometer directly correlates to a representative temperature of the sea surface or skin layer. While these narrow field-of-view radiometers are useful for climatalogical studies, a large map of temperature produced by an infrared imager reveals more about the sub-pixel scale processes at the air-sea interface (with respect to satellite images). Essentially, the imager could be thought of as an array of the point measurements provided by narrow field-of-view radiometers.

McAlister and McLeish (1965) performed some of the first measurements of sea surface temperature mapping using an infrared scanner. They recorded signatures of what appeared to be fronts, large-scale ocean eddies, free-convective patterns, wind streaks, and breaking waves along with the foam from the whitecaps. Peltzer *et al.* (1987) used an infrared imaging system to measure the detection of ship wakes during the day. As the diurnal thermocline was well established, the thermal wake signatures recorded by the imaging system emphasize the contrast between the cool center of the wake produced by the upwelling of the underlying water and a warmer undisturbed surface. These measurements highlight the heating of the ocean which usually occurs during the daytime. The ocean skin layer, however, is more often cooler than the underlying water. Jessup (1993) presents 2-D measurements of nighttime breaking wave events when a cool skin layer has developed. The warm signature of an actively breaking crest and the turbulent wake left behind indicate a disruption of the cool skin layer.

The measurements presented here will provide further insight into the processes of the cool skin layer. Aboard the R/P FLIP (Floating Instrument Platform) in January 1992 about 400 nautical miles off the coast of San Diego, warm free-surface wakes against the background of a cool

skin layer were observed by using an infrared imager. The size of the signatures, on the order of a meter, emanating from a 1 cm diameter surface-piercing cable far exceeded expectations. Not only was the size of the disturbance excessive, but also the recovery time of the skin layer was on the order of **minutes**. Other investigators (Clauss *et al.*, 1970; Ewing and McAlister, 1960) have claimed that the skin layer recovers after nearly 10 s following the disruption due to breaking waves. Grassl (1976) suggests that above wind speeds of 10 m/s wave breaking is so prevalent the skin layer never re-establishes itself. On the other hand, this investigation will show that at high wind speeds the skin layer recovers much faster than expected for both artificial (wire wakes) and natural (wave breaking) disturbances. The subject of skin layer recovery is crucial to the premise of this thesis.

The recovery of the skin layer is an important variable in determining the rates of gas flux which regulate the transfer of CO_2 between the atmosphere and the oceans. Typically, modelers of gas flux use the recovery time of the skin layer to estimate the surface renewal time (Hasse,1990; Gemmrich and Hasse, 1992). The surface renewal model relates the average flux at the surface to the driving concentration difference. The time associated with the surface renewal model most often is approximated as 10 s in accordance with the results of Clauss *et al.* (1970) and Ewing and McAlister (1960). The results forthcoming emphasize the variability of the skin layer recovery rate and the need to further explore its relationship to the physics of gas, heat, and momentum flux models.

The skin layer recovery process is not the only topic central to the objective of this thesis. Curious daytime features of cool wakes and a transition from warm to cool wakes depict the small-scale spatial variability and the temperature variation with depth during the day. The occurrence of these features necessitated the calculation of the net heat flux, Q_{net}, and a comparison of the ΔT models which will emphasize the difficulties associated with the prediction of the skin layer characteristics via modeling.

The main objectives of this thesis are to:

1) demonstrate the feasibility of using infrared imagery to visualize turbulence at an air-water interface,

2) investigate the spatial and thermal changes in time of skin layer disturbances,

3) determine the dependence of the skin layer recovery rate upon the level of the skin layer disruption,

4) compare the behavior of skin layer recovery under high wind speeds for artificial and natural disturbances with low wind speed cases,

5) compare the currently available ΔT models, assess their performance, and discuss the possibility for accurate prediction.

The organization of this thesis is as follows. Chapters 2, 3, and 4 present an extensive literature survey on the relevant areas to this thesis. Chapter 2 discusses the interaction of air and water specifically as it relates to the ocean skin layer. Chapter 3 presents the background on electromagnetics required to utilize and interpret the techniques of infrared radiometry. Chapter 4 develops the theory behind wakes, turbulence, and waves, along with the effects a free-surface has on the flow characteristics. Chapter 5 presents the results of detailed measurements and analysis of skin layer disturbances, and compares the models for ΔT. Chapter 6 contains a summary and the conclusions of this thesis.

CHAPTER 2

The Air-Sea Interface

2.1 Physical Processes Affecting Sea Surface Temperature

In defining the skin layer, an understanding of the heat budget over the open ocean is imperative. An illustration of the processes relevant over the open ocean is portrayed in Figure 2.1. The net heat transfer across the sea surface (positive downward into the ocean, or in the positive z-direction) is given by

$$Q_{net} = Q_{IR} + Q_G + Q_S + Q_H + Q_E \tag{2.1}$$

where Q_{IR} (invariably negative) is the infrared radiation emitted by the sea surface, Q_H (positive or negative) is the sensible heat flux, Q_E (usually negative) is the latent heat flux, Q_G (always positive) is the downwelling infrared radiation from the sky, clouds and atmosphere, and Q_S (regularly positive) is the solar radiation. The incoming solar and infrared radiation attempt to equilibrate with the outgoing infrared radiation and sensible and latent (evaporative) heat fluxes.

The exiting sensible and latent turbulent heat fluxes can be parameterized using the bulk formulae

$$Q_H = C_H \rho_a c_{pa} (T_a - T_b) U_{10} \tag{2.2}$$

and

$$Q_E = C_E \rho_a L_e (q_a - q_s) U_{10} \tag{2.3}$$

where C_H and C_E are the transfer coefficients, ρ_a is the density of air, c_{pa} is the specific heat of air, L_e is the latent heat of vaporization, T_b is the bulk sea temperature, T_a is the bulk air temperature, q_s is the saturated specific humidity in air at the water surface, q_a is the actual specific humidity in air at the measurement height, and U_{10} is the wind speed measured at 10 meters (Geernaert, 1990). From these parameterizations, the wind speed
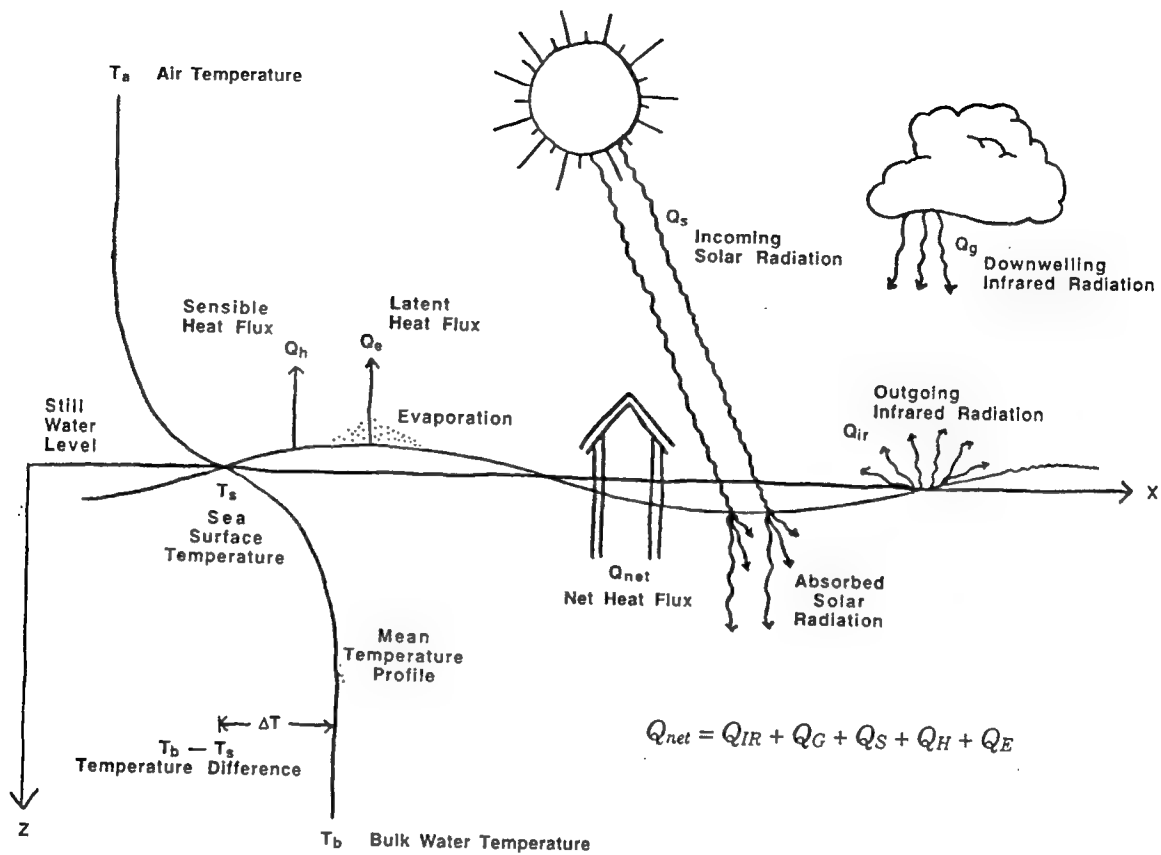
Figure 2.1   Illustration of the factors influencing the thermal boundary
layer at the air-water interface.

$$Q_{net} = Q_{IR} + Q_G + Q_S + Q_H + Q_E$$

Table 2.1   Percentage of absorbed solar radiation after Schmidt (1908), for
clear water (from Hasse, 1971).

Depth of Water (cm)	10^{-3}	10^{-2}	10^{-1}	1	10	10^2	10^3	10^4
Percentage Absorbed	0.6	4.8	14.1	27.0	45.1	64.1	81.8	98.6

dependence is clearly seen and can increase the heat flux considerably. Notwithstanding, evaporation generally dominates the vertical heat flux on the ocean, which can be positive outward even when the air temperature is greater than the bulk sea temperature (Katsaros, 1980a; Schluessel *et al.*, 1990). As turbulent fluxes, though, the sensible and latent fluxes cannot exchange the heat directly across the sea surface. Instead, molecular processes exchange the heat across the skin layer, while the turbulent fluxes carry the heat up to and away from the sea surface. Only solar radiation can penetrate past the ocean surface to greater depths.

Hasse (1971) and Saunders (1967a) have referenced Schmidt (1908) who showed that 98.6 % of the solar insolation is absorbed over approximately an 100 meter depth of clear ocean water, while 14.1 % is absorbed within the top millimeter. The results from Schmidt (1908) are given in Table 2.1. For more turbid coastal waters, the absorption depth of solar radiation could be much less. While the absorption depth of solar radiation depends on the turbidity of the ocean, all the outgoing heat fluxes escape from the skin layer establishing the net vertical heat flux. The absorbed fraction of solar radiation within the skin layer is often on the order of the exiting heat fluxes. Therefore, during the fierce mid-day sun the net heat flux outward is often less intense and sometimes inverted.

Incoming and outgoing infrared (longwave) radiation represent the "passive" fluxes. As stated previously, the turbulent fluxes dominate the processes. Even though explicitly listed in the heat budget equation, the importance of the longwave radiation lies in the measurement procedures and will be discussed in detail later.

2.2 Cool Skin Layer Model

Initial models of the boundary layer at the ocean surface have been difficult to develop, most of the obstacles being traced to measurement complications. While the models have been based upon hypothesis, much of our present understanding of the skin layer relies upon experiment.

Because the skin layer is at the free-surface, we assume a restriction of vertical motions occurs within it and consequently the temperature gradient through the skin layer is presumed linear. This is only an approximation at the free surface as non-linear profiles have been predicted (Liu and Businger, 1975) and verified in the laboratory (Katsaros *et al.*, 1977) and in the field (Khundzhua and Andreyev, 1974; Khundzhua *et al.* 1977). Therefore, heat transfer near the free-surface occurs by molecular conduction and thermal radiation.

Since conduction processes dominate over convection near the interface, the largest temperature gradients transpire there (McAlister and McLeish, 1969). Fourier's law of heat conduction states,

$$Q_{net} = -k\frac{\partial T}{\partial z} \tag{2.4}$$

where k is the thermal conductivity and $\partial T/\partial z$ is the temperature gradient in the direction of heat flow. The vertical direction, z, normal to and zero at the still water level, is measured positive downward. Accordingly, a large difference in ocean bulk and surface temperatures may occur over a very small distance. The difference between the bulk ocean temperature, T_b, and that at the surface, T_s,

$$\Delta T = T_b - T_s \tag{2.5a}$$

is referred to as the **bulk-skin temperature difference**. Defining the molecular conduction layer as δ_k, the temperature gradient $\partial T/\partial z$ is approximated by $\Delta T/\delta_k$ and Fourier's law now becomes

$$Q_{net} = -k\frac{\Delta T}{\delta_k}. \tag{2.5b}$$

As an initial indication, the molecular conduction layer is on the order of a millimeter (Katsaros 1980a,b; Robinson *et al.*, 1984).

The existence of a skin layer on the ocean is largely the consequence of local winds and sea surface rigidity. Saunders (1967a) proposed a model shown in Figure 2.2 in which the convective processes occurring just below the ocean surface are due to wind-driven turbulence. Wind forces generate turbulent motion in the interior of the ocean. The turbulence, however, is damped near the air-sea interface and usually vanishes within a thin sublayer at the surface. Across this sublayer, transport processes occur by molecular diffusion. Saunders (1967a) suggests that within the "quasi-laminar" sublayer of thickness δ_v, the tangential wind stress is transmitted to the ocean by viscosity. He then argued that the relation

$$\delta_v \sim \frac{v}{u_{*w}} \tag{2.6}$$

where

$$u_{*w} = \left(\tau / \rho_w \right)^{\frac{1}{2}} \tag{2.7}$$

can be obtained dimensionally as von Kármán (1934) did. Here, τ is the shear stress, ρ_w is the density of water, u_{*w} is the friction velocity within the water, δ_v is the viscous shear sublayer, and v is the kinematic viscosity.

A difficulty arises in the definition of τ. Some authors cite τ as a wind stress (Saunders, 1967a; Grassl, 1976) while others define it as a current or surface shear stress (Katsaros, 1980a; Robinson et al., 1984). Regardless, any surface shear stress in the ocean, τ_w, is mainly induced by the atmospheric shear or wind stress, τ_a. Thus τ_w is proportional to τ_a. However, the proportionality constant appears to be dependent on the stage of wave growth (Katsaros, 1980b) and is not well defined. For the purposes of this discussion, the friction velocity in the ocean is a function of the atmospheric shear,

$$u_{*w} = f(\tau) = f(\tau_a) \tag{2.8}$$

where τ_a is parameterized by another bulk formula
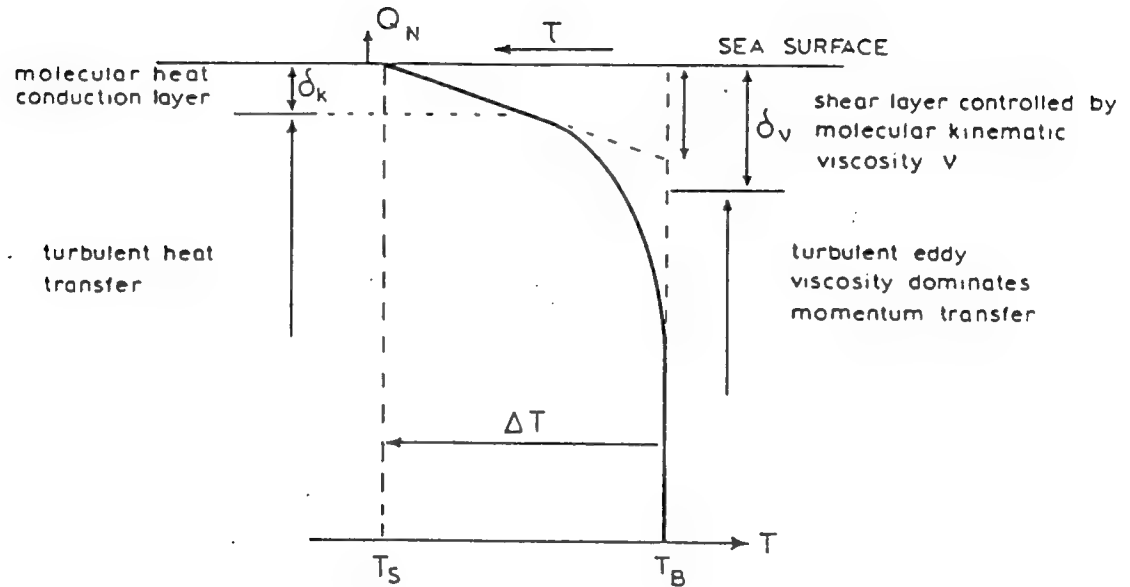
Figure 2.2   Definitions of the layers near the surface for the model
proposed by Saunders (from Robinson *et al.*, 1984) where Q_N is
Q_{net}.

$$\tau_a = C_D \rho_a U_{10}^2 \qquad (2.9)$$

given

$$C_D = (0.44 + 0.063 U_{10}) \times 10^{-3} \qquad (2.10a)$$

for wind speeds of 6 to 22 m/s according to Smith (1980), or

$$C_D = (0.63 + 0.066 U_{10}) \times 10^{-3} \qquad (2.10b)$$

for wind speeds of 2.5 to 21 m/s following from Smith and Banke (1975). C_D represents a resistance or drag coefficient and remains a topic of intense study. Numerous experimenters have found other parameterizations which have been catalogued by Geernaert (1990).

Now the Prandtl number,

$$Pr = \frac{\nu}{\alpha} \qquad (2.11)$$

is the ratio of kinematic viscosity to the thermal diffusivity, α, and provides a relationship between the hydrodynamic and thermal boundary layers. Thus the ratio of these two quantities should portray the relative magnitudes of diffusion of momentum and heat in the fluid. The rigid boundary expression, given in Holman (1990),

$$\frac{\delta_k}{\delta_v} = \frac{1}{1.026} Pr^{-\frac{1}{3}} \qquad (2.12)$$

predicts an approximation for the relative thicknesses of the boundary layers. In our case, the Prandtl number is a function of temperature and salinity and customarily ranges from 6 to 13 for sea water. Therefore,

$$\delta_k \approx \frac{1}{2} \delta_v \qquad (2.13)$$

indicating the molecular conductive layer is thinner than the viscous layer.

Accepting the rigid boundary analogy, the molecular conduction layer co-exists with a slightly larger viscous layer whose thickness is inversely proportional to the square root of the wind stress. Combining (2.5b), (2.6), and (2.13), the temperature difference can be written as,

$$\Delta T = -\lambda_o \frac{\nu Q_{net}}{k u_{*w}} \qquad (2.14)$$

assuming the thermal and viscous layers are of the same magnitude. The constant of proportionality λ_o is determined experimentally and absorbs the effects of the transfer of tangential wind stress to the ocean's surface shear stress and the relative deviation between the molecular conductive and viscous layers.

Although latent and sensible heat fluxes and friction velocity all increase proportionally with wind speed, ΔT may increase, decrease, or remain the same. For a given net upward heat flux, ΔT decreases with increasing wind speed. However, the net heat flux will not remain constant with increasing wind speed and may increase faster than the conduction layer decreases resulting in an increased ΔT. A continued increase in wind speed may eventually destroy the cool skin layer (Grassl, 1976; Schluessel *et al.*, 1990). Even when the skin layer is destroyed by the wind, it is conceivable that evaporation continues to cool the surface but the surface motion is powerful enough to prevent the total re-establishment of the skin layer.

2.3 Validity of Model

Saunders (1967a) based his model on the fact that the Richardson number for the upper meter of the ocean is small except in very light winds (< 2 m/s). The heat transfer is forced rather than free. Robinson *et al.*

(1984) point out that forced convection arises from shear flow driven by the surface shear stress and free convection is buoyancy driven. The ratio of gravitational forces associated with heat loss to the atmosphere and shear forces driven by the tangential wind stress is represented by the appropriate Richardson number

$$Ri = \frac{z}{L_{mo}} = \frac{gravitational\ forces}{shear\ forces} \tag{2.15}$$

where

$$L_{mo} = \frac{\rho_w u_{*w}^3}{Kg\overline{\rho'w'}} \tag{2.16}$$

is the Monin-Obukhov length, K is the von Kármán constant, g is the acceleration due to gravity, and $\overline{\rho'w'}$ is the vertical flux of density (Saunders, 1973; Robinson et al., 1984). Saunders (1973) showed that even for very light winds L_{mo} is of the order of 1 meter, and hence the flow is shear driven in the upper few centimeters. In dead calm, when the Richardson number is extremely large, the surface temperature of the ocean may still differ significantly from its interior value.

Free convection dominates with the absence of shear in the surface layer caused by vanishing ocean currents and wind speed. Grassl's (1976) experience during GATE Phase III led him to believe that conditions of dominant free convection do not occur when drift currents as small as 0.5 m/s and extremely slight wind conditions exist. Katsaros (1977), however, citing Hasse (1971), emphasizes that even with no mean water currents and with the wind speed dropping below 2 m/s, free convection is likely to dominate. According to studies of free convection between horizontal plates (Rossby, 1969; Chu and Goldstein, 1973) and with a free surface boundary (Katsaros et al., 1977), the net heat flux is given by

$$Q_{net} = Ak\left(\frac{gC_{te}}{\alpha v}\right)^{1/3} \Delta T^{4/3} \tag{2.17}$$

where C_{te} is the coefficient of thermal expansion and A is an arbitrary constant determined from experiment. The dimensional argument is summarized below.

Katsaros (1980a) comments that with no wind stress or waves on a water surface the motions are driven by buoyancy forces under conditions of upward heat flux. The cold boundary layer grows in depth by conduction, becomes unstable, collapses and sinks into the warmer bulk water below. In shallow layers, familiar Bénard convection cells of thermal circulation develop (Bénard, 1901). In deep enough water, the motions become turbulent and also independent of depth at a large enough Rayleigh number (approximately $> 10^7$). The Rayleigh number expresses the balance between the driving buoyancy forces and the diffusion of heat and momentum which retard the motion and tend to stabilize it. The Rayleigh number can be defined as

$$Ra = \frac{C_{te}g}{\alpha v} \Delta T d^3 \tag{2.18}$$

where d is the depth of water. The non-dimensionalized heat flux given by the Nusselt number

$$Nu = \frac{Q_{net}d}{k\Delta T} \tag{2.19}$$

is also a function of the Rayleigh number in the form

$$Nu = ARa^n \tag{2.20}$$

where n and A are experimentally-determined constants. Katsaros et al. (1977) provided an extensive study of the processes involved and determined $n \approx \frac{1}{3}$ and $A = 0.156$. Assuming depth independence, (2.18), (2.19), and (2.20) reduce to

$$\Delta T \sim Q_{net}^{\frac{3}{4}} \tag{2.21}$$

an abbreviated form of (2.17). Substituting Fourier's conduction law of (2.5b) into the previous equation we arrive at

$$\delta_k \sim Q_{net}^{-1/4}. \tag{2.22}$$

Therefore, in free turbulent convection, ΔT increases in magnitude with an increase in Q_{net} while δ_k decreases.

Katsaros *et al.* (1977) developed a schematic of the free convection processes involved in which three regions are portrayed in Figure 2.3. The aforementioned molecular layer resides closest to the surface and is thinner than that existing in forced convective flow and on the order of 0.1 δ_k. Just below, the thermal source layer of thickness on the order of 0.5 δ_k resides. Here, the colder, heavier water plunges while the warmer water from below advects vertically. Below this is the turbulent convective region where heat becomes well-mixed and stable.

2.4 <u>Field and Laboratory Observations of ΔT and Values for λ_o</u>

Woodcock (1941) and Woodcock and Stommel (1947) made some of the earliest observations of temperature profiles at the air-water interface on fresh and salt water ponds. Using a mercury thermometer 9 cm long and 1.5 mm in diameter, they measured ΔT's of 0.5 to 1.0 °C between the "surface" and 0.2 m depth while the wind speed was less than 2 m/s. The measurements occurred at night with the air 5 - 15 °C cooler than the water.

Obvious difficulties arise in measuring the molecular conduction layer with a device 1.5 mm in diameter. To avoid these, numerous experimenters have implemented infrared radiometers which measure the intensity of radiation emitted from the depths of about 10 - 100 μm, depending on the type of radiometer (Maul, 1985). Since the cool skin layer is on the order of a millimeter thick, this is truly representative of the
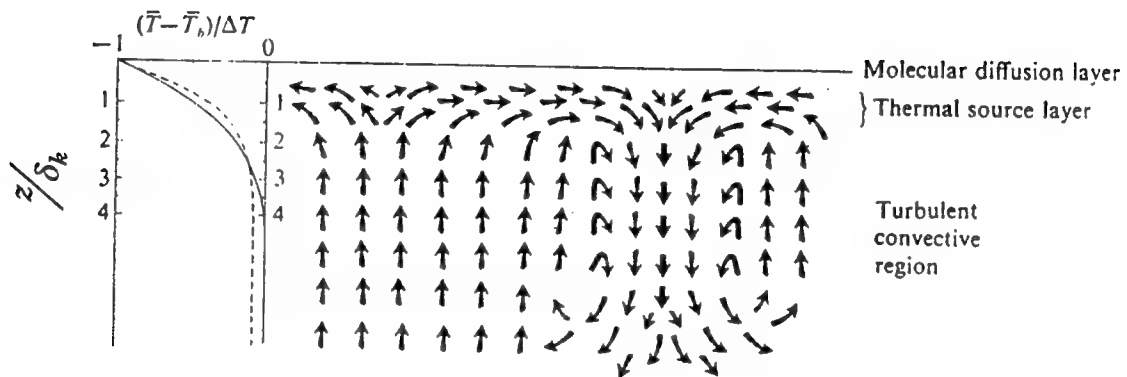
Figure 2.3   Schematic diagram of a model of the thermal boundary layer
delineating the source region of cold thermals. Solid line is the
theoretical mean temperature profile based on time-averaged
conductive profiles. Dashed line represents the mean observed
temperature profile. $\overline{T}$ is the mean observed temperature, $\overline{T}_b$
is the mean bulk temperature, ΔT is the total temperature
drop, and $\delta = \delta_k$ as defined from Equation (2.5) (from Katsaros
et al., 1977).

surface temperature. Ewing and McAlister (1960) employed a stirring technique shown in Figure 2.4 using a pump from below the water surface which essentially breaks the skin layer and mixes it with the water below. By doing this, they were able to measure directly with one instrument ΔT's near 0.6 °C at night off Scripp's Pier with a 0.5 m/s breeze. Hill (1972) and Katsaros (1977) also used this technique to measure ΔT's. Katsaros (1977) looked specifically at very low wind speed conditions, i.e. free convection, searching for extreme values of ΔT. She discovered average ΔT's which ranged from 0.4 to 2.4 °C in the lab and up to 2.5 °C in the field under various bulk air-water temperature differences. She shows the dependence of ΔT on the bulk air-water temperature difference in Figure 2.5 using results from her study along with previous investigators.

Saunders (1967b) made aerial radiometric measurements of the interface while correcting for the imperfect transparency of the atmosphere and nonblackness of the sea surface. Surface vessels, 300 m below, obtained bulk temperatures which amounted to ΔT's ranging from 0.2 to 0.35 °C. McAlister and McLeish (1969) made similar measurements of the skin layer in the laboratory with a radiometer close to the surface resulting in ΔT's of 1.0 °C with a wind speed of 4.5 m/s. Hill (1972) performed a laboratory experiment taking advantage of the stirring technique similarly employed by Ewing and McAlister (1960). He reported ΔT's ranging up to about 1.0 °C with $u_{*a} < 35$ cm/s ($U_{10} \approx 10$ m/s). This value for the aerodynamic friction velocity, u_{*a}, defined as

$$u_{*a} = \left(\frac{\tau_a}{\rho_a} \right)^{1/2} \qquad (2.23)$$

marked the change from aerodynamically smooth to rough flow as evidenced in Figures 2.6a and b. Accordingly, a large decrease in ΔT to 0.1 °C prominently distinguished this transition shown in Figure 2.7, where the reciprocal of the heat transfer coefficient, γ, is a measure of the ΔT.
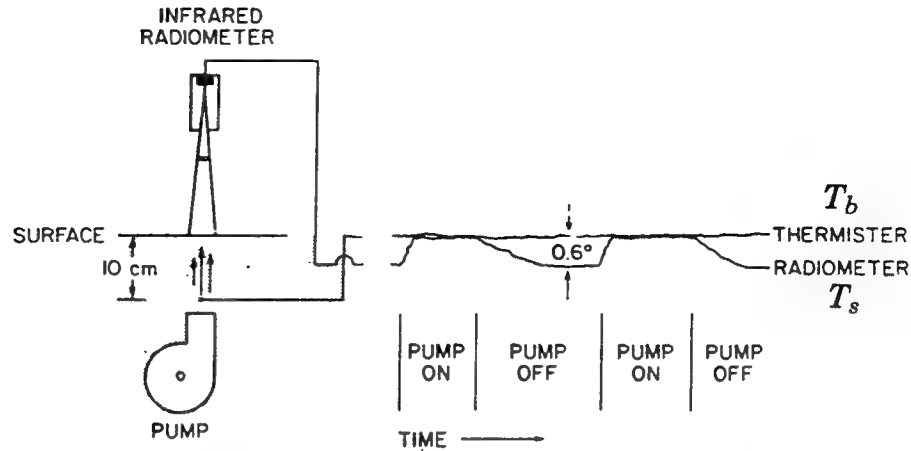
Figure 2.4   Schematic demonstration of the experimental set-up employed
by Ewing and McAlister (1960) to measure the bulk-skin
temperature difference, ΔT (from Maul, 1985).
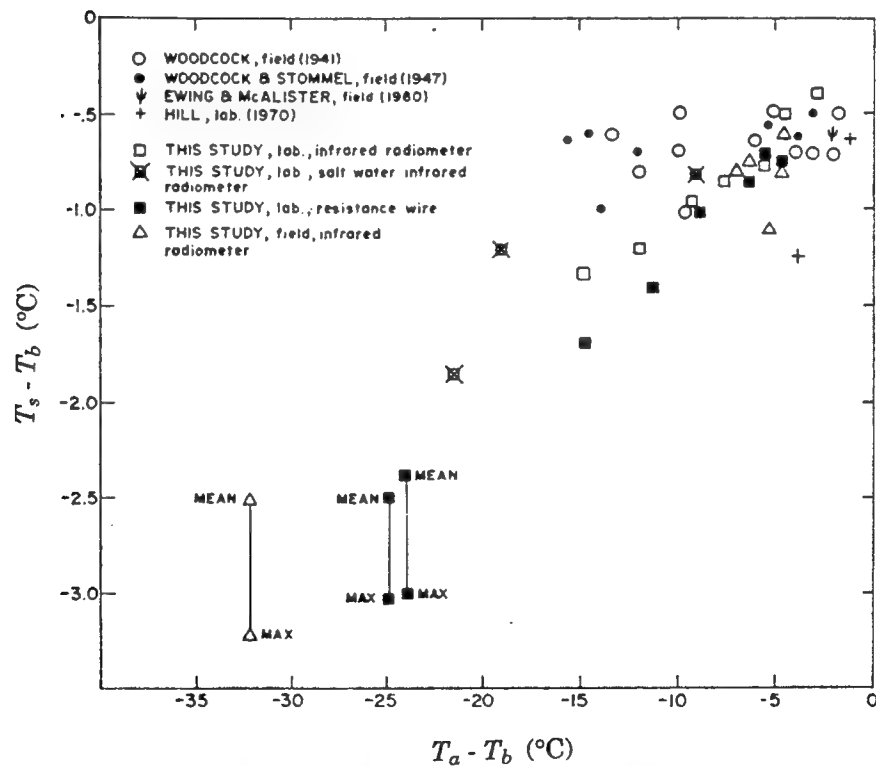
Figure 2.5   Measured values of negative temperature deviations of the free
surface boundary layer in water at low wind speeds versus air-
water temperature difference from several investigators (from
Katsaros, 1977).

a.

b.
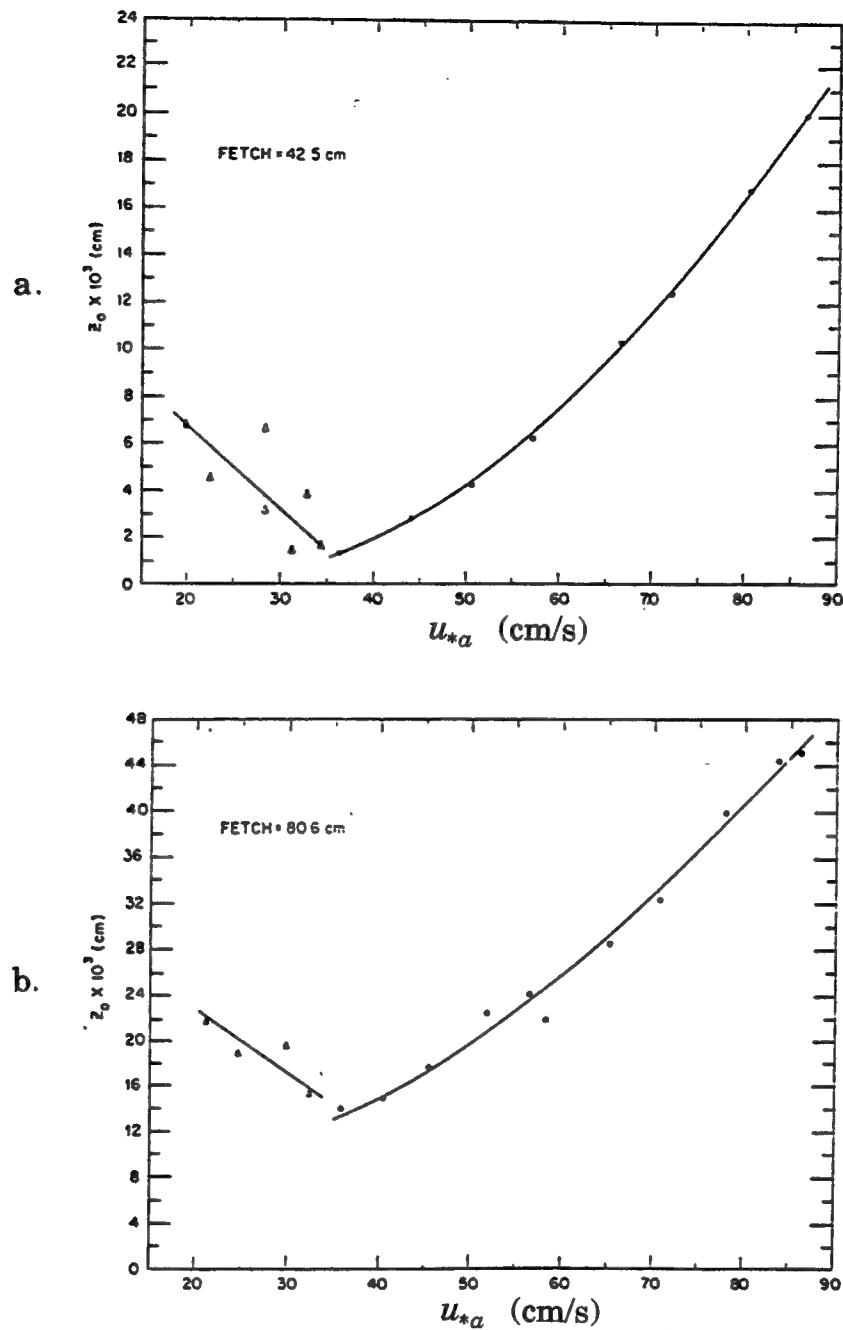
Figure 2.6a-b   Variation of roughness length, z_o, with aerodynamic friction velocity (from Hill, 1972). The roughness length, which is dependent upon wave conditions, describes the region within a wind velocity profile near the water surface where molecular effects dominate over turbulent ones.
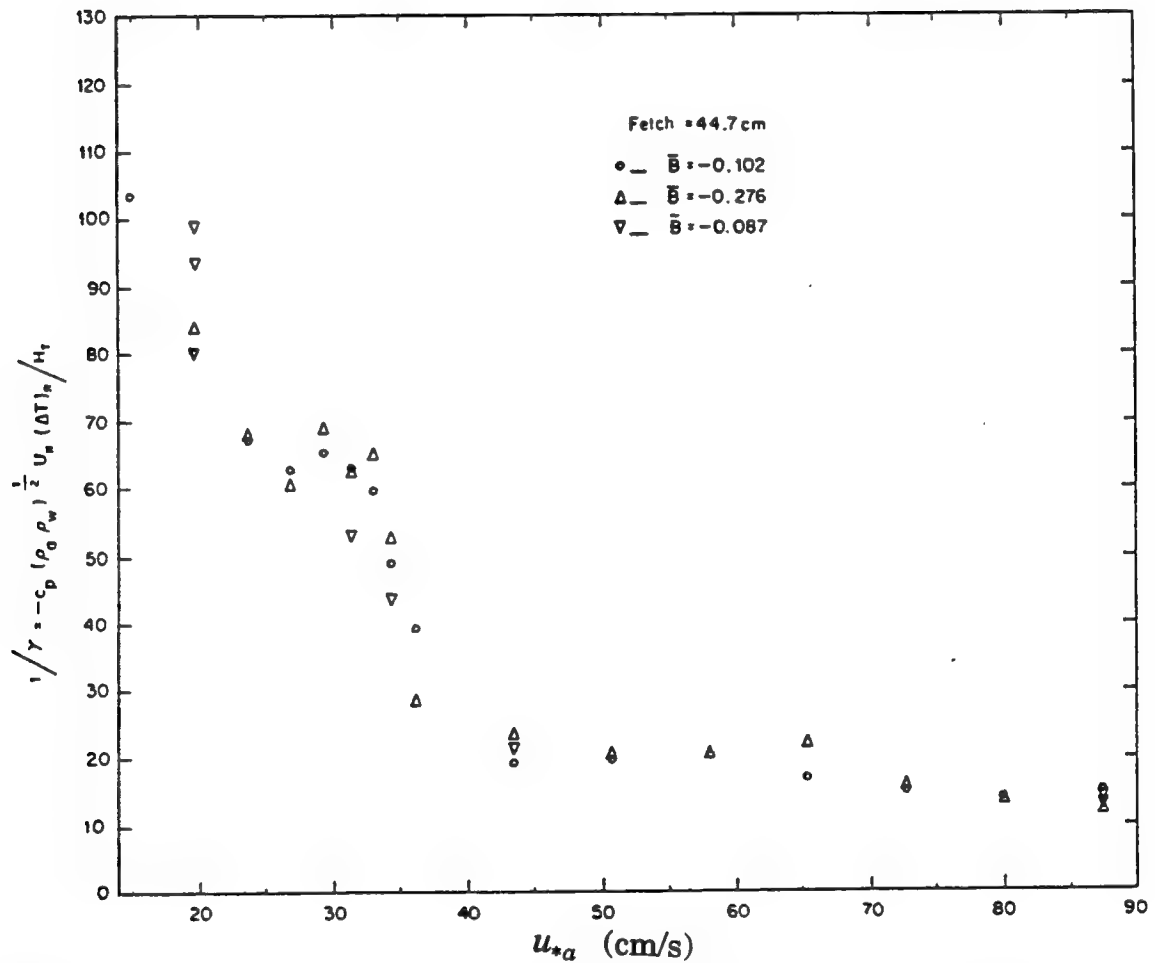
Figure 2.7   Variation of the reciprocal of water boundary layer heat transfer coefficient, γ, with local air-friction velocity for different Bowen ratios, $\overline{B}$, showing the transition from smooth to rough conditions. The Bowen ratio is that of sensible to latent heat flux (from Hill, 1972).

Hasse (1971) extended from Saunders the dependence of ΔT on the ratio of heat flux to wind speed and found nighttime $\Delta T's$ near 0.4 °C and daytime around 0.1 to 0.2 °C under moderate winds. Paulson and Parker (1972) used a similar laboratory apparatus as Hill (1972) to find $\Delta T's$ ranging from 1.1 to 1.8 °C under low wind conditions. They found an average value of $\lambda_o = 15$ to be independent of heat flux and wind stress as Saunders (1967a) had predicted, but which was larger than Saunders' suggested value of λ in the range of 5 to 10. Laboratory measurements by Hill (1970) show that $\lambda_o = 11$ without waves, while with wind-generated waves present $\lambda_o = 4$. The set of field data accumulated by Hasse (1971) shows $\lambda_o = 8$. This wide variety of values for λ_o suggests that possibly wave effects are significant.

Simultaneous to understanding more about gas exchange rate processes, Kanwisher (1963) originated the discussion of how waves could affect the heat budget and consequently the bulk-skin temperature difference and the molecular conduction layer. Figure 2.8 shows the effect of wind velocity and waves on the gas exchange rate. Without mechanically generated waves, notice the small effect of wind at low velocities until a critical value is reached which is interestingly about the same velocity where capillary waves commence (Keller, private communication). Kanwisher's measurements indicate that above this threshold wind velocity of 3 m/s, the gas exchange rate increases with the square of the velocity. Without wind and in the presence of mechanically generated waves, the gas exchange rate is enhanced. However, as wind is applied over mechanically generated waves, it reaches a velocity where the waves actually inhibit gas exchange as compared to the case without waves. Essentially, the gas flux is reduced by surface waves at higher wind speeds while augmented at lower ones.

We recall that λ_o absorbed the effects of the transfer of wind stress to the ocean's surface shear stress and wave generation, and the relative deviation between the molecular conductive and viscous layers. Numerous
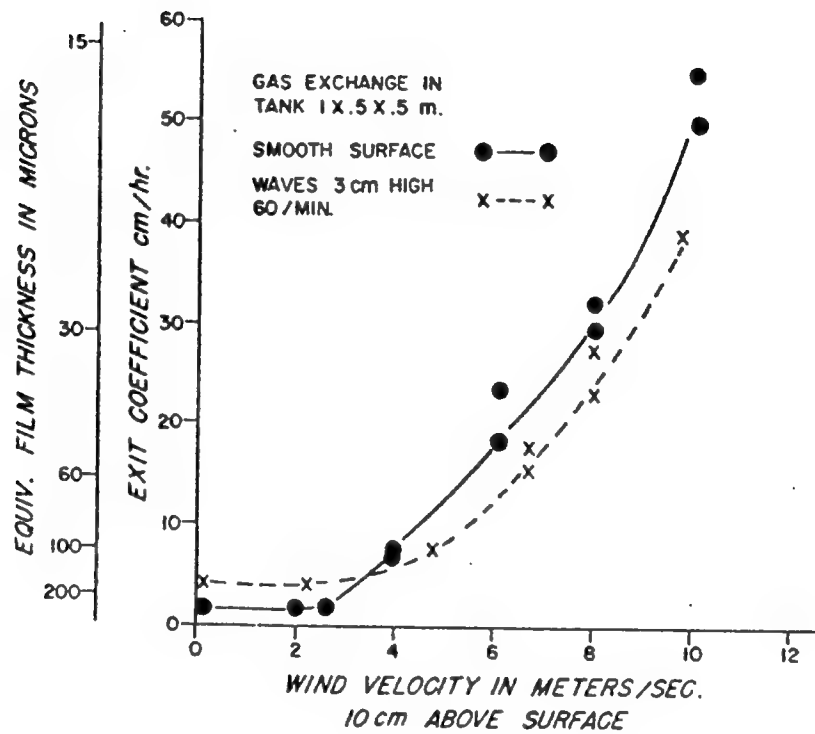
Figure 2.8   Liquid-air gas exchange variation with wind velocity. Waves accelerate exchange at low velocities and decrease it at high wind speeds (from Kanwisher, 1963).

authors (Saunders, 1967a; Paulson and Parker, 1972; Saunders, 1973; Robinson *et al.*, 1984) suggest the presence or absence of waves may be an important factor affecting the comparison of theory and observations. The appropriate τ in Saunders' model is not the wind stress, but the viscous stress in the molecular layer just below the air-water interface. As previously discussed, Saunders (1967a) replaced the viscous stress with the total wind stress, hence, approximating the friction velocity in the water as

$$u_{*w} = \left(C_D U_{10}^2 \frac{\rho_a}{\rho_w} \right)^{\frac{1}{2}} \qquad (2.24)$$

allowing the difference to be absorbed by λ_o. Measurements by Dobson (1971) indicate that as much as 80 % of the total wind stress is transferred into waves through normal pressure forces, allowing for only 20 % of τ_a to be transmitted by shear into the viscous sublayer. Hasselmann *et al.* (1973) concur with Dobson according to results during the JONSWAP experiment. The reduction in τ_a transmitted by shear results in a decrease in water friction velocity. Therefore, using the full wind stress to approximate the friction velocity in the ocean will tend to overestimate λ_o during the generation and maintenance of waves.

Grassl (1976) made field measurements and found, contrary to Hill (1970), that λ_o increased (from ≈ 2 to 6) with increasing wind speed ($U_{10} \approx 1$ to 10 m/s) as shown in Figure 2.9 while $\Delta T's$ ranged from 0.17 to 0.21 °C. He deduced that the strong variation of λ_o reveals that quite distinct parts of τ_a are used for wave generation at different wind speeds. Hence, he estimated the ratio of total wind stress, τ_a, and that part necessary to generate or maintain a wave field, τ_{wv}. The results displayed in Figure 2.10 suggest nearly complete usage of the wind stress for wave generation at low wind speeds which decreases sharply at higher wind speeds. Upon the generation of waves, less of τ_a is needed for the purposes of wave field maintenance as the wind speed increases allowing τ_a to come to approximate τ_w. Wesely (1979) complicates the problem further by reporting a rather stable $\lambda_o \approx 6$ or 7 for wind speeds ranging from 3 to 8.5
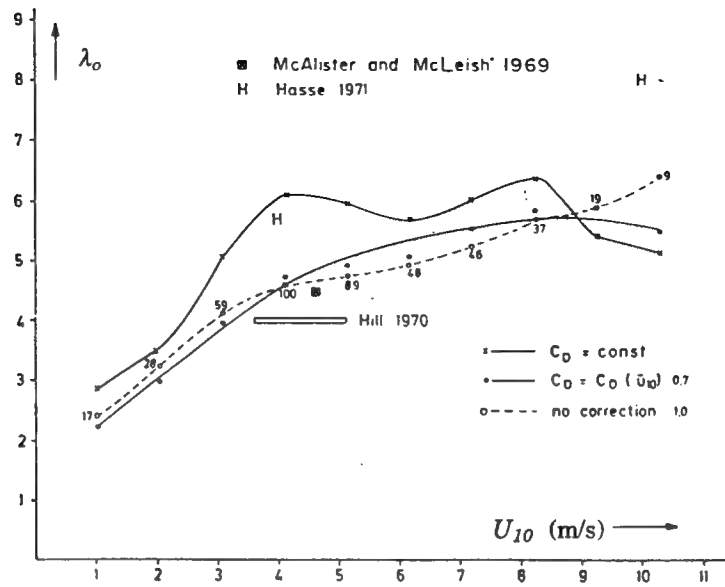
Figure 2.9   The dependence of the factor λ_o on the mean wind speed, U_{10}. Values presented in or derived from different publications are included. The line with crosses is valid for C_D held constant at 1.3×10^{-3}, while a corrected (open circles) and uncorrected (solid circles) bulk parameterization of the wind stress is also denoted. The correction for C_D is to counteract the shielding of the measurement area by the ship (from Grassl, 1976).
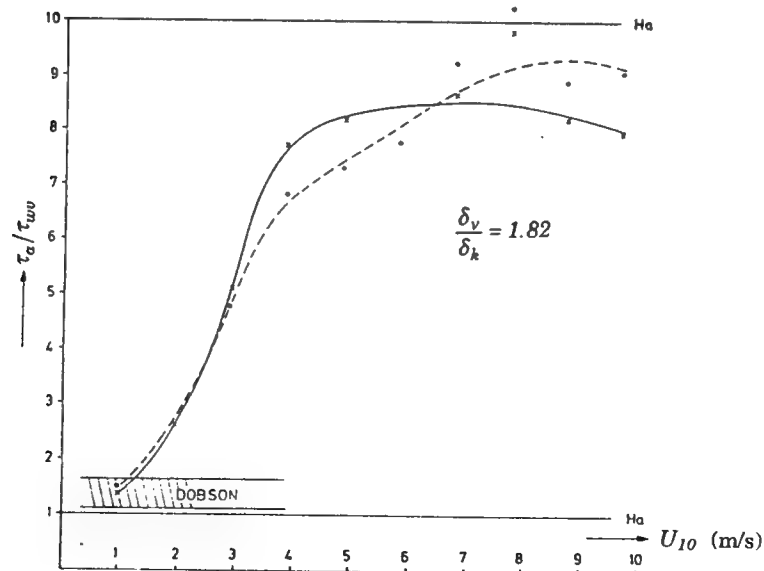
Figure 2.10   Total wind stress to wave supporting stress τ_a / τ_{wv} dependence on the mean wind speed U_{10} using $C_D = (0.63 + 0.066 U_{10}) \times 10^{-3}$. The dashed line was generated by omitting all of the data with $\Delta T \geq 0.4$ °C (from Grassl, 1976).

m/s and $\Delta T's$ from 0.3 to 1.5 °C on a cooling pond. He pointed out that the results of $\lambda_o = 6$ at a bulk water temperature of 15 °C and $\lambda_o = 7$ at 35 °C suggest the relative importance of the Prandtl number effect. Simpson and Paulson (1980) aboard R/P FLIP found $\Delta T's$ of 0.16 to 0.29 °C and $\lambda_o = 7$ for wind speeds of 5.6 to 9.2 m/s. The restricted range of wind speeds resulted in no conclusions about a possible variation in λ_o. On a similar yet separate FLIP experiment, Paulson and Simpson (1981) attempted to investigate the modification of λ_o with wind stress. They found a value of $\lambda_o = 6.5$ to be independent of wind speed for the range of 3 to 11 m/s. Upon further inspection of Grassl (1976), they noticed λ_o appeared relatively stable between 5 and 6 for wind speeds ranging from 4 to 10 m/s while steadily decreasing below 4 m/s. However, Schluessel *et al.* (1990) concluded that λ_o distinctly increases from 1 to 8 with increasing wind speed ($U_{10} \approx 1 - 11$ m/s). This trend corroborates Grassl's initial work relating λ_o with wind speed and is shown in Table 2.2.

Witting (1971) put forth another possible origin for the discrepancy. In a theoretical analysis, he revealed that steep capillary waves can decrease the temperature difference, ΔT, by a factor of 9 across infinitesimal molecular layers and about 7 - 8.5 for 1 - 2 mm layers. Irrotational non-breaking gravity waves were not nearly as effective (factor of only 1.38). Witting suggests that his theoretical results may constitute an explanation of the laboratory results of Hill (1970), who found an abrupt drop in ΔT by a factor of 3 while increasing wind speed and holding the average Q_{net} constant. In all of the cases the abatement occurred with the incipient generation of waves, usually capillary in nature. The drop in ΔT may simply have been a manifestation of the large decrease in temperature gradients necessary for heat conduction when capillary action takes place which could tend to decrease λ_o. The effect of wave action on temperature difference may have actually been greater than expected by Witting as λ_o may have been overestimated due to the reduced transfer of wind stress to the shear layer during wave generation. Witting also points out that if radiation and evaporation dominate ocean cooling, the average heat flux with waves present usually exceeds that without waves, agreeing

Table 2.2   Dependency of λ_o on wind speed (from Schluessel *et al.*, 1990).

U_{10} (m/s)	1	2	3	4	5	6	7	8	9	10	11
λ_o	1.1	2.2	2.2	2.0	2.9	4.0	4.5	4.7	5.9	8.0	8.4

Table 2.3   Depth of viscous boundary layer, total heat flux, temperature drop and λ_o as a function of mean wind speed (from Grassl, 1976).

U_{10} (m/s)	Q_{net} (W/m^2)	λ_o	ΔT (°C)	δ_ν (mm)
1	76.3	2.23	0.174	0.62
2	93.0	2.97	0.187	0.41
3	110.0	3.96	0.213	0.28
4	125.6	4.75	0.213	0.21
5	134.1	4.92	0.196	0.18
6	151.7	5.06	0.180	0.14
7	174.7	5.53	0.189	0.12
8	187.8	5.84	0.192	0.10
9	207.5	5.42	0.167	0.09
10	234.7	5.48	0.170	0.08

with Kanwisher's (1963) initial results for low wind speeds. Gravity waves
should outperform large amplitude capillary waves due to a possible
"blocking effect" induced by the absorption of radiation emitted from one
part of the wave at another location.

Despite the breadth of experiments, conclusive evidence remains
elusive as too many seemingly contradictory reports exist. Compounding
the problem, it is difficult to compare laboratory experiments with large
(ocean) and small (ponds or lakes) scale field experiments especially when
such scatter is involved in the findings. Moreover, the skin layer appears to
be more and more a local phenomenon and thus the goal of a universal λ_o is
less fruitful. Regardless, obvious discrepancies continue to emerge and
point to the numerous unknown factors associated with the air-water
interface. In opposition to a rigid boundary condition, Saunders (1973)
points out that the existence of the free boundary allows for flow parallel to
the air-sea interface which reduces the sublayer thickness. Therefore, in
addition to the wave effects listed above, surface tension may also modify λ_o
and ΔT.

Surface tension, σ, of clean water is a strong function of temperature.
The surface tension of cold water is greater than that of warmer water.
The Marangoni effect is motion energized by surface tension gradients.
Surface tension variations due to temperature create motions from warm to
cold regions (areas of lower surface tension spread into areas of higher
surface tension). Katsaros (1980a) states that under low wind speeds, the
Marangoni effect is most important in the initial stages of free convection in
deep water. The effects of buoyancy dominate the form of convection in the
deeper layers while the surface tension affects the thin surface layers of
water (< 2 cm). As the convection reaches full development, the Marangoni
effect diminishes and begins to amplify the convection as a second order
effect.

Contamination of a surface affects the surface tension and its
temperature dependence (Katsaros, 1977). While surfactants reduce

$\partial\sigma/\partial T$, other competing factors may offset this effect. For convection, divergent regions (warmer) retain less surface-active materials (higher surface tension) while the converging regions (cooler) contain more surfactants (lower surface tension). Therefore, the Marangoni effect may be diminished or possibly negated. Jarvis and Kagarise (1962) and Jarvis (1962) describe the suppression of water surface motion which exists when a surface-active material is present. They attribute the retardation of flow to a decrease in the Marangoni effect and the viscous stress on the water. Furthermore, by examining various surface-active monolayers (~ 20 Å or usually one molecule thick) with different hydrocarbon chain lengths and degrees of close-packedness, they report that some surfactant materials affect evaporation and thus alter the heat flux. The more close-packed and longer the hydrocarbon, the greater resistance to evaporation at high film pressures and thus higher recorded temperatures near the surface.

When certain slicks quell evaporation, the latent heat flux decreases, reducing the net heat flux exiting the ocean. The presence of a slick also inhibits the motion of the surface and the capacity of the wind stress to generate turbulence near the surface. The reduction in u_{*w} could result in the thickening of the viscous sublayer. Since the heat flux has diminished and the boundary layer thickness increased, the temperature change across the skin layer, ΔT, may be insignificant. The presence of most organic surface films at the air-sea interface, however, does not inhibit evaporation according to Garrett and Smith (1984). Even if the surface-active material does not hinder evaporation, the slick still will provide a reduction in u_{*w}. As the net heat flux remains constant, the bulk-skin temperature difference will increase assuming the ocean is cooling off. In some cases where flow is converging on the ocean surface, slicks conglomerate and become much thicker than 20 Å providing an extra layer through which molecular conduction occurs, thus increasing the ΔT.

2.5 Thickness for the Thermal Boundary Layer

During the development of the cool skin layer model in Section 2.2, the thermal boundary layer thickness was assumed to be on the order of a millimeter without any discussion of confirmation. Experimental results appear consistent with the hypothesis that a boundary layer exists at the ocean surface through which heat escapes predominantly by molecular conduction. Quantitative support for the skin layer depth is presented here. In one of the initial estimations of laminar sublayer thickness, Kanwisher (1963) demonstrated the existence of the laminar sublayer at the water surface under moderate wind speeds in laboratory experiments on gas exchange rates between air and water. According to the gas exchange rate equation used by Kanwisher,

$$Gas\ Flux = \frac{\Delta concentration \cdot diffusibility}{thickness} \qquad (2.25)$$

where the Δ concentration is found from the solubility times the change in partial pressures of air and water. Previously, we spoke at length regarding the effect of wind and waves on the gas exchange rate. From (2.25), the gas flux is inversely proportional to the thickness of the diffusive layer and consequently the wind and waves have the opposite effect upon the sublayer as seen in Figure 2.8.

More formal estimates of the skin layer depth were deduced by McAlister (1964) and McAlister and McLeish (1965). They developed a two-wavelength region infrared radiometer to effectively measure the temperature at two depths, 0.06 and 0.50 mm, simultaneously. Calculation of the heat flux by Fourier's law proved to be within experimental error of the total heat flux from the surface. They concluded that the result indicated that conduction dominated and occurred within the top millimeter. McAlister and McLeish (1969) expanded their own discussion to look at the effects of wind speed (i.e. turbulence). Previously, they had obtained results for wind speeds of 2 to 3 m/s. Using the previous radiometer setup, they observed the effects of higher wind speeds up to 10 m/s and found that above 5 m/s increasing deviations from the predicted

temperature profiles resulted. According to this result, the conduction
layer had thinned to shallower depths than the measurement range used.
By employing another two-wavelength region infrared radiometer
measuring down to only 0.025 and 0.075 mm they believed that turbulence
would not affect the flow within the measured region. Thus the first
estimates of the skin layer were on the order of a millimeter even for wind
speeds up to 10 m/s. More recently, McKeown (1993) utilized an
interferometer sensing radiation in the 2 to 5 μm wavelength range. The
technique directly measures a continuous temperature profile within the
first 100 μm at the air-water interface with possible applications for suitable
instruments down to 1 mm.

Wu (1971) also provided an estimation of the oceanic thermal
boundary layer thickness. He used the analysis provided in Section 2.2,
specifically von Kármán's laminar sublayer thickness relation

$$\delta_v = 11.5 \frac{v}{u_{*w}} \tag{2.26}$$

in conjunction with the results of 30 independent field investigations of
wind stress and C_D, where u_{*w} is defined by (2.24). Summarizing the
results shown in Figure 2.11, he found the thermal layer estimated between
4 and 0.25 mm for $U_{10} < 15$ m/s and between 0.25 and 0.1 mm for $U_{10} > 15$
m/s and explicitly showed the dependence of the Prandtl number by
displaying both the viscous and thermal estimates which are half δ_v. Note
that the analysis by Wu assumes the air-water interface acts as a solid
boundary.

Hill (1972) derived a formula combining Fourier's conduction law in
(2.5b) with a heat transfer equation of the form

$$Q_{net} = -\gamma c_{pw} \left(\rho_w \rho_a\right)^{\frac{1}{2}} (\Delta T) u_{*a} \tag{2.27}$$
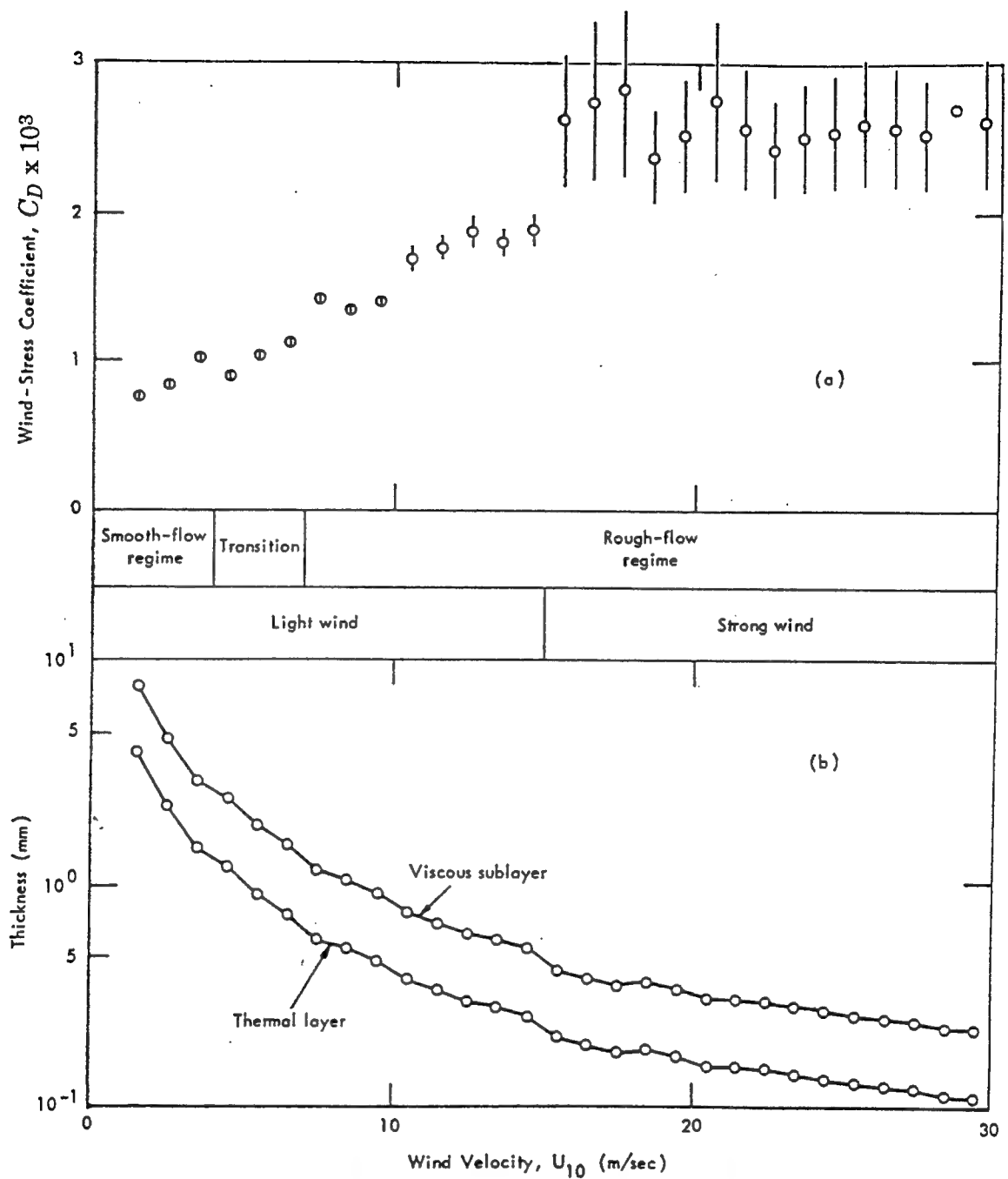
Figure 2.11 Wind-stress coefficient, viscous-sublayer thickness, and thermal-layer thickness at different sea conditions (from Wu, 1971).

where c_{pw} is the isobaric specific heat of water and γ is the experimentally determined heat transfer coefficient to arrive at

$$\delta_k = \frac{k}{c_{pw}(\rho_w \rho_a)^{1/2}}\left(\frac{1}{\gamma u_{*a}}\right).$$

(2.28)

Using measurements from Hill (1970) along with (2.28), he calculated the variation of water boundary layer thickness with local air-friction velocity as displayed in Figure 2.12. Of particular interest, the skin layer ranges between 2.0 and 0.5 mm for $u_{*a} < 35$ cm/s ($U_{10} \approx 10$ m/s) and for the rough regime of $u_{*a} > 35$ cm/s it ranges down to 0.07 mm at the highest wind speeds. Although Hill and Wu made estimates of the same order, discrepancies did emerge.

The model which has been employed throughout this chapter assumes that the skin layer is similar to that which would exist over a rigid surface as evidenced by (2.26). Wu's (1971) estimate specifically does not consider surface tension, σ, although it would appear that it must play some role in determining the thermal boundary layer thickness. Surface tension will allow the interface some rigidity but less than a solid boundary. Levich (1962) derived an expression for the laminar sublayer thickness of a free-falling thin film, assuming surface tension as the mechanism of turbulence damping near the surface. Omholt (1973) suggests his result

$$\delta_{v\sigma} = B\left[\frac{\nu(\sigma/\rho_w)}{u_{*w}^3}\right]^{1/2}$$

(2.29)

should also be applicable to the ocean surface, where B is a dimensionless constant and $\delta_{v\sigma}$ is the viscous sublayer accounting for surface tension. Figure 2.13 shows the sublayer thicknesses calculated from (2.26) and (2.29) along with the indirect estimates by Hill (1972) from measurements of heat flux and temperature differences across the skin layer. According to (2.29),
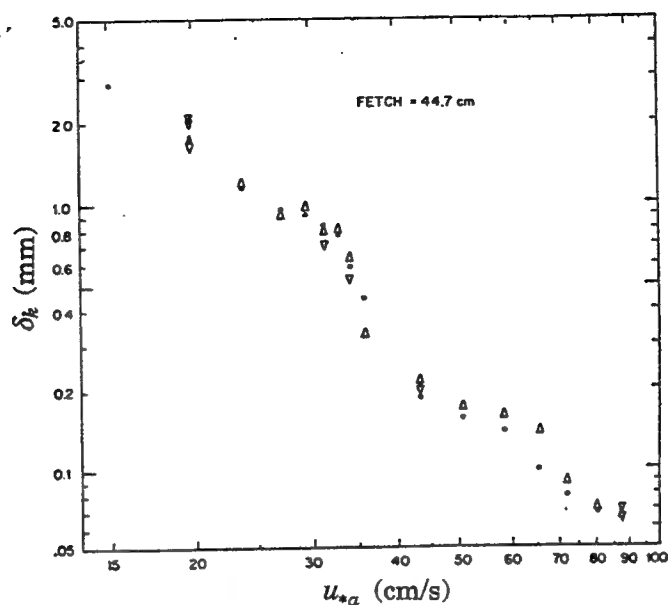
Figure 2.12 Variation in calculated water boundary layer thickness with local air-friction velocity (from Hill, 1972).
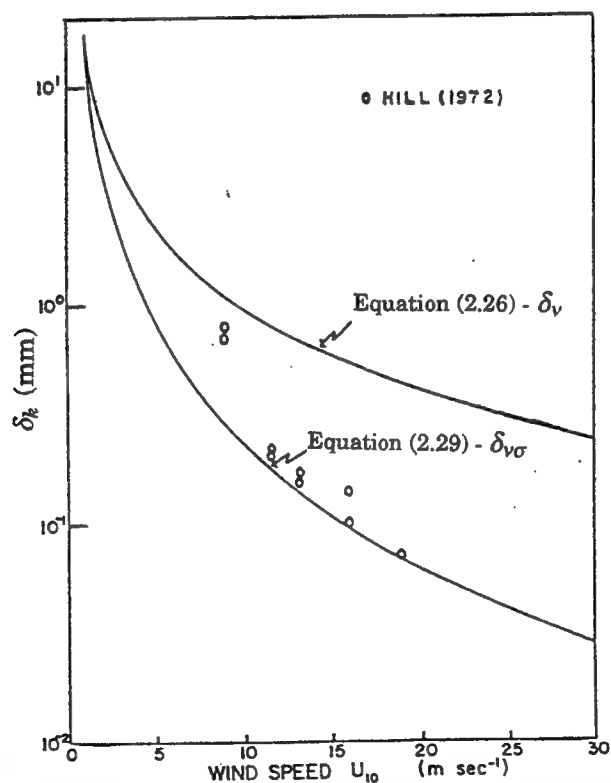
Figure 2.13 The oceanic sublayer thickness. The curves associated with Equations (2.26) and (2.29) depict the viscous sublayer, while Hill's (1972) data represent the thermal boundary layer thickness.

the boundary layer thickness accounting for surface tension decreases faster with increasing wind speed than for (2.26). The close agreement between (2.29) and Hill's estimates may be coincidental. The equations of (2.26) and (2.29) are used for calculating the viscous sublayer which is expected to be larger than the thermal sublayer attained by Hill. The importance of Omholt (1973), however, is in raising discussion of the free surface boundary condition.

Saunders (1973) continues this discussion and points out that while the wind regards the sea surface as an undulating rigid boundary, the ocean treats the interface as a free boundary. From either perspective, fluid velocities normal to the moving boundary must vanish while the free surface supports non-zero velocities parallel to it. Only on a rigid boundary must the parallel components also vanish (i.e. the no-slip condition). In order to better understand the physical properties of the viscous sublayer, several authors have attempted to measure the velocity profile at the surface. McLeish and Putland (1975) performed one such investigation using clouds of microscopic hydrogen bubbles as tracers in a wind-water tunnel experiment. Figures 2.14a-b show the downwind (U) and crosswind (V) mean water velocities produced by a 9.0 and 5.5 m/s air flow respectively. Both flows were essentially laminar and show the viscous layer to be on the order of a millimeter. Figure 2.15 represents the velocity profile produced from the same air speed of 5.5 m/s at a position farther downstream where the flow was fully turbulent. The linear portion of the profile at the surface indicates the viscous sublayer which is thinner than the computed profile at a solid boundary with the same stress shown by the straight and curved lines in Figure 2.15.

Grassl (1976) tabulated values for λ_o and calculated the viscous boundary layer from field measurements using

$$\delta_v = \frac{k\Delta T}{\lambda_o Q_{net}}$$

(2.30)
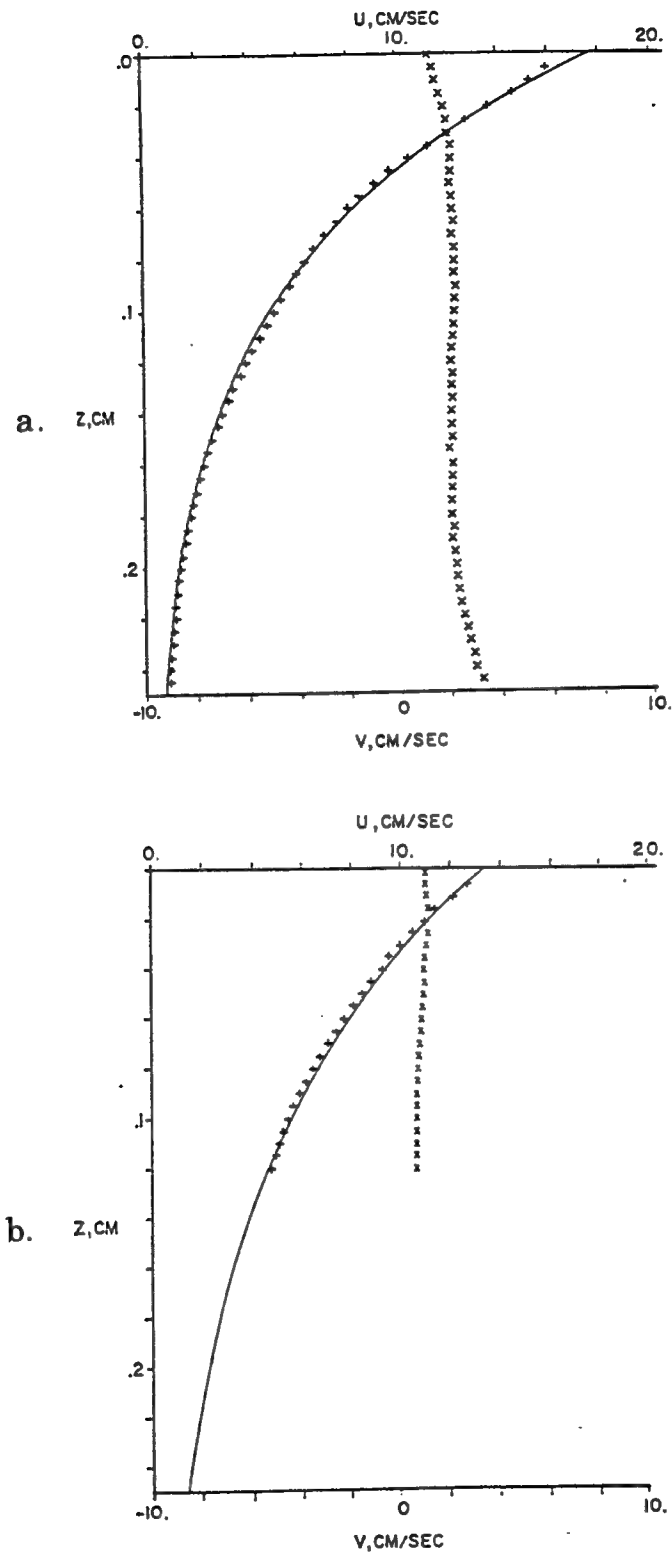
Figure 2.14a-b   Water velocity profile in an essentially laminar flow, +
downwind and x crosswind. The fitted line is an
exponential curve (from McLeish and Putland, 1975).
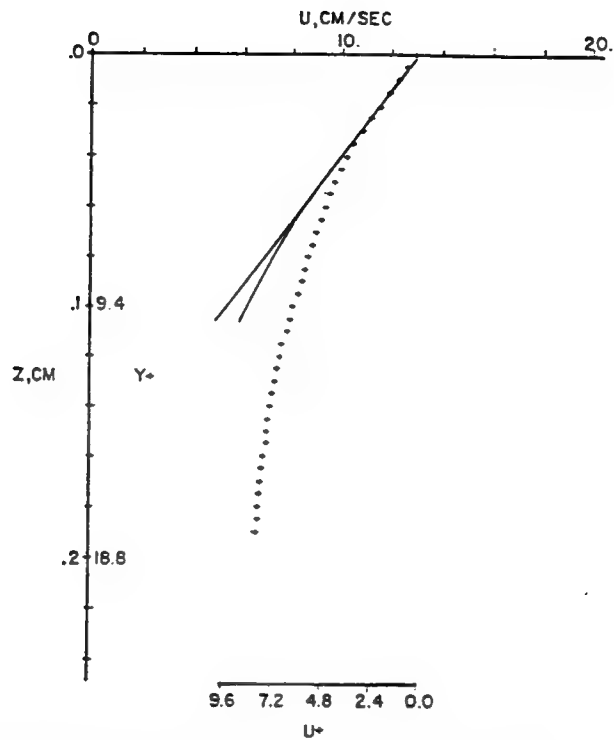
Figure 2.15 Water velocity profile in a turbulent flow. The straight line fits
the surface slope, and the curved departing line follows the
mean profile at a solid boundary (from McLeish and Putland,
1975).
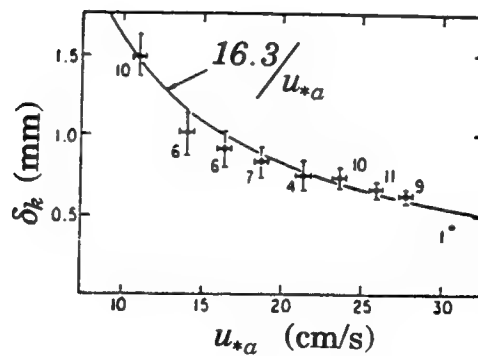
Figure 2.16 Values of δ_k estimated from Equation (2.5) versus u_{*a}
calculated from the bulk aerodynamic relationships. The
numbers near the points and the standard error bars are the
number of 10-min samples used (from Wesely, 1979).

from the combination of (2.6) and (2.14). The values are listed in Table 2.3. Khundzhua *et al.* (1977) measured the temperature gradient across the interface of the Black Sea and found that for wind speeds of up to 6 - 8 m/s, the temperature profile is linear in a layer 0.2 - 0.6 mm while the full non-linear profile extended down to 3.5 mm on average. Finally, Wesely (1979) estimated the thickness of the thermal boundary layer from measurements over a cooling pond and found the results shown in Figure 2.16.

2.6 Breaking of the Skin Layer

As we have seen, numerous authors have reported detection of a cool surface layer at wind speeds up to 10 m/s. As noted earlier, however, the cool skin layer can be destroyed resulting in an increase in the infrared surface temperature. When the friction velocity increases up to a critical point and beyond, the turbulent eddies from below intermittently penetrate and disrupt the conduction layer allowing the underlying warmer water to mix up to the surface. Many authors have encountered this phenomenon upon which the re-establishment process of the cool skin layer by molecular conduction will commence. Kline *et al.* (1967) described the encroachment of the laminar boundary layer by turbulent eddies which rip at and remove fluid from this laminar region. The process outlined by Kline *et al.* is known as "surface renewal" and limits the growth of the thermal boundary layer in both δ_k and ΔT. Jarvis (1962) also acknowledged that increased air velocity over a water surface would increase surface mixing, but was more interested in slicks' effects on surface motion and evaporation. Saunders' (1967a) model, then, provides an impetus for a comprehensive study into the wind speed "threshold" which has yet to be explored.

Liu and Businger (1975) predicted non-linear temperature profiles not only for forced convection according to the observations of Kline *et al.* (1967) but also for free convection from the observations of Townsend (1959) and Spangenberg and Rowland (1961). Khundzhua *et al.* (1977) and Khundzhua and Andreyev (1974) verified these predictions in the field while

Katsaros *et al.* (1977) did so in the laboratory. Regardless of whether free or forced convection dominates, surface renewal due to either turbulent bursting ejecting fluid into the boundary layer or the instability of negatively buoyant plumes results in highly non-linear mean temperature profiles.

Wave breaking also disrupts the skin layer. Several authors have investigated, or observed, the effect of breaking waves on the infrared measurements. The stirring technique described by Ewing and McAlister (1960) demonstrated the effect. Using a pump lowered 15 cm beneath the water which produced a jet of the warmer underlying water directed towards the surface, they effectively broke the skin layer. A warm infrared temperature signature resulted which approximated the thermistor measured bulk water near the pump. When the pump was turned off, the cool skin layer re-established within 5 seconds. They also reported an inability to measure the effects from less substantial disturbances. Again, a possible threshold may exist below which the skin layer remains unbroken. Ewing and McAlister (1960) also made measurements of actual breaking waves which are consistent with those of the impinging jet upon the surface. Simultaneous with a breaking event, they observed a transient increase in the infrared surface temperature. Contrary to the pump demonstration, a stronger, more enduring, cool signature associated with the foam of a breaking wave appeared. The complete signature proceeded for roughly 12 seconds, upon which the cool skin layer returned.

Gasparovic *et al.* (1974) also clearly demonstrate this effect from field measurements made aboard the R/V Cove. Figure 2.17 graphically illustrates the spontaneous momentary spike in the apparent infrared temperature (~ 0.25 °C). As the vessel was in transit during the measurement, the cold signature accompanying the foam due to breaking as observed by Ewing and McAlister (1960) is noticeably absent from the record. Simpson and Paulson (1980), using a radiometer aboard the R/P FLIP, propose that during the passage of varying amplitude waves, occasional warm temperature spikes of 0.3 °C correspond to areas where the wave action has thinned and even destroyed the surface skin. The wave
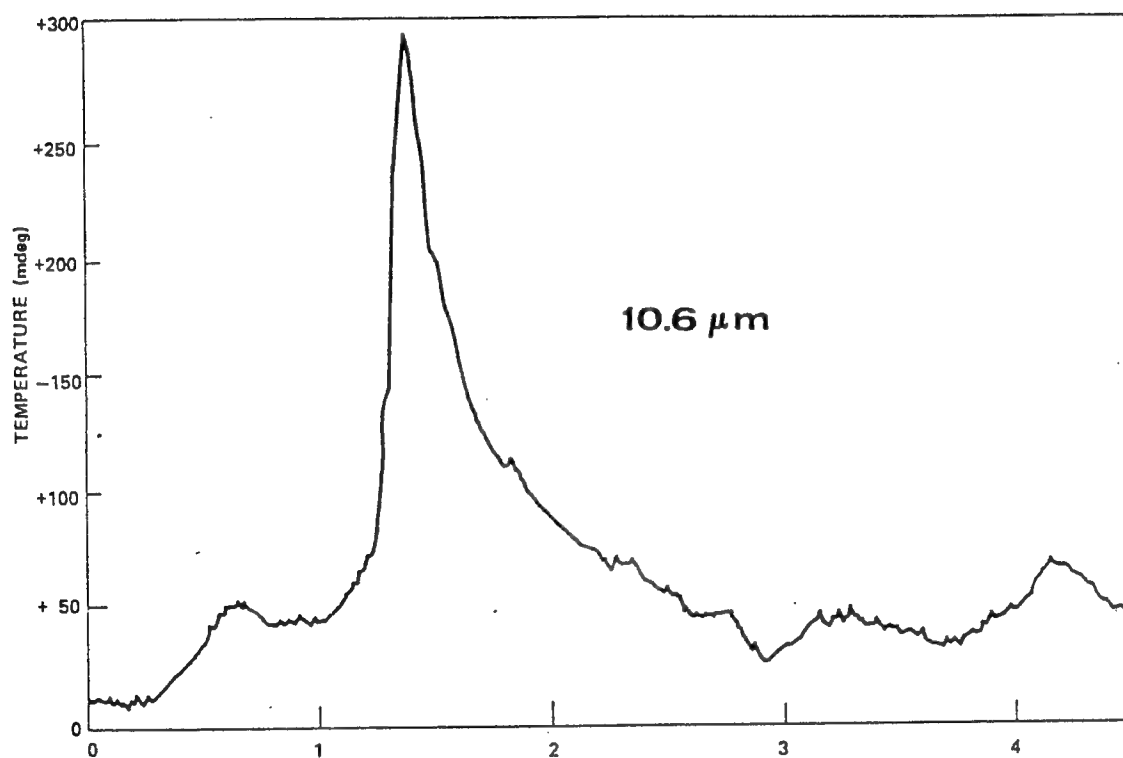
Figure 2.17 Apparent temperature increase recorded at 20° incidence
angle when a surface wave broke within the field-of-view on
the night of August 16, 1973 (from Gasparovic *et al.*, 1974).

behavior discussed involved two scenarios. Specifically, they conjectured that breaking and capillary wave enhancement on the steeply sloping side of the shorter period gravity waves (0.4 Hz) could rupture the surface layer. Likewise, upwind on the lee side of the dominant swell (0.06 Hz), locally enhanced wind stress could thin the thermal viscous layer either directly or through the generation of capillary waves (Witting, 1971).

Witting (1972) discusses the possible mechanisms which induce the variation in temperature difference on the ocean surface. The passage of surface waves produces a straining of the thermal boundary layer resulting in compression and thickening of the sublayer on the crest while expansion and thinning in the trough. Assuming a uniform conductive heat transfer across the interface, Witting calculated measurable fluctuations in skin temperature for sufficiently small wave periods (< 3 sec). His computations showed that surface temperature maximums lead the wave crests by 1/8 of a period for $\Delta T > 0$ and minimums similarly lead for $\Delta T < 0$. Miller and Street (1978) performed laboratory experiments with mechanically generated waves propagating in the same direction as the wind speed, which ranged from 1 - 10 m/s, and measured the amplitudes and phases of temperature waves for negative heat flux. The amplitude of the temperature wave is defined as $\Delta \tilde{T}_s = T_{s_{max}} - T_{s_{min}}$ and is directly proportional to the bulk-skin temperature difference, ΔT. In agreement with Witting's (1972) theory, the peak of the temperature wave occurred on the leeward side of the mechanical wave at low wind speeds (radiation dominating the heat transfer). However, the character of the temperature wave is strongly dependent upon the wind speed. For moderate to high winds (latent and sensible heat fluxes dominant), the temperature wave is relatively larger with its trough on the leeward side. Field investigators have suggested that at wind speeds greater than 10 m/s, the thermal boundary layer is completely eliminated due to the breaking processes (Grassl, 1976; Schluessel et al., 1990). Grassl suggests that because "white capping" dominates above 10 m/s, a renewal time for the skin layer of 10 seconds reported by Clauss et al. (1970) is inadequate to re-establish the layer. Schluessel et al. (1990), however, acknowledge the fact that the cool

skin layer does recover within 10 to 12 seconds as described by Ewing and McAlister (1960) and Clauss et al. (1970).

In a recent article, Jessup (1993) produced a 2-D mapping of the sea surface using an infrared scanner resulting in a sequence of breaking wave images depicting the disruption of the skin layer (apparent maximum $\Delta T \sim 0.4\ ^\circ C$) as seen in Figure 2.18. The warm patch in the wake of the breaker observed during 8 m/s winds persists for only 1 second, contrary to the previous reports of 10 to 12 second skin layer recovery times. He also reports, from comparing daytime infrared breaking wave sequences with video images, that the infrared images show no noticeable decrease in surface temperature from the effect of the foam as seen in Figures 2.19a and b. The actively breaking crest, however, produces a significant signature both during the day and at night, while the warm turbulent wake is only prevalent at night. These results suggest that the actively breaking crest actually produces an apparent change in the measurement, possibly due to reflections from different, or all, parts of the sky, along with changes in emissivity caused by increased surface roughness. These electromagnetic properties and others will be discussed thoroughly in the ensuing chapter.

Jessup (1993) also argues that the discrepancy between his recovery time of 1 second, as opposed to 10 to 12 seconds reported by Ewing and McAlister (1960) and Clauss et al. (1970), suggests that the skin layer renewal time is a function of wind speed. Statistics presented by Jessup et al. (1991) showed at a fixed point for a wind speed of 10 m/s, breaking crests occurred 10 to 20 % of the time. Assuming an intermission of several wave periods between breakers, the skin layer would have plenty of time to recover even for a renewal time of 10 to 12 seconds, contrary to Grassl's hypothesis. The measurement by Jessup (1993) of 1 second recovery times supports the conjecture of its wind speed dependence and that solely the breaking process cannot explain the skin layer's destruction. The subject of skin layer recovery is crucial to the premise of this thesis.
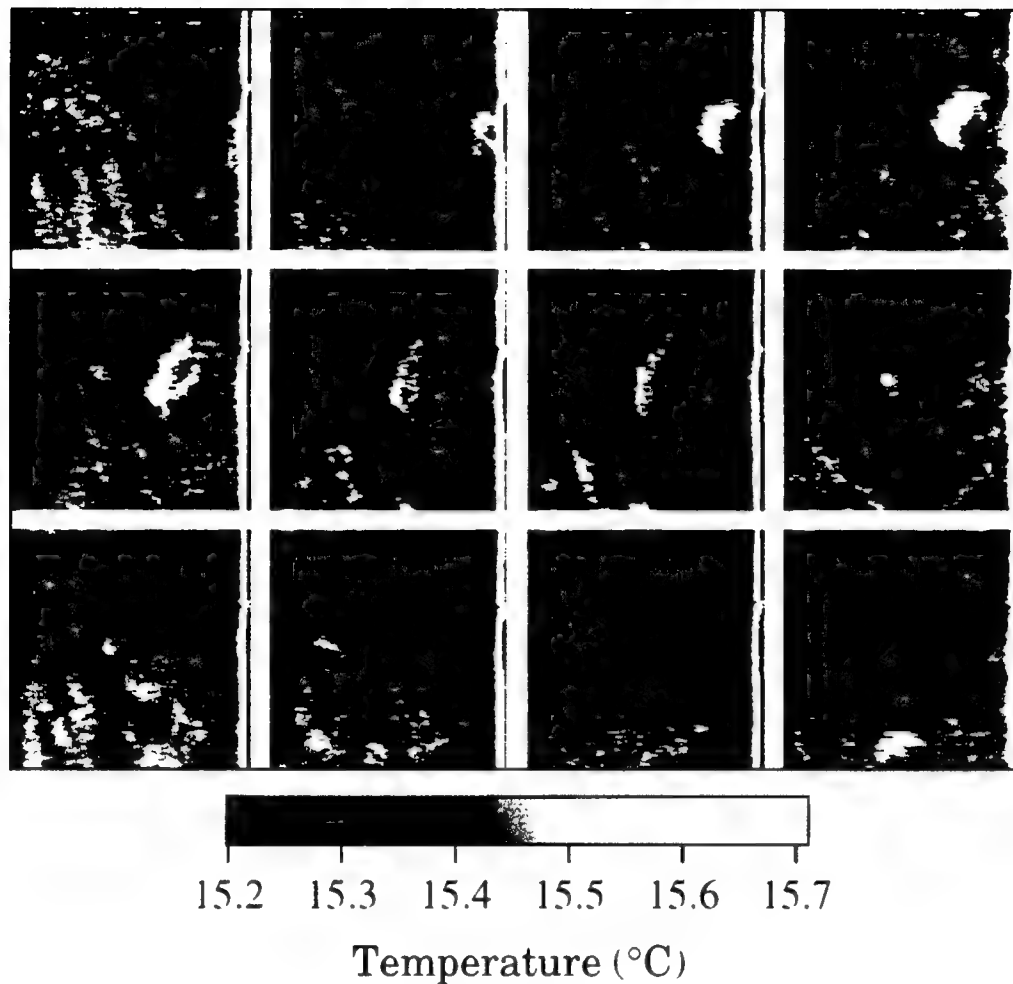
Figure 2.18 Nighttime sequence of infrared images of a breaking wave under moderate wind speed of 8 m/s and large swell (SWH 4.0 m) showing apparent temperature change associated with the actively breaking crest. Time increases left to right, top to bottom; each frame is approximately 10 m by 10 m with a time step of 0.32 s between frames. The roughly circular patch left behind after the wave breaks is interpreted as the disruption of skin layer due to the turbulent wake. The skin layer recovers in 1-2 s (from Jessup, 1993).
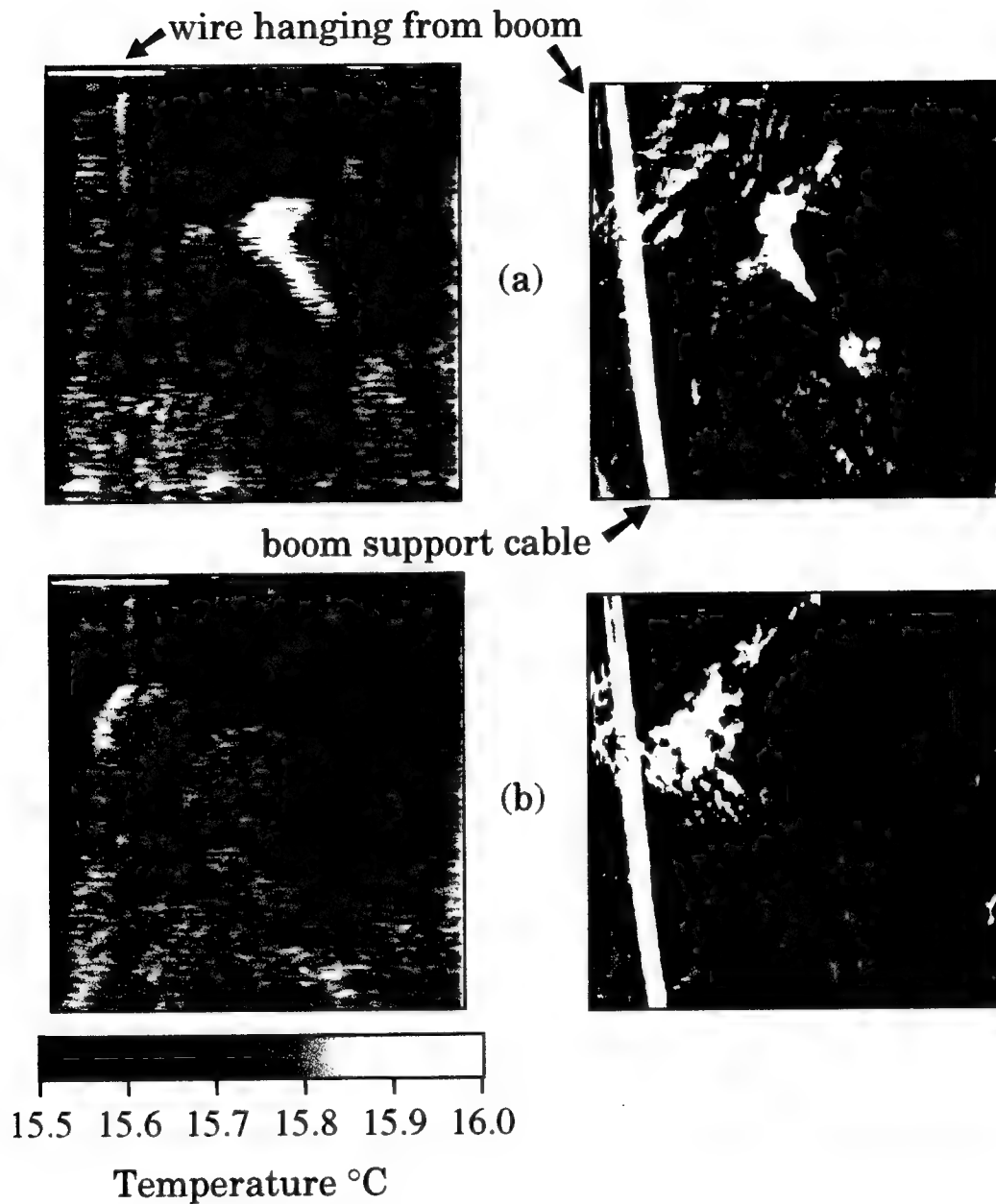
Figure 2.19a-b   Daytime breaking wave snapshots in the infrared and visible [(a) and (b) separated by approximately 1.9 s]. Notice the clearly denoted crest in both the infrared and visual (a), while no detectable signature of the foam exists in the infrared (b) (from Jessup, 1993).

CHAPTER 3

Electromagnetic Radiation

3.1 Introduction

Remote sensing of the ocean is the interpretation of electromagnetic radiation. Active remote sensors (e.g., those exploiting microwave wavelengths) incorporate a transmitter which strikes a target with radiation and then observes the reflected signal. On the contrary, passive remote sensing, usually associated with utilizing infrared, visible, and microwave wavelength sensors, relies on the detection of naturally occurring radiation. Since 1865, Maxwell's equations of the unified theory of electricity and magnetism have been used to predict the wave-like behavior of electromagnetic radiation. His analysis proved that the propagation speed of light in free space is related purely to electric and magnetic quantities by

$$c = \frac{1}{\sqrt{\varepsilon_o \mu_o}} = 2.9979 \times 10^8 \ ^m/_s \qquad (3.1)$$

where $\varepsilon_o = 8.85 \times 10^{-12}$ C^2/N-m^2 is the permittivity constant associated with Coulomb's law and $\mu_o = 4\pi \times 10^{-7}$ Tesla-m/ampere is the permeability constant associated with Ampere's law. Although referred to as the "speed of light", c is the speed of electromagnetic waves in general no matter what their wavelengths or frequencies. In addition, radiation traveling in free space at the speed of light does not require an intervening medium for its propagation as Maxwell's predecessors believed. His prediction led to the concept of the electromagnetic spectrum shown in Figure 3.1 where the nature and speed of all the waves is the same, differing only in frequency (v_e), and therefore wavelength (λ) through the relation

$$c = \lambda v_e. \qquad (3.2)$$
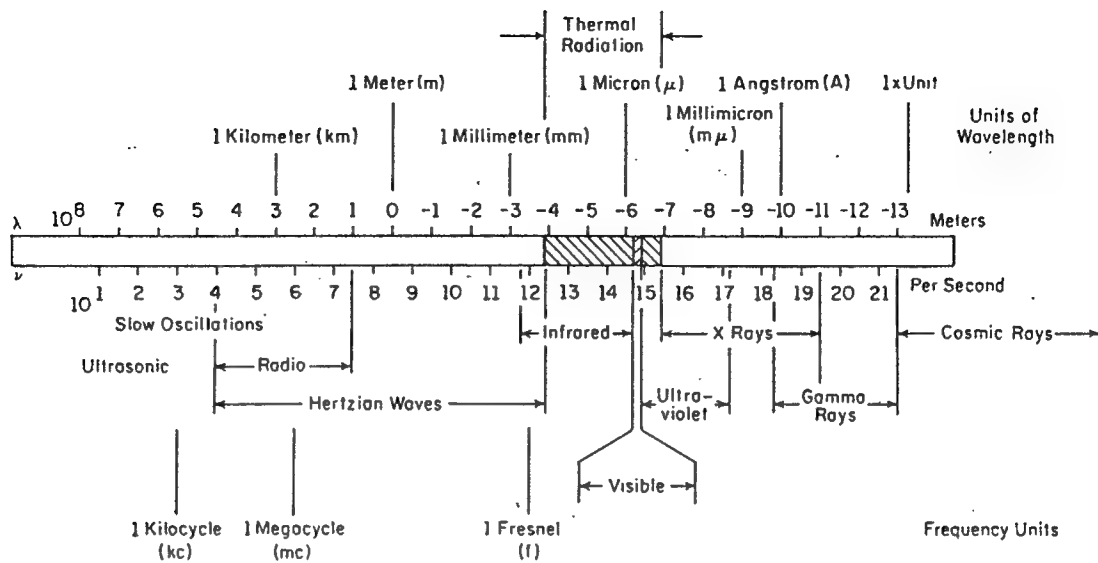
Figure 3.1 Electromagnetic wave spectrum. Infrared radiation ranges from 1 μm to 100 μm peaking at around 10 μm (from Kreith, 1962).
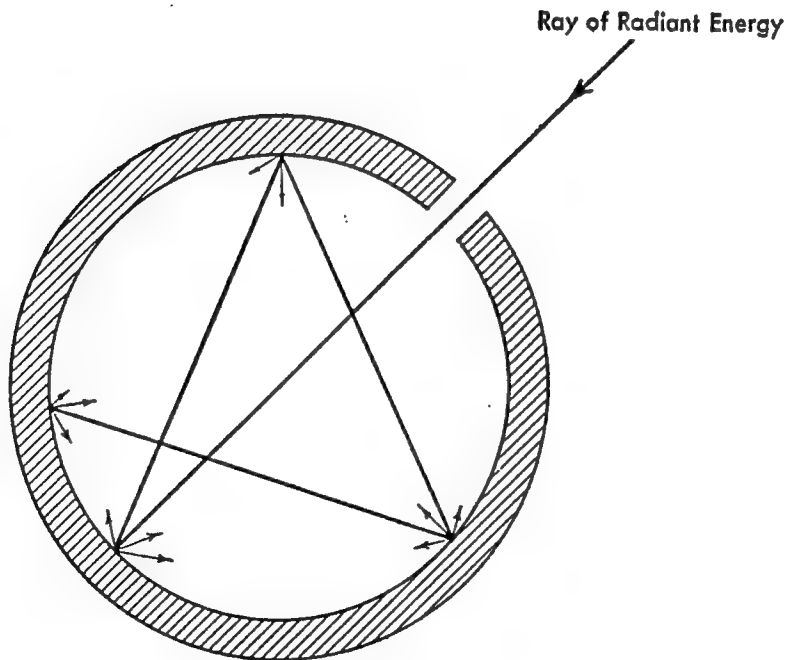
Figure 3.2 Reflection of radiation in a cavity (from Kreith, 1958).

Maxwell's theory, however, could not explain the phenomenon of blackbody radiation, or the so-called "cavity" radiation depicted in Figure 3.2. Max Planck provided a detailed model of the processes taking place at the cavity walls. He conjectured that the atoms making up the surface behave like tiny electromagnetic oscillators, each with a characteristic frequency of oscillation. The oscillators emit electromagnetic energy into the cavity and absorb energy from it. Thus, the possibility arose to deduce the characteristics of the cavity radiation from those of the oscillators with which it is in equilibrium.

Planck assumed an oscillator can only have energy given by

$$E = nh\nu_e \tag{3.3}$$

where ν_e is referred to in this context as the oscillator frequency, h is Planck's constant, and n is a quantum number. This assumption asserts that the oscillator energy is quantized. Secondly, oscillators do not radiate energy continuously, but only in "jumps", or quanta. These quanta of energy are emitted when an oscillator changes from one state of quantized energy to another. Thus, the frequency of radiation, ν_e, depends entirely on the nature of the source. Although Planck had quantized the source of electromagnetic radiation as discrete energy levels which can be explained through probability and statistics, he still treated the propagation of radiation as an electromagnetic wave.

A few years later, Einstein declared that the energy in a light beam travels through space in concentrated bundles or particle-like energy packets called photons. The energy associated with a single photon ($n=1$) is

$$E = h\nu_e. \tag{3.4}$$

Einstein's hypothesis suggests that electromagnetic radiation traveling through space behaves like a particle and not like a wave at all. While

photons emphasize the statistical or quantized properties of electromagnetic radiation, waves adequately describe the time-averaged effects of electromagnetic radiation for the purposes of our discussion.

3.2 Blackbody Radiation

Planck's main purpose in quantizing electromagnetic energy was to explain the phenomenon of blackbody radiation. **Blackbodies** are known as ideal thermal radiators whose radiation characteristics are completely identified from their specified temperature. Planck's radiation law describes the spectral exitance of thermal emission from a body at temperature, T, in °K as

$$M_{b\lambda}(\lambda,T) = \frac{C_1}{\lambda^5 \left[e^{C_2/\lambda T} - 1 \right]} \tag{3.5}$$

where λ is in micrometers (µm). Planck defined the empirical constants

$$C_1 = 2\pi c^2 h \quad \text{and} \quad C_2 = hc/k_b \tag{3.6}$$

where k_b is Boltzmann's constant. By inserting the experimental values for C_1 and C_2, Planck found $h = 6.626 \times 10^{-34}$ W-s² and $k_b = 1.38 \times 10^{-23}$ J/°K. Commonly, C_1 and C_2 are written as

$$C_1 = 3.7418 \times 10^8 \text{ W-µm}^4/\text{m}^2 \tag{3.7a}$$

and

$$C_2 = 1.4387 \times 10^4 \text{ µm-°K} \tag{3.7b}$$

allowing $M_{b\lambda}$ to have units of W/m²-µm. Thus the **spectral exitance** (also known as the **emittance**), $M_{b\lambda}$, is the radiant flux density of electromagnetic radiation per unit bandwidth centered at λ leaving a unit surface area for a given temperature.

Previous to Planck, Wien had attempted to predict the behavior of the blackbody radiation over the entire spectral range. Wien's expression turns out to be an important limiting case of Planck's law. Wien's Law occurs when the term $C_2/\lambda T$ in the denominator of (3.5) is quite large. Thus, the term $exp(C_2/\lambda T)$ is much greater than unity and leads to the approximation

$$e^{C_2/\lambda T} - 1 \approx e^{C_2/\lambda T} \tag{3.8}$$

in the limit $C_2 \gg \lambda T$. Therefore, Planck's law of (3.5) reduces to Wien's radiation law

$$M_{b\lambda}(\lambda,T) = \frac{C_1}{\lambda^5 e^{C_2/\lambda T}}. \tag{3.9}$$

Figure 3.3a illustrates the spectral emittance as a function of wavelength for two temperatures encompassing the possible range on the sea surface along with curves acquired from Wien's approximation. For these typical conditions under which the ocean heat flux is measured, Wien's approximation agrees nicely for shorter wavelengths but deviates from Planck's curve for wavelengths greater than the spectral peak as portrayed in Figures 3.3a and 3.3b. The diversions may be less than 10 % for the emittance according to Figure 3.3b, but increase with temperature. Even minuscule diversions in emittance have a marked effect on the temperature deviations, as we will see later in Section 3.3.

Finally, integrating (3.5) over all the wavelengths calculates the total power per unit area emitted from a blackbody

$$M_b(T) = \int_0^\infty \frac{C_1}{\lambda^5 \left[e^{C_2/\lambda T} - 1 \right]} \partial\lambda. \tag{3.10}$$
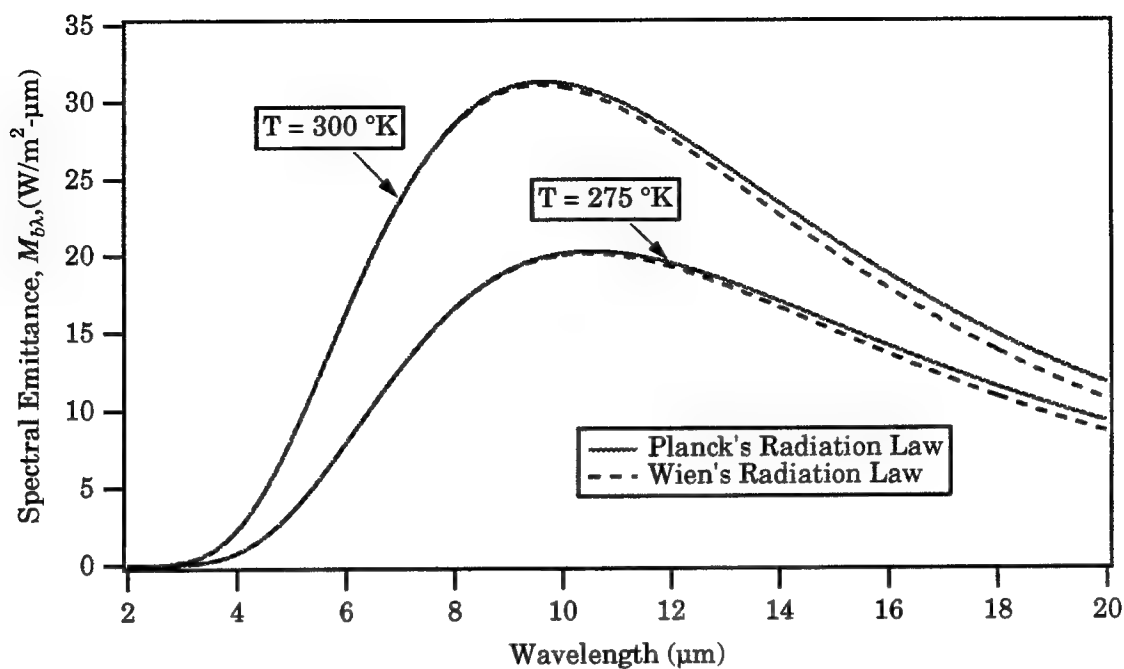
Figure 3.3a Spectral emittance according to Planck's and Wien's radiation laws encompassing the possible temperatures encountered on the ocean.
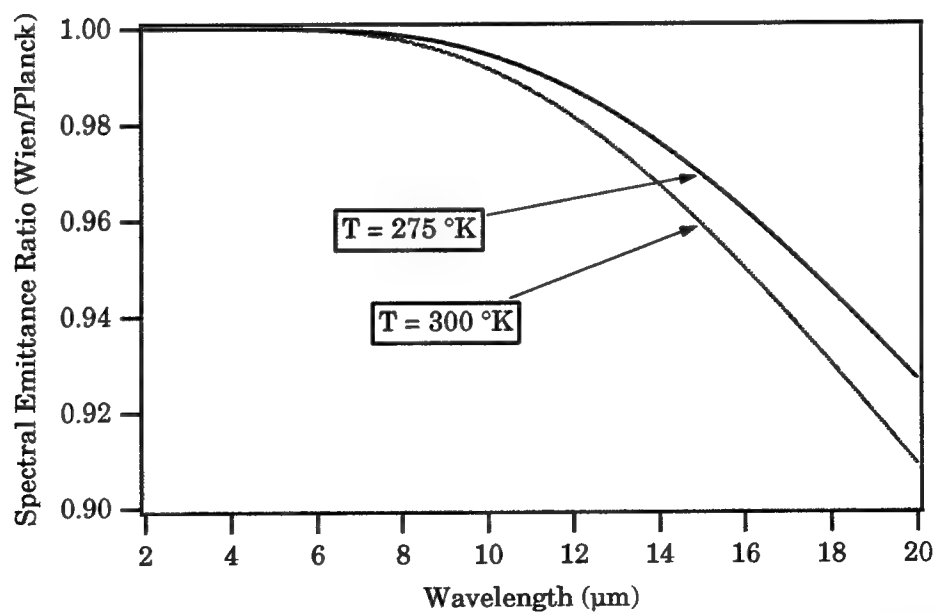
Figure 3.3b Deviation from Planck's blackbody radiation law according to Wien's approximation.

The integration is simplified by switching to the frequency domain as outlined in Maul (1985) and results in the expression for the total radiant exitance known as the Stefan-Boltzmann law

$$M_b(T) = \frac{2\pi^5 k_b^4}{15c^2 h^3} T^4 = \sigma_b T^4 \qquad (3.11)$$

where $\sigma_b = 5.6696 \times 10^{-8}$ W/m²-°K⁴ is the Stefan-Boltzmann constant. The total radiant emittance is seen to be dependent only on the fourth power of absolute temperature.

In order to provide some consistency in further discussions, Table 3.1 displays relevant electromagnetic radiation terminology. An intrinsic point to this discussion involves clarification between radiance and flux density. Flux density refers to the time rate of energy per unit area while radiance refers to the flux density per solid angle. In order to understand the concept of solid angle, picture a sphere. Within the sphere a cone exists with its apex at the center of the sphere. The cone intersects the surface of the sphere outlining a curvilinear surface area. The solid angle, Ω, is measured in steradians (abbreviated sr) and defined as

$$\Omega = \frac{A_s}{r_d^2} \qquad (3.12)$$

where A_s is surface area outlined by the cone on the shell of the sphere and r_d is radial distance from the center to the shell of the sphere. Likewise, for an infinitesimal solid angle,

$$d\Omega = \frac{dA_s}{r_d^2} \qquad (3.13)$$

where

$$dA_s = r_d^2 \sin\theta \, d\theta \, d\phi \qquad (3.14)$$

resulting in

Table 3.1   Terminology used in electromagnetic radiation.

Name	Symbol	Definition	Expression	Units	Alternates
Energy	E	Radiant Energy		Joule [J]	
Flux	Φ	Time Rate of Energy	$\dfrac{\partial E}{\partial t}$	Watt [W]	Power
Flux Density		Flux Per Unit Area	$\dfrac{\partial \Phi}{\partial A}$	$W\!\!\Big/\!m^2$	
Exitance	M	Exitent Flux Density	$\dfrac{\partial \Phi}{\partial A}$	$W\!\!\Big/\!m^2$	Emittance
Irradiance	I	Incident Flux Density	$\dfrac{\partial \Phi}{\partial A}$	$W\!\!\Big/\!m^2$	Incidence
Radiance	R	Flux Density Per Solid Angle	$\dfrac{\partial^2 \Phi}{\cos\theta\,\partial\Omega\partial A}$	$W\!\!\Big/\!sr\cdot m^2$	Sterance, Brightness

$$d\Omega = sin\,\theta d\theta d\phi \qquad\qquad (3.15)$$

for the spherical geometry defining the solid angle in Figure 3.4.

Radiance is outgoing radiation while **brightness** is incoming radiation. Both are defined as the flux per solid angle per area from an extended source projected in the direction of the radiation as shown in Figure 3.5. Considering a small surface area dA oriented as in Figure 3.5, the projected area is $dAcos\theta$ and the radiance or brightness is defined as

$$R = \frac{d^2\Phi}{cos\,\theta d\Omega dA}. \qquad\qquad (3.16)$$

Although the relation is derived for black surfaces, it holds for other surfaces as long as they are diffuse radiators. Specifically, a surface which reflects radiation from any direction uniformly and diffusely into a hemisphere is known as a **Lambertian surface**. The subsequent analysis assumes the surface is Lambertian. The **irradiance**, I, is the total radiant power falling onto an infinitesimal surface area, dA, from all directions in a hemisphere oriented perpendicular to dA. The **exitance**, M, is the total radiant power emitted by an infinitesimal element of surface area into a hemisphere and written simply as

$$M = \frac{d\Phi}{dA}. \qquad\qquad (3.17)$$

Integrating the radiance given in (3.16) over the solid angle, we arrive at the expression

$$\frac{d\Phi}{dA} = \int_{\Omega} R\,cos\,\theta d\Omega. \qquad\qquad (3.18)$$

Combining (3.17) with (3.18), and substituting (3.15) for the infinitesimal solid angle yields
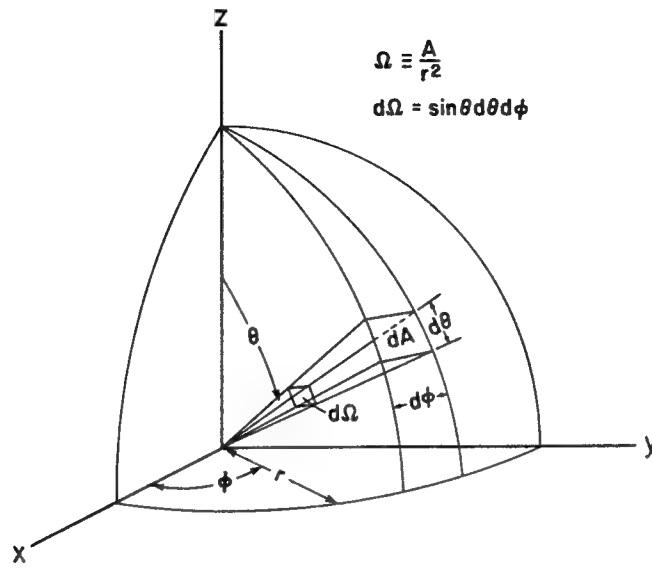
Figure 3.4　Geometry defining the solid angle, Ω, the steradian (from Maul, 1985).
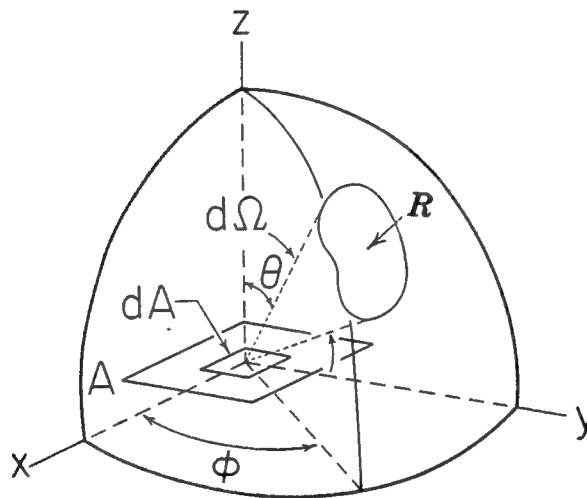
Figure 3.5　The radiance, R, is the exitent radiant flux per solid angle $d\Omega$ per area projected onto the surface, $dA\cos\theta$ (from Stewart, 1985).

$$M = R \int\limits_{0}^{2\pi} d\phi \int\limits_{0}^{\pi/2} \sin\theta \cos\theta \, d\theta$$

$$M = \pi R$$

(3.19)

The relationship in (3.19) holds for irradiance of a blackbody as well. Thus, the emittance of a diffuse surface is π times its radiance.

3.3 General Radiation Properties

All bodies emit electromagnetic radiation known as thermal radiation as a result of their temperature. When radiant energy impinges on the surface of a body, part is reflected, part is absorbed, and part is transmitted as shown in Figure 3.6. The incident flux density of energy, I, is known as the irradiance. According to the law of conservation of energy,

$$a + r + \tau_e = 1$$

(3.20)

where

$a = absorptivity \ (fraction \ of \ irradiance \ absorbed)$
$r = reflectivity \ (fraction \ of \ irradiance \ reflected)$
$\tau_e = transmissivity \ (fraction \ of \ irradiance \ transmitted)$

The relative magnitudes of a, r, and τ_e not only depend on the temperature, surface characteristics, and material but also vary with wavelength and incidence angle, θ. Depending upon the context, incidence angle refers to the angle measured from the perpendicular of a surface to either a ray of radiation or a line of sight. Most liquids are optically opaque and the ocean is no exception. Because no radiation is transmitted out the bottom of the ocean (Stewart, 1985), the transmissivity is effectively zero and (3.20) becomes

$$a(\lambda,T,\theta) + r(\lambda,T,\theta) = 1$$

(3.21)
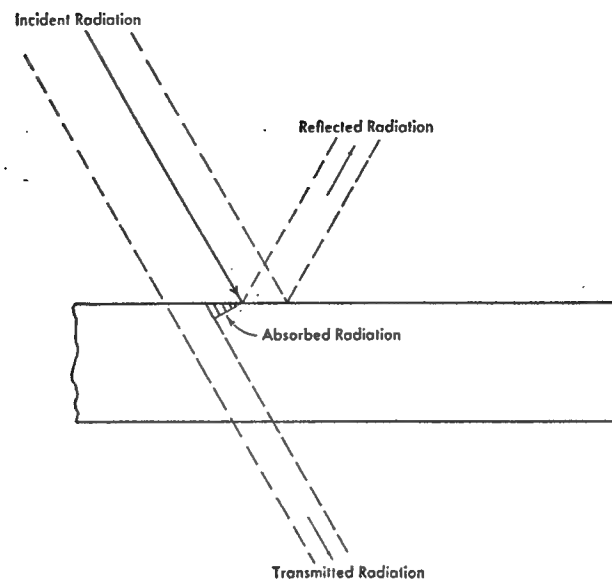
Figure 3.6   Reflection, absorption, and transmission of radiation (from Kreith, 1958).
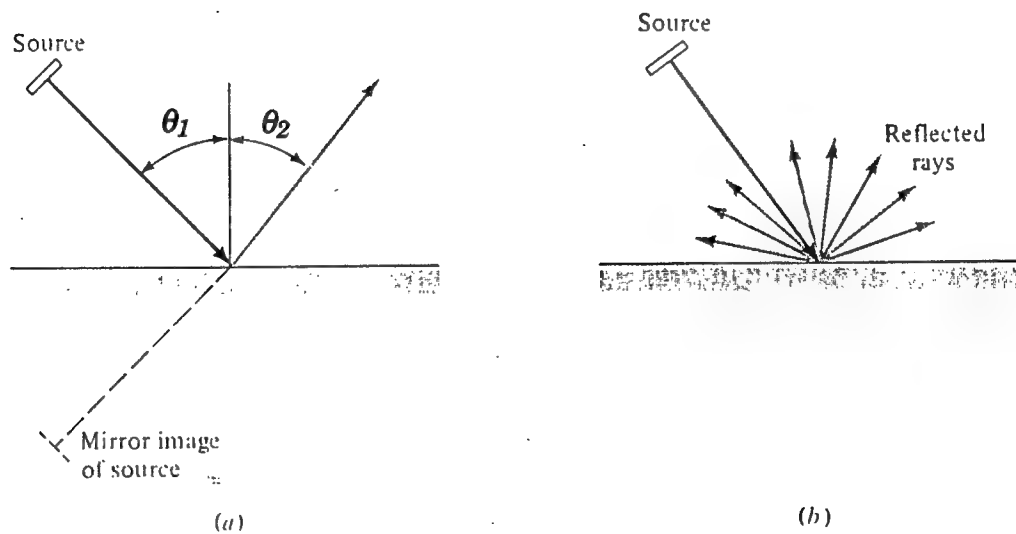
Figure 3.7   (a) Specular ($\theta_1 = \theta_2$) and (b) diffuse reflection (from Holman, 1990).

where the functional relationships are indicated.

Two types of reflection may occur when radiation strikes a surface as shown in Figure 3.7. When a surface is highly polished and smooth, the angle of reflection equals the angle of incidence, and the reflection of radiation is termed **specular**. A rough surface, however, will indiscriminately reflect the radiation isotropically in all directions and the radiation is termed **diffuse**. No real surface is either specular or diffuse. For example, a mirror is quite specular for visible light but may exhibit diffuse characteristics over the wavelength range of thermal radiation. The influence of surface roughness on thermal radiation properties is a matter of serious concern and should be acknowledged.

Previously in Section 3.2, we mentioned that blackbodies are referred to as perfect emitters. However, a **blackbody** can be defined either as a body which absorbs all incident radiation upon it or as a radiator which emits the maximum possible level of thermal radiation at all wavelengths. To clarify the concept of a blackbody, consider the following experiment. Suppose a small body B_1 of surface area A_1 is placed in an evacuated enclosure which is perfectly insulated. Radiation will be exchanged between the body and the walls of the enclosure until equilibrium is attained where both the body and the walls have reached the same temperature. Hence, the rate at which the body emits radiation must equal the rate at which it absorbs radiation. Given the irradiance of the walls, I, the absorptivity, a_1, and the emittance of the body, $M_{1\lambda}$, an energy balance yields

$$A_1 I a_1 = A_1 M_{1\lambda}. \tag{3.22}$$

Repeating the experiment for any body, including a blackbody, we arrive at relations similar to (3.22) from which

$$\frac{M_\lambda}{a} = \frac{M_{1\lambda}}{a_1} = \frac{M_{2\lambda}}{a_2} = \cdots \tag{3.23}$$

where M_λ is the spectral emittance of any body.

The relation of (3.23) known as Kirchhoff's law states that at thermal equilibrium the ratio of the spectral exitance of a surface to its absorptivity is the same for all bodies. According to (3.21), the absorptivity of any body is limited to values between 0 and 1. **Kirchhoff's law** places an upper limit on the maximum exitance of a body, $M_{b\lambda}$, when

$$a(\lambda, T, \theta) = a_b(\lambda, T, \theta) = 1 \tag{3.24}$$

a condition precisely applicable to a blackbody. The emittance of real surfaces, however, is less than that of an ideal blackbody, resulting in a ratio of the actual exitance of a surface to that of a blackbody known as the **emissivity**

$$\varepsilon(\lambda, T, \theta) = \frac{M_\lambda(\lambda, T)}{M_{b\lambda}(\lambda, T)} \tag{3.25}$$

of a body. While the emissivity of most real surfaces is wavelength dependent, a body whose emissivity is independent of wavelength is defined as a **graybody**. Figure 3.8 demonstrates the comparison of blackbody, graybody and actual ocean emissivity effects on the measured exitance from a surface at 285 °K.

Substituting the upper limit of absorptivity given by (3.24) into (3.23),

$$a(\lambda, T, \theta) = \frac{M_\lambda(\lambda, T)}{M_{b\lambda}(\lambda, T)} \tag{3.26}$$

also. Restating Kirchhoff's law by equating (3.25) and (3.26)
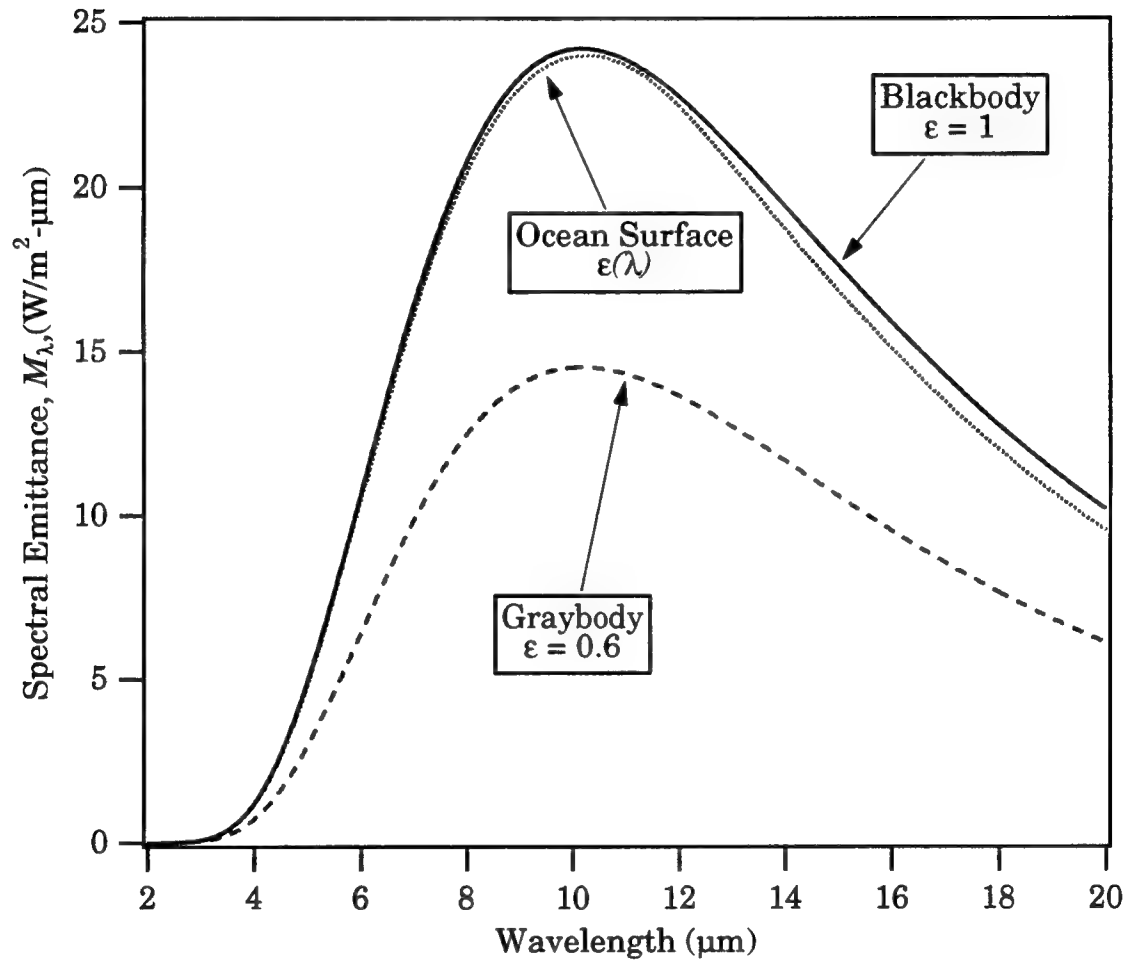
Figure 3.8   Spectral emittance for a blackbody, graybody, and real surface at a temperature of 285 °K (~ 12°C).

$$a(\lambda,T,\theta) = \varepsilon(\lambda,T,\theta) \qquad\qquad (3.27)$$

shows that during thermodynamic equilibrium, the absorptivity and emissivity of a body are equal. Substituting (3.27) into (3.21)

$$\varepsilon(\lambda,T,\theta) + r(\lambda,T,\theta) = 1 \qquad\qquad (3.28)$$

is attained. Unless the reflectivity, r, is zero (i.e. $\varepsilon = 1$), the temperature associated with M_λ is called the **apparent** or **brightness temperature**, T_o, at that wavelength. Brightness temperature is defined as the temperature of a blackbody required to produce the same spectral exitance as a real body at a specific wavelength. If M_λ is measured and the emissivity known, the true temperature of the real body can be extracted using (3.25) and (3.5). Figure 3.9 demonstrates the significance of minute variations in emissivity upon the apparent temperature of a body with an actual temperature of 15 °C.

The concept of emissivity is crucial to the understanding of thermal radiation and to the dilemma Planck and his contemporaries encountered. At a given temperature the exitance out of the hole of a cavity, as shown in Figure 3.2, is identical for all materials, despite the fact that the emittance of the outer surface is different from that of the cavity and the emittance is different for each of the respective materials. Most materials possess emissivities less than unity allowing for the reflectivity to be non-zero according to (3.28). The outer surface of a cavity is subject to only one reflection and therefore emits less than that of a blackbody. Conversely, any radiation entering the small hole of the cavity will be partly absorbed and partly reflected repeatedly. When the original radiation finally reaches the hole again and escapes, the reflected energy leaving the cavity is negligible due to deterioration by successive absorption and reflection cycles. Regardless of the surface or composition of the walls, the cavity acts as a blackbody because nearly all the radiation incident upon it has been absorbed. Consequently, the emitted radiation back through the hole will be that of a blackbody according to
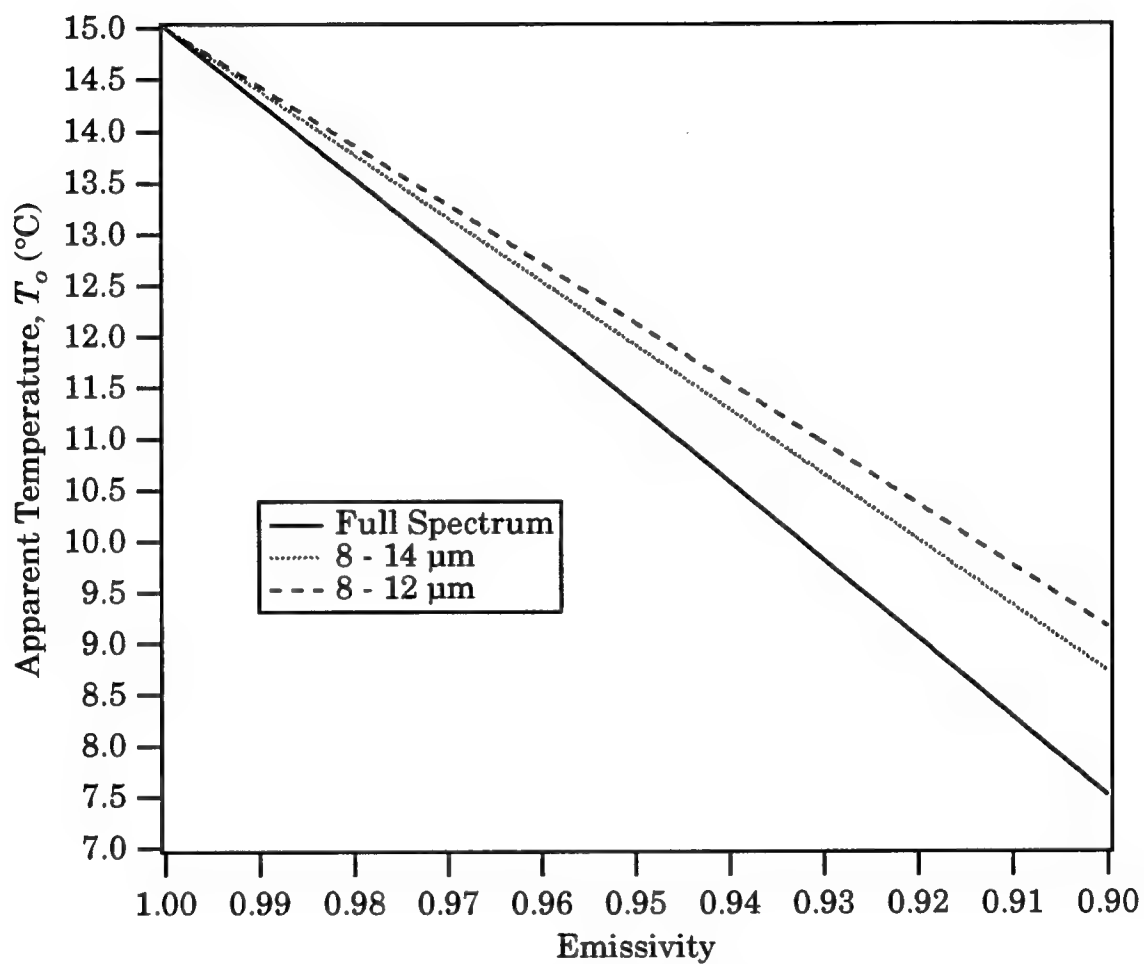
Figure 3.9   Effect of emissivity upon measured apparent temperature.

(3.27) which states the emissivity of the inner cavity walls is equivalent to the absorption which has grown to unity.

3.4 Characteristic Environmental Behavior of Radiation

If the primary advantage of satellite remote sensing is the non-intrusive mapping of the sea surface, then the major disadvantage is the existence of the atmosphere masking the view of the ocean. The atmosphere is opaque to electromagnetic radiation at many wavelengths and only a few windows exist through which radiation may be transmitted, as shown in Figure 3.10. Air molecules, water vapor, and other aerosols can absorb or scatter most radiation passing through them, while water droplets in clouds may completely change the transmission properties of the atmosphere. Although the atmosphere may change with time and location, causing variation in absorption, the overall qualitative characteristics of the absorption spectrum remain. Earlier, we noted that the peak of the spectral emittance for temperatures between 5 and 27 °C is around 10 µm. Fortuitously, the transmission of the atmosphere is very high within the wavelength band of 8 - 12 µm due to the low absorptance of ozone, carbon dioxide, and water vapor. As shown in Figure 3.11, the 8 - 12 µm range provides a prime region, or window, in the electromagnetic spectrum for observing the sea surface except for the 9 µm band of high absorption from ozone.

In the Section 3.3, we initiated the discussion of emissivity and its strong dependence on wavelength and viewing angle. In reality, the reflectivity of a surface is directly dependent on wavelength and viewing angle, and upon substitution into (3.28), the emissivity is obtained. Usually, the well-known Fresnel equations (Maul, 1985) are used to calculate the reflectance of an air-water interface. The basis of the Fresnel equations depends on the incidence angle and on the complex index of refraction

$$N(\lambda) = n(\lambda) + in_k(\lambda) \qquad (3.29)$$
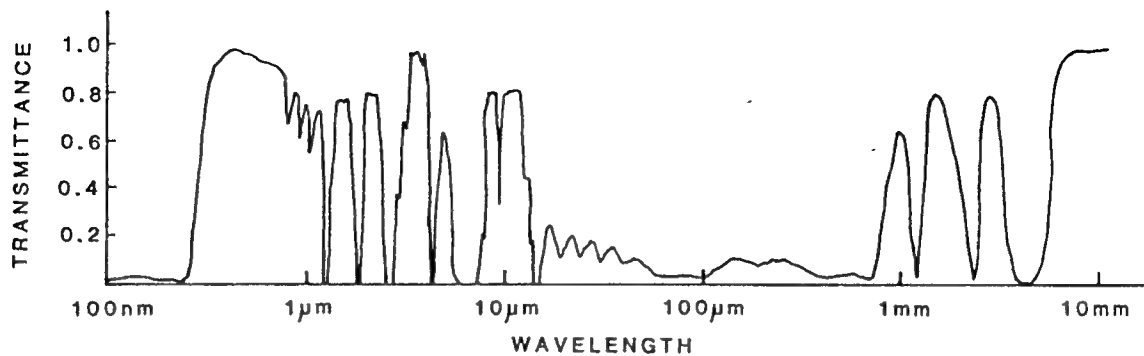
Figure 3.10 Approximate transmittance of electromagnetic waves through the atmosphere (from Robinson, 1985).
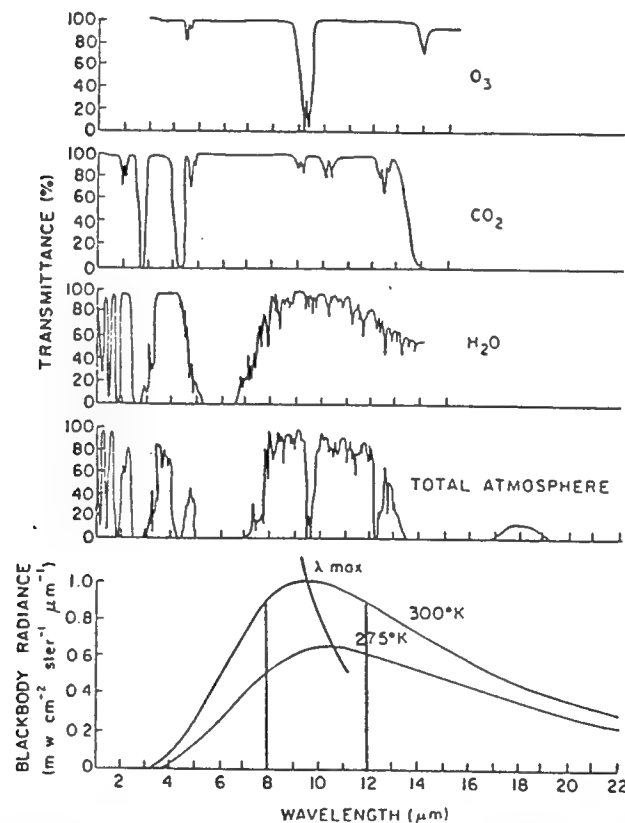
Figure 3.11 Upper curves: Transmission spectra of the three principal absorbing atmospheric gases (ozone, carbon dioxide, and water vapor) and the whole atmosphere at vertical incidence for infrared wavelengths.
Lower curve: Thermal radiation according to Planck's law for the temperature range of 275 °K to 300 °K peaks between 10 and 11 μm (from Katsaros, 1980b).

where the real part n is the index of refraction and imaginary part n_k is the **extinction coefficient**. Numerous authors including Friedman (1969), Hobson and Williams (1971), and Downing and Williams (1975) have performed in-depth studies of the properties of pure and sea water and painstakingly found the values for the index of refraction and extinction coefficient, where traditional values are depicted in Figure 3.12. At nadir incidence ($\theta = 0°$), the calculated reflectivity of pure water is displayed as a function of wavelength in Figure 3.13 according to the Fresnel equations. According to (3.28), the emissivity as a function of wavelength is found directly from the reflectivity curve. In the infrared wavelength range of 1 - 16 μm, the emissivity of pure water observed from nadir is always greater than 0.95 as seen in Figure 3.14. Paulson and Simpson (1981) concluded that the emissivity of water in the wavelength band of 8 - 15 μm is $\varepsilon = 0.986$ which matched the direct measurement of Saunders (1970).

Reflectivity is also a strong function of incidence angle. Using the complete expressions of reflectivity for a complex index of refraction, Figure 3.15 displays the reflectivity at two specific wavelengths as a function of incidence angle. Notice the sharp increase in reflectivity at incidence angles greater than the Brewster's angle of 53°. Brewster's angle is defined as the incidence angle at which no vertically polarized electromagnetic radiation is reflected, and varies slightly from wavelength to wavelength. As the reflectivity increases with incidence angle, the emissivity decreases resulting in less emission from the actual body being measured. A complete picture of the reflectivity as functions of both wavelength and incidence angle is vividly portrayed in Figure 3.16 for the infrared wavelength region. As we will see, background radiation will be an important factor in deciphering the actual temperature of a real surface.

The reflectance curves are highlighted by the interesting abrupt changes transpiring at 3, 6, and 14 μm. Hobson and Williams (1971) report that strong absorption bands occur at 2.9, 6.1, and 14.6 μm and could be related to these sharp variations. The **absorption coefficient** (technically
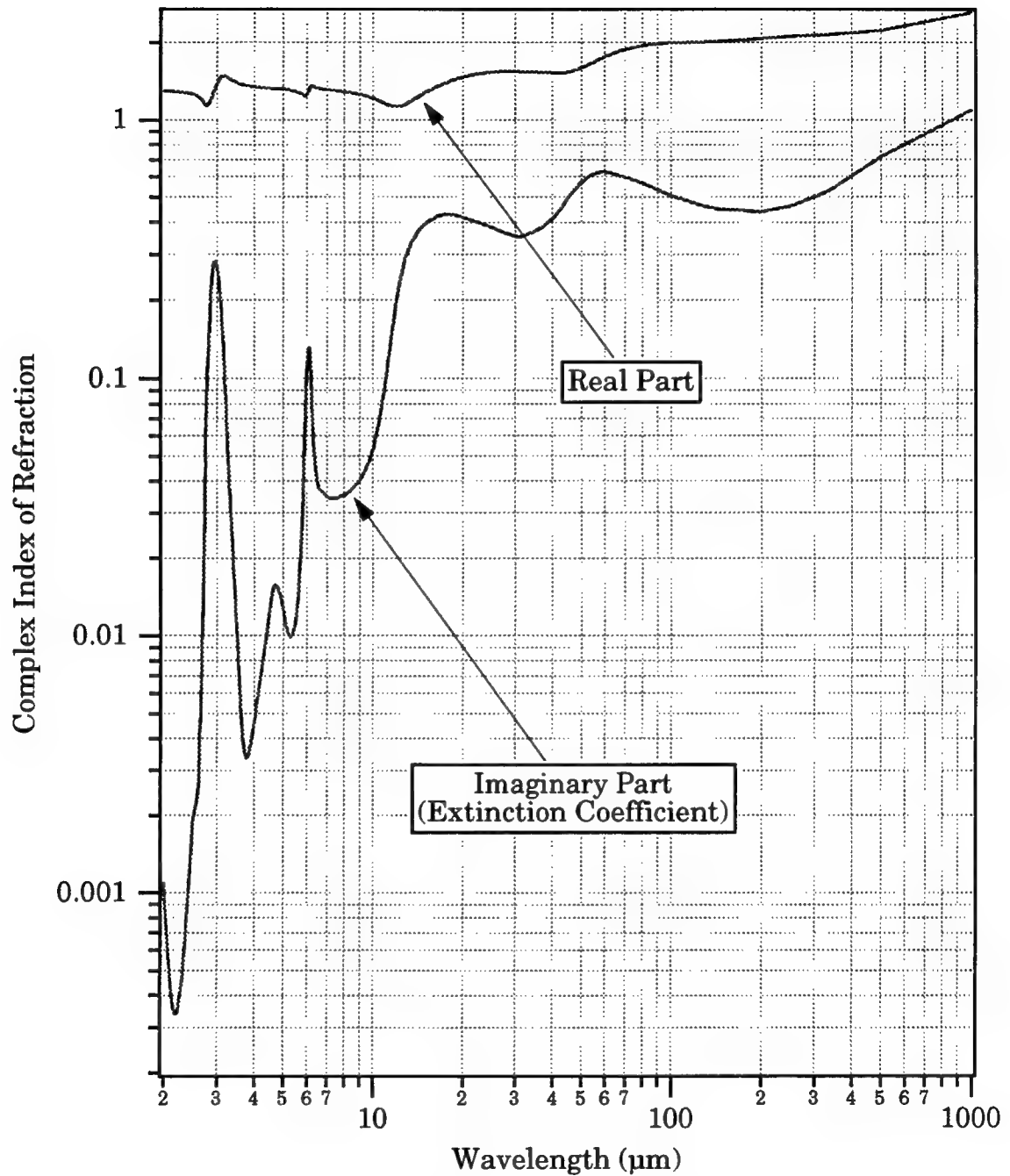
Figure 3.12 Traditional values of complex index of refraction (data from Downing and Williams, 1975) from 2 to 1000 μm in wavelength. Temperature effects are small at visible and infrared wavelengths except for beyond 10 μm where temperature becomes an important variable.
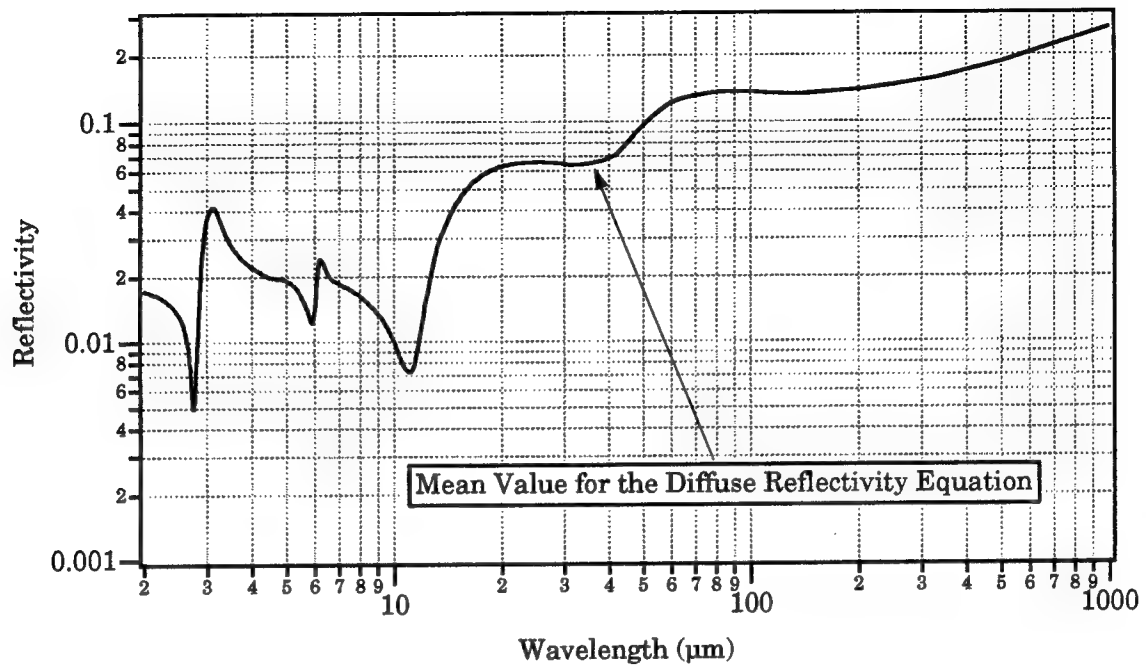
Figure 3.13 The calculated reflectivity of pure water at zero incidence angle.
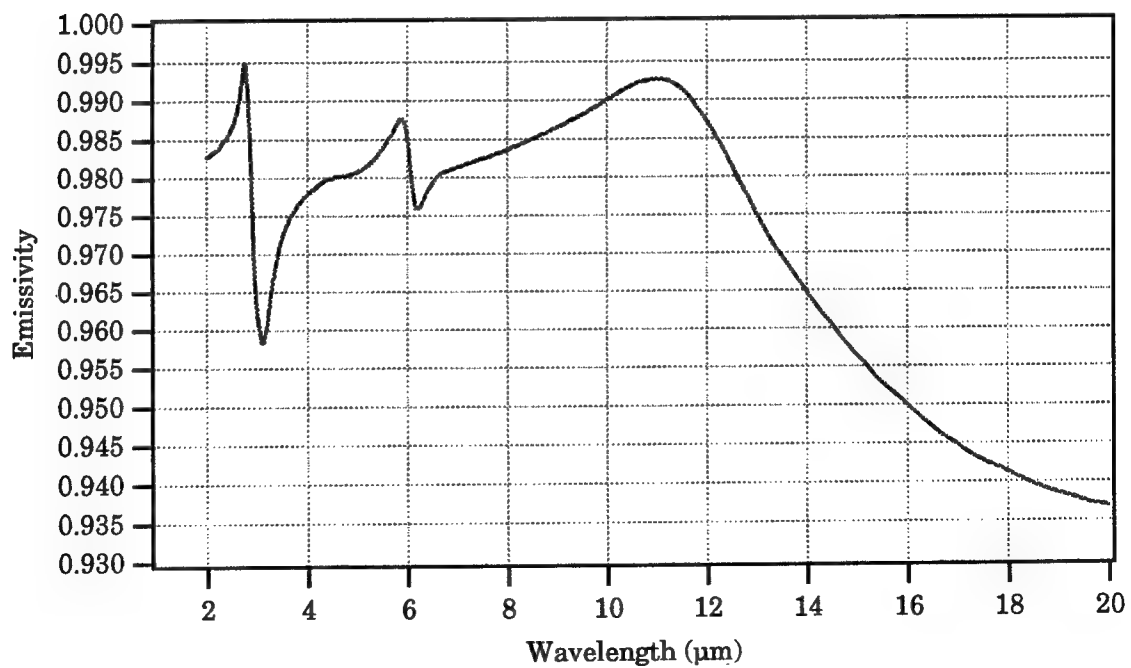
Figure 3.14 Emissivity of pure water for the infrared wavelength range at normal incidence angle.
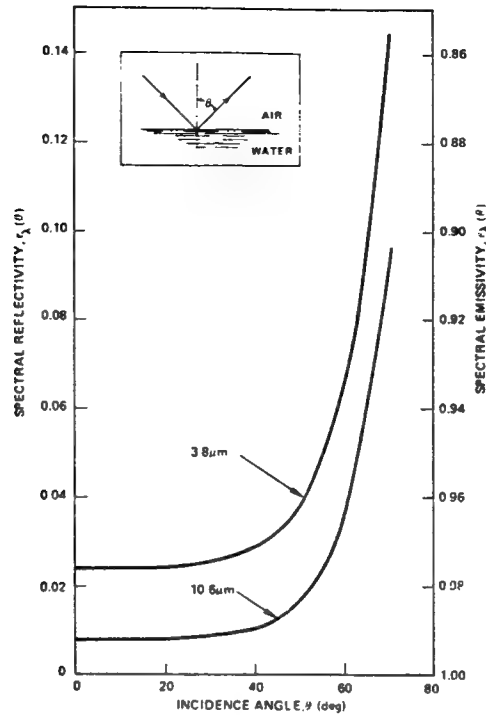
Figure 3.15 Spectral reflectivity and emissivity of water as a function of incidence angle (from Gasparovic *et al.*, 1974).
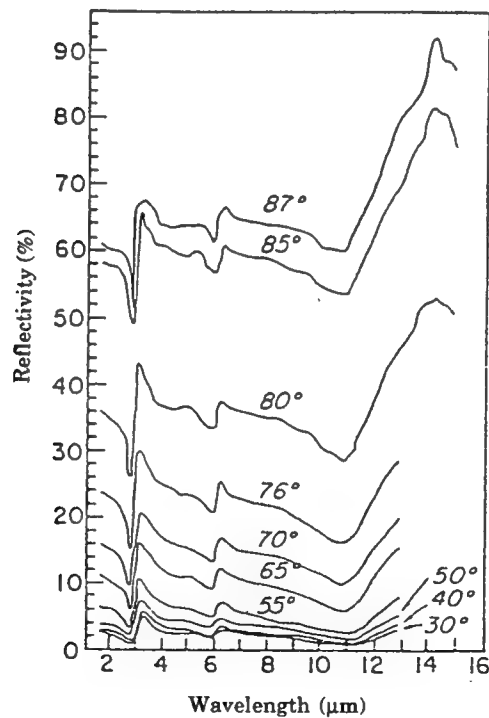
Figure 3.16 Reflectivity of water as a function of wavelength and incidence angle (from Katsaros, 1980b).

different from absorptivity) is related to the **extinction coefficient** (also the **absorption index**) through

$$a_c(\lambda) = \frac{4\pi n_k}{\lambda}. \tag{3.30}$$

The absorption coefficient displayed in Figure 3.17 as a function of wavelength corresponds directly to the reflectivity illustrated in Figure 3.13. The characteristic reflectance feature associated with each of the major absorption bands provides the reader with substantiation of the physical significance of (3.21). Any variation in reflectivity results in a counteraction by the absorption.

Another physical interpretation of the absorption coefficient emerges from the discussion of the **effective optical depth** into a medium. Two explanations arise depending on the wave or particle perspective of radiation. In the wave sense, the amplitude of the electric field vector is damped by 1/e as the energy propagates a distance d_{eo} into the attenuating medium. In a particle sense, the probability of a photon passing through a non-dimensional distance $a_c d_{eo}$ in a volume of unit thickness is also 1/e. Thus, the distance

$$d_{eo}(\lambda) = \frac{1}{a_c(\lambda)} \tag{3.31}$$

is termed the e-folding, or effective optical, depth. In the infrared range of wavelengths, the optical depth varies significantly and is plotted in Figure 3.18. McAlister (1964), McAlister and McLeish (1965), and McAlister and McLeish (1970) have capitalized on the optical depth variability and patented several two-wavelength radiometers to measure directly the temperature gradient in the upper millimeter of the ocean.

3.5 The Balance of Radiation Sources and Sink
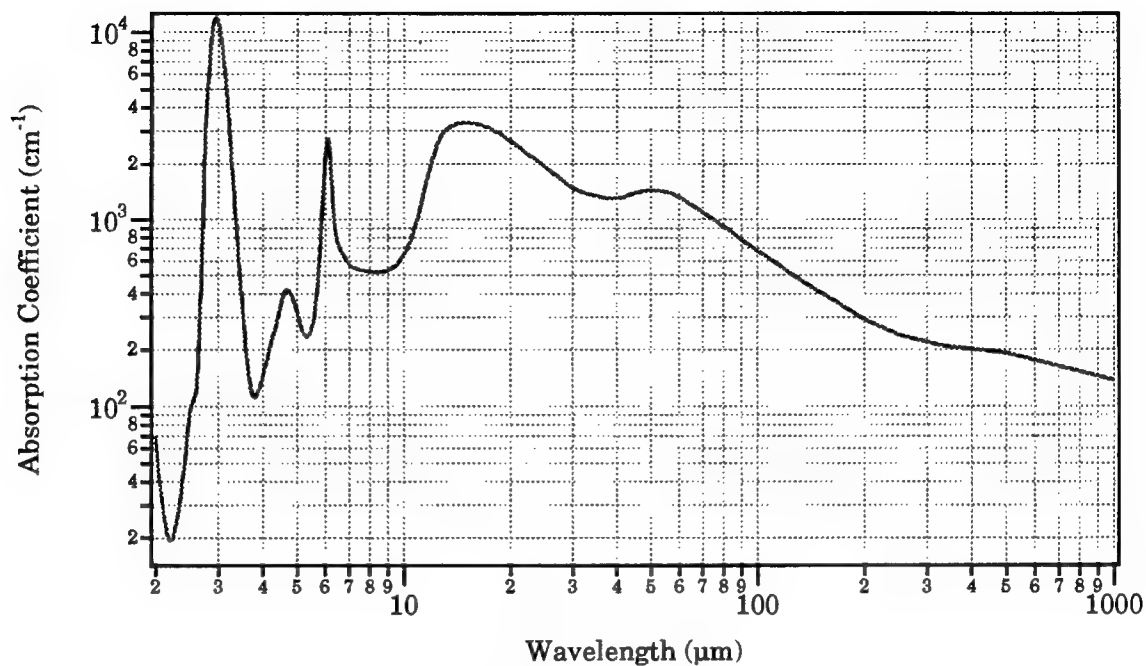
Figure 3.17 Absorption coefficient for pure water computed from the extinction coefficient of the complex index of refraction.
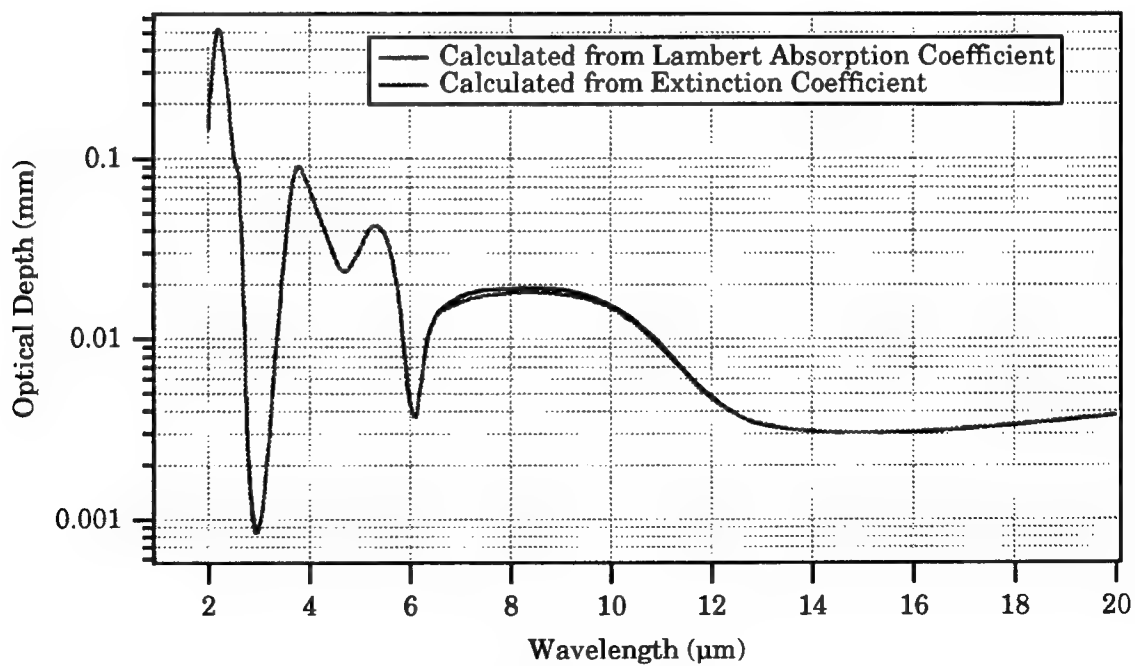
Figure 3.18 Optical depth of infrared radiation.

Numerous processes of interaction can take place between the intended source of electromagnetic radiation and the infrared sensor. Most importantly, radiation leaving the sea surface and reaching the sensor directly provides a measure of the temperature from the depths of about 10 μm or less. En route to the sensor, radiation leaving the ocean surface may be absorbed or scattered out of the field of view of the sensor by the atmosphere. Likewise, the atmosphere is capable of redirecting radiation into the field of view from the sea surface and elsewhere while also re-emitting the radiation previously absorbed by the atmosphere constituents. Relevant to thermal infrared emission, any radiation that the generally cool atmosphere absorbs by its constituent matter is re-emitted at a lower temperature with a consequent shift in the spectral peak to longer wavelengths. Thus, the atmosphere reduces the radiation reaching the sensor and reduces the apparent surface temperature.

When converting the measured infrared radiance to surface temperature, deviations from unity of the emissivity of water amplify in importance. Since reflectivity and emissivity are functions of incidence angle, one must consider the observing angle and surface disturbances such as waves or roughness. Including the considerations of the reflected signal, the observed flux density depicted in Figure 3.19 is

$$
\begin{aligned}
M_{o\lambda}(T_o) = & \int_{\lambda_1}^{\lambda_2} \bar{\varepsilon}_w(\lambda,\theta) M_{b\lambda}(\lambda,T_s) \partial\lambda \\
& + \int_{\lambda_1}^{\lambda_2} [1-\bar{\varepsilon}_w(\lambda,\theta)] M_{r\lambda}(\lambda,T_r) \partial\lambda \qquad (3.32) \\
& + atmospheric\ effects
\end{aligned}
$$

where $M_{o\lambda}$ is the observed exitance and $M_{r\lambda}$ is the background radiation reflected into the sensor. The brightness temperature, T_o, refers to the temperature of the observed body if reflection effects were ignored, while T_s
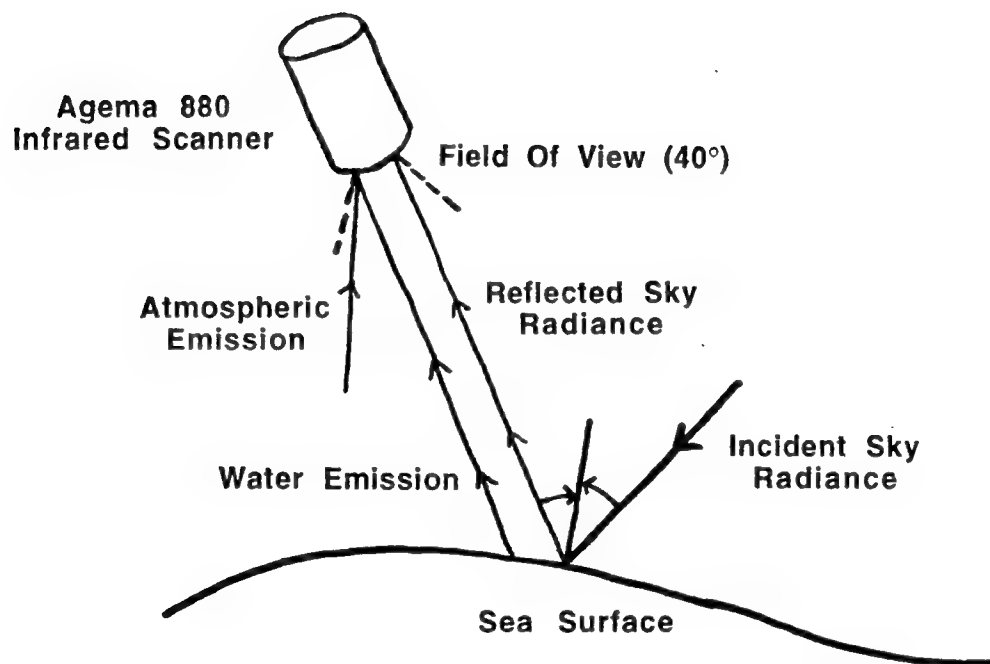
Figure 3.19 Illustration of the three sources of the flux density received by a downward looking infrared radiometer over the ocean.

and T_r correspond to the actual sea surface and effective background temperatures. The emissivity of water, $\bar{\varepsilon}_w$, is averaged for the entire field of view over the local incident angles made with a surface, especially with a wavy one. The wavelengths λ_1 and λ_2 indicate the waveband sensed by the observer. If the observer is less than 300 m above the emitting surface, atmospheric emission, absorption, and scattering are insignificant (Katsaros, 1980b) except for those effects upon the background radiation reflected into the sensor.

Background radiation provides the most difficult problem when measuring the spectral exitance of the ocean or any surface. Any deviation from unity in the emissivity can corrupt the observed exitance signal with reflected background radiation. An obvious producer of background radiation is the sun. The sun emits radiation at shorter wavelengths (peaking in the visible) compared with the thermal emission of the earth and ocean (peaking around 10 μm) which is at a much lower temperature as shown in Figure 3.20. Apparently, even at the wavelength of the sea-surface emission peak, the direct solar radiation ($T \approx 5900$ °K) would be substantially greater than the earth's radiation ($T \approx 300$ °K). At night this is not a problem, while during the day the reflected solar radiation would appear to become pertinent. However, taking into account the solid angle, or steradian, between the earth and the sun, the blackbody irradiance depicted in Figure 3.20 diminishes. The sun, with a mean radius of 695 Mm, radiates closely to a blackbody at a mean distance, r_d, of 149.7 Gm from the earth. According to (3.12), the solid angle, Ω, is now 6.771 x 10^{-5} sr taking the area, A_s, to be approximated by π times the mean radius of the sun squared. Thus, multiplying the brightness by the solid angle results in the spectral solar irradiance depicted in Figures 3.20 and 3.21 which is much less than anticipated (Stewart, 1985). Near 10 - 12 μm, the thermal emission by the sea surface turns out to be substantially greater than the reflected solar radiation, whereas at 3 - 4 μm the surface exitance might be seriously masked by the reflected solar irradiance (Robinson, 1985). Saunders (1967b) considered the effect of reflection of direct solar radiation on measurements made in the 8 - 12 μm range by a radiation thermometer
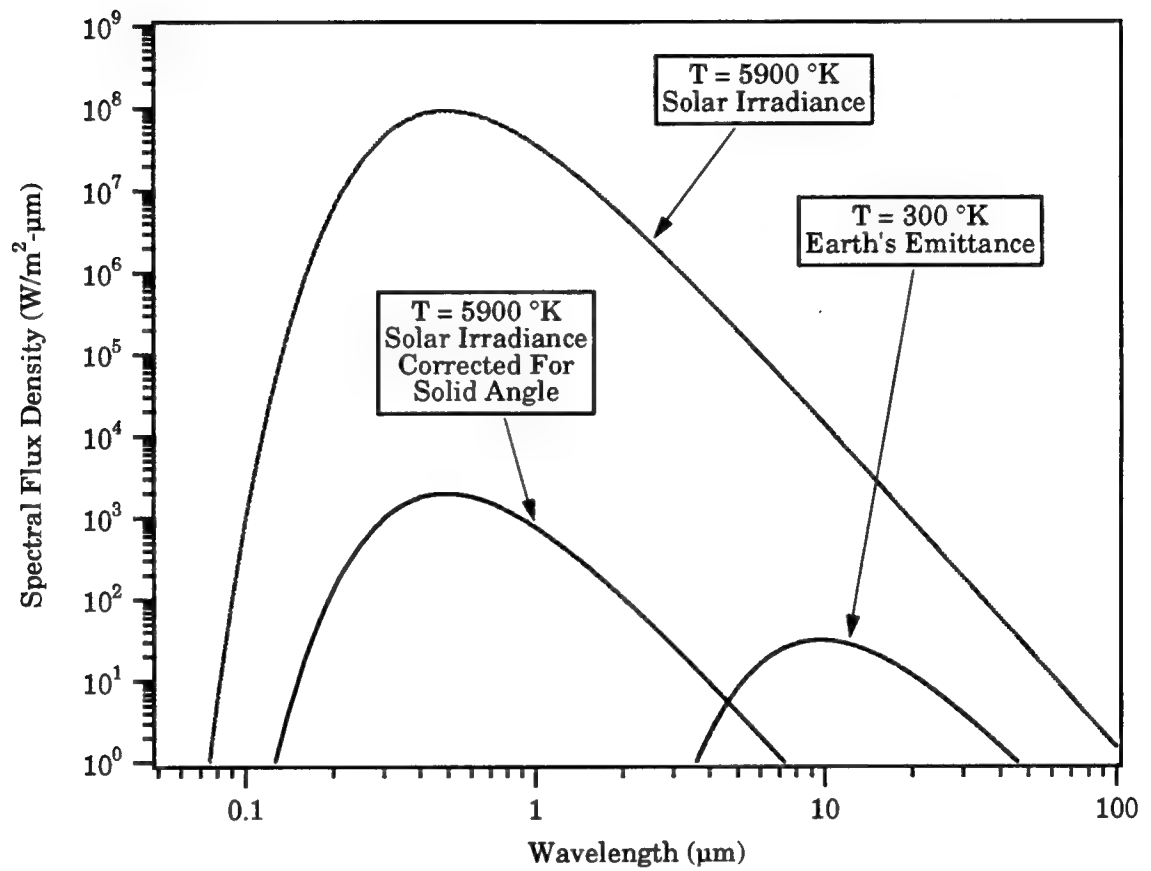
Figure 3.20 Spectral irradiance of the sun, both corrected and uncorrected for the steradian, along with the spectral emittance of the earth.
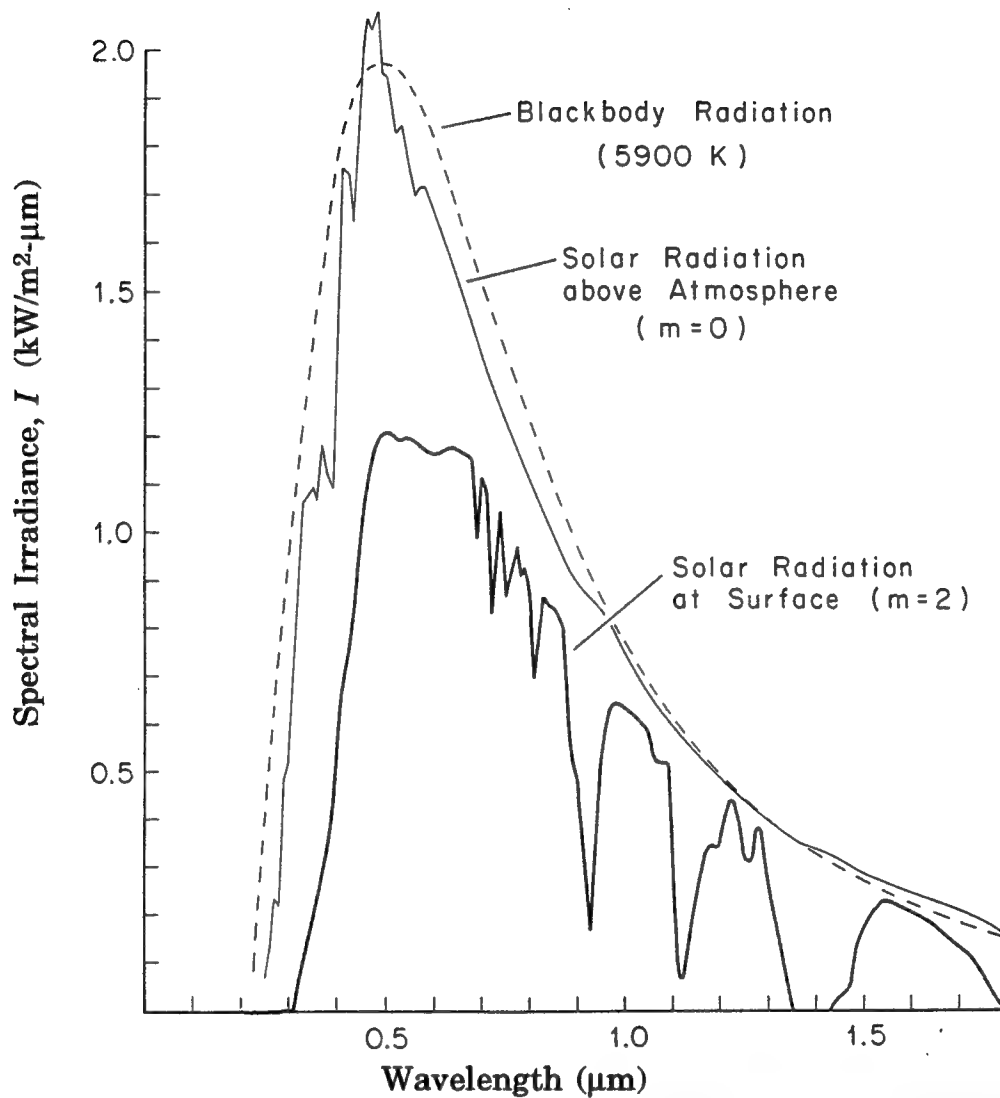
Figure 3.21 Spectral irradiance of direct sunlight before and after it passes through a clear atmosphere, together with the blackbody radiation curve of the sun (5900 °K) accounting for the steradian. The number of standard atmospheric masses is designated by m. Thus, $m = 2$ is applicable for sunlight when the sun is 30° above the horizon (from Stewart, 1985)

directed normal to the surface. As waves spread the image of the sun over a large glittering area, the effect depends on the surface roughness described by the root mean square slope, σ_r. He showed that for solar elevations greater than 80° (measured from the horizon), reflected solar radiation could cause an apparent temperature increase of up to 0.15 °C under calm conditions ($\sigma_r = 0.1$). For solar elevations less than 60°, the apparent temperature increase diminishes to 0.01 °C or less regardless of sea condition.

Reflection of the sun's irradiance has been shown to have minimal significance even at high elevation angles. The rest of the sky, including clouds, poses a more complicated difficulty. By definition, the window region discussed earlier between 8 and 12μm has low absorption due to its high transmissivity. Therefore, the spectral exitance of a clear sky is generally low because it is a poor emitter. Nevertheless, for very long path lengths through the atmosphere encountered when viewing the horizon, the atmosphere becomes a good absorber even in this window and approaches blackbody characteristics at air temperature. Under a clear sky, the exitance of a calm sea is maximum at normal incidence angle where the reflectivity is a minimum. As the incidence angle increases, the observed radiance decreases because the exitance of the ocean surface $\varepsilon M_{b\lambda}$ decreases faster than the reflected irradiance $(1-\varepsilon)M_{r\lambda}$ increases. Approaching the horizon, however, the reflected sky emission increases rapidly counteracting the sharp decrease in ocean surface exitance. Saunders (1968) illustrates these characteristics in Figure 3.22.

Clouds typically have greater emittance than a clear sky due to their higher concentration of water vapor, a good absorber. Hence, the increase in background radiation from the clouds may cause a distorted measured exitance as depicted in Figure 3.22 also. Peacock et al. (1981) and Gasparovic et al. (1982) provided a graphic example of cloud reflection. Figure 3.23 exhibits a scanned gray-scale thermal image of 6 nautical miles of sea surface taken from an aircraft with the large variations of reflection due to incidence angle removed. The light areas (warmer than darker
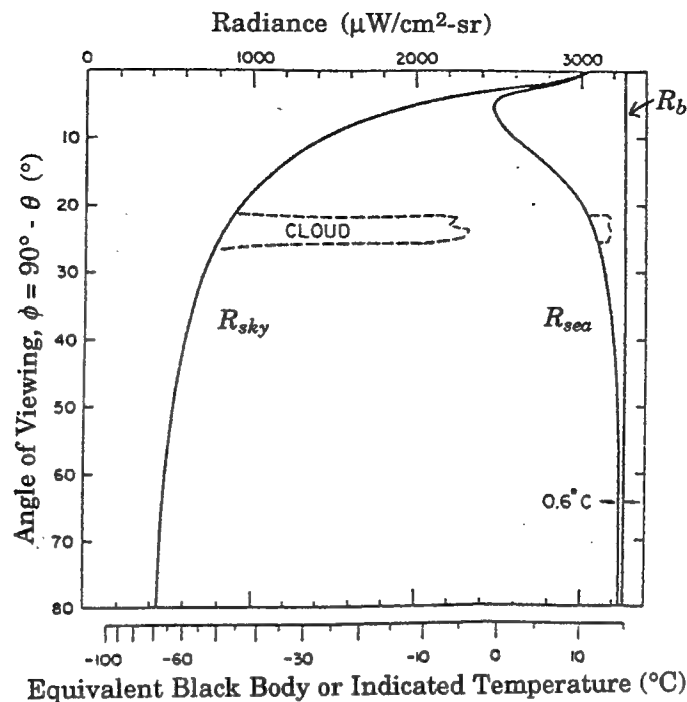
Figure 3.22 Typical distributions of the radiance of a calm sea, R_{sea}, and of a cloudless sky, R_{sky}, in the region of 8.2 - 12.5 μm. R_b is the radiance of a blackbody having the same temperature of 15 °C as that of the ocean (from Saunders,1968).
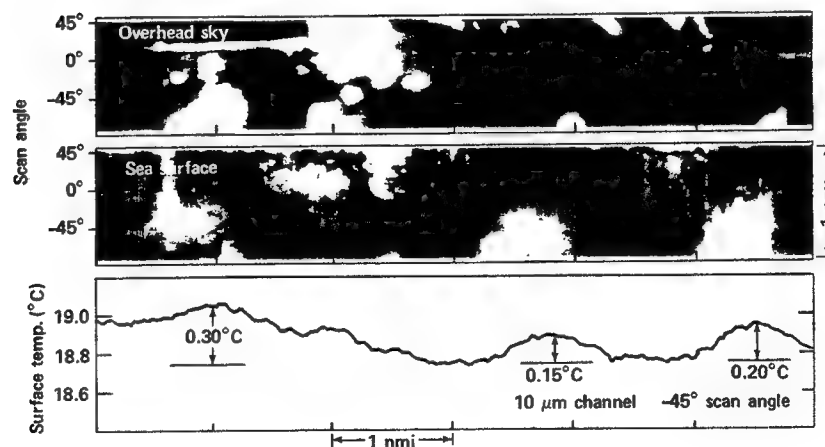
Figure 3.23 Reflected cloud image (from Gasparovic *et al.*, 1982). Clouds are visible by direct observation of the overhead sky and by reflection from the ocean surface. The trace in the bottom figure shows the variation recorded along the -45° scan angle line through the sea surface temperature image.

areas) in the sea surface thermal image correspond directly to the reflections of the clouds in the overhead sky. The bottom trace is a slice from the thermal image at -45° where cloud reflections contribute distinct changes in apparent temperature of 0.15 - 0.30 °C. Gasparovic *et al.* (1974) also clearly demonstrate this effect from field measurements made aboard the R/V Cove. Figure 3.24 shows nighttime plots of 3.8 μm sky and ocean radiometer signals. The first twelve minutes depict a clear sky while the sudden spike around 16 minutes indicates the passage of a single cloud causing a large change in the apparent ocean temperature due to the reflected image.

Assuming the ocean is flat, the measured cloud emittance combined with the water reflectivity results in an expected cloud reflection on the ocean surface which is compared with the measurements in Figure 3.25. The difference between the computed and measured results arises from the effects of surface waves, i.e. roughness, which tend to spread the image over a larger spatial extent and to reduce the intensity at the center. This might explain the blurring of the cloud reflections in Figure 3.23. Saunders (1968) provided an explanation for the roughness effect of the ocean on exitance by duplicating the sun-glitter analysis performed by Cox and Munk (1954). Specifically, the emittance of the surface increases with roughness at oblique angles of incidence ($\theta > 50°$) while for $\theta < 50°$ the exitance is independent of roughness as shown in Figure 3.26. More interestingly, he identifies a phenomenon called the "infrared horizon" or the "horizon contrast". Close to the horizon ($\theta = 85°$ to 90°), the surface exitance continues to decrease for a given roughness whereas the calm surface depicted in Figure 3.22 and redrawn in Figure 3.26 approaches the measured sky emittance. For a rough sea, the surface appears colder at the horizon than it would for a calm sea.

The effect of sky reflection or background radiation into the radiometer at varying surface slopes becomes a major difficulty. The explanation lies in the topic of shadowing. When a rough sea is viewed at the horizon, the slopes on the back sides of the waves and deep in the
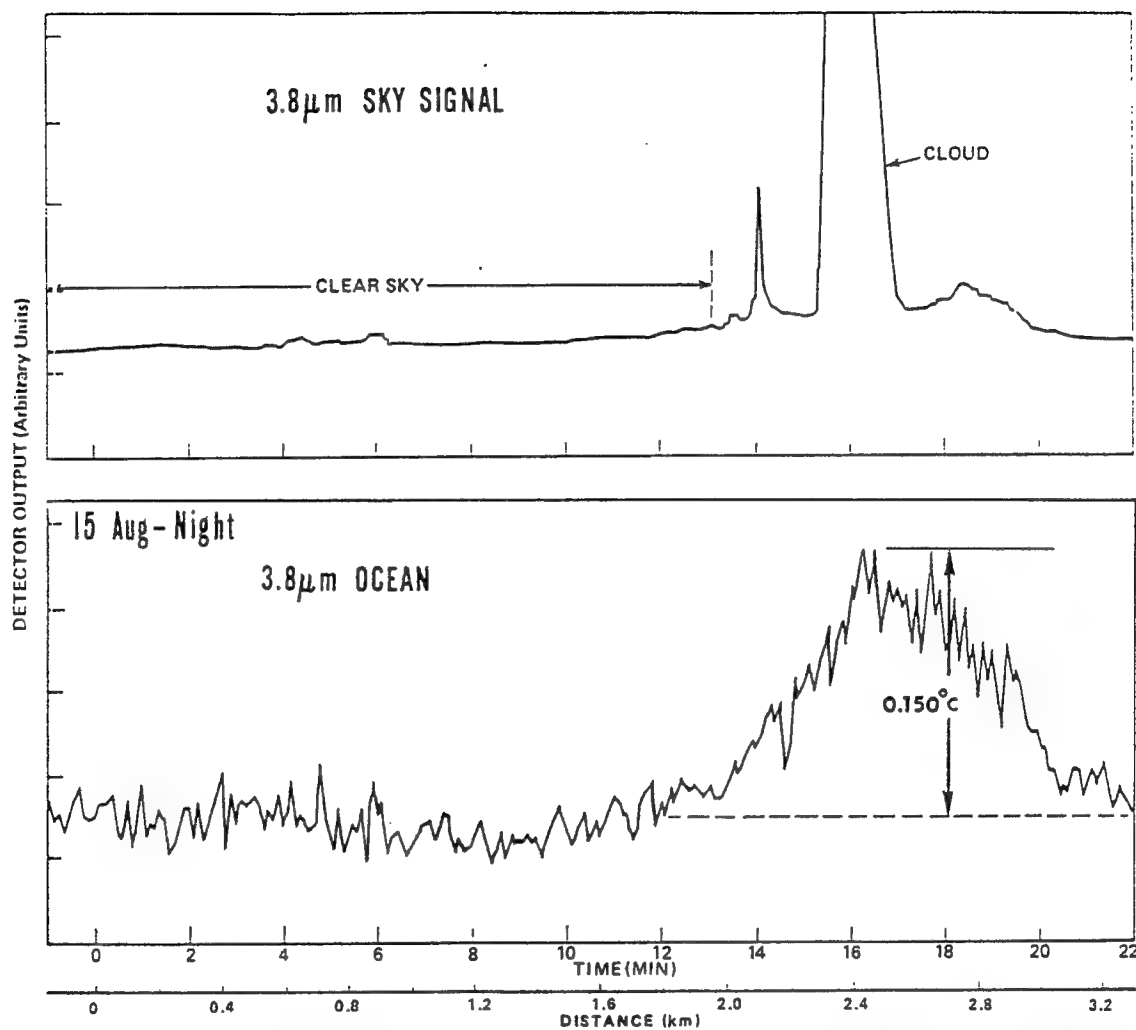
Figure 3.24 Data segment from the 3.8 μm channel on August 15, 1973 at 20° incidence angle. Each point plotted represents an average over 4.5 seconds with the vessel underway at 3.5 m/s (from Gasparovic *et al.*, 1974).
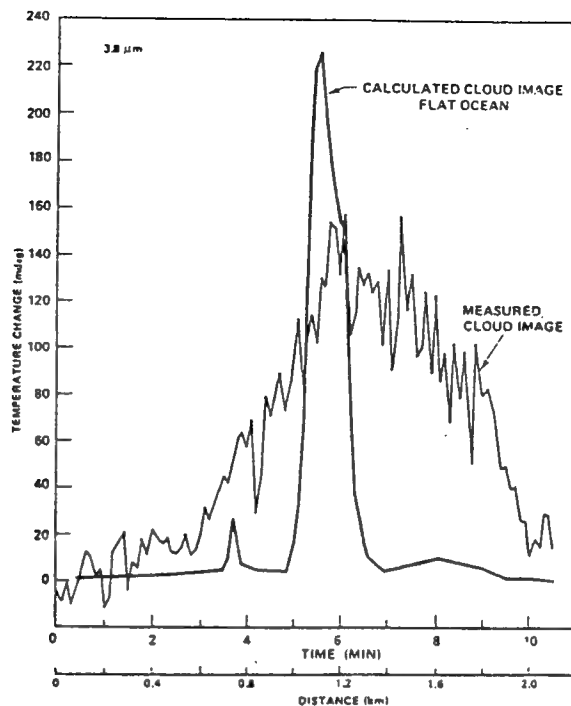
Figure 3.25 Comparison of the measured cloud image in the ocean from Figure 2.24 with a calculated image of the ocean, assuming the sea is flat (from Gasparovic *et al.*, 1974).
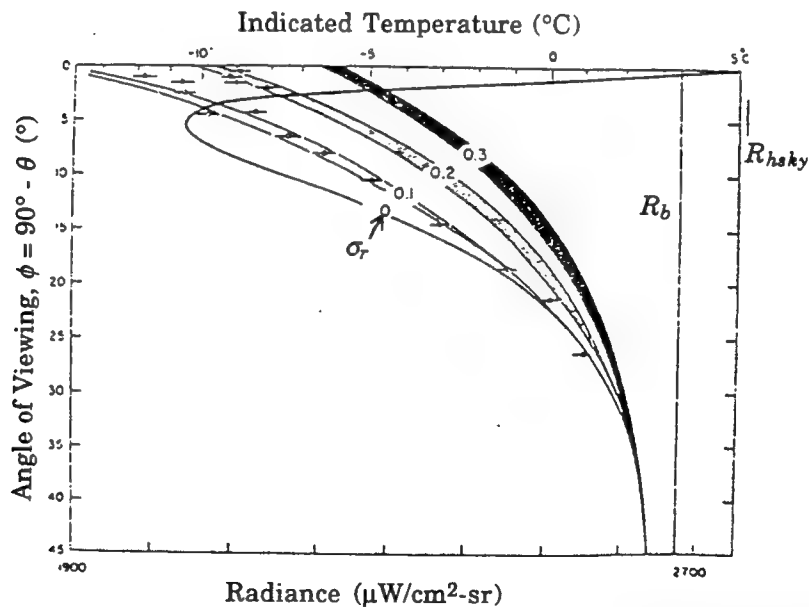
Figure 3.26 Radiance of the ocean as a function of viewing angle, ϕ, and surface roughness, σ_r, for March 15, 1966. R_b is the radiance of a blackbody having the same temperature as that of the ocean. R_{hsky} is the radiance of the sky at the horizon only. The wind speed was 2 -3 m/s (from Saunders, 1968).

troughs are hidden from sight. Only the fronts of the waves are exposed resulting in two effects. First, the local angle of incidence is smaller thus reducing the reflectivity. Simultaneously, the ray reflected into the line of sight from the smaller zenith angle originates from higher in the sky dome. (Zenith angle is measured identical to incidence angle only looking up along a line of sight.) In other words, the warm sky region near the horizon is never reflected into the line of sight, but is replaced with the colder sky from higher elevation angles. The combination of an increased surface emissivity and decreased sky emittance results in the continued decrease of apparent sea surface temperature shown in Figure 3.26. Variable cloudiness, then, coupled with a rough sea presents a very difficult problem since the whole sky dome does not have a uniform emittance.

Surface-active materials not only have hydrodynamic effects but also electromagnetic consequences in the infrared. The emissivity of surfactants is generally less than that of water. Comparing a thick film (~ 1 - 2 mm) of surfactant which did not hinder evaporation with a monolayer of the same substance in an evaporation-free container produced the following results (Jarvis and Kagarise, 1962). The thick film of surfactant appeared cooler than a clean water surface at the same real temperature, while the surface-active monolayer gave the equivalent temperature of the clean surface. Depending on the sensitivity of the radiometer, the monolayer may still influence emissivity even if the changes in temperature are too small to be detected by the radiometer. The difference in temperature between a thick film and a monolayer is probably due to differences in reflectivity (i.e. emissivity) between water and surfactants. However, even if the reflectivity of the 20 Å monolayer is different from that of water, it's contribution to the total emittance of the water-surfactant surface is negligible because the radiometer senses to roughly a 10 μm layer. Thus, depending on the slick's thickness, the sky or any background reflection will become more important as it will produce more of the radiation received by the radiometer depending upon the change in reflectivity. For thicker layers such as those near converging flows on the

ocean, the optical depth of the surface-active material becomes important along with a more complete knowledge of the its emissivity characteristics.

CHAPTER 4

Wakes, Wave Theory, and Turbulence

4.1 Introduction

The term wake is commonly applied to the whole region of non-zero vorticity on the downstream side of a body in a uniform stream. Vorticity is mathematically defined as

$$\vec{\omega} = \nabla \times \vec{u} \tag{4.1}$$

and describes twice the local rotation of fluid parcel where $\vec{u} = (u,v,w)$ is the velocity field. The velocity distribution in the wake is likely to be complicated in the neighborhood of the body, even when the flow is steady, as in the case of flow separation or the development of the Kármán vortex street. Far downstream the direct effect of the presence of the body has disappeared and the streamlines have become parallel. In this region the vorticity shed from the body surface is being advected in the stream direction, and diffused by viscosity. Eventually advection is more important than stream wise diffusion since the vorticity is continually spreading and the stream wise gradient of velocity is small compared with that in the lateral plane. Thus, the boundary-layer approximations apply, although for smaller Reynolds numbers or for bluff bodies they apply farther downstream. Along with the continual spreading of the wake, frictional forces tend to make the velocity uniform. Far downstream the departure from the free-stream velocity is small. The application of these assumptions will be considered later in the presentation of laminar and turbulent wakes. First, a discussion of the flow in the neighborhood of a bluff body, in particular a circular cylinder, is appropriate.

4.2 Near Wake of a Circular Cylinder

Consider a circular cylinder with diameter, D, in steady translational motion with speed, U, through an undisturbed, infinite body

of fluid with density, ρ, and viscosity, μ. The non-dimensional quantities describing the flow field depend on the Reynolds number

$$Re = \frac{\rho U D}{\mu}. \tag{4.2}$$

The Reynolds number can be thought of as the ratio of inertial to viscous forces in a flow field. When $Re \ll 1$, the inertial forces are considered to be negligible compared to the viscous forces. Conversely, when $Re \gg 1$ the opposite may be expected and the viscous forces may be negligible.

In the intermediate range neither assumption is valid exclusively. At $Re \ll 1$, the dominant process is the diffusion of vorticity away from the cylinder. The fluid in immediate contact with the cylinder is dragged along at the same speed as the cylinder according to the "no-slip" condition at the boundary, leading to the generation of vorticity at the cylinder. The vorticity generated diffuses from the cylinder which is moving steadily. Vorticity diffuses over a distance L from its source on the cylinder in a time on the order of L^2/v, and during this time the cylinder moves a distance UL^2/v. For diffusion distances, L, on the order of the cylinder dimension, D, and $Re \ll 1$, the diffusion process dominates and the vorticity distribution exhibits approximate symmetry near the cylinder as in Figure 4.1, for $Re = 0.25$. On the other hand, for diffusion distances $L < D$, the motion of the cylinder has the effect of leaving the vorticity behind in a region at the rear of the cylinder. The latter situation initiates the discussion of back flow and separation.

Consider in Figure 4.2 the accelerating flow between points A and B. The local strength of vorticity at A, or the integrated vorticity across the boundary layer thickness at A, is less than at B. The advected vorticity downstream from A is less than from B. Thus, positive vorticity (CCW) must be generated at B in order to maintain the vorticity strength. Between C and D, the opposite occurs due to the decelerating flow and negative vorticity (CW) is generated at D. However, the flow is only weakly

83

$R = 0.25$

$R = 13.05$

$R = 3.64$

$R = 39.0$

$R = 9.10$

$R = 57.7$
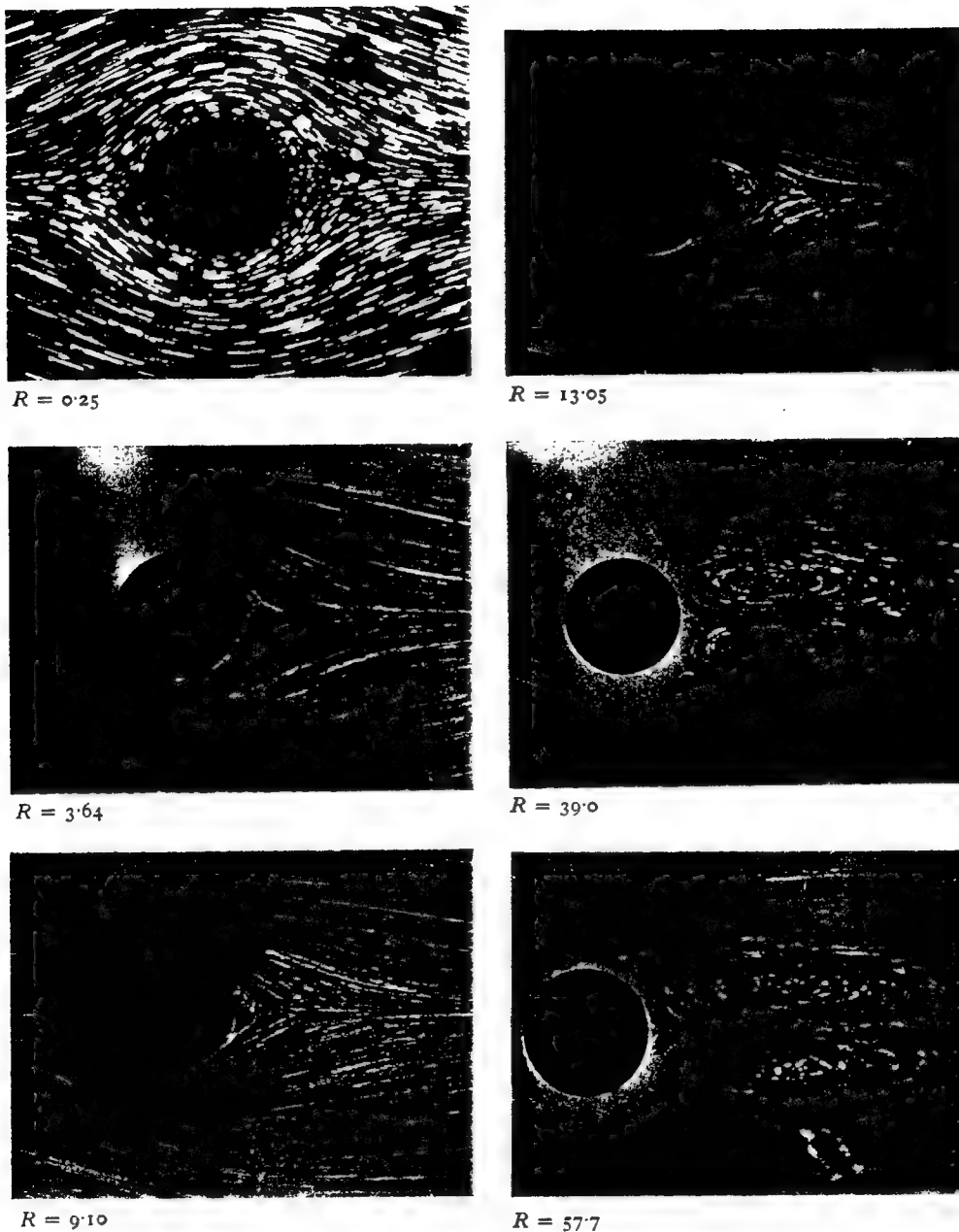
Figure 4.1   Streamlines of steady flow (from left to right) past a circular
cylinder of diameter, D. The photograph at $R = Re = 0.25$ shows
the movement of solid particles at a free surface, and all others
show particles illuminated over an interior plane normal to
the cylinder axis (from Batchelor, 1967).
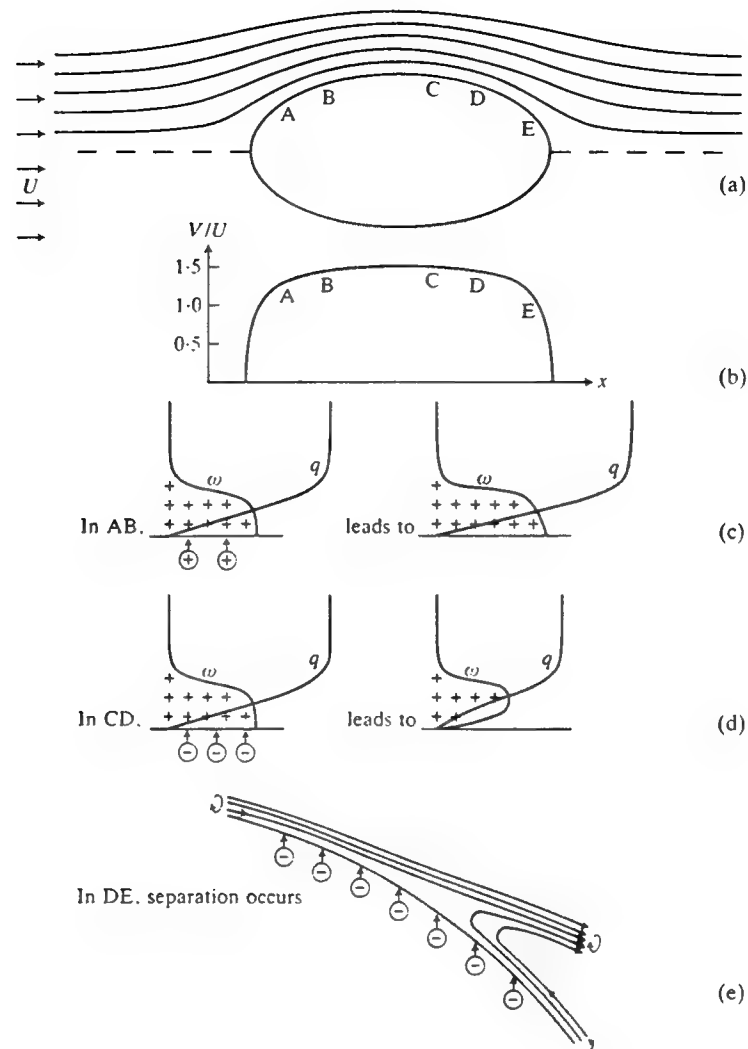
Figure 4.2   Separation of a boundary layer for flow around an elliptic
cylinder at rest in an oncoming stream of velocity, U, directed
along the major axis of its elliptic cross-section where ω and q
represent the distributions of vorticity and fluid speed
respectively within the boundary layer (from Lighthill, 1986).

decelerating and the slight negative vorticity is hardly noticed as the diffusion of positive vorticity dominates. Between D and E, the flow is strongly decelerating and the diffusion of negative vorticity dominates. At E, a reversed flow must develop. When the reversed flow and the stream flow meet, the flow separates.

In Figure 4.1 a region of slowly circulating fluid immediately behind the cylinder is evident at Re = 9.10, and as the Reynolds number increases further the region becomes elongated and the motion intensifies. Within the region the flow exhibits two groups of closed streamlines arranged symmetrically. Each group comprises a "standing eddy" with the top having a clockwise circulation and the bottom the opposite. Clearly, as Reynolds number increases advection becomes more effective in sweeping the vorticity downstream than diffusion away from the cylinder. More and more vorticity is carried around to the rear of the cylinder, the vorticity being of negative sign (CW) near the upper surface and positive near the lower. Ultimately, more vorticity than is needed for the no-slip condition is located behind the cylinder, and a backward flow is induced. The backward flow counters the forward-moving fluid and deflects it away from the rear of the cylinder, which in turn tends to strengthen the rotation of the standing eddy. An alternative explanation of separation arises from viewing these progressive photos.

As the Reynolds number increases between 30 and 40, the steady flow further downstream appears to become unstable to small disturbances, while the eddies remain stable and attached to the body. The instability gives rise to a slow "sinusoidal" oscillation of the wake as shown in Figure 4.3. As the Reynolds number increases beyond the point at which the instability first appears, the oscillations of the wake move closer to the cylinder (depending upon experiment, these oscillations might roll up before affecting the eddies). When the Reynolds number approaches 60, the oscillations begin to affect the two standing eddies immediately behind the cylinder. The two standing eddies oscillate together in lateral position, and appear to shed some rotating fluid at the end of every half-period,
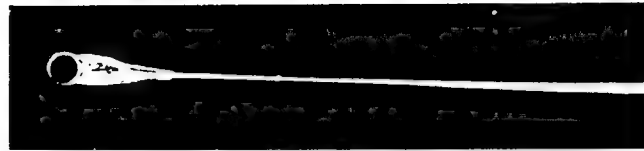
$R = 32$

$R = 55$
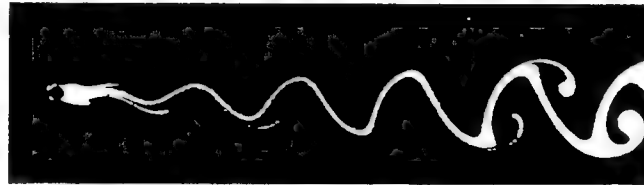
$R = 65$
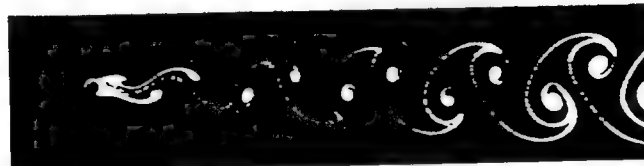
$R = 73$
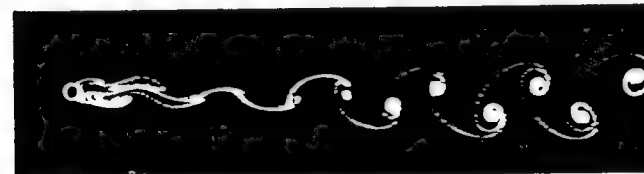
$R = 102$

$R = 161$

Figure 4.3   Streaklines in the wake behind a circular cylinder in a stream
of oil (from Batchelor, 1967).

alternately on top and on bottom. The frequency, F_o, of this "shedding" can be described by the non dimensional Strouhal number

$$St = \frac{F_o D}{U} = \frac{local\ \ acceleration}{advective\ \ acceleration} \qquad (4.3)$$

denoting the ratio of local to advective accelerations. Most of the fluid passing close to the cylinder appears to gather itself into discrete lumps of vorticity, arranged in two regular staggered rows on either side of the stream-wise line through the center of the cylinder. Each vortex in the row has the same sign, while the two rows differ in sign (i.e. CW on top and CCW on bottom).

This regular array of vortices in the wake is known as the Kármán vortex street, and moves downstream with a velocity slightly less than the free stream. The two eddies immediately behind the cylinder are not clearly recognizable for values of Re much above 100, but the vortex street continues to form in the wake up to much larger Re numbers. The vortices themselves become unstable at $Re \approx 200$ and become turbulent at $Re \approx 400$. The vortex street is recognizable up to $Re \approx 2500$ and up to $Re \approx 4 \times 10^5$ periodic oscillation of the flow near the cylinder is detectable, although irregular. The Strouhal number ≈ 0.2 throughout this range.

Von Kármán provided a classic argument of the stability of two parallel periodic vortex-rows as documented by Milne-Thomson (1949). Von Kármán showed for a non-viscous fluid the equilibrium has a 1st-order instability (i.e. deviations from the array grow exponentially), unless the ratio of the transverse height between rows, h, to the spacing between vortices within each row, a, is equal to 0.281. Lamb (1945) furthers the analysis and shows that indeed, at least for neutral stability, the ratio of $h/a = 0.281$ is valid for all cases except for maximized initial disturbance. Many references in the literature are made to this as the "stable spacing ratio". However, various investigators cited by Birkhoff and Zarantonello (1957) have shown that the spacing ratio also has a higher-order instability.

Moreover, since h is invariant in a non-viscous fluid, the ratio of h/a is determined by its initial value, and not by the stability of this downstream. Finally, the break up of the real vortex-street does not proceed via irregular wandering of the point vortices, as considered by von Kármán. Thus, the varying observed ratios must be due to some cause other than a tendency of a "stable" spacing-ratio, contrary to what was once thought. Possibly, the regular nature of the periodic shedding of vortices causes the street to be stable and not the actual spacing-ratio resulting in the Strouhal number regularity over a large range of Reynolds numbers.

As a note for later discussion, an unsteady flow develops near the cylinder in the $50 < Re < 110$ range, and the drag force oscillates with the formation of each eddy. In addition, the top-to-bottom asymmetry of the flow gives rise to an oscillating lift force. As the flow forms a clockwise eddy, it rushes past the top of the cylinder somewhat faster than the flow across the bottom. This causes the pressure on the top to be less, resulting in a lift force upward in the cross-flow direction. When this clockwise eddy fully develops and breaks away, the opposite occurs and a downward lift force results. These alternating lift forces, as documented in Figure 4.4 could cause transverse oscillations which could regularize the vortex shedding and the Strouhal number.

4.3 Far Wake of Non Lifting Bodies (Laminar Case)

Vorticity is generated as the flow goes over a body and is swept into the wake. As this vorticity is carried downstream, the positive vorticity in the lower half-plane diffuses toward the centerline, where it meets the negative vorticity of the upper plane. Furthermore, at the outer edges of the wake, the vorticity diffuses outward to spread the wake. As mentioned earlier, the boundary layer equations govern the wake flow as the Reynolds number is large confining the viscous effects to thin regions where steep velocity gradients exist. Inviscid flow theory fails near a "no-slip" boundary, as a velocity gradient estimated as
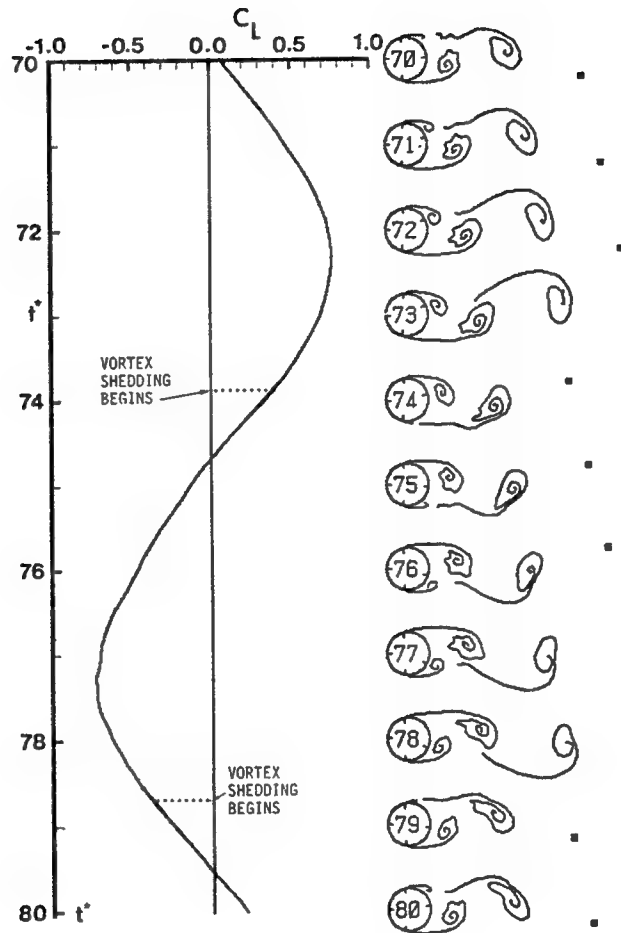
Figure 4.4   Evolution of lift due to vortex shedding in the wake of a circular
             cylinder at the later stages of impulsively-started flow where
             C_L is the coefficient of lift and t^* is a non-dimensional timestep
             (from Sarpkaya and Isaacson, 1981).

$$\frac{\partial u}{\partial y} \sim O\left[\frac{U}{D}\right] \tag{4.4}$$

results in an unreasonably small quantity. For the thin region near a body termed the boundary layer of thickness, δ, the velocity gradient

$$\frac{\partial u}{\partial y} \sim O\left[\frac{U}{\delta}\right] \tag{4.5}$$

more realistically approximates the order of magnitude. Note two important facts that $\delta << D$ and as the $Re \to \infty$, δ approaches zero.

Formulation of the boundary layer phenomenon initiates with the Navier-Stokes equations. Consider the x-direction (streamwise) momentum equation

$$\frac{\partial u}{\partial t} + u\frac{\partial u}{\partial x} + v\frac{\partial u}{\partial y} = -\frac{1}{\rho}\frac{\partial P}{\partial x} + v\left(\frac{\partial^2 u}{\partial x^2} + \frac{\partial^2 u}{\partial y^2}\right) \tag{4.6}$$

and the continuity equation for an incompressible fluid

$$\frac{\partial u}{\partial x} + \frac{\partial v}{\partial y} = 0 \tag{4.7a}$$

or

$$\nabla \cdot \bar{u} = 0 \tag{4.7b}$$

where u is the x-direction velocity component, v is the y-direction (cross-stream) velocity component, t is the time, P is the pressure, ρ is the density of the fluid and v is the kinematic viscosity. Scaling of (4.6) will provide valuable insight into the nature of the boundary layer behavior. We now scale the dimensional variables, $x = x*D$, $y = y*\delta$, $u = u*U$, $P = P*\rho U^2$, $t = t*D/U$, and using continuity from (4.7a) arrive at a characteristic vertical velocity for $v = v*U\delta/D$. Applying these scalings and dropping *, the x-direction Navier-Stokes equation becomes non-dimensionalized as

$$\frac{\partial u}{\partial t} + u\frac{\partial u}{\partial x} + v\frac{\partial u}{\partial y} = -\frac{\partial P}{\partial x} + \frac{1}{Re}\left(\frac{\partial^2 u}{\partial x^2} + \left(\frac{D}{\delta}\right)^2 \frac{\partial^2 u}{\partial y^2}\right). \qquad (4.8)$$

Applying similar scaling to the y-direction momentum equation results in

$$\frac{\partial P}{\partial y} = 0 \qquad (4.9)$$

the pressure is a function of x and t only and constant across the boundary layer. All the terms in (4.8) are of $O(1)$ except for the last two. Applying the limit $Re \to \infty$, the second to last term vanishes while the final term is indeterminate. The logical choice is that the last term is $O(1)$; otherwise we arrive at the inviscid flow theory solution or a boundary layer with constant shear stress and a linear velocity profile. Therefore,

$$\delta \sim \frac{D}{\sqrt{Re}} \sim \sqrt{vt} \qquad (4.10)$$

and the dimensional boundary layer equation takes the form

$$\frac{\partial u}{\partial t} + u\frac{\partial u}{\partial x} + v\frac{\partial u}{\partial y} = -\frac{1}{\rho}\frac{\partial P}{\partial x} + v\frac{\partial^2 u}{\partial y^2} \qquad (4.11)$$

where δ is the boundary layer thickness describing the length scale of diffusion.

The propagation of vorticity follows directly. Within the boundary layer, the z-component of vorticity is

$$\zeta = \frac{\partial v}{\partial x} - \frac{\partial u}{\partial y} = -\frac{\partial u}{\partial y} \qquad (4.12)$$

according to our boundary layer assumptions. Using Prandtl's boundary layer (4.11)

$$\frac{\partial \zeta}{\partial t} = -\frac{\partial}{\partial y}\frac{\partial u}{\partial t} = -\frac{\partial}{\partial y}\left(-\frac{1}{\rho}\frac{\partial P}{\partial x} + v\frac{\partial^2 u}{\partial y^2} - u\frac{\partial u}{\partial x} - v\frac{\partial u}{\partial y}\right)$$

$$= v\frac{\partial^2 \zeta}{\partial y^2} - \left(\frac{\partial u}{\partial x} + \frac{\partial v}{\partial y}\right)\zeta - u\frac{\partial \zeta}{\partial x} - v\frac{\partial \zeta}{\partial y} \tag{4.13}$$

and employing continuity from (4.7a)

$$\frac{D\zeta}{Dt} = v\frac{\partial^2 \zeta}{\partial y^2} \tag{4.14}$$

where

$$\frac{D}{Dt} = \frac{\partial}{\partial t} + \bar{u}\cdot\nabla \tag{4.15}$$

is the total derivative of a variable. Thus, (4.14) describes vorticity advecting downstream, while at the same time diffusing laterally into the fluid domain.

In addition to the boundary layer assumptions outlined above, the "far wake" approach to a solution allows for two more assumptions. As the wake continually spreads, departure of the wake velocity, u_w, from the free-stream velocity, U, is small sufficiently far downstream such that

$$|U - u_w| << U \tag{4.16}$$

as the frictional forces tend to make the velocity profile uniform across the wake. Second, the velocity and pressure in the irrotational flow outside the wake are approximately uniform, and so the pressure is assumed uniform in the wake. The following analysis is outlined in Panton (1984) with a diagram of the flow shown in Figure 4.5.

We assume that similarity exists in terms of the velocity defect,

$$u = U - u_w \tag{4.17}$$
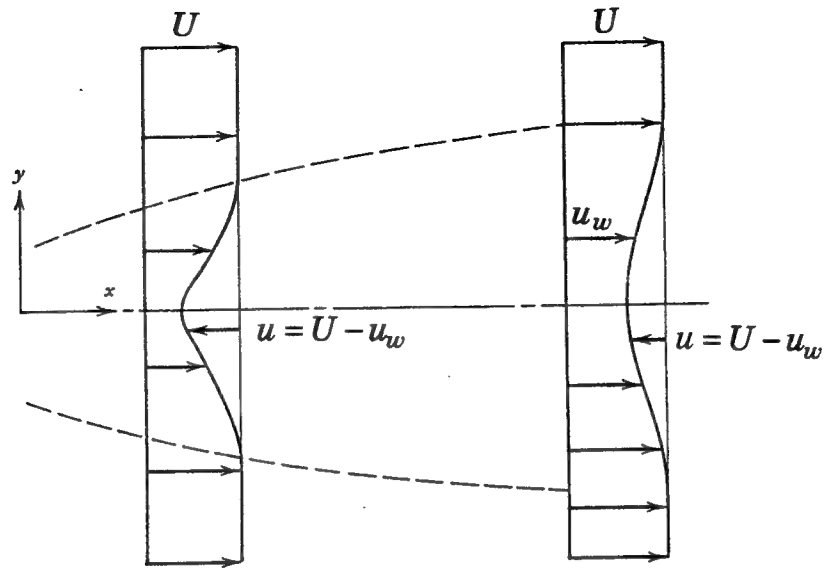
Figure 4.5   Laminar wake of a bluff body, i.e. circular cylinder (from Panton, 1984).
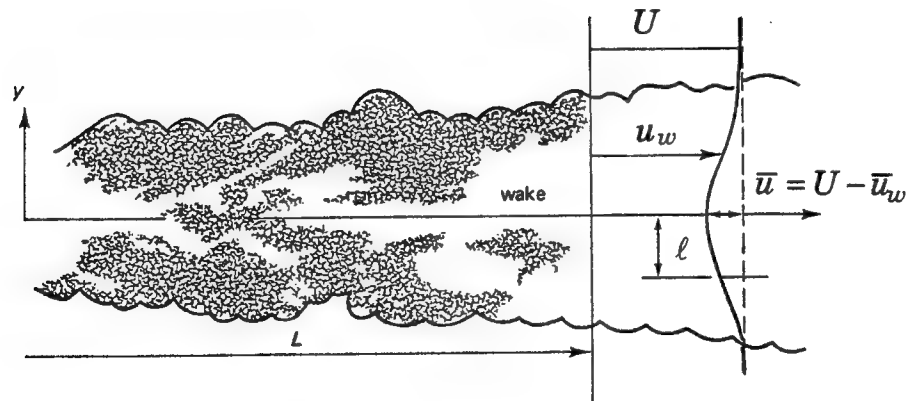
Figure 4.6   Plane turbulent wake of a circular cylinder (from Tennekes and Lumley, 1972).

where u_w is the velocity profile across the wake. Introducing the scalar stream function, ψ, in the form

$$d\psi = \frac{\partial \psi}{\partial x} dx + \frac{\partial \psi}{\partial y} dy \qquad (4.18)$$

allows description of the velocity along a streamline. Defining $u = \partial \psi / \partial y$ and $v = -\partial \psi / \partial x$ yields the stream function "exact", or truly a function of x and y, as

$$-\frac{\partial v}{\partial y} = \frac{\partial u}{\partial x} \qquad (4.19a)$$

or

$$\frac{\partial^2 \psi}{\partial y \partial x} = \frac{\partial^2 \psi}{\partial x \partial y}. \qquad (4.19b)$$

The relation in (4.19a) equals the continuity equation of (4.7a). Thus, the stream function automatically satisfies mass-conservation. Following from (4.18) when ψ is constant

$$\frac{v}{u} = \frac{dy}{dx}\bigg|_{\psi=constant} \qquad (4.20)$$

states that the velocity vector tangent to the curve $\psi = constant$ defines the streamline. Our scaling assumes similarity of the form

$$\psi = A x^P f(\eta) \qquad (4.21)$$

where

$$\eta = \frac{y}{B x^q} \qquad (4.22)$$

with the constants $A, B, p,$ and q to be chosen during the analysis. Substituting ψ and η into the boundary-layer (4.11) results in terms proportional to

$$U\frac{\partial u}{\partial x} \propto UB^2 x^{2q-1}\left[(p-q)f' - q\eta f''\right]$$

$$-u\frac{\partial u}{\partial x} + v\frac{\partial u}{\partial y} \propto ABx^{p+q-1}\left[(q-p)f'^2\right.$$
$$\left. +2q\eta f'f'' - pff''\right]$$

(4.23)

$$v\frac{\partial^2 u}{\partial y^2} \propto vf'''$$

Recall that the drag force, F_D is related to the momentum thickness, Θ_m, through

$$F_D = \rho U^2 \Theta_m = \rho U^2 \int\left[\frac{u_w}{U}\left(1 - \frac{u_w}{U}\right)\right]dy \qquad (4.24)$$

defining the momentum flux equal to the momentum deficit. Substituting ψ and η into (4.24) arrives at

$$F_D = \rho Ax^p \int\left[U - \frac{A}{B}x^{p-q}f'\right]f'd\eta. \qquad (4.25)$$

We now seek a self-similar solution for which f is independent of x. Similarity cannot be accomplished unless $p = 0$, $q = 0.5$, and $x \rightarrow \infty$. The final constraint restricts the solution to the "far-wake", allowing (4.23) and (4.25) to govern the far wake in the form

$$f''' + \frac{UB^2}{2v}\left[\eta f'' + f'\right] = 0 \qquad (4.26)$$

and

$$F_D = \rho AU\int f'd\eta. \qquad (4.27)$$

The equation in (4.26) has the solution

$$f' = e^{-\eta^2} \tag{4.28}$$

when the coefficient in front of the bracket

$$\frac{UB^2}{2v} = 2 \tag{4.29}$$

such that,

$$B = \left(\frac{4\eta}{U}\right)^{\frac{1}{2}}. \tag{4.30}$$

Inserting (4.28) into (4.27) reveals

$$A = \frac{2F_D}{\rho\sqrt{\pi U}} \tag{4.31}$$

Hence, the final expressions become

$$\eta = y\sqrt{\frac{U}{4vx}}, \tag{4.32}$$

$$\psi = \frac{F_D}{2\rho\sqrt{\pi U}} erf(\eta), \tag{4.33}$$

and

$$U - u_w = \frac{F_D}{\rho\sqrt{4\pi vxU}} e^{-\eta^2}. \tag{4.34}$$

Therefore, as the "far" wake decays downstream, the velocity defect decreases as $x^{-\frac{1}{2}}$ and with a Gaussian distribution profile in y according to (4.34), while the thickness of the laminar wake increases parabolically, $b_\ell \sim x^{\frac{1}{2}}$ according to (4.32). Surprisingly, all bodies produce a wake for Reynolds numbers greater than zero with this solution being valid. The actual influence of the Reynolds number is such that one need not go "far" downstream when Reynolds number is high.

4.4 General Characteristics of Turbulence

Turbulent flow is difficult to define precisely, and as such we choose to characterize some of its properties. Turbulence exhibits an irregularity, or randomness, which prevents a deterministic approach to the problem forcing one to rely on a statistical description. Consider a steady laminar flow which transforms into an unstable, unsteady ($\partial/\partial t(\bullet) \neq 0$) flow. One now observes significant fluctuations, u_i', about the mean flow velocity, $\bar{u}_i$, which results in an instantaneous velocity of

$$u_i = \bar{u}_i + u_i'. \tag{4.35}$$

where the subscript $i = 1,2,3$ denotes the tensor notation for the quantities along the coordinates x, y, and z which allows for simplicity in later derivations. Mean flow values averaged over an extended period allow for the time-averaged fluctuations to be zero, $\overline{u_i'} = 0$, and the flow to be "steady" in the mean, $\partial \bar{u}_i/\partial t = 0$. The irregularities created by turbulence have certain spatial structures known as eddies which encompass a continuous distribution of shapes and sizes. Once generated, turbulence diffuses into non-turbulent regions causing rapid mixing and increased rates of momentum, heat, and mass transfer.

Turbulence is a flow property, as opposed to a fluid property, and as such turbulent flows always occur at high Reynolds numbers where inertial effects dominate. In addition, turbulent flow is three-dimensional and characterized by high levels of fluctuating vorticity. The scales of eddies produced from the rotational flow extend from the largest, comparable to the thickness or size of the turbulent region, to the smallest restricted by viscous forces which tend to destroy them. More importantly the steep velocity gradients cause viscous shear stresses which perform deformation work increasing the internal energy of the fluid at the expense of the kinetic energy of the turbulence. Consequently, turbulent flow displays a much greater dissipative nature requiring a continuous supply of energy to maintain itself or else it decays rapidly. Finally, turbulence is a

continuum phenomenon stating that the smallest scales occurring in a turbulent flow usually exceed any molecular ones.

Reynolds performed the velocity decomposition of (4.35) in order to develop equations to govern the mean quantities of turbulent flow. Applying the velocity decomposition to (4.7b) the continuity equation becomes

$$\frac{\partial u_i}{\partial x_i} = \frac{\partial}{\partial x_i}(\bar{u}_i + u_i') = \frac{\partial \bar{u}_i}{\partial x_i} + \frac{\partial u_i'}{\partial x_i} = 0. \tag{4.36}$$

If (4.36) is averaged, the second term vanishes allowing

$$\frac{\partial \bar{u}_i}{\partial x_i} = 0 \tag{4.37}$$

while subtracting (4.37) from (4.36) allows

$$\frac{\partial u_i'}{\partial x_i} = 0. \tag{4.38}$$

Substituting the Reynolds decomposition into the Navier-Stokes equations and following the rules of averaging we find that the mean flow would satisfy

$$\bar{u}_j \frac{\partial \bar{u}_i}{\partial x_j} + \overline{u_j' \frac{\partial u_i'}{\partial x_j}} = -\frac{1}{\rho}\frac{\partial \bar{P}}{\partial x_i} + \nu \frac{\partial^2 \bar{u}_i}{\partial x_j^2} \tag{4.39}$$

if the second term on the left-hand side were absent. This term represents the mean transport of fluctuating momentum through the interaction of the turbulent velocity fluctuations. We may write this term as

$$\overline{u_j' \frac{\partial u_i'}{\partial x_j}} = \overline{u_j' \frac{\partial u_i'}{\partial x_j}} + \overline{u_i' \frac{\partial u_j'}{\partial x_j}} = \frac{\partial}{\partial x_j}\left(\overline{u_i' u_j'}\right) \tag{4.40}$$

employing (4.38). The Navier-Stokes equations now become

$$\rho \bar{u}_j \frac{\partial \bar{u}_i}{\partial x_j} = -\frac{\partial \bar{P}}{\partial x_i} + \frac{\partial}{\partial x_j}\left(\mu \frac{\partial \bar{u}_i}{\partial x_j} - \rho \overline{u_i' u_j'} \right) \tag{4.41}$$

by inserting (4.40) into (4.39). The contribution of turbulent motion to the "mean" stress tensor is given by

$$\tau_r = -\rho \overline{u_i' u_j'} \tag{4.42}$$

known as the Reynolds stress tensor associated with the fluctuating flow.

In order to solve (4.41), we must develop relations between the mean and fluctuating flow — the closure problem. An initial phenomenological theory developed by Boussinesq and advanced by Prandtl presents the basic idea. For the moment, let us assign for the 2-D problem

$$\tau_r = -\rho \overline{u'v'} = \rho \nu_e \frac{\partial \bar{u}}{\partial y} \tag{4.43}$$

where ν_e represents the "apparent", "virtual", or "eddy" viscosity and is a property of the flow unlike ν which is a fluid property. Prandtl, as well as others such as G. I. Taylor, has put forth the notion of a "mixing length". He envisioned a turbulent exchange based on the assumption that fluid masses displaced transverse to the direction of the mean flow carry their momentum invariably over a distance, ℓ. Therefore, the mixing length is defined as the distance in the cross-stream direction which must be covered by a lump of fluid traveling with its original mean velocity in order to make the difference between its velocity and the velocity in its new position equal to the mean transverse fluctuation in the turbulent flow. The actual mechanism is probably more complicated, but the initial concept of a characteristic length is necessary for turbulent flow. According to his estimate of

$$v_e = \ell^2 \frac{\partial \overline{u}}{\partial y},$$

(4.44)

which is analogous to the kinetic-theory model for molecular viscosity, the mixing length is much like the mean free path in a gas. Even though the eddies in turbulence are incapable of the independent action of molecules, the concept works well with fairly simple assumptions for ℓ which allow solution to the problem of closure in (4.41).

Thus, Prandtl's mixing length hypothesis stated as

$$\tau_r = -\rho \overline{u'v'} = \rho \ell^2 \left| \frac{\partial \overline{u}}{\partial y} \right| \frac{\partial \overline{u}}{\partial y}$$

(4.45)

provides crude yet useful results for the asymptotic rate of growth and mean velocity profile for wakes. However, some errors plague Prandtl's argument including the fact that the eddy viscosity $v_e = 0$ when $\partial \overline{u}/\partial y = 0$ as occurs at the wake center. Experiments by Townsend (1949) show that the eddy viscosity has a maximum on the center line of the axis. Also, Prandtl's idea that only one scale exists for turbulence is quite incorrect as already pointed out. The larger eddies primarily affect the lateral spreading of the wake, while the smaller ones influence the momentum transfer within the wake. Moreover, his formulas say nothing about the turbulent energy decay rate.

Turbulence consists of fluctuating motion with a vast range of length scales. Consider the flow past a cylinder as the Re increases where the largest eddies begin to form of size $\ell \sim D$ and sweep into the wake. The time interval elapsed between the origin of the eddy and its downstream position, L, is of order L/U, allowing an estimate of $\ell \sim u'^* t \sim u'^* L/U$ where u'^* represents a characteristic velocity fluctuation for this length scale. Basically, we have equated the turbulent "diffusion" and advective time scales. As the wake continues to form we measure fluctuations, or eddies, of different size. Progressing farther downstream we discover that the eddy

size spectrum approaches constancy, or fully developed turbulence. The eddies range from $\ell \gg \ell_o \gg \ell_k$ where ℓ_o represents the median-sized eddies and ℓ_k the smallest, or Kolmogorov, eddies.

For the larger eddies we define a Reynolds number, $Re_\ell = u'^* \ell / v$, so that for $Re \gg 1$ we also expect $Re_\ell \gg 1$. However, these large scale eddies behave as if inviscid, acquire instabilities and produce smaller eddies with smaller Reynolds numbers, $Re_{\ell_o} = u_o'^* \ell_o / v$, where $u_o'^*$ is the characteristic turbulent velocity for these eddies. Still smaller eddies continue to form until finally a small, stable Reynolds number, $Re_{\ell_k} = u_k'^* \ell_k / v$, is reached where $u_k'^*$ represents the Kolmogorov scale velocity. The Reynolds number has become so small that viscous effects are important and the Kolmogorov eddies lose energy to heat. The preceding outline of the "Energy Cascade" explains the flow of energy from the mean flow down the scales of turbulence to the smallest scales. The energy flux per unit mass input from the mean flow and cascading down is then

$$\varepsilon_t \sim \left(u'^*\right)^3 \Big/ \ell \qquad (4.46)$$

which should equal the energy dissipated on the Kolmogorov microscale. Thus, we can form Kolmogorov length, time, and velocity scales as

$$\ell_k = \left(v^3 / \varepsilon_t\right)^{1/4}$$
$$t_k = \left(v / \varepsilon_t\right)^{1/2} \qquad (4.47)$$
$$u_k'^* = \left(v\varepsilon_t\right)^{1/4}$$

with $Re_{\ell_k} = u_k'^* \ell_k / v = 1$ which illustrates that the small-scale motion is quite viscous and the dissipation adjusts itself to the energy supply through the length scales. The equation in (4.4) states that the large-scale inertial dynamics can estimate the viscous dissipation of energy. Dissipation is a passive process which proceeds at a rate dictated by the inviscid nature of

larger eddies. Finally, substituting (4.46) into (4.47) we obtain the relations between the largest and smallest eddies

$$\ell_k/\ell = (Re_\ell)^{-3/4}$$
$$t_k/t = (Re_\ell)^{-1/2} \qquad (4.48)$$
$$u_k'^*/u'^* = (Re_\ell)^{-1/4}$$

demonstrating the wide separation between scales which enlarge as the Reynolds number increases.

4.5 Free Turbulent Flows: 2-D Wakes

Turbulent flows are termed free if they are not confined by solid walls. As discussed, a wake is formed behind a solid body which is being dragged through fluid at rest, or behind a solid body placed in a stream of fluid. The velocities in the wake are smaller than those in the main stream and the losses in the wake amount to a loss of momentum which is due to the drag on the body. The spread of the wake increases with distance from the body and the differences between the velocity in the wake and the free stream become smaller. Qualitatively such flows resemble similar flows in the laminar case; however large quantitative differences exist as discussed in Section 4.4.

At this time, we shall restrict the discussion to two-dimensional free shear plane flows for the far wake (i.e. $\ell/L \to 0$). We observe that all mean quantities are independent of time and are constant in the z-direction and $\overline{w} = 0$. Also, the fluctuating velocity field, u_i', is isotropic (u', v', and w' are all the same order of magnitude). Applying similar scaling practices used for laminar flow, we attempt to retain all the $O(1)$ terms in (4.41) assuming that Re_ℓ is sufficiently large, $u'^*/U = O(\ell/L)$, and $u'^*/\overline{u} = O(1)$ where $\overline{u} = U - \overline{u}_w$ is now the velocity defect in the wake. The cross-stream momentum equation provides

$$\frac{\partial \overline{v'v'}}{\partial y} = -\frac{1}{\rho}\frac{\partial \overline{P}}{\partial y} \tag{4.49}$$

which when integrated yields

$$\overline{P} + \rho\overline{v'v'} = P_o \tag{4.50}$$

where P_o is the pressure outside the turbulent wake and assumed to be streamwise constant (i.e. $\partial P_o/\partial x = 0$). Differentiating (4.50) we find

$$\frac{\partial \overline{v'v'}}{\partial x} = -\frac{1}{\rho}\frac{\partial \overline{P}}{\partial x} \tag{4.51}$$

needed in the next step. Invoking the outlined assumptions and substituting (4.51) for $\partial\overline{P}/\partial x$, the streamwise momentum equation reduces to

$$U\frac{\partial \overline{u}}{\partial x} = -\frac{\partial \overline{u'v'}}{\partial y} \tag{4.52}$$

while applying a more stringent condition, $1/Re_\ell = O(\ell/L)$, in order for the viscous terms to be the same order as the other neglected ones. As we have stated for $Re \gg 1$ we also expect $Re_\ell \gg 1$ which allows for $1/Re_\ell \sim \ell/L \ll 1$ as required for the validity of (4.52). In fact, $Re_\ell = u'^*\ell/v = v_e/v$ provides an estimate for the eddy viscosity as $v_e = u'^*\ell$. Essentially when Re_ℓ is very large, we imply that the Reynolds stress is much larger than the viscous one.

Schlichting (1960) outlines the classic analysis for a plane turbulent wake providing a qualitative nature of the flow while Figure 4.6 offers a diagram similar to the laminar case. In spite of the broad range of turbulent length scales, one may argue that large eddies of $O(\ell)$ contribute more to the momentum transfer and growth of the wake. Therefore, the free-shear (4.52) is permissible, where the viscous term is approximated as

$$\frac{\partial \overline{u'v'}}{\partial y} = 2\ell^2 \left|\frac{\partial \overline{u}}{\partial y}\right| \frac{\partial \overline{u}}{\partial y} \tag{4.53}$$

according to Prandtl's mixing length hypothesis of (4.45). An additional assumption is that the mixing length is proportional to the width of the turbulent wake, b_t, and thus

$$\frac{\ell}{b_t(x)} = \beta = constant \tag{4.54}$$

or the ratio of the two is constant.

Schlichting states, similar to the laminar case, the width of the wake and velocity defect are designated by

$$b_t = G(C_{dc}xD)^{1/2} \tag{4.55}$$

and

$$\overline{u} = U - \overline{u}_w = U\left(\frac{C_{dc}D}{x}\right)^{1/2} f(\eta) \tag{4.56}$$

where D is the diameter of the cylinder, C_{dc} is the coefficient of drag for the cylinder, and G is an arbitrary constant to be found from the momentum integral (in terms of drag force) and introduces the similarity variable

$$\eta = \frac{y}{b_t}. \tag{4.57}$$

In a manner comparable to the analysis of laminar wakes, we solve the free-shear equation for plane flow using the shearing stress hypothesis and the momentum integral and find that the width of the wake becomes

$$b_t = \beta(10C_{dc}xD)^{1/2} \tag{4.58}$$

while the velocity defect is

$$U - \bar{u}_w = \frac{U}{18\beta}\left(\frac{10C_{dc}D}{x}\right)^{\frac{1}{2}}\left(1 - \eta^{\frac{3}{2}}\right)^2 \qquad (4.59)$$

From experiment, Schlichting finds that the ratio $\beta = \ell/b_t = 0.18$.

One notices that similar to the laminar case the width of the turbulent wake (actually $2b_t$) increases parabolically with $x^{\frac{1}{2}}$ and the velocity defect decreases as $x^{-\frac{1}{2}}$. The preceding solution constitutes an approximation for large distances x downstream where measurements show for $x/C_{dc}D > 50$ the solution is valid. One will also notice that the shape of the velocity distribution within the wake is not Gaussian in this analysis of the turbulent case. Tennekes and Lumley (1972) present an alternative analysis arriving at a Gaussian distribution for the wake velocity. However, the Gaussian velocity profiles differ negligibly from those found here as shown by Schlichting (1960).

In addition to the problems discussed in Section 4.4, another problem arises from experimental observations. The profiles outlined here and in Tennekes and Lumley describe the flow excellently near the center of the wake. A discrepancy exists where the calculated profiles approach the free stream velocity more slowly than observed near the outer portions of the wake. Evidently, due to the assumption of a constant eddy viscosity, the eddy viscosity near the wake edges is incorrectly overestimated. Actually, the flow fluctuates between laminar and turbulent in the neighborhood of the outer boundaries of the wake. When a point is in the irrotational flow, the Reynolds stress is zero. Hence, the relative fraction of time a point remains within the turbulent region, or intermittency, forces the eddy viscosity to diminish as the edge of the wake is approached.

4.6 <u>Oscillating or Periodic Flow</u>

From Section 4.2, it is evident that there is a fundamental interaction between the body and the separated flow particularly in the region of the cylinder's near wake. The dynamics of this interaction under a steady flow is of major importance in determining the time-dependent fluid resistance, or drag, and the characteristics of the flow-induced vibrations which cause lift. Theoretically, it is not yet possible to predict the flow when separation leads to a large scale wake comprised of alternating vortices. It is particularly difficult to model the time-dependent flow about a cylinder as in the case of wave motion. In such cases, the separation points undergo large excursions and the roles played by the region in front of the cylinder and behind it are periodically interchanged. The flow in wave motion can be thought of as accelerating the cylinder in one direction, decelerating it to a stop, and then accelerating it again in the opposite direction. The possible range of Reynolds numbers could be large and thus, interesting flow patterns could arise. An outline of the linear wave theory is appropriate and provides a 1st-order small amplitude analysis applicable in the description of the infrared signature of free-surface wakes.

For an inviscid irrotational flow, the velocity field, $\bar{u}$, is expressed as the gradient of the scalar potential, Φ_o,

$$\bar{u} = \nabla \Phi_o \tag{4.60}$$

according to (4.1) through mathematical identity. Continuity requires that the velocity potential satisfies Laplace's equation

$$\nabla^2 \Phi_o = 0 \tag{4.61}$$

following substitution of (4.60) into (4.7b). Applying the appropriate boundary conditions on (4.61) we arrive at a non-linear wave problem. Performing a perturbation analysis and collecting the lowest order terms allows for a linearized set of equations, resulting in the velocity potential

$$\Phi_o = \frac{a_o g}{\omega_o} \frac{\cosh\left[k_o(d-z)\right]}{\cosh\left(k_o d\right)} \sin\left(k_o x - \omega_o t\right) \qquad (4.62)$$

and a surface elevation of

$$\eta_o = a_o \cos\left(k_o x - \omega_o t\right) \qquad (4.63)$$

forming the basis of Airy wave theory. The variable $a_o = H_o/2$ is the wave amplitude with wave height H_o, $\omega_o = 2\pi/T_o$ is the wave frequency with wave period T_o, while $k_o = 2\pi/L_o$ is the wavenumber where L_o is the wavelength. In solving the linear wave problem, we define the dispersion relation

$$\omega_o^2 = \left(g k_o + \frac{\sigma}{\rho_w} k_o^3 \right) \tanh\left(k_o d\right) \qquad (4.64)$$

describing the phenomenon that waves of different frequencies, or wavelengths, travel at different speeds. According to (4.63), an observer moving with and retaining the same relative position to the crest of a wave travels at the phase speed

$$C_p = \frac{\omega_o}{k_o} \qquad (4.65)$$

specific to that wave for a given frequency and wavenumber.

The remainder of our theory assumes "deep" water waves where

$$\left.\begin{array}{l} \sinh\left(k_o d\right) \approx \cosh\left(k_o d\right) \approx \frac{1}{2} e^{k_o d} \\[2mm] \tanh\left(k_o d\right) \approx 1 \end{array}\right\} \quad for \ k_o d \gg 1. \qquad (4.66)$$

Accordingly, the dispersion relation now becomes

$$\omega_o^2 = \left(gk_o + \frac{\sigma}{\rho_w} k_o^3 \right)$$ (4.67)

which satisfies the requirement that $\partial^2 \omega_o / \partial k_o^2 \neq 0$ for a dispersive wave system, while the phase speed now converts to

$$C_p = \frac{\omega_o}{k_o} = \sqrt{\frac{g}{k_o} + \frac{\sigma}{\rho_w} k_o} \ .$$ (4.68)

Equal contributions from the gravity and surface tension restoring forces to the phase speed occur when $L_o = 1.73$ cm. For the gravity wave regime

$$C_p = \frac{\omega_o}{k_o} = \sqrt{\frac{g}{k_o}} \qquad \text{for } L_o \gg 1.73 \text{ cm}$$ (4.69)

and longer waves propagate faster than shorter ones. However, in the capillary wave regime

$$C_p = \frac{\omega_o}{k_o} = \sqrt{\frac{\sigma}{\rho_w} k_o} \qquad \text{for } L_o \ll 1.73 \text{ cm}$$ (4.70)

and the shorter waves lead the longer ones. Clearly from the direct relationship between phase speed and (4.67), components with different wavenumbers separate out in space as they propagate for dispersive wave systems.

While surface waves propagate with a phase speed, C_p, the particles affected by these waves travel in an orbital trajectory with instantaneous horizontal and vertical velocities designated by

$$u_o = \frac{\partial \Phi_o}{\partial x} = a_o \omega_o e^{-k_o z} \cos(k_o x - \omega_o t)$$ (4.71)

and

$$w_o = \frac{\partial \Phi_o}{\partial z} = -a_o \omega_o e^{-k_o z} \sin(k_o x - \omega_o t)$$ (4.72)

and accelerations of

$$\frac{\partial u_o}{\partial t} = a_o \omega_o^2 e^{-k_o z} \sin(k_o x - \omega_o t) \tag{4.73}$$

and

$$\frac{\partial w_o}{\partial t} = a_o \omega_o^2 e^{-k_o z} \cos(k_o x - \omega_o t). \tag{4.74}$$

True ocean waves exhibit an important non-linear characteristic due to the non-circular orbital motions of the fluid particles. Stokes provided a second-order correction to the paths of fluid particles portrayed according to linear wave theory (Lighthill, 1978). Stokes showed that the time-averaged Lagrangian velocity of a fluid particle is non-zero through the term

$$\overline{u}_\ell = a_o^2 \omega_o k_o e^{-2k_o z} \tag{4.75}$$

referred to as the Stokes' drift, which represents the mean horizontal particle velocity over one wave period.

Consider a structure that is small with respect to the wavelength of the wave. For example, in the case of a cylindrical cable "small" refers to the diameter-wavelength ratio. The cable causes little interference or change in the wave kinematics. As such, diffraction effects are negligible and the drag and inertial components of the wave forces become important. In the analysis we arrive at the Morison equation,

$$F_T = F_D + F_I = C_{dc} \rho D \left(\frac{|u_o| u_o}{2} \right) + C_m \rho \left(\frac{\pi D^2}{4} \right) \frac{\partial u_o}{\partial t} \tag{4.76}$$

where F_T is the total force, F_D is the drag force, F_I is the inertial force, u_o is the horizontal instantaneous local velocity of the wave, $\partial u_o / \partial t$ is the horizontal instantaneous local acceleration of the wave, C_{dc} and C_m are the drag and inertial coefficients, and D is the diameter of the cylinder (Sarpkaya and Isaacson, 1981). From Airy theory we know that u_o and

$\partial u_o / \partial t$ vary in magnitude and direction throughout the wave period. The horizontal velocity is maximum positive at the crest, maximum negative at the trough, and zero at the points halfway between the two. The horizontal acceleration is maximum positive at the still water level on the front of the wave, maximum negative at the rear of the wave at the still water level, and zero at the crest and the trough. Another factor to consider is that in deep water, the velocities and accelerations essentially vanish with depth. Therefore, the velocity profile near the surface is not uniform with depth and adds to the already complicated situation.

Now let us review the discussion of a steady flow wake behind a cylinder. At $1 < Re < 50$, attached vortices within the eddies in the near wake form and the flow remains laminar. In the range of 50 - 200, the flow remains laminar but the near wake begins to oscillate and vortex shedding occurs. Up to $Re < 2 - 3 \times 10^5$, the vortices shed are turbulent at birth and the far wake becomes increasingly irregular. The transitional period has begun and at $Re \approx 5 \times 10^5$ the flow undergoes first a laminar separation just before the top of the cylinder, followed by a reattachment to the cylinder, and then a turbulent separation to form a narrow wake. The net result is that the area of the large separation region has decreased and the pressure has almost come back to the free-stream value. Accordingly, the drag depicted in Figure 4.7 dramatically decreases, as well as the lift force. For periodic flow around a cylinder (i.e. wave motion), this drag and lift decrease may occur at smaller Reynolds numbers. Finally, the drag coefficient continues to show an increase up to $Re \approx 10^7$. The boundary layer itself is turbulent and attached on the front half of the cylinder, while separation occurs slightly earlier than before and results in the moderate drag increase.

The Strouhal number designates a relationship between the vortex shedding frequency, F_o, the cylinder diameter, D, and the free stream velocity, U, as detailed in (4.3). A full description of the range of Strouhal numbers corresponding to the range of Reynolds numbers discussed above is tabulated in Table 4.1 and illustrated in Figure 4.8. The net result of the alternate vortex shedding is an oscillating side thrust, upon a cylinder in
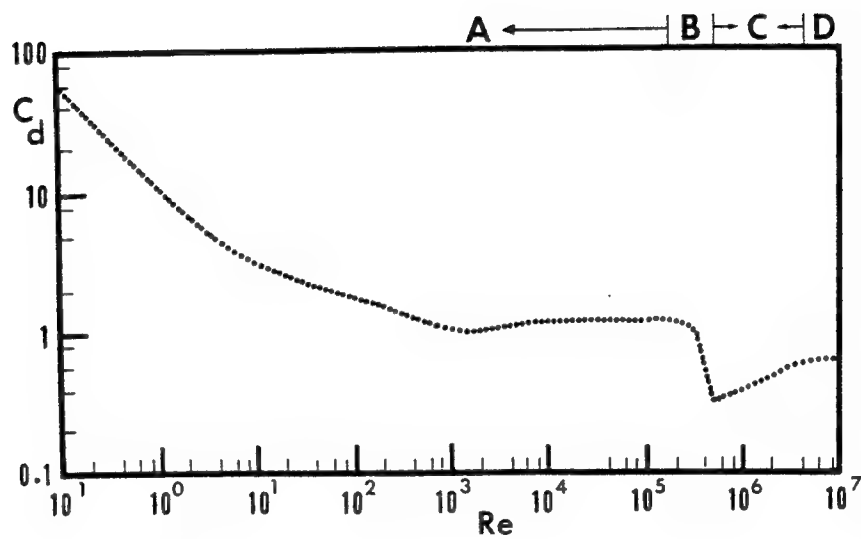
Figure 4.7   Drag coefficient, $C_d = C_{dc}$, for circular cylinders as a function of Reynolds number (from Sarpkaya and Isaacson, 1981).

Table 4.1   Incompressible flow regimes and their consequences (from Sarpkaya and Isaacson, 1981).

	A Subcritical	B Critical	C Supercritical	D Post-supercritical
Boundary layer	laminar	transition	turbulent	turbulent
Separation	about 82 deg.	transition	120 - 130 deg.	about 120 deg.
Shear layer near separation	laminar		laminar separation, bubble turbulent reattachment	turbulent
Strouhal number	$S = 0.212 - \frac{2.7}{Re}$	transition	0.35 - 0.45	about 0.29
Wake	Re<60 laminar; 60<Re<5000 vortex street Re > 5000 turbulent	not periodic		
Approximate Re range	$< 2 \times 10^5$	2×10^5 to 5×10^5	$5 \times 10^5 - 3 \times 10^6$	$> 3 \times 10^6$
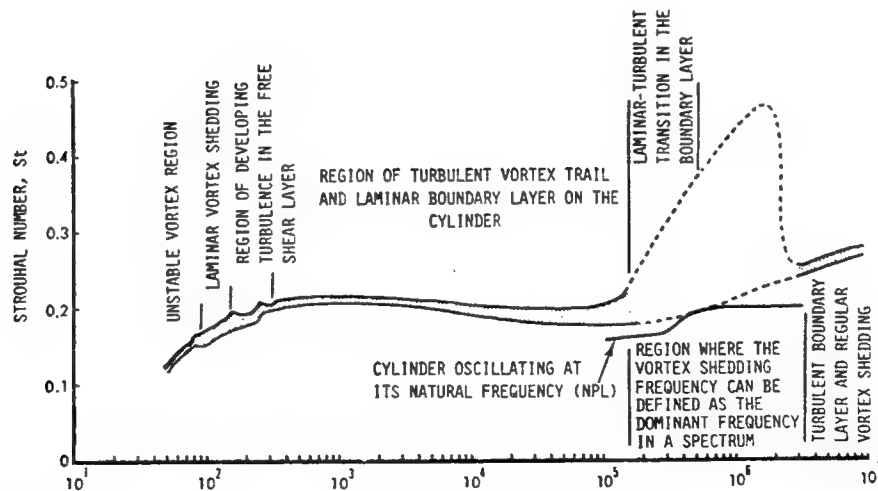
Figure 4.8   The Strouhal-Reynolds number relationship for circular cylinders (from Sarpkaya and Isaacson, 1981).

the direction opposite the last detached vortex. A visual time history of the side thrust, or lift force, which exists at practically all Reynolds numbers is offered in Figure 4.4. The alternate shedding vortices give rise to a transverse pressure gradient. Unsteady hydrodynamic forces arising from this pressure gradient can excite dynamic response. Resonance can occur when the natural body frequency is near the exciting frequency.

Two scenarios have been proposed and could possibly exist. The instantaneous in-line force follows from Morison's equation while the transverse force due to the vortex shedding described above results from an appropriate lift coefficient. The exciting forces are particularly important for bodies which may undergo in-line and/or transverse oscillations of the cylinder since the vortex shedding frequency locks onto the frequency of the transverse oscillations of the cylinder when the vortex shedding frequency is in the neighborhood of the natural frequency of the cylinder. Even the smallest transverse oscillations of a cylinder (e.g., amplitude of oscillation/diameter = 0.05) distinctly regularize the vortex shedding. The shedding of vortices also gives rise to oscillations in the drag force at a frequency twice the vortex-shedding frequency. The magnitudes of these oscillations are relatively small. However, violent in-line oscillations at a frequency twice that of vortex shedding may develop and even alter the character of the vortex formation in the near wake. All or some of these effects may occur in the present situation of the thermal infrared wire wakes.

4.7 Recent Literature

The problem of the wake formation behind bluff bodies has received a great deal of attention. Since Roshko (1954) made extensive measurements of vortex shedding frequencies, copious articles have addressed the issue of vortical wakes behind cylinders. Berger and Wille (1972) supply an excellent history of periodic flow phenomenon. Many of the articles have spoken of the low Reynolds number flows in which both oblique and parallel modes of shedding occur. Another feature of laminar vortex shedding is

the discontinuous nature of the Strouhal-Reynolds number curve. Slaouti and Gerrard (1981) outline the end effects on the wake of a vertically-oriented circular cylinder towed horizontally. For a clean surface as in Figure 4.9, the vortices shed spanwise from the cylinder align perpendicularly at the free surface while the end effects inclinate the vortices and eventually disrupt the formations downstream near the bottom. Recently, Williamson (1989) scrutinized these observations showing that oblique shedding and the Strouhal discontinuity are directly related. Regardless of free-stream turbulence, non-uniformities or cylinder vibrations, the discontinuity exists due to the end effects of the cylinder set-up. Other authors such as Roshko (1961) have studied flows with Reynolds numbers over 10000 and found that the flow can be separated into four regimes: subcritical, critical, supercritical, and transcritical/post-supercritical as shown in Table 4.1. Bearman (1969) supplies information about the critical to supercritical regime and noticed a marked increase in the Strouhal number from roughly 0.2 to 0.35 - 0.45 occurs. I must emphasize that only an average Strouhal number for Reynolds numbers exceeding 2×10^5 can be attained. Sarpkaya and Isaacson (1981) along with Bearman (1984) provide an excellent synopsis of the mechanics of vortex shedding including a complete discussion of the frequency dynamics involved. Regardless of the countless articles written on the subject of wakes and vortex shedding, continued interest has addressed the difficult problems at the free-surface.

Traditionally, the air-water interface has been considered a "free-surface" assuming the stress tensor vanishes everywhere in the air domain with only a constant ambient gas pressure. Notwithstanding, Yeh (1991) presents a flow circulation approach regarding the creation of vorticity within a fluid domain by only two mechanisms. The first, baroclinic torque, represents the interaction between the density and pressure gradients while the second, a "viscous-shear torque", portrays an interaction of the density gradient and viscous shear forces. Extending the argument to the air-water interface, Yeh (1992) approaches the problem as a fluid-fluid interface rather than a boundary surface on which the stresses
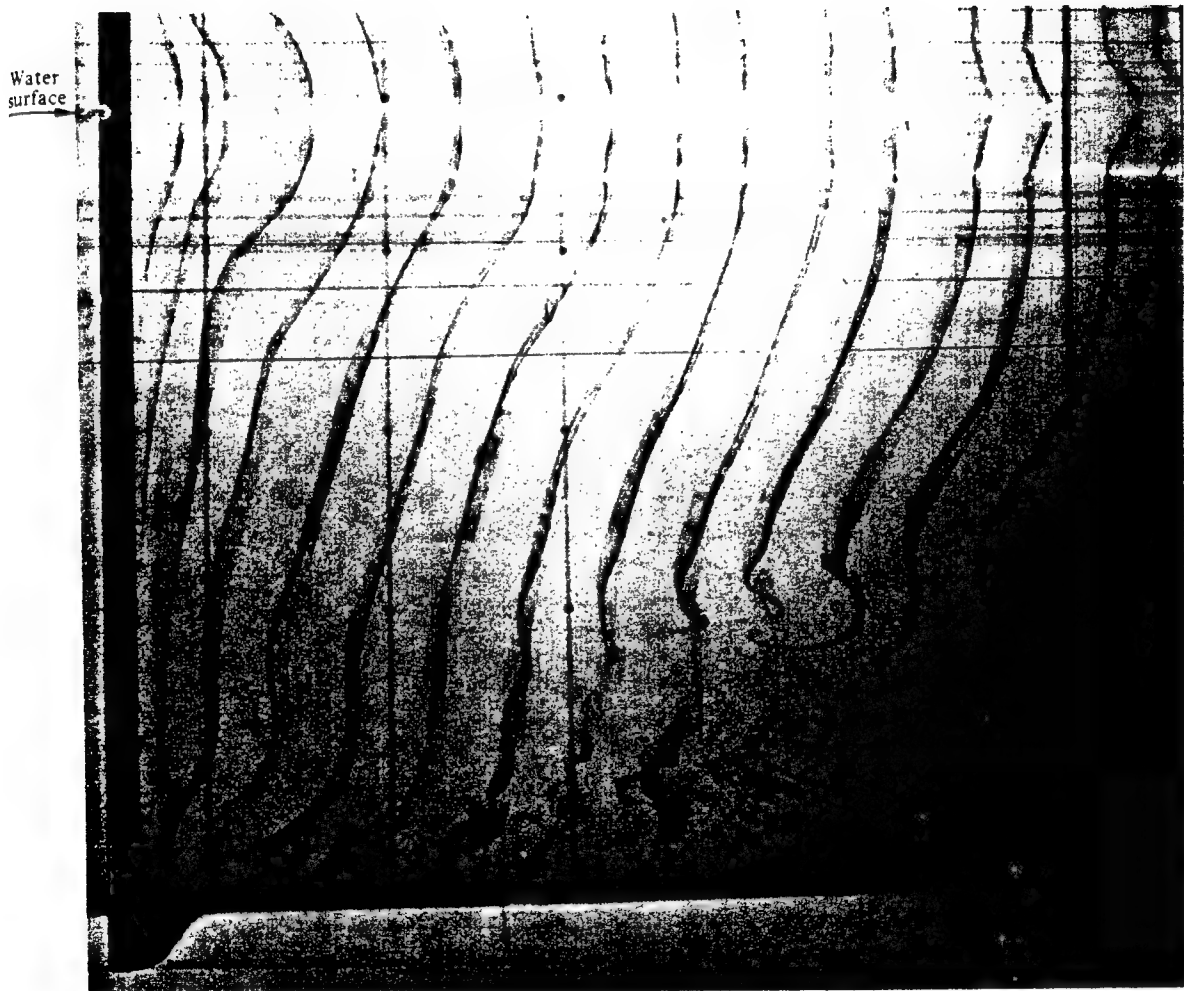
Figure 4.9   Effect of a clean water surface on the flow configuration in the
            wake of a circular cylinder towed from right to left at a $Re = 127$
            (from Slaouti and Gerrard, 1981).

vanish and finds the production of vorticity by the same mechanisms. According to Yeh (1991) in fact, the small magnitude of the stress tensor in air does not necessarily mean a small magnitude of acceleration caused by the net viscous force acting upon a fluid particle due to the fact that the air density is also small. He suggests, in essence, that small changes in vorticity in the air cause substantial changes in water vorticity. The application of the "free-surface" condition for an air-water interface appears unjustified when considering vorticity, and it should be regarded as a fluid-fluid interface.

Observations by many investigators support this proposal. Bernal and Kwon (1989) found that vortex rings formed under and initially parallel to the air-water interface appear to break up and connect to the surface. Hence, according to Helmholtz's theorem the vortex tubes extend into the air domain. Song *et al.* (1990) also demonstrated that for a vortex ring approaching the air-water interface at an angle (20°) vortices normal to the surface appear and persist. Weigand and Gharib (1994) report similar bifurcation and even trifurcation re-connection patterns of vortex ring interaction with the air-water interface. Further, they suggest that these strong vortices aligned normal to the surface persist and engulf the smaller mutually-interacting structures, thus reconcentrating the vorticity. However, when a vortex ring or pair interact with a surface contaminated with surfactant, the vortex rebounds following the production of secondary vorticity (Bernal *et al.*, 1989; Hirsa *et al.*, 1990; Willert and Gharib, 1994).

Returning to the case of wakes, Hirsa and Logory (1994) align a surface-piercing flat plate with a uniform flow and observe the widening of the wake as one approaches the air-water interface from below. The peak in the surface-normal vorticity, ζ, shows a slight decrease at the surface as opposed to the deeper wake. Also within the surface layer (~ 3 - 9 mm), measurements indicate the presence of surface-parallel structures of transverse vorticity, ξ, on both sides of the wake which align at small angles to the streamwise direction. They propose that these quasi-streamwise structures induce a velocity outward, thus accounting for the

observed doubling of the wake width. Sarpkaya (1994) provides a more extensive treatment summarizing the observations at an air-water interface. As one approaches the surface from below, amplification of the streamwise and transverse turbulent velocities occurs, coupled with the sharp reduction in the vertical turbulent velocity. Thus, the turbulent kinetic energy, or the mean squared fluctuations, in the vertical component is only a small fraction of the total turbulent kinetic energy. Specifically, attenuation of low frequency (large scale) vertical fluctuations results in a net energy gain at the same scales for streamwise and spanwise turbulence. Lin and Pao (1979) previously have suggested that stratification inhibits the vertical motion due to the fact that vertical turbulence decays faster than the horizontal fluctuations. Thus, the air-water interface behaves as a highly stratified fluid layer which actually redistributes the normal component of turbulent kinetic energy into streamwise and transverse components at large eddy scales rendering the near-surface turbulence anisotropic. The predominant coherent structures associated with these observations involve circulating surface depressions whose merging characteristics lead to a reverse energy cascade and eddy longevity along with large flattened eddies. With the onslaught of two-dimensional turbulence, vortices coalesce giving rise to larger vortical structures.

Much of the current interest in "free-surface" turbulence stems from the application to deciphering remotely sensed ship wakes on the open ocean. There is a growing effort to understand the synthetic aperture radar (SAR) signature of ship wakes depicted in Figure 4.10. Milgram *et al.* (1993a and b) discuss the suppression of short sea waves in the wakes of ships and the synthetic aperture radar (SAR) images they produce. Using the techniques proposed by Peltzer *et al.* (1991) and Peltzer *et al.* (1992), surface tension measurements along with wave energy distributions across the wake exhibit a strong correlation. Milgram *et al.* (1993a and b) suggest that turbulence and concentration of surfactants along the outskirts of the wake caused by the passage of a ship attenuate the short waves. The same turbulence which attenuates these short waves could also cause the destruction of the cool skin layer.
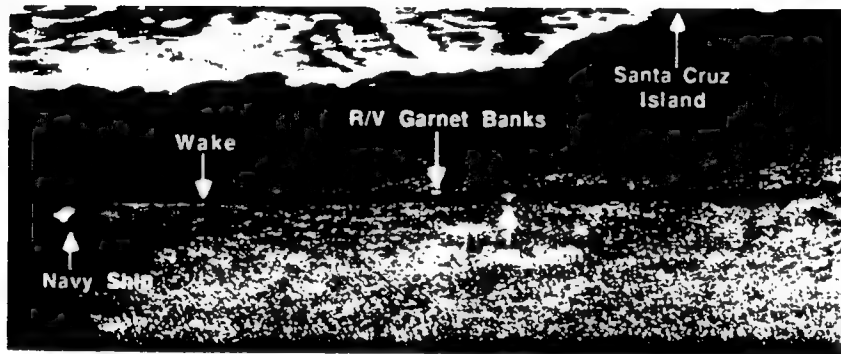
Figure 4.10 L-band SAR image of a wake produced by a Navy ship
travelling at 25 knots (12.9 m/s) with a 5 knot (2.6 m/s) tailwind
from the port-stern quarter on January 28, 1989. R/V Garnet
Banks made surface tension measurements at the time. The
length of the wake shown in the image is 6.9 km (from Peltzer
et al., 1991).

Notwithstanding, thermal wake detection has had only a sprinkle of interest in the published literature. Garber *et al.* (1945) initially used bathythermograph soundings coupled with thermopiles at different depths in an attempt to track ships. More recently, Peltzer *et al.* (1987) made cursory measurements of the infrared and microwave signatures of ship wakes. Figures 4.11a and b show that the cool daytime wakes treated with an organic surfactant, oleyl alcohol, were more intense and persistent than the untreated wakes. They attribute the lack of re-entry of warmer surface water into the cool turbulent wake to the inhibition of surface dispersive processes by the organic film. Schwartz and Priest (1988) have studied the effect of sky reflection and found that an infrared thermal ship wake can appear even in the absence of an actual temperature difference. Cervenka (1989) used a computer model to predict the thermal macrowake and to compare with the infrared image. He reports an excellent simulation which fit the measurements. Indeed, Peltzer *et al.* (1987), Schwartz and Priest (1988), and Cervenka (1989) all have studied infrared ship wakes, but more probing research into the effective factors and dynamical characteristics of wakes at the air-sea interface is needed in addition to an understanding of the free-surface flow structure. Moreover, most of the work with infrared ship wakes has been performed during the day when the skin layer is warm as opposed to the cool skin layer at night. One might expect then at night to detect warm wakes.
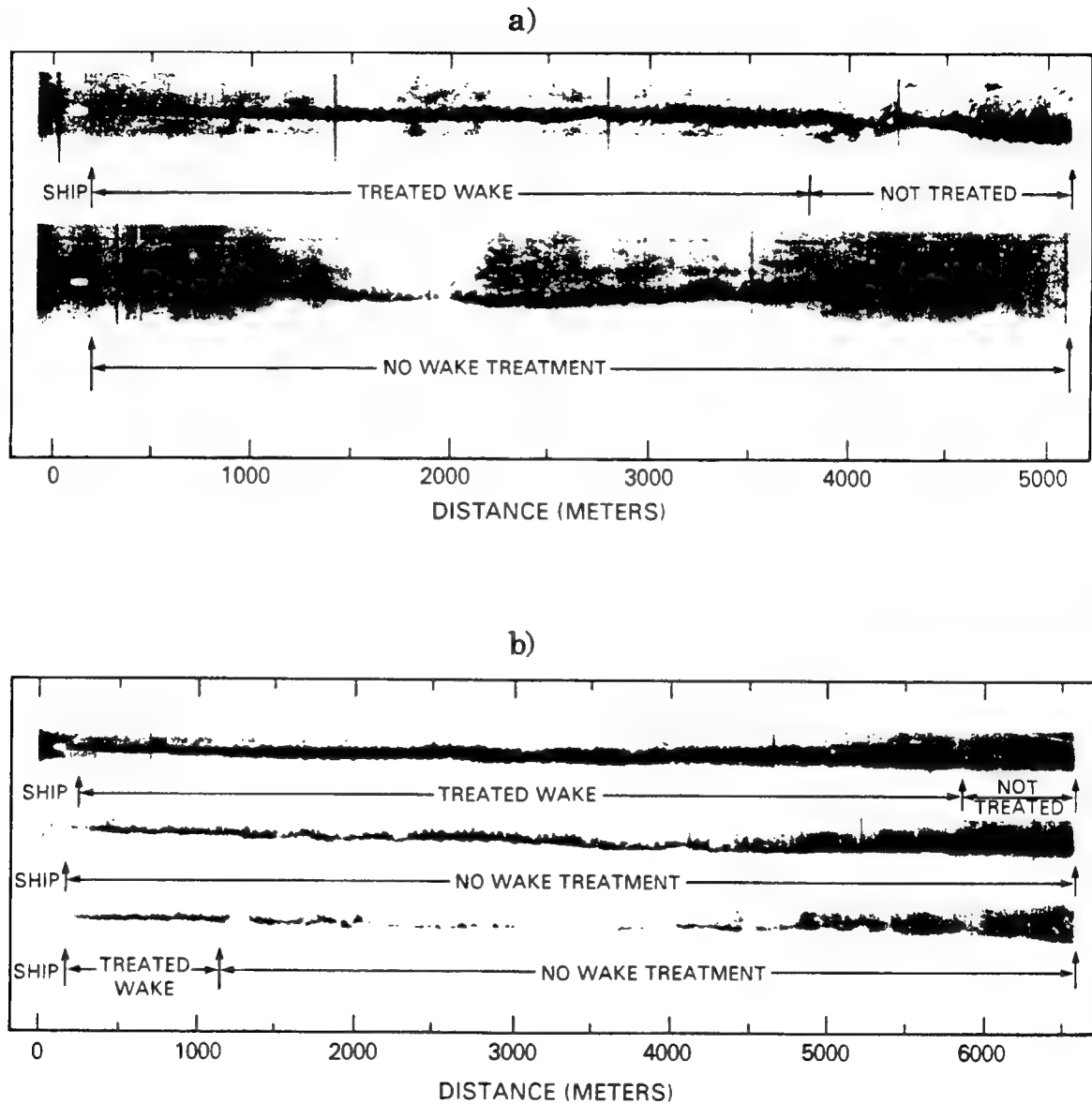
Figure 4.11   Thermal infrared wake signatures of the USNS Hayes
traveling from right to left in the image. a) On July 13, 1982,
the images were taken from a flight altitude of 457 m with the
wake segments 4960 m long. b) On July 14, 1982, the images
were taken from a flight altitude of 305 m with the wake
segments 6380 m long (from Peltzer *et al.*, 1987)

CHAPTER 5

Experimental Results and Discussion

5.1 Introduction

In January 1992, the Applied Physics Laboratory (APL) in Seattle collected an extensive data set 400 nautical miles off the coast of San Diego aboard the Floating Instrument Platform (FLIP). The impetus arose from the necessity to improve our understanding of both the atmospheric and oceanic factors influencing infrared remote sensing of the sea surface. In the process, we discovered numerous features illustrating the spatial and temporal variability of infrared sea surface temperature (IR SST). Furthermore, we repeatedly observed a distinct infrared signature of surface wakes generated by two instrument cables hanging from FLIP's port boom. Prior to an analysis of these features, it is essential to outline the instrumentation and data collection procedure.

5.2 Instrumentation

In the past, oceanographers primarily used narrow beam radiometers for a point measurement of the sea-surface temperature. APL employed three radiometers, two Heimann model KT-19 instruments and one Barnes model PRT-5. All three possess approximately a 2° field-of-view in the spectral range from 8 to 14 μm with a manufacturer's specified absolute accuracy of ± 0.5 °C. From calibrations performed in the field and discussed in Section 5.5, the absolute accuracy reached ± 0.1 °C. Mounted on FLIP's instrument boom at a height of 10 m, the narrow beam radiometers measured the average IR SST from a spot size of 0.4 m in diameter. The PRT-5 specifications stipulate a sensitivity of better than 0.1 °C at a response time of 50 milliseconds for all ranges of target temperatures, while the KT-19 quotes the same sensitivity at a response time of 0.3 seconds looking at a 20 °C target. The fact that the sensitivity of the KT-19 varies with target temperature and response time does not affect our range of temperature measurements from 12 to 17 °C. However, we

found that the Heimann model KT-19 drifted during the day when diurnal solar heating directly affects the instrument. The top of Figure 5.1 highlights the comparison of the uncalibrated measurements made by the KT-19 and PRT-5. During the night and early morning, both measured the identical changes in IR SST, though without calibrated absolute accuracy. In contrast, during the day the unprotected instruments appeared to drift relative to each other. Because the instruments were not shielded from direct solar radiation, the KT-19 heated up significantly as evidenced by the measured internal temperature shown at the bottom of Figure 5.1. The KT-19 measures the temperature of an internal blackbody and performs a one-point calibration. Drastic temperature changes corrupt the internal calibration of the KT-19. From laboratory experiments, we observed that the KT-19, while measuring a constant temperature target of 24 °C, does in fact drift nearly 0.3 °C during a 10 °C increase in internal temperature as shown in Figure 5.2. The PRT-5 sets an internal reference blackbody at 40 °C and is thus unaffected by solar heating. We believe that the relative drift exhibited in the field was solely due to the Heimann model KT-19 based upon our laboratory verification and knowledge of how the PRT-5 and KT-19 work. Hence, all of the following IR SST measurements will refer to the Barnes model PRT-5.

In conjunction with the narrow beam radiometers, APL utilized an infrared imager made by Agema. The Thermovision 880 model longwave infrared scanner provided a 40° field-of-view in the spectral range of 8 to 12 μm with a manufacturer's stated absolute accuracy of ± 2.0 °C. The noise equivalent temperature (NET) of 0.05 °C allows for the detection of minute variations in temperature for use as a flow visualization tool. Agema provided a PC-based system complete with the CATSE software package allowing for display and manipulation of the scanner images. The scanner outputs 4 fields of data per frame at a field rate of 25 Hz or frame rate of 6.25 Hz. However, the CATSE system is only able to digitize 2 of the 4 fields per frame resulting in an image size of 140 x 140 pixels. As with any optical instrument with a large field-of-view, the scanner significantly distorts the image spatially as seen in Figure 5.3. The figure displays the heat
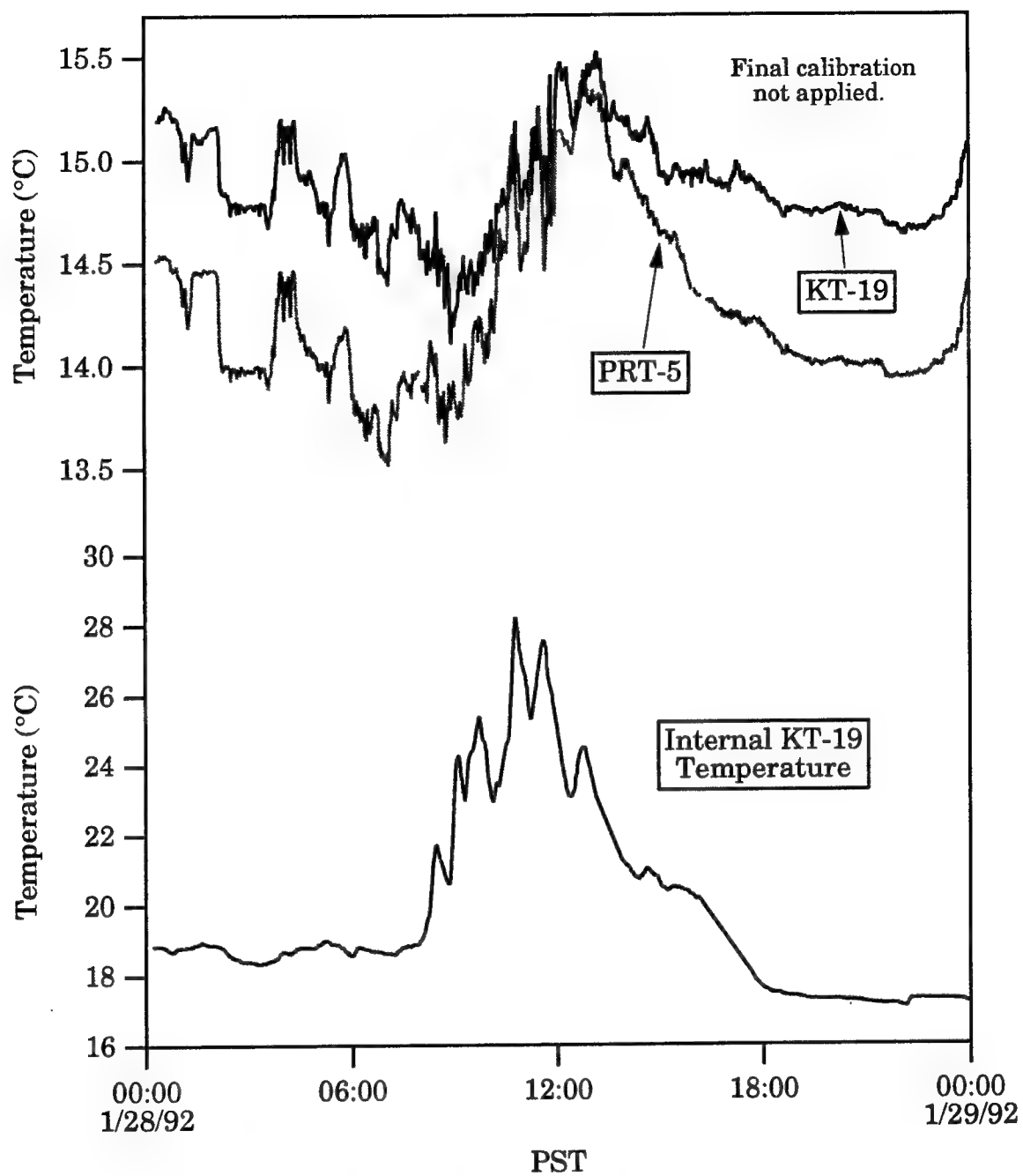
Figure 5.1   Comparison of KT-19 and PRT-5 measurements of IR SST and the effect of internal instrument heating.
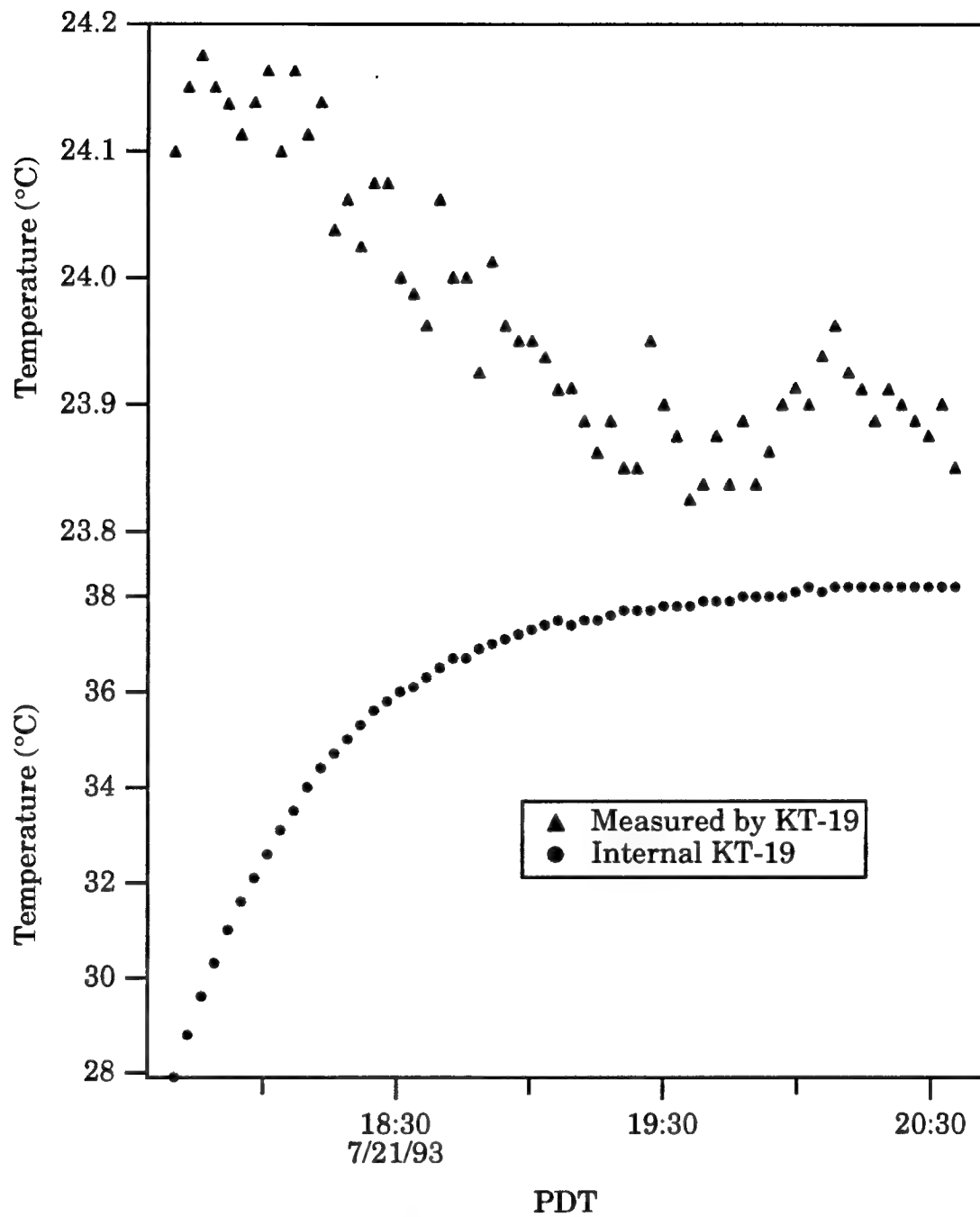
Figure 5.2   Typical result of laboratory tests conducted on the effect of intense heating on the KT-19. The KT-19 measurement of a constant temperature target at 24 °C drifts nearly 0.3 °C during a 10 °C increase in internal instrument temperature.
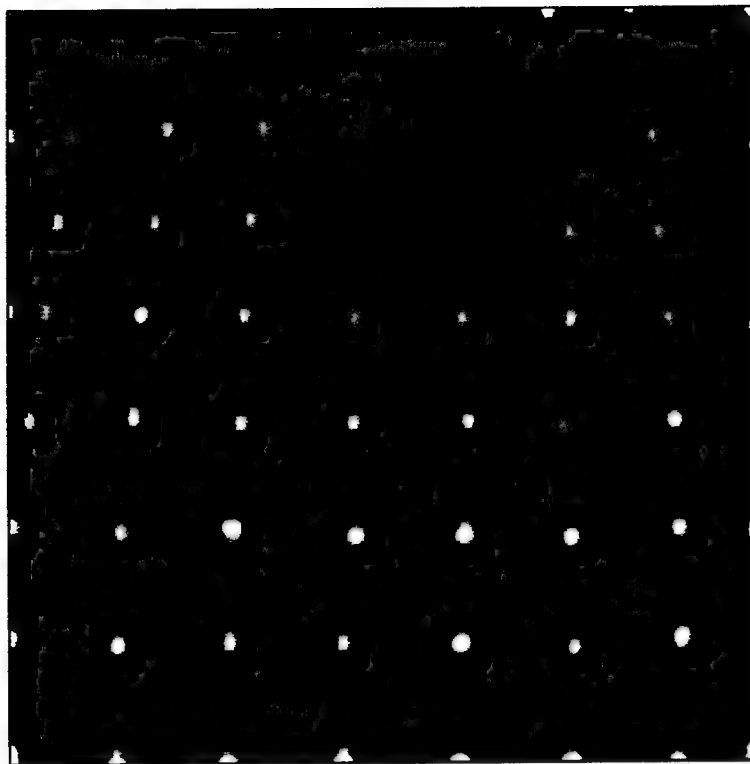
Figure 5.3   Infrared image showing the spatial distortion. Candles
spaced evenly (roughly 12 cm apart) provide the heat detected
by the scanner.

generated by candles equidistant from each other (roughly 12 cm apart) with a few placed on the left and right-hand sides to frame the image. At a distance 1 meter above the viewing plane and an incidence angle of 20°, the scanner foreshortened in the vertical and converged in the horizontal approaching the top of the image. In order to correct for distortion, we developed a scheme which calculated spatial positions according to pixel values from the image to produce the result in Figure 5.4. The result corroborated the calculations from geometric considerations alone. Therefore, 10 meters above the ocean surface at an incidence angle of 20° the scale of a scanner image was roughly 7.7 m wide at the base, 10.0 m wide at the top, and 9.3 m tall. Unless otherwise noted, the scanner was usually oriented parallel to the port boom such that it viewed the surface directly under the boom.

A wave-following thermistor chain using Sea-Bird model SBE-3 oceanographic thermometers provided the vertical profile of temperature below the ocean surface at depths of 0.1, 0.5, 1.0, 2.0, and 5.0 meters. Propeller and vane anemometers at 10 m and 25 m monitored the wind speed and direction. The R. M. Young Wind Monitor-RE model 05701 mounted on the 10 m port boom has a manufacturer's stated speed threshold sensitivity of 0.2 m/s with a direction sensitivity of 0.4 m/s at 10° displacement (0.6 m/s at 5° displacement). Likewise, an R. M. Young Wind Monitor-AQ model 05305 mounted on the mast at a height of 25 m has a manufacturer's stated speed threshold sensitivity of 0.4 m/s along with a direction sensitivity of 0.5 m/s at 10° displacement (0.7 m/s at 5° displacement). Concurrently, an R. M. Young aspirated slow-response thermistor measured the air temperature, and a shielded Rotronics probe model 41367 monitored the relative humidity. An Eppley model PSP upward-looking hemispheric pyranometer measured the solar irradiance. In addition, an Eppley model PIR upward-looking hemispheric pyrgeometer measured the irradiant longwave radiation from the sky. Finally, a commercially available Delavan model C/420-0 liquid level meter and a scatterometer nadir to the surface used as an altimeter provided complementary measurements of surface displacements. The K_u-Band
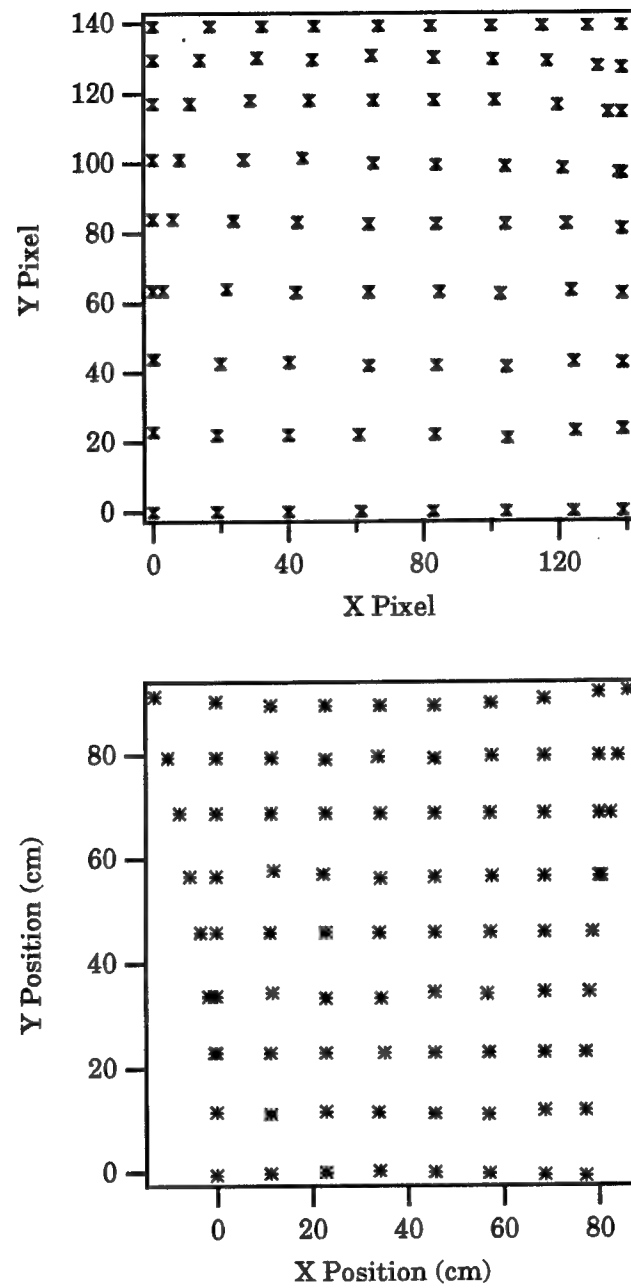
Figure 5.4   Top plot is the location of the candles in pixel space. Bottom
plot is the location of the candles in actual space.

continuous wave scatterometer used aboard FLIP returned a signal from the illuminated area of a 1.5 m spot and was similar in design to the one described by Keller and Plant (1990). Figure 5.5a shows FLIP prepared to make measurements with the thermistor chain hanging from the boom before deployment. Figure 5.5b shows some of the instrumentation mounted on and deployed from the port boom.

The wire wave gauge malfunctioned at times because of an intermittent grounding problem. Moreover, the wire wave gauge's continually noisy signal questioned the very nature of the gauge's ability to make correct measurements and suggested it might actually underestimate the wave height. Due to these difficulties, our confidence lay with the altimeter as it was more reliable and precise than the wire wave gauge. Figure 5.6 shows a comparison between the altimeter and the wire wave gauge. The method for determining the period of individual waves is to measure the timespan between zero crossings on the up-slope of the surface displacement time series. The wave height is defined as the difference between the maximum and minimum surface displacement within that period. From Figure 5.6, we observe that the wire wave gauge actually underestimates the wave heights by nearly 20 % for larger waves and 25 to 30 % for smaller waves. Though more desirable, the altimeter was used intermittently during the measurement period considered here. As the wire wave gauge provided more continuous data, it was utilized unless otherwise noted that the radar was turned on simultaneously.

During the initial mounting of the instruments, the reflection of the boom into the field-of-view of the infrared sensors was observed. Figure 5.7a displays the visual reflection of the port instrument boom on the water surface under calm conditions. As mentioned previously, Simpson and Paulson (1980) made similar measurements aboard FLIP mounting a PRT-5 at nadir incidence from the boom. They argued in their appendix that the effect of reflected radiation from the boom was negligible. However, Figure 5.7b shows the apparent change in the temperature of the sea surface due to its deviation from unity in emissivity. The visual reflection of the
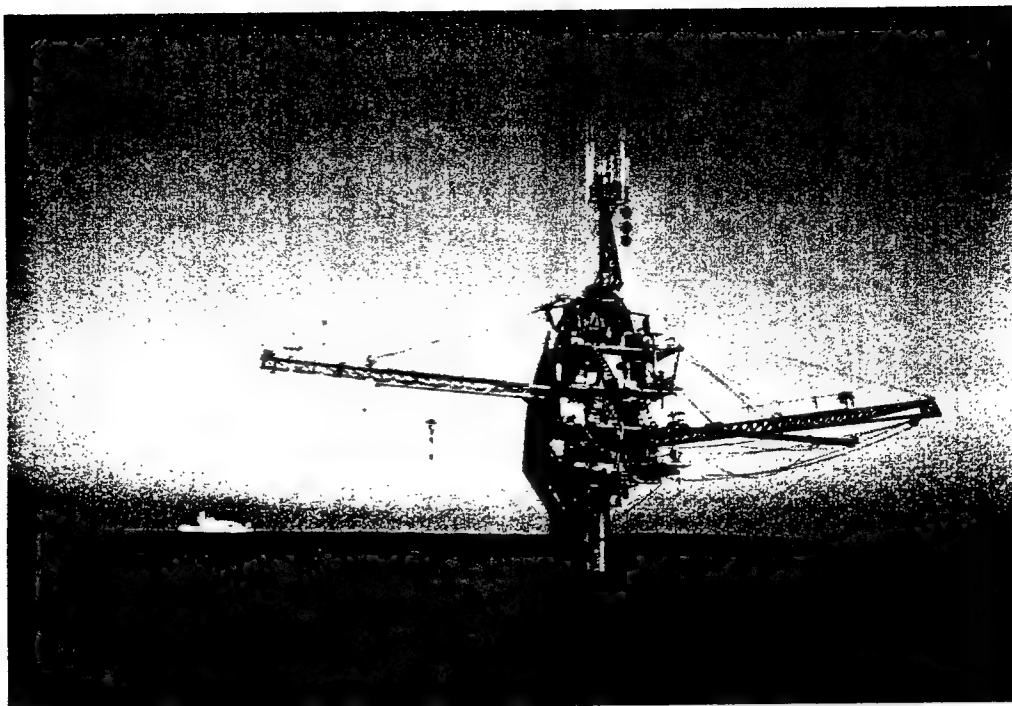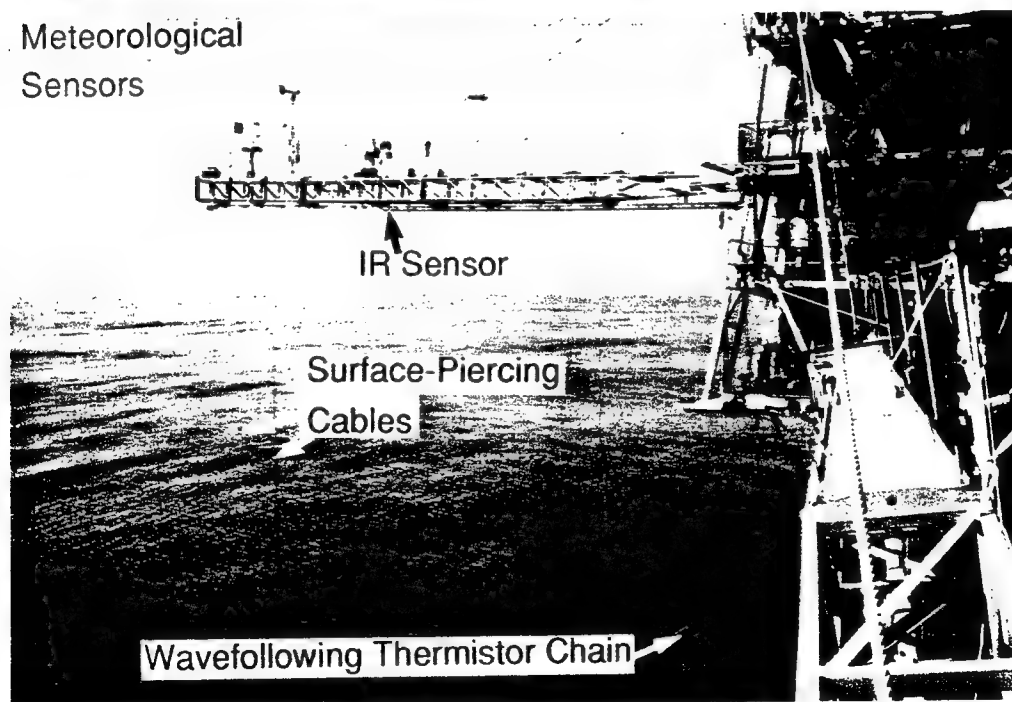
Figure 5.5a-b   Photographs showing instrument deployment aboard FLIP. In the bottom photograph (b), note the surface-piercing cables at the end of the boom and the thermistor chain buoy in the lower right corner.
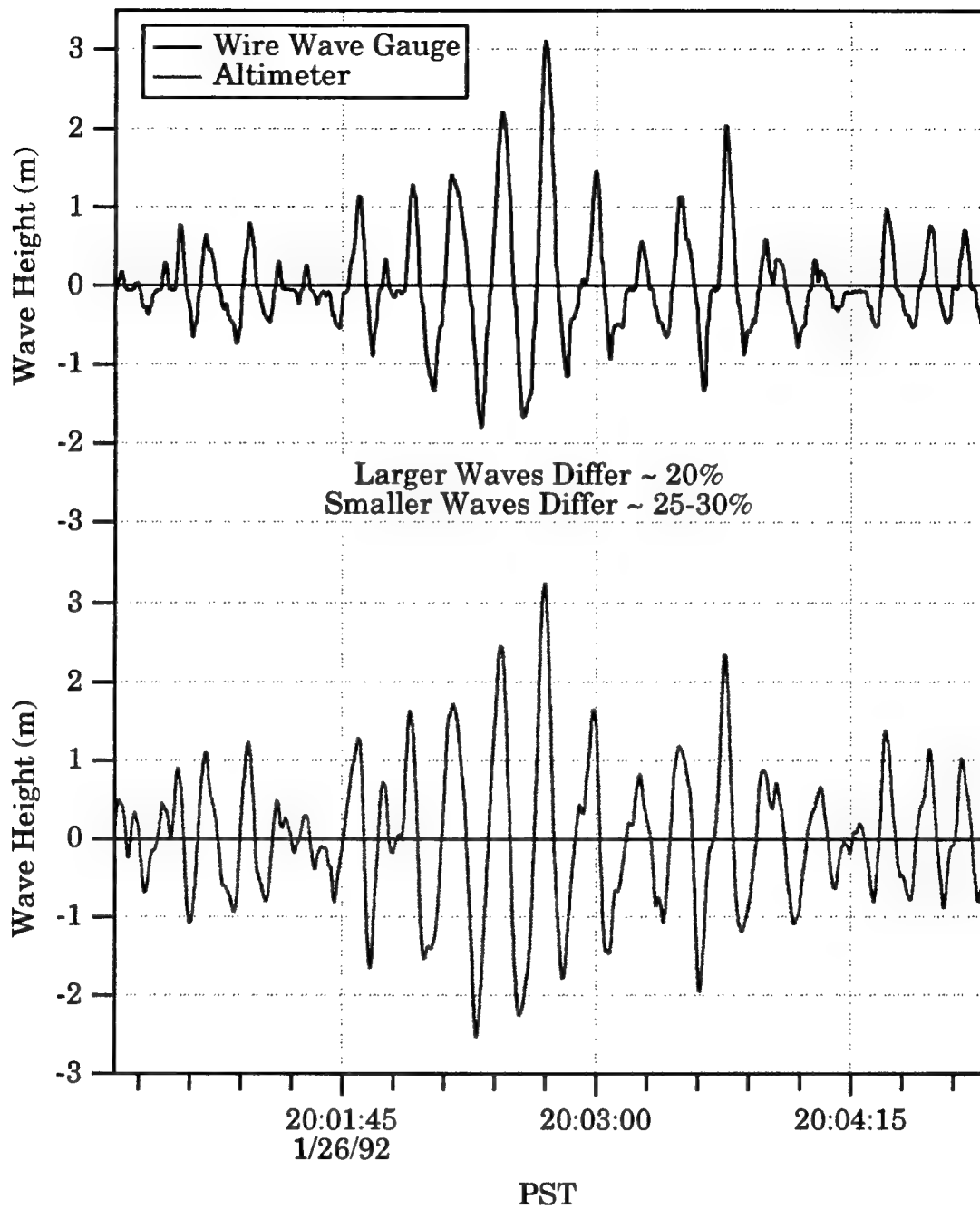
Figure 5.6   Comparison of the wire wave gauge and the altimeter. The wire wave gauge underestimates the heights of the larger waves by 20% and the smaller ones by 25 - 30%. The wave periods agree satisfactorily.
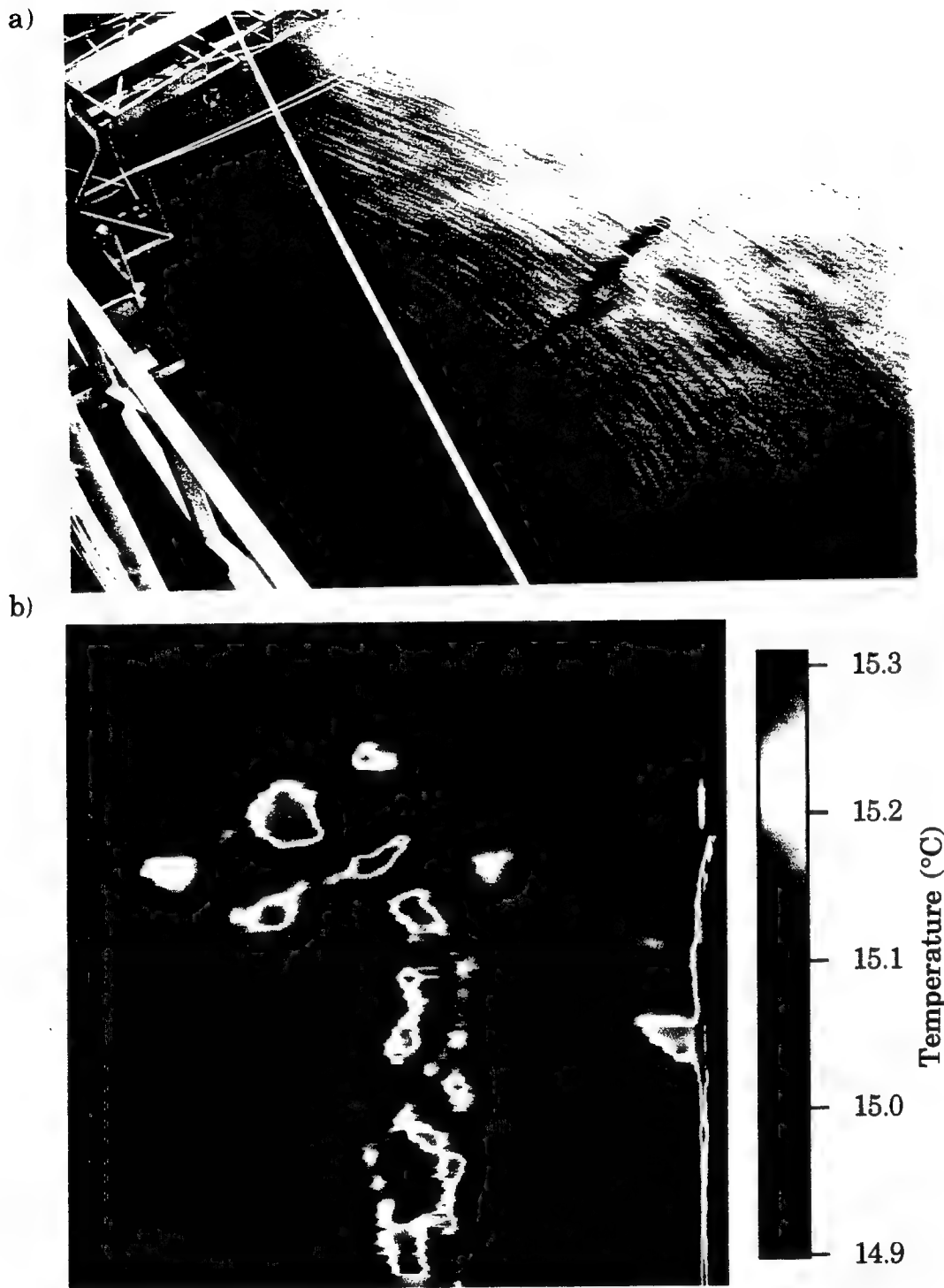
Figure 5.7a-b   a) Photograph of the boom reflection on the sea surface.
b) Corresponding image of infrared reflection of the
boom while looking down at the sea surface and oriented
parallel to the boom.

See Plate in Appendix.

instrument boom corresponds directly to the infrared reflection of the radiation given off by the port boom. The boom's reflection, roughly 0.4 °C greater than the background image temperature, is located in the center of Figure 5.7b and extends to the base of the image. While the boom reflection caused an apparent change in temperature, the instrument cables in the upper left portion of the image produced a real one. The cables provided a disruption of the cool skin layer which allowed the warmer water from below to mix to the surface. The wakes emanating from the cables reached temperatures roughly 0.4 °C greater than the skin layer. The errors induced by the boom reflection had the same order of magnitude as these wake signatures. To avoid reflections from the instrument boom, the KT-19 and PRT-5 mounted on the boom aimed at an incidence angle of 15° for most of the experiment. Likewise, the upward-looking KT-19 aimed at a corresponding zenith angle of 15° and was used to correct for sky reflection.

5.3 Observations and Analysis of Wake Signatures

The cool skin effect at the air-water interface provides a means to detect and characterize the infrared signature of free-surface wakes. Aboard FLIP, two instrument cables deployed from the port boom, each 1 centimeter in diameter, pierced the ocean surface as seen in Figure 5.5b. The wire wave gauge cable was the one located farthest out on the boom. Due to the grounding problems, the wire wave gauge was modified by attaching to the cable 1" diameter PVC tubing cut into 1" sections spaced at 1 m intervals. A 0.25 cm grounding cable was then attached to these PVC sections, separating it from the wave gauge cable. In addition to the grounding wire attachment, the wave gauge cable was greased twice within a twenty-four hour span, once at 16:00 on January 23rd and again at 11:37 on the 24th. The grease wore off the cable initially resulting in the second greasing. We assumed most of the grease wore off the cable following the second greasing. Since FLIP drifted freely and water waves propagated past, wakes emanated continuously from the cables. The disturbance produced by the relative flow past the cables ruptured the skin layer and mixed the warmer bulk water from below to the surface. The

resulting change in surface temperature against the background of the pre-existing cool skin layer allowed for the detection of the warm wakes shown in the upper left corner of Figure 5.7b. However, the wakes did not always form these ordered structures due to the wave-current alignment. Frequently when the waves and current were not aligned, the wakes appeared to wind aimlessly due to a swooping nature of the flow, which carved out the wake pattern on the surface as seen in Figure 5.8. The environmental conditions present during the discovery of these two types of wake patterns are outlined in Table 5.1. Case 1 represents the ordered structure and Case 2 the serpentine. Notice the extremely low wind speed in both of these cases. Grassl (1976) believes that conditions of dominant free convection do not occur when drift currents as small as 0.5 m/s and extremely slight wind conditions exist. Katsaros (1977), however, citing Hasse (1971), emphasizes that even with no mean water currents and with the wind speed dropping below 2 m/s, free convection is likely to dominate. The environmental conditions present during Cases 1 and 2 might have induced free convection in light of the small ocean currents of 25 cm/s on average for the experiment.

The formation of the wake pattern was directly related to FLIP's drifting with the current combined with water waves' oscillatory motion past the cable. For Case 1 on January 26, the wakes in Figure 5.7b highlight the distinctive formation that occurred when the waves and current align. The large turbulent patches coupled with the long slender wakes indicate a continually pulsating flow. Figure 5.9 depicts the arrangement of environmental conditions for Case 1. According to the GPS (Global Positioning System) data taken every 20 minutes, FLIP drifted bearing 306° at 15 cm/s with an orientation of 280° (the heading of the keel which usually aligns with the wind). All directions were measured in degrees True throughout the experiment. From the scanner image, we observed that FLIP drifted against the current (heading 126°) as the swell approached from the west at 270° or 280° according to FLIP's watch log kept by the crew. Thus, the alignment of the long waves and the current

Figure 5.8   Infrared image of the serpentine nature of the wakes
emanating from the instrument cables when the waves and
current are not aligned. The wakes are located in the upper
left corner. A guy wire runs diagonal through the image.
Hints of boom reflection appear below the wakes.

Table 5.1   Environmental conditions for Cases 1 and 2.

Case	1 - Ordered	2 - Serpentine
Date	January 26, 1992	January 25, 1992
Time	19:31 —> 20:40 PST	19:10 —> 19:50 PST
Wind Speed	2.1 ± 0.2 m/s	1.0 ± 0.2 m/s
Wind Direction (True)	284° ± 9°	25° ± 10°
Drift Speed	15 cm/s	12 cm/s
Drift Direction (True)	302° ± 15°	296° ± 6°
Compass Heading (True)	270° ± 8°	19° ± 6°
Wave Direction (True)	~ 270°	~ 270°
Air Temperature	Steadily Decreasing 14.7 °C to 14.6 °C	Steadily Decreasing 14.6 °C to 14.4 °C
Relative Humidity	88.9 % ± 0.6%	Steadily Increasing 92.7 % to 93.5 %
T @ 0.1 cm	14.34 °C ± 0.01 °C	14.78 °C ± 0.06 °C
T @ 0.5 cm	14.35 °C ± 0.01 °C	14.78 °C ± 0.06 °C
T @ 1.0 m	14.34 °C ± 0.01 °C	14.69 °C ± 0.11 °C
T @ 2.0 m	14.35 °C ± 0.01 °C	14.33 °C ± 0.15 °C
T @ 5.0 m	14.31 °C ± 0.01 °C	13.93 °C ± 0.06 °C
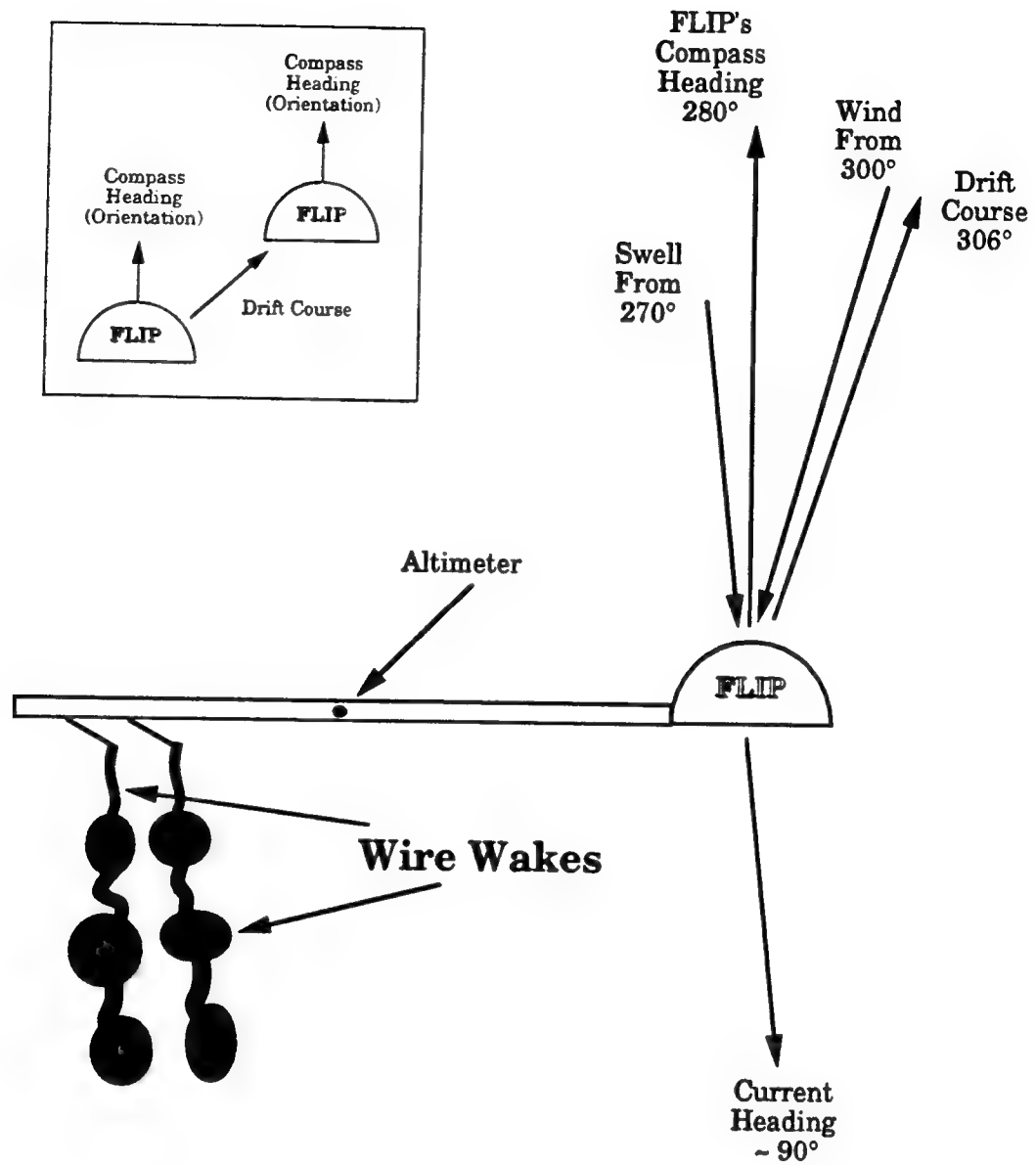
Figure 5.9   Arrangement of the environmental conditions for Case 1. All directions are in degrees True. Drift course is determined from the GPS data retrieved every 20 minutes.

producing large variations in relative flow past the cables allowed for the ensuing cyclic portrayal in Figure 5.10 (more detailed look at Figure 5.7b).

As the crest of the wave propagated past the cable, the maximum positive orbital velocity in the direction of the current resulted in a substantial relative flow past the cable. A large surface motion induced by the relative flow produced a long slender wake because the cable remained stationary relative to the large surface motion. Conversely, as the trough of the wave passed the large patch-like features formed. The current and orbital velocities counteracted each other leaving the surface relatively motionless, allowing the wire to interact with its own wake for an extended period of time. Any slight surface motion due to the smaller wind waves resulted in an additional interaction of the cable within its own wake. The in-line force produced from the passage of the swell crest caused the cable to swing gently, with the same magnitude as any surface motion induced from the existing current or smaller wind and gravity waves. Furthermore, the transverse forces on the cable accentuated its motion, resulting in more concentrated mixing within the recently disturbed slender wake. Upon passage of yet another wave crest, the turbulent patch accelerated away from the cable, increasing the level of disruption within the patch and forming another long slender wake. The large circular turbulent patches were on the order of 1 meter in diameter while the long slender wakes were only a few tens of centimeters in width(< 25 cm). The previous depiction of the pulsating wake formation indicates that large-scale vortex shedding (eddies > 1 m) did not produce these patterns. Nonetheless, the relative flow past the cable would generate vortex shedding with eddies on the order of the cable diameter (1 cm). Remarkably, the wire was only 1 centimeter in diameter and still produced significantly large structures, roughly 100 times the size of the cable. The structures persisted within the field-of-view of the scanner for nearly 60 seconds until they drifted out of the image in the direction of the mean current.
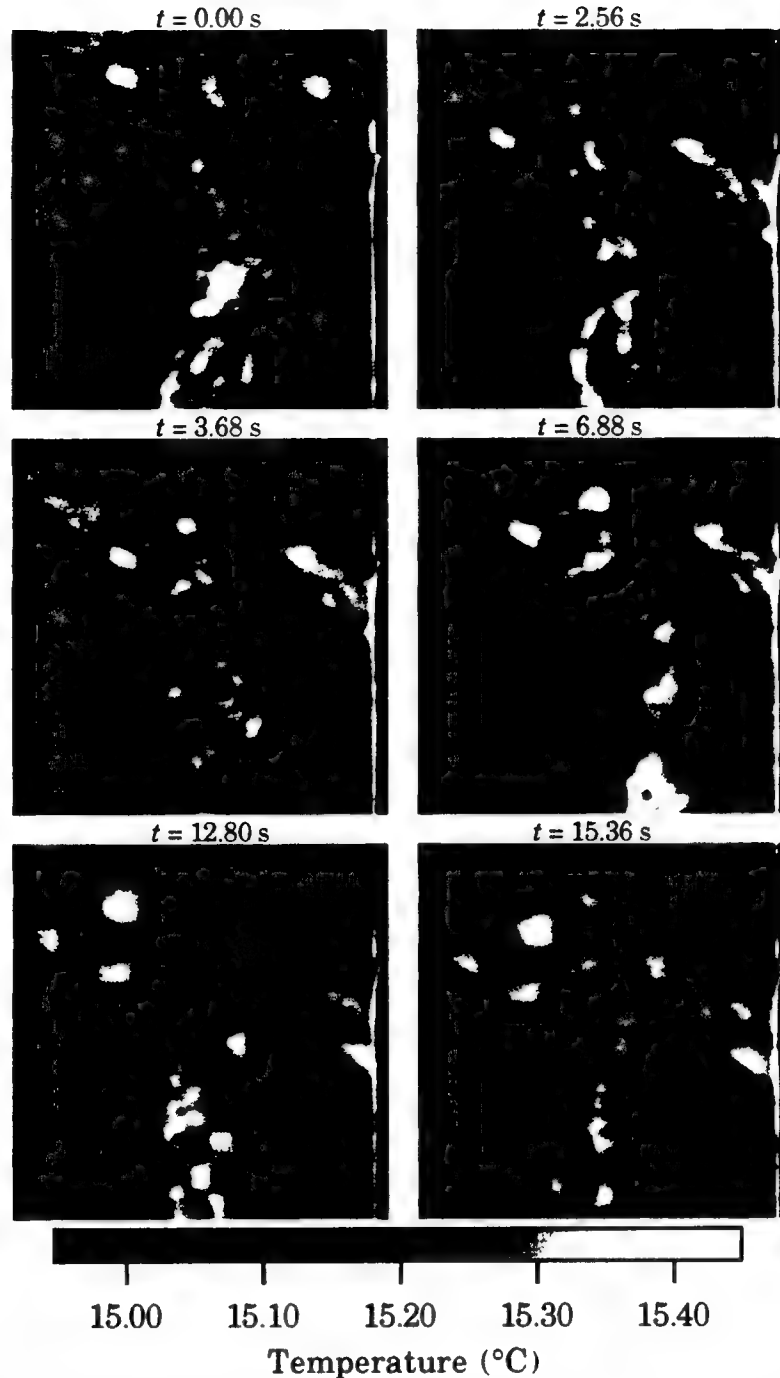
Figure 5.10 Time series of infrared images depicting the ordered wakes emanating from the surface-piercing cables under low wind conditions when the swell waves propagate in the direction of the current. The long slender wakes develop by the superposition of the crest of the swell and the current velocities. The patches form when the velocity in the trough counteracts the current. The cable diameter is 1 cm while the patches are on the order of 1 m.

See Plate in Appendix.

For Case 2 on January 25, FLIP drifted in the direction of 296° at roughly 12 cm/s while its orientation was 17° as depicted in Figure 5.11. From the scanner images, the current driving FLIP was assumed greater than the drift speed and in the same direction, since no record of current speed or direction was available at that time. The port boom, located 90° counter-clockwise from the keel, pointed with the drift and current allowing the wakes to disappear towards the top of the image with the mean current. However, the swell approached the cables from the west at 260° or 270° according to FLIP's watch log kept by the crew. Figure 5.12 displays a typical progression of the wake formation for Case 2 as a wave (period, T_o = 9.9 s, and height, H_o = 2.7 m) passed by the cable from a different direction than the current. In this case, we used the altimeter data to calculate the wave height and period. Again, the relative flow past the cable due to the oscillatory wave motion and the mean current drives the evolution of the wakes. According to linear wave theory, the maximum positive orbital velocity of 87 cm/s at the crest generated a large swooping motion downward in the image. As the current continued past the cable, the wake structure was displaced slightly. Upon the return of the maximum negative orbital velocity in the trough, the cable carved out the completion of a backwards "C" structure. Less exaggerated surface motion due to the smaller wind waves incited the smaller wake disturbances. These wakes mimicked the long slender wakes formed in Case 1. The cycle continued with some regularity according to the size and period of the swell. Downstream, however, the wake structures dispersed and interacted with each other evolving into a wider less-defined surface pattern.

We now return to the patch-like formations emanating from the cables exemplified by Case 1. Following a single patch evolution throughout its prolonged existence illustrates the growth and decay patterns commonly observed. Figure 5.13 shows the time series of a patch-like wake produced from a wave (period, T_o = 6.4 s, and wave height, H_o = 1.0 m). The first image (t = 0.00 s) displays the uniform undisturbed cool skin layer. The strong acceleration and deceleration of the relative flow as
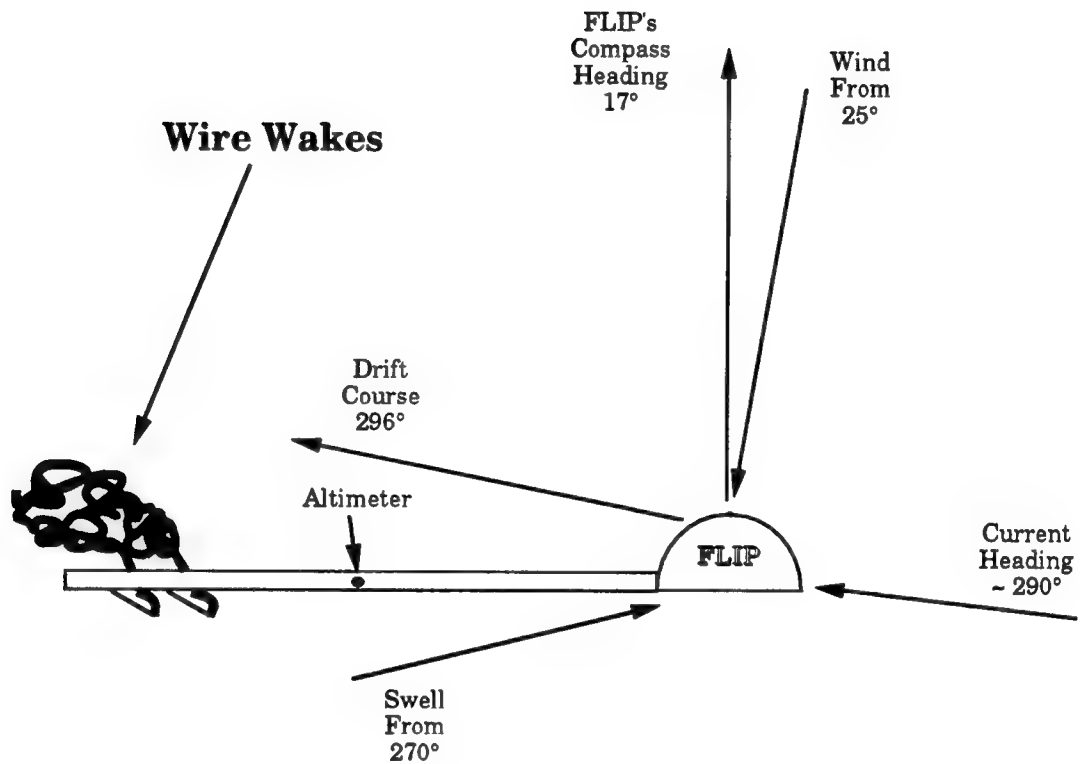
Figure 5.11 Arrangement of the environmental conditions for Case 2. All directions are in degrees True. Drift course is determined from the GPS data retrieved every 20 minutes.

$t = 0.00$ s $t = 2.24$ s

$t = 3.36$ s $t = 5.44$ s

$t = 9.12$ s $t = 10.72$ s

14.4   14.5   14.6   14.7   14.8   14.9   15.0
Temperature (°C)

Figure 5.12 Time series of infrared images depicting the serpentine wakes emanating from the cables when the waves and current are not aligned.

See Plate in Appendix.

142

Figure 5.13 Time series of infrared images following one particular turbulent patch. The image size is roughly 1.5 m x 1.5 m. When the temperature within the patch reaches a maximum, the patch continues to grow in size. Upon maximum spatial growth, the wake recovers substantially as it propagates off the image after roughly 41 seconds.

See Plate in Appendix.
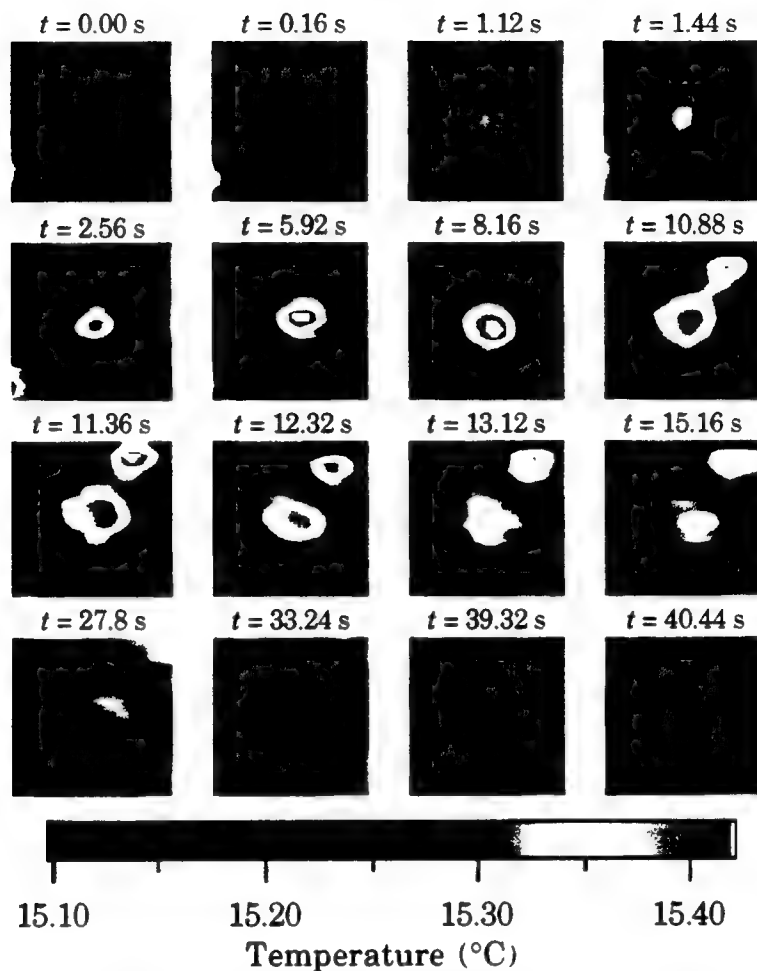
the crest passed with an orbital velocity of 51 cm/s caused a range of Kármán vortex shedding as observed from an impulsively started and stopped cylinder in Section 4.2. The disturbance associated with the chaotic flow initiated the breakage of the skin layer. With the slight relative flow related to the arrival of the trough, the cable interacted within this newly generated turbulent wake and evolved into an impressive patch. The next swell crest traveled by and the surface motion accelerated the patch away from the cable. The temperature within the wake reached a maximum at t = 5.92 seconds denoted by the white area within the images. The disturbance, however, continued to spread rupturing the previously undisturbed surface skin layer for some time after the initial patch developed (the time is on the order of 2 times the T_o which created the disturbance). The turbulent patch proceeded to grow in size even though the cable no longer interacted within it. Finally, the patch reached a peak width and slowly decayed in size with time until it eventually drifted off the image after approximately 41 seconds.

Quantitative analysis of the size, temperature, and duration of the wake structures required an objective technique to measure the patch widths and temperature differences. Taking a cross-section of the turbulent patch from the image in both the x- and y-directions resulted in a roughly Gaussian distribution of temperature, T, against position in pixels, x_p or y_p. Figure 5.14 presents some cross-sectional profiles of temperature from the same wake in Figure 5.13 at different stages of development. Finding the first moment of the distribution for the x-direction slice

$$x_m = \frac{\int x_p T(x_p)dx_p}{\int T(x_p)dx_p} \qquad (5.1)$$

gives the mean of the distribution. Taking the second moment results in the variance whose square root is the standard deviation
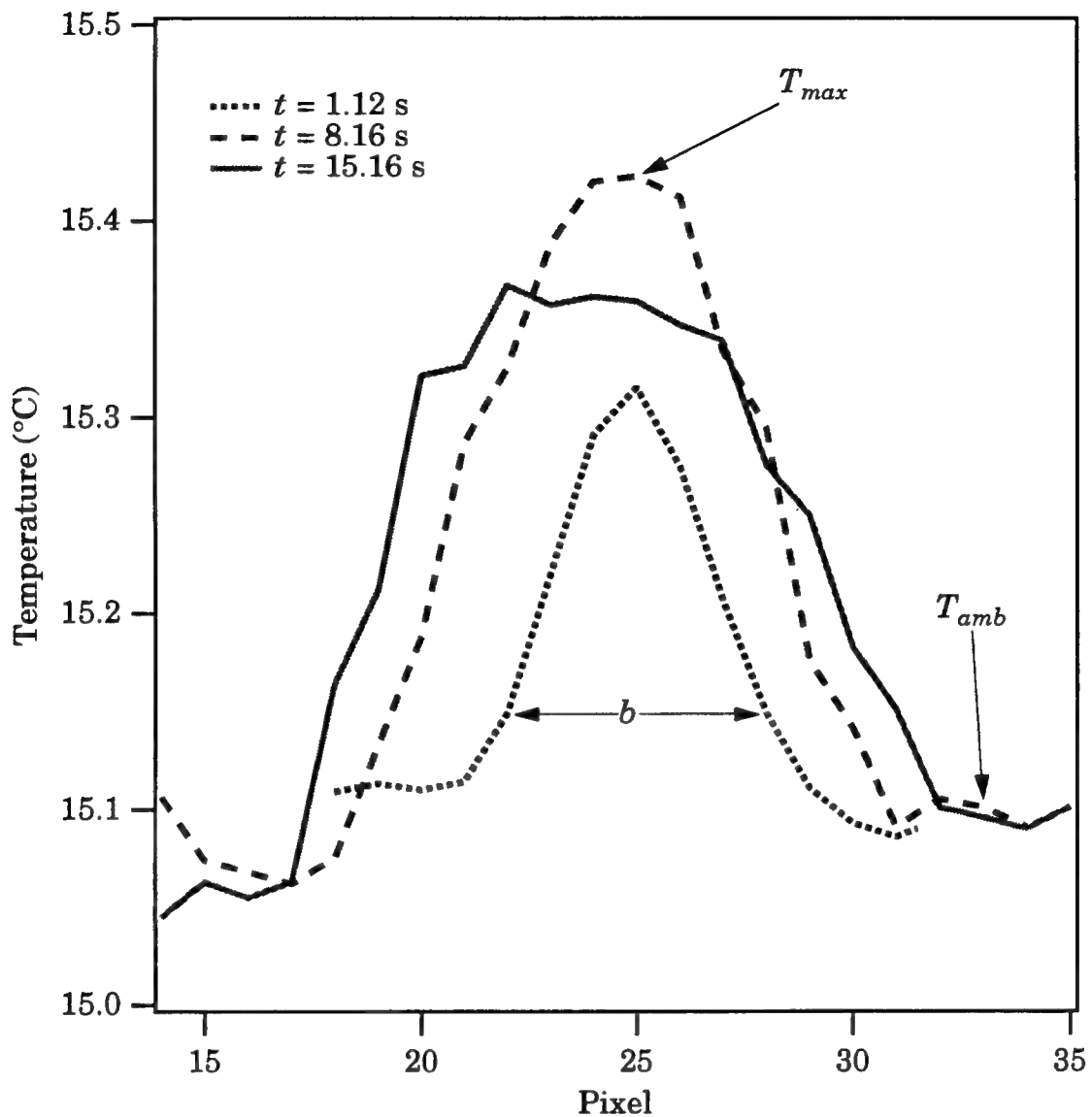
Figure 5.14 Cross-sectional profiles of temperature from the same wake in Figure 5.13 at different stages of development. The characteristic wake dimension, b, approximates the size of the patch while T_{max} - T_{amb} measures the ΔT_w. While the temperature within the patch begins to diminish, the patch continues to enlarge spatially.

$$\sigma_x = \sqrt{\frac{\int \left(x_p - x_m\right)^2 T(x_p)dx_p}{\int T(x_p)dx_p}}.$$ (5.2)

Adding and subtracting the standard deviation from the mean provided two positions in pixels, which when converted to distance and differenced provided the wake width. Repeating the process for the y-direction cross-section and averaging the x and y wake widths resulted in the characteristic wake dimension, b, in meters used in the analysis. Also, we defined the temperature difference, ΔT_w, across the patch as the maximum temperature, T_{max}, attained within the turbulent patch and the undisturbed skin layer temperature, T_{amb}. Figure 5.14 reveals that the wake grew in size and temperature from its initial stages until the temperature within the wake reached a maximum. Astonishingly, while the temperature within the patch began to diminish, the patch continued to grow spatially signifying some level of disruption of the skin layer.

Conventionally, the wake of a bluff body has been characterized by the Reynolds number

$$Re_o = \frac{u_o}{\nu}D$$ (5.3)

where $u_o = a_o\omega_o$ represents the maximum orbital velocity in this case and D is the diameter of the cable (1 cm). The wave which produced the patch-like wake in Figure 5.13 generated a flow characterized by a Reynolds number of $Re_o = 5.05 \times 10^3$. Clearly, the instantaneous velocity would have changed rapidly as a wave propagated past the cable due to the unsteady nature of the flow. Actually, the instantaneous velocity past the cable would have increased when considering the effect of the background current superimposed on the maximum orbital velocities during the passage of a crest as opposed to a surface velocity ≈ 0 in the trough. Also, the analysis underestimated the orbital velocity since we have used the wire wave gauge data to determine the wave height. In fact, the average velocity of the

horizontal surface motion, $\bar{u}_{sc}$, determined from the scanner images as a crest passed was 70 cm/s compared to 50.5 cm/s calculated as the maximum orbital velocity. While $\bar{u}_{sc}$ was not an instantaneous velocity (averaged over 2 seconds), it verified that the superimposed current and the underestimation of the wave conditions resulted in an underestimated Reynolds number calculated from the maximum orbital velocity alone. As pointed out in Table 4.1, wakes in general become turbulent for $Re > 5000$ which was the case here when considering the effect due to the current alone. Free stream or shear-generated turbulence, which must exist on the open ocean for the molecular sublayer to develop, results in a lower threshold necessary for the wakes/patches to be turbulent. The flow needed to create a turbulent wake when free stream turbulence exists decreases and the Reynolds number associated with this flow is reduced. Therefore, the deduction that these wakes/patches were turbulent is justified.

However, the conventional Reynolds number was not the most appropriate characterization of the disturbance producing these wake signatures. Figure 5.15 depicts three examples of the time series produced when performing the analysis of the characteristic wake dimension outlined previously. The three examples display 2nd order polynomial fits and exhibit the effects of varying wave heights and periods. We observed that larger waves generated larger more persistent patches, as the wakes formed continuously with the periodicity of the wave field. As a separate wave created each turbulent patch, we chose to characterize the magnitude of the wave disturbance by a wave Reynolds number

$$Re_w = \frac{a_o \omega_o}{v k_o} \qquad (5.4)$$

based upon the maximum orbital velocity, $u_o = a_o \omega_o$, and the wavenumber, k_o. Clearly, the larger waves resulted in correspondingly larger Re_w's. The maximum orbital velocity estimated the intensity of the disruption while the wavenumber quantified the duration. The diameter of the cables remained constant and the mean current was assumed to be uniform over
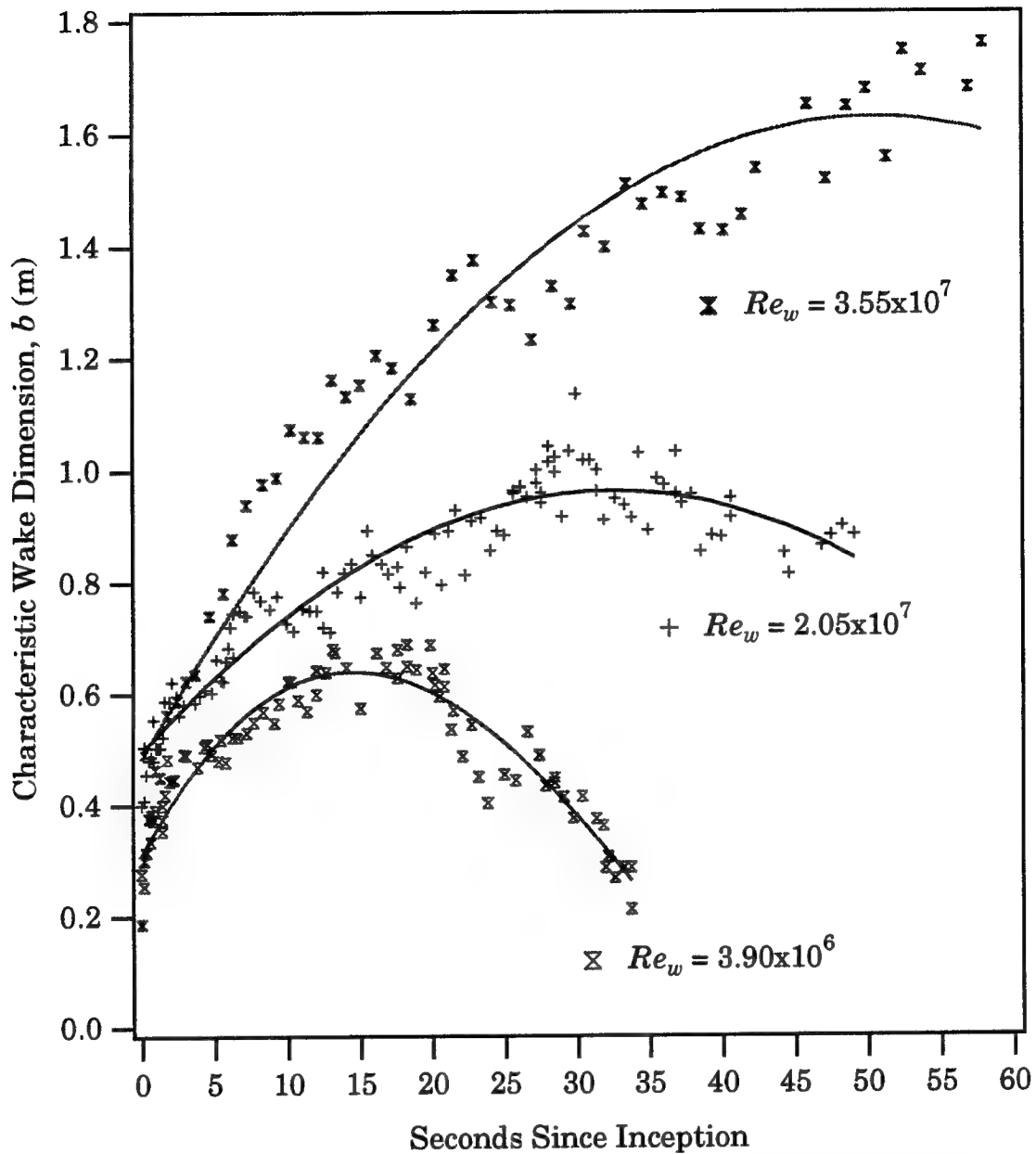
Figure 5.15 Time evolution of patch diameter, b, for 3 different wave
Reynolds numbers, Re_w, for the individual wave producing the
patch. Waves with larger Re_w produce larger wakes that
reach maximum size later in time, resulting in longer skin
layer recovery times. Skin layer disruptions lasting up to 60 s
were measured, after which time they traveled out of the field-
of-view. Extrapolation of the curve for the largest Re_w
observed results in a skin layer recovery time of
approximately 120 s.

the course of the measurement timespan of Case 1. Therefore, the wave Reynolds number parameterization provided an appropriate measure of the input disturbance produced by the passage of an individual wave.

The wave Reynolds number describing the disruption becomes Re_w = 3.90 x 10^6, 2.05 x 10^7, and 3.55 x 10^7, respectively, for the wake patch evolutions shown in Figure 5.15. (The wave periods were T_o = 6.5, 11.6, and 11.7 s, with wave heights of H_o = 0.78, 2.28, and 3.89 m, respectively, for the time series in Figure 5.15.) Notice the continued growth of the wake width even after the turbulent patch drifted away from the source of the disturbance--the cable. The patch-like disturbances reached larger maximum wake dimensions with increasing Re_w. Consequently, the duration of the patches' life increased with Re_w. The wakes not only increased in size and duration with increasing Re_w, but also attained their maximum width later as Re_w increased. The trend of increasing turbulent patch width long after the wire has exited the wake occurred even for the smallest of waves. Tables 5.2a and 5.2b list the 15 wake formation and decay sequences analyzed for this study along with the pertinent parameters. Subsequently, we can now display a full range of wave Reynolds numbers characterizing the observations from the field experiment in Figure 5.16. The patch-like wakes ranged significantly in maximum characteristic wake dimension between 0.5 and 1.7 m and in duration of existence between 35 and 80 seconds. None of the patches, however, completely recovered before drifting off the image. Figure 5.17 emphasizes the stark contrast between the turbulent patch size, which is on the order of a meter, and the 1 cm diameter of the surface-piercing cable producing the disruption. We normalized the maximum wake dimensions by the cable diameter resulting in large values on the order of 10 to 100 for b_m/D, the normalized maximum wake dimension. Employing our characterization of a wave Reynolds number, we observed that the scaled maximum wake dimension, b_m/D, of each turbulent patch increased parabolically with wave Reynolds number. The second-order correlation in Figure 5.17 suggested that the deep-water nature of wavelength ($L_o \sim T_o^2$ according to the dispersion relation) dictated the strength of the disruptive

Table 5.2a   Wave parameters for January 26th, 1992 arranged according to Re_w.

Number	Approximate Inception Time (ddd:hh:mm:ss) (PST)	Wave Height, H_o (m)	Period, T_o (s)	Wave Reynolds Number, Re_w (10^6)
1	026:19:31:37	0.78	6.5	3.9
2	026:19:31:52	1.03	6.4	5.1
3	026:19:32:17	0.96	6.9	5.2
4	026:19:31:44	1.00	8.0	6.2
5	026:19:32:25	0.85	9.9	6.6
6	026:19:31:59	1.29	8.4	8.4
7	026:20:04:38	1.24	11.0	10.6
8	026:19:56:21	1.57	11.1	13.6
9	026:19:51:51	1.55	13.7	16.6
10	026:19:34:39	1.48	15.3	17.6
11	026:19:35:16	1.77	13.1	18.1
12	026:19:31:25	2.28	11.6	20.5
13	026:19:34:25	2.64	12.4	25.6
14	026:19:33:16	2.61	13.4	27.2
15	026:19:45:58	3.89	11.7	35.5

Table 5.2b   Wave parameters for January 26th, 1992 arranged according to Re_w.

Number	Maximum Horizontal Orbital Velocity, u_o (cm/s)	Conventional Reynolds Number, Re_o (10^3)	Representative Surface Velocity From Scanner, $\bar{u}_{sc}$ (cm/s)
1	37.6	3.76	59
2	50.5	5.05	70
3	43.3	4.33	54
4	39.0	3.90	61
5	27.1	2.71	62
6	48.4	4.84	—
7	35.3	3.53	67
8	44.4	4.44	—
9	35.7	3.57	—
10	30.5	3.05	72
11	42.4	4.24	74
12	61.8	6.18	105
13	66.7	6.67	116
14	61.3	6.13	110
15	104.7	10.47	159
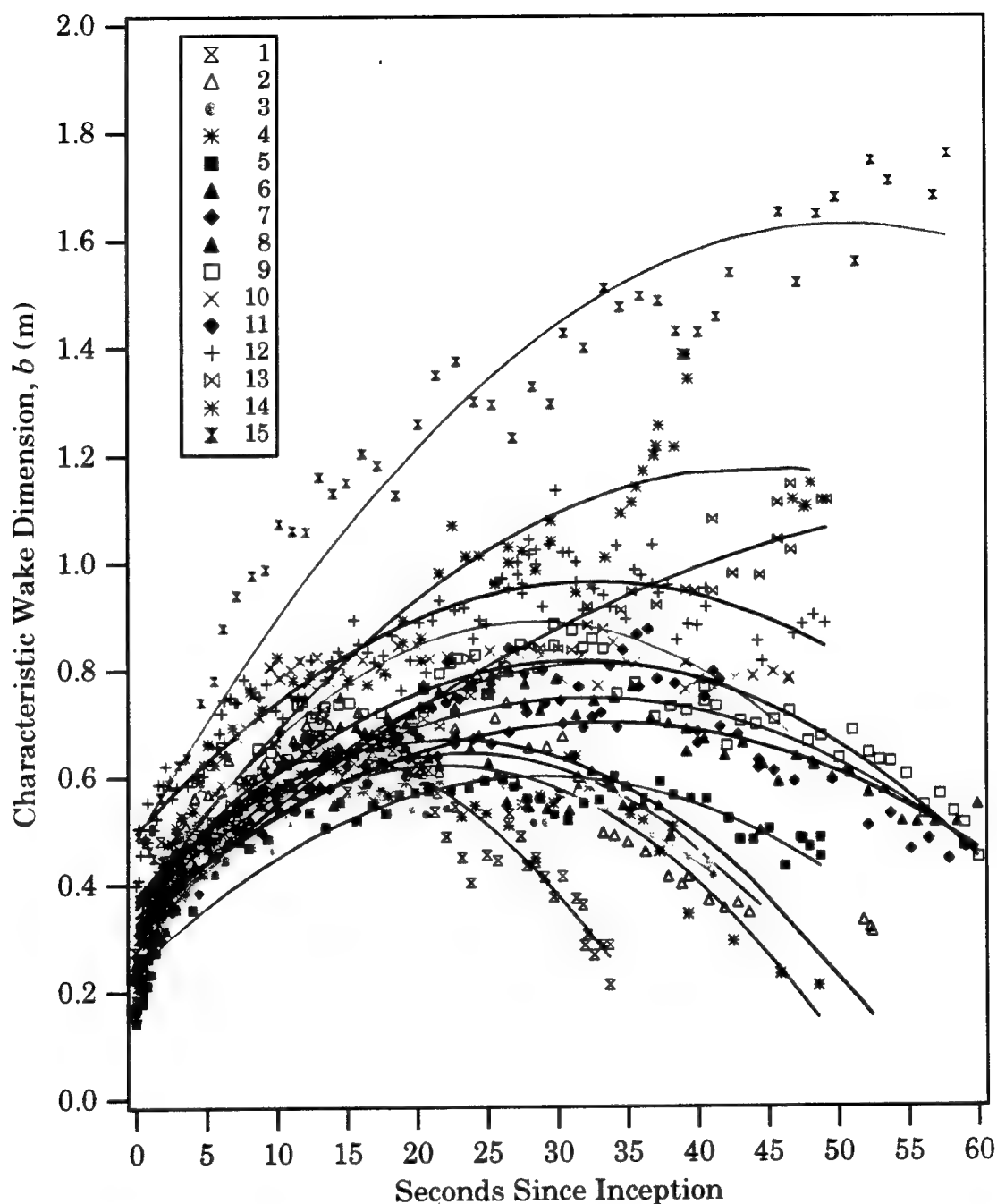
Figure 5.16 Time evolution of characteristic wake dimension, b, for the 15 individual patches produced by the swell. The patch-like wakes range significantly in maximum dimension between 0.5 and 1.7 m. None of the disturbances have recovered completely before drifting out of the field-of-view. Two of the patches exist in the field-of-view for up to 80 s, though not explicitly shown here.
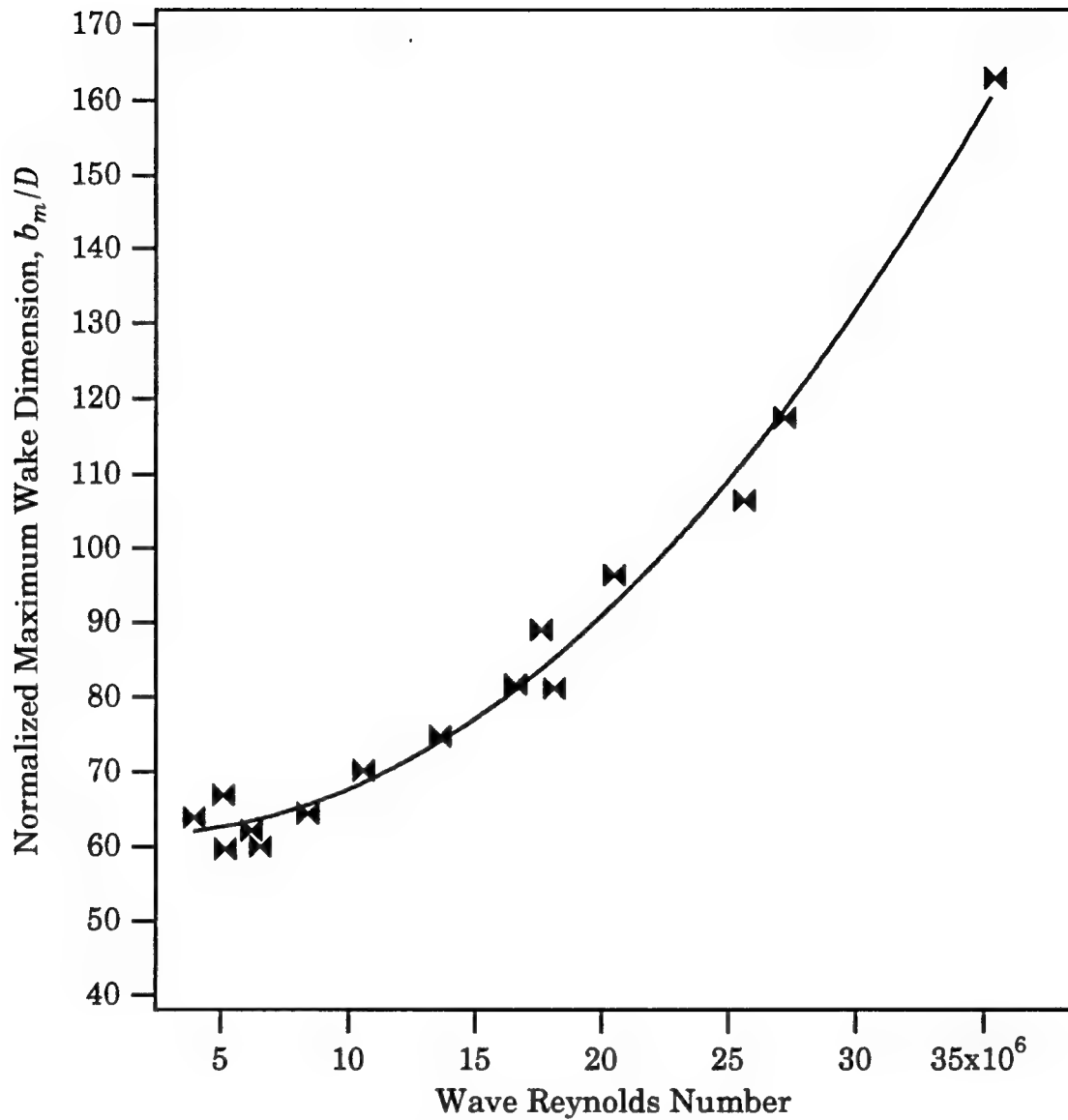
Figure 5.17 The normalized maximum characteristic wake dimension, b_m/D, as a function of Re_w emphasizes the stark contrast between the turbulent patch size and the surface-piercing cable diameter of 1 cm. The parabolic correlation between b_m and Re_w suggests the deep-water nature of wavelength ($L_o \sim T_o^2$) dictated the strength of the disruptive process. Longer swell waves produced a longer initial disruption.

process. Longer swell waves produced a longer duration of the initial disturbance. Having attained a peak width, the patches slowly decayed and extended out of the scanner's view without fully recovering. Extrapolating the complete evolution and decay cycle for the patch with the largest Re_w resulted in a 120 second lifetime.

Consistent with our description of the wake/patch formation, bigger waves produced longer lifetimes and larger patch widths. For longer waves, the patches achieved a higher degree of disruption, described by the Re_w, than for shorter waves. The logical choice for scaling the duration of the turbulent patch, t, was the period of the wave, T_o, producing the wake. Accordingly, Figure 5.18 demonstrates the effect of such scaling, aligning the maximum wake widths about a point of $t/T_o = 2$ for the lower range of Re_w, 3.5 for the medium range and 5 for the largest wave Reynolds number. The range of t/T_o suggested that the appropriate scaling might have included a turbulent time scale or a skin layer recovery time. Initial scalings of the patch width, however, by both the amplitude of the wave, a_o, and the wavelength, L_o, resulted in a less than desirable outcome. Nevertheless, the formation of the scaling parameter $ba_o\omega_o/\nu$ in Figure 5.18 provided three distinct groupings according to wave Reynolds number. These separate regions suggest an eddy viscosity should replace the molecular viscosity. The diffusion mechanism within each grouping of wake sequences according to Re_w remained relatively the same. For each distinct grouping, however, this mechanism for diffusion differed substantially. Actually, the eddy viscosity not only would have changed throughout the lifetime of each growth and decay cycle, but also behaved differently for each separately defined wake. The free-surface turbulence/vortical interaction described in Section 4.7 may have explained this behavior.

Not only did the patch width experience a growth and decay cycle, but the difference, ΔT_w, between the maximum temperature within the turbulent patch and the undisturbed surface also encountered this process. The maximum temperature difference across the patch generated by the
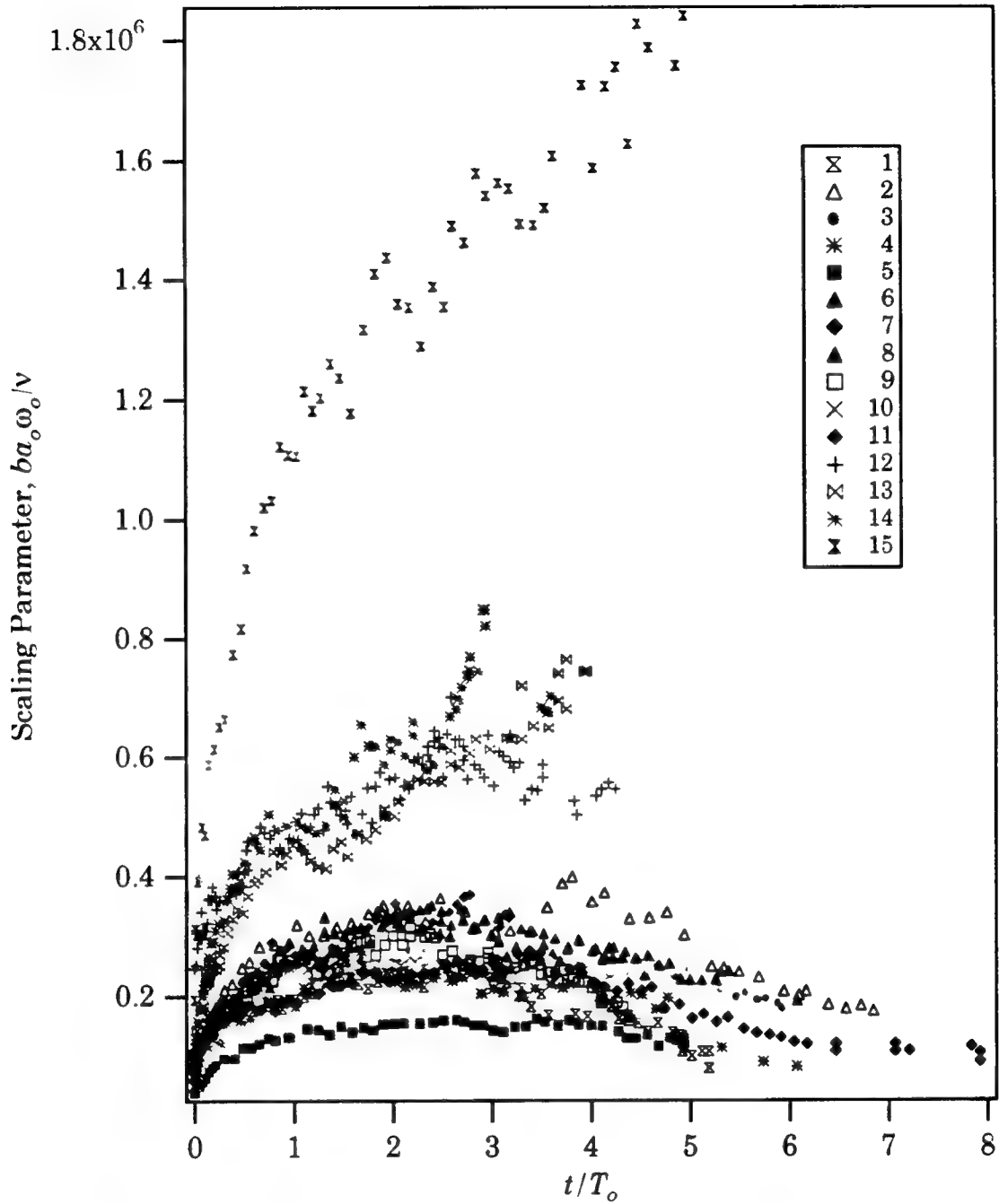
Figure 5.18 Scaling analysis of the the 15 individual patches produced by the swell. Both t/T_o and $ba_o\omega_o/\nu$ separate out into three distinct regions according to the Re_w. The regions follow from bottom to top as low, mid, and high range Re_w.

disruption of the cool skin, ΔT_w, provided a measure of the bulk-skin temperature difference, ΔT, and ranges from 0.4 to 0.5 °C. Figure 5.19a portrays the time series of ΔT_w for the same wake patch evolutions described in Figure 5.15. Contrary to b, ΔT_w reached a maximum quickly regardless of Re_w. The ΔT_w recovered faster at low Re_w while the duration of recovery increased with increasing Re_w. For a more complete description, Figure 5.19b displays ΔT_w as a time series for each wake scenario along with a linear fit extending from the maximum. The slope of the line corresponds to a rate of decay or skin layer recovery. The point of each sequence at which the maximum ΔT_w occurred was relatively abrupt as opposed to the occurrence of the maximum wake width, b_m, of Figure 5.17. The time at which the maxima occurred for both ΔT_w and b is displayed in Figure 5.20. As mentioned, the rapid occurrence time of the ΔT_w maxima remained relatively low irrespective of wave Reynolds number. However, the time at which the b maxima occurred increased with wave Reynolds number illustrating the leisurely continued spreading. Therefore, as the wave Reynolds number increased, the difference in time between the occurrence of ΔT_w and b maxima increased. The rate at which ΔT_w decayed in Figures 5.19a and b represented the skin layer recovery and is displayed in Figure 5.21 as a function of wave Reynolds number. As anticipated we observed that the rate of skin layer recovery sharply decreased for increasing Reynolds number. (The skin layer recovery rate actually increased, but the magnitude decreased.) Nonetheless, the skin layer recovered while the wake continued to grow in size. Once the maximum width, b_m, occurred, b decayed at a rate which gradually decreased with increasing Re_w as seen in Figure 5.22.

5.4 Discussion of the Wake Signatures

The turbulence and vorticity generated in the wake of the cable gave rise to highly strained fluid motions near the free-surface. Even though suppression of the vertical turbulent fluctuations existed, the quasi two-dimensional turbulence still disturbed the surface and broke up the skin layer. The vortical flow in the wake/patch aligned perpendicular to the
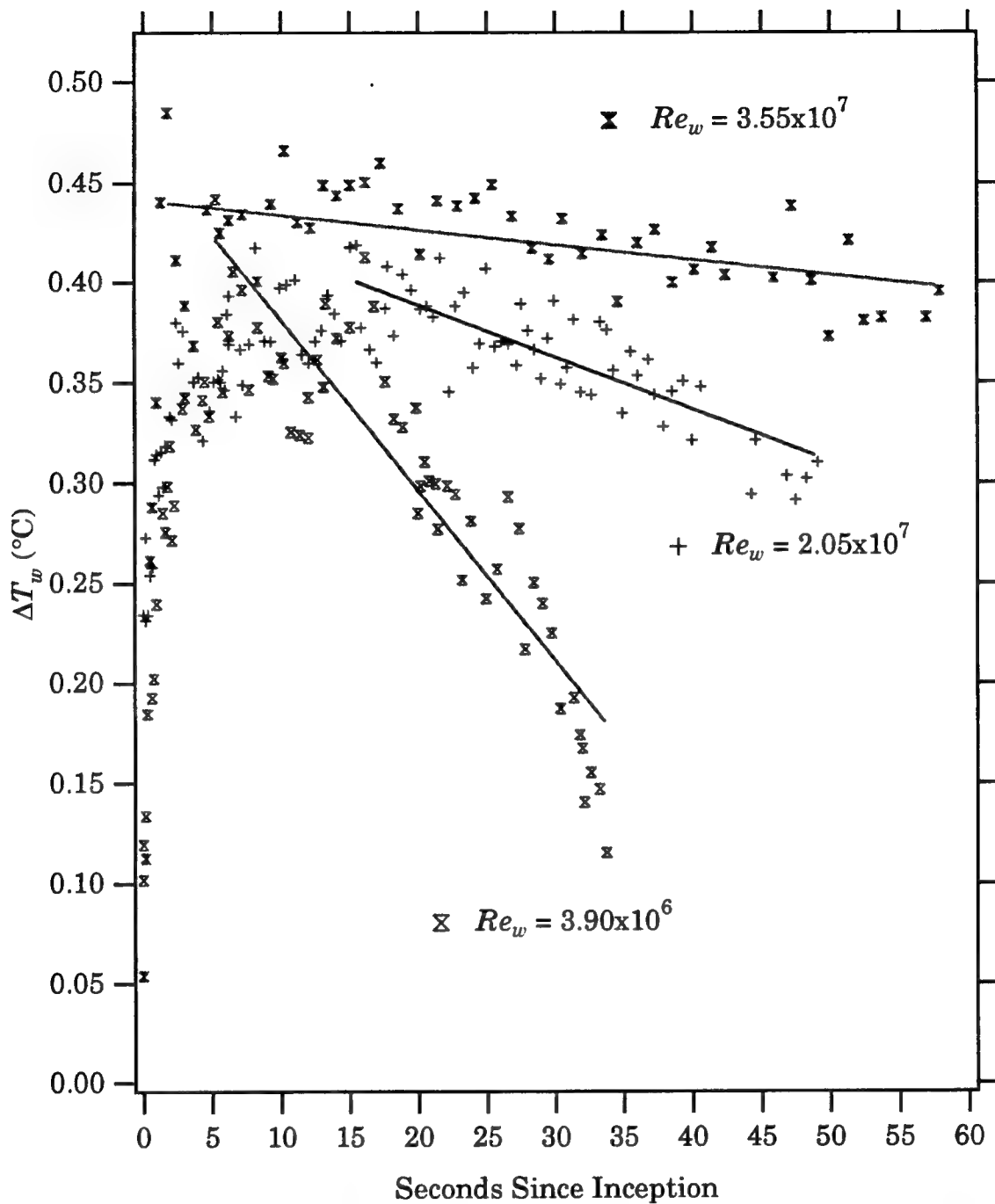
Figure 5.19a   Time series of maximum temperature difference between the patch and the undisturbed surface for the identical 3 patches produced by the swell in Figure 5.15. While the patches rapidly reach a peak ΔT_w regardless of Re_w, the rate of recovery of the skin layer is a function of Re_w. The slope of the line fitted from the maximum ΔT_w is taken as the skin layer recovery rate.
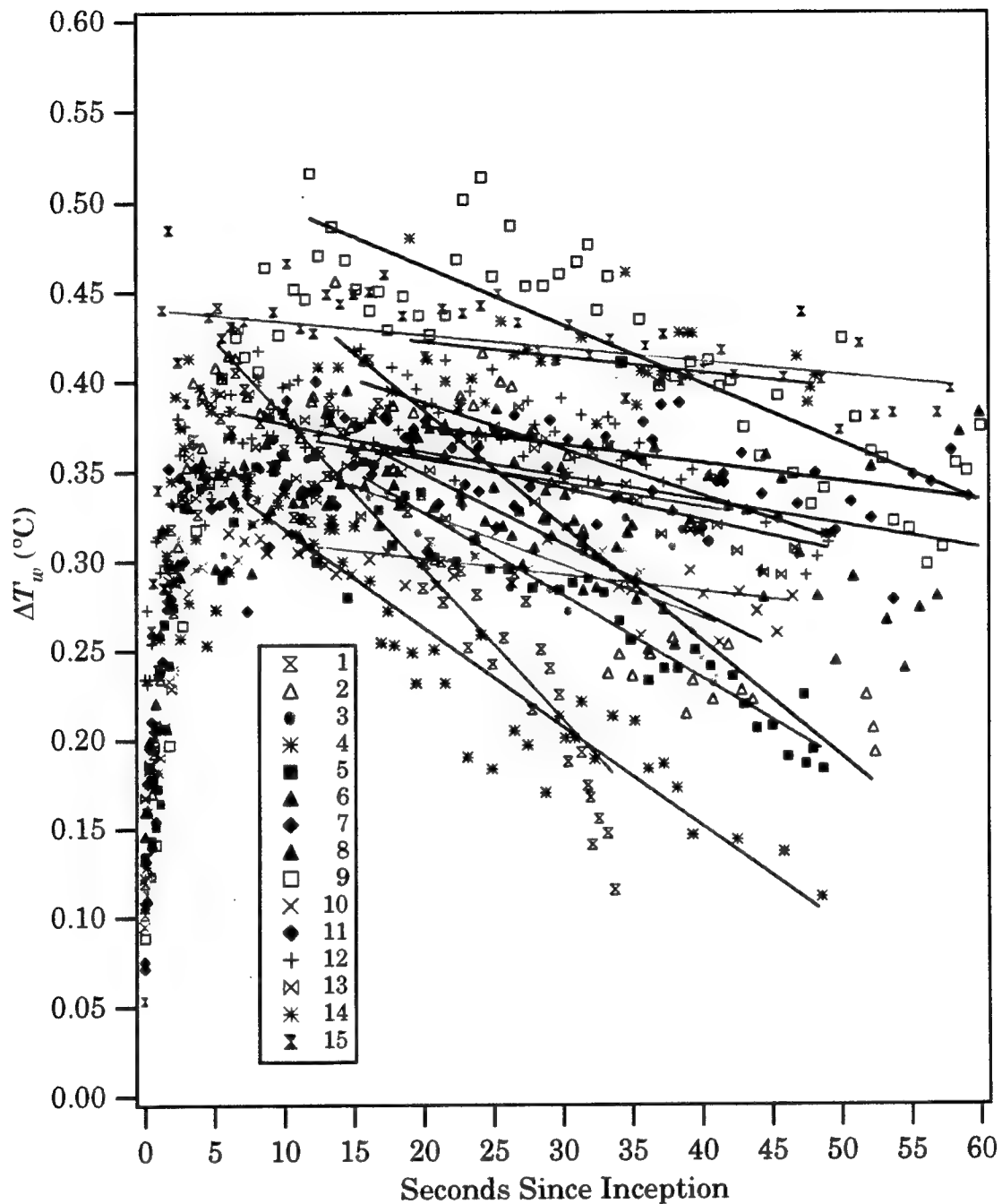
Figure 5.19b   Time evolution of maximum temperature difference between the patch and the undisturbed surface for the 15 patches produced by the swell. While all patches rapidly reach a peak ΔT_w regardless of Re_w, the rate of recovery of the skin layer is a function of Re_w. The slope of the line fitted from the maximum ΔT_w is taken as the skin layer recovery rate.
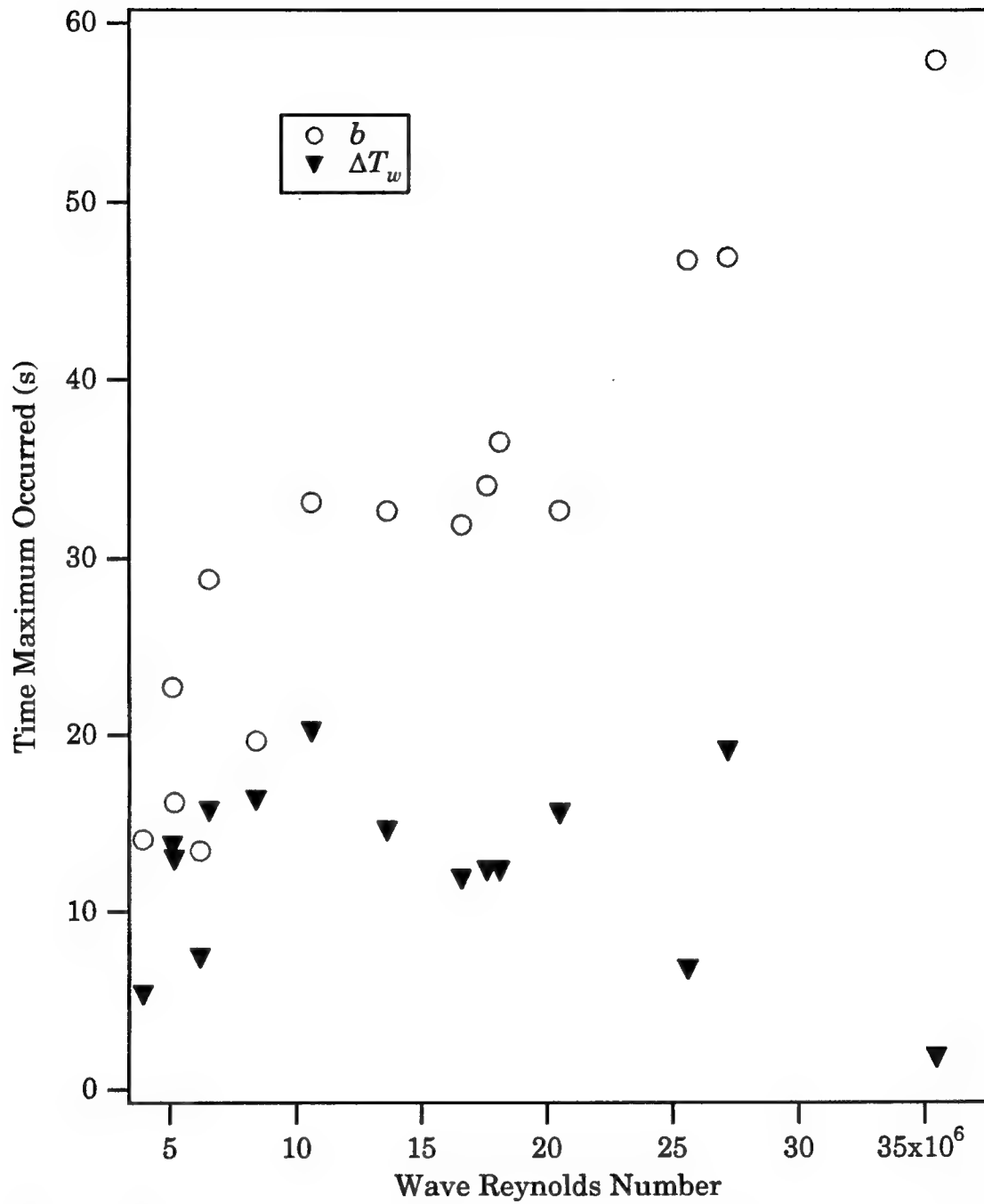
Figure 5.20 The time at which the maxima occurred for both ΔT_w and b as a function of Re_w. The time of the maximum ΔT_w remained relatively constant irrespective of Re_w. However, b_m occurred later and later as Re_w increased which suggests the continued spreading of the disruption.
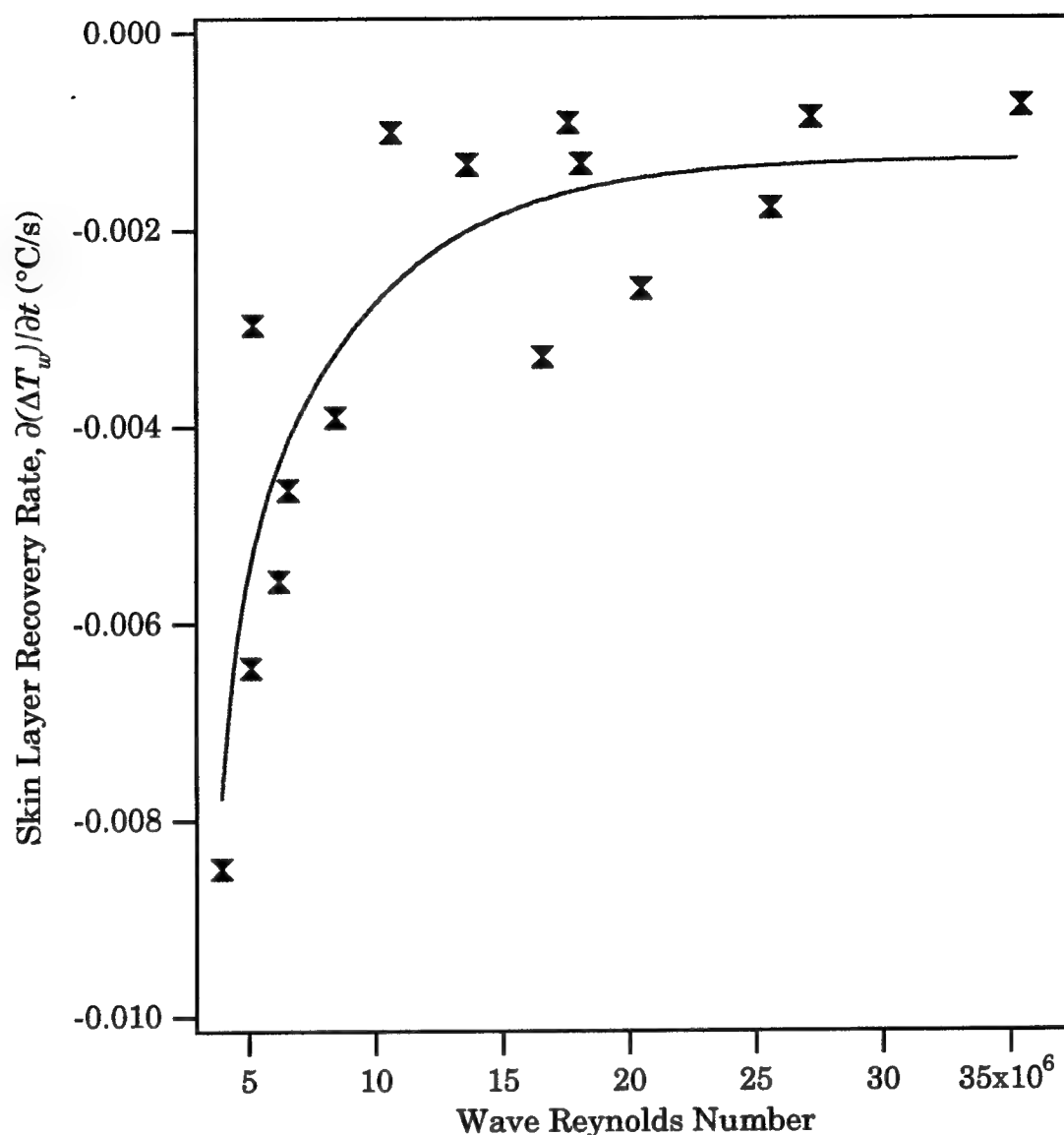
Figure 5.21 Skin layer recovery rate, $\partial(\Delta T_w)/\partial t$, for 15 individual patches versus wave Reynolds number, Re_w. For small Re_w, the $\partial(\Delta T_w)/\partial t$ decreases rapidly with increasing Re_w. The apparently small and constant $\partial(\Delta T_w)/\partial t$ at high Re_w indicates that in these cases the surface disruption dominates over the skin layer recovery. Since the net heat flux was constant, these results show that the strength of the surface disruption played a strong role in determining the skin layer recovery rate.
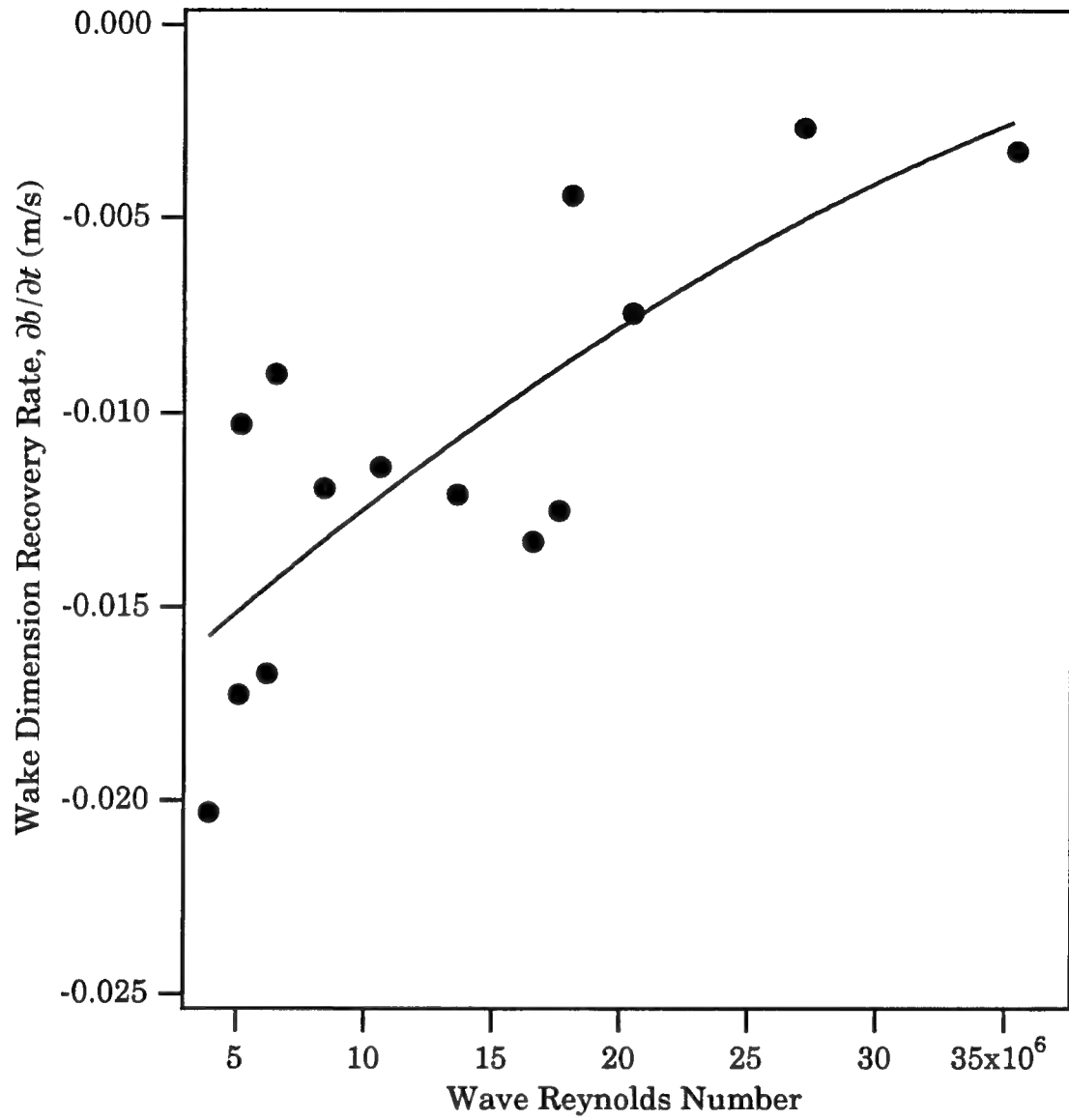
Figure 5.22 Patch width recovery rate, $\partial b/\partial t$, for 15 individual patches versus wave Reynolds number, Re_w. Contrary to the skin layer recovery rate, $\partial b/\partial t$ gradually decreases with increasing Re_w.

surface and developed an upwelling effect bringing the warmer water from below to the surface. The molecular layer now had been ruptured by the turbulent vortical flow. The continued enlarging of the patch suggested a "spreading" of vorticity/turbulence which disrupted the previously undisturbed surface skin layer even after the initial wake disruption by the cable.

The increased disturbance due to the longer period waves generated more turbulence and consequently resulted in extended decay. From the energy cascade model put forth in Section 4.4, the energy flux, $\varepsilon_t \sim \left(u'^*\right)^3 \big/ \ell$, is constant down the cascade implying the mean flow input to the larger length and time scales should equal the viscous dissipation occurring at the Kolmogorov scale. For the case at hand, however, the flow was obviously not steady. Not only did the turbulence and vorticity generated advect and diffuse, but as Weigand and Gharib (1994) suggested the strong vortices aligned normal to the surface engulfed the smaller structures, thus reconcentrating the vorticity and prolonging its lifetime. Furthermore, Sarpkaya (1994) proposed that the merging characteristics of these dominant coherent structures produce a reverse energy cascade and eddy longevity. The turbulence and vorticity generated by the cable mutually interacted producing larger scales which persisted and continued to do so after the wire had left the patch. Together with the idea of a reverse energy cascade, the wake width itself may have been the best scale for the largest turbulent eddies produced at a free-surface.

The destruction of the skin layer phenomenon was how we measure these infrared signatures of warm wakes and deduce something about the free-surface turbulence and vortical interaction. More importantly, the time scale for the re-establishment of the skin layer related directly to the level of disruption. For the cases outlined in Section 5.3, we have observed the wakes under very low wind speeds (< 2 m/s) and always at night when the net upward heat flux of roughly - 80 to - 95 W/m^2 resulted in a cool skin layer. (The net heat flux is calculated formally in Section 5.6.) At low wind speeds, the shear turbulence transferred from the air to the ocean was very

low resulting in a thicker boundary layer or molecular sublayer. With the unstable nature of the "heavier" cool skin on top of "lighter" warm bulk water, the level of turbulence generated by the wake of the cable was enough to instigate the breakage of the skin layer. Coupling the effects of the free-surface on the vortical, turbulent flow with the nature of the skin layer developed under low wind speeds leads to a very long re-establishment time of the ruptured skin layer. Therefore, the turbulence generated in the wake of the cable was directly responsible for the re-establishment time of the skin layer, or the duration of the patch.

Discussion of a higher wind speed case provides a contrasting example to demonstrate this point. For higher wind speeds (between 5 - 10 m/s), the flow was initially more turbulent due to the enhanced shear stress transfer across the air-water interface. Although the boundary layer was now much thinner than at low wind speeds, the heat flux accelerated to between -125 and -135 W/m². The generation of turbulent energy in the wake of the wire disrupted the skin layer which recovered almost instantaneously. Playing a video of the scanner in fast-forward mode, we verified these wisps of wakes with a few examples of scanner image snapshots shown in Figure 5.23. (An obvious sign that the wind speed had increased was that the reflection of the boom had been spread out substantially by the increased surface roughness.) Table 5.3 lists the environmental conditions associated with these wispy wakes labeled as Case 3. The thin dark features in the upper left corner correspond to the wires with the small lighter features at the bottom of the wires being the wakes. These features lasted for less than a second verifying the very quick recovery time of the skin layer. In contrast to the low wind speed case, the initial conditions here suggested that the turbulence generated by the passage of the cable was small compared with what already existed near the air-sea interface under high wind speeds. Conversely, under low wind speeds the ratio of initial turbulence to that generated by the wake formation was great, resulting in the persisting duration of the wake and extended recovery time.
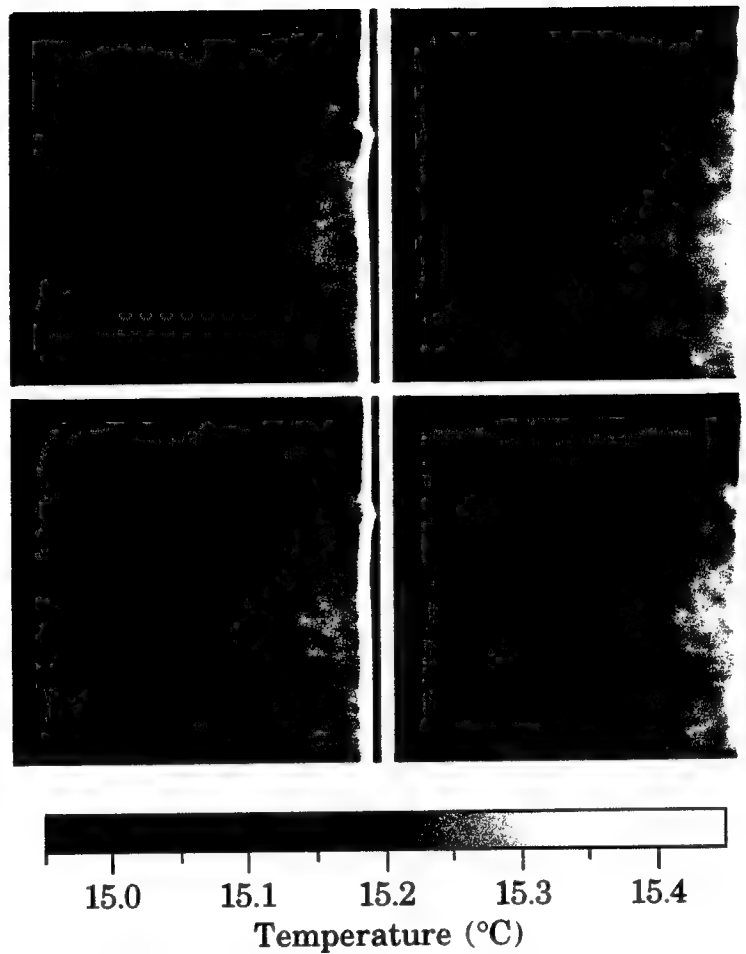
Figure 5.23 Snapshots of wispy wakes emanating from the surface-piercing cables. The dark vertical bands in the upper left corner are the cables while the faint white signatures at the bottom of the cables signify the wispy wakes. The wispy wakes last for less than a second.

See Plate in Appendix.

Table 5.3   Environmental conditions for Cases 3 and 4.

Case	3 - Wispy Wakes	4 - Puffy Patchiness
Date	January 28, 1992	January 26, 1992
Time	22:35 —> 23:34 PST	21:05 —> 22:05 PST
Wind Speed	7.3 ± 0.4 m/s	0.7 ± 0.3 m/s
Wind Direction	$34° \pm 2°$	$287° \pm 19°$ (40 min.) $126° \pm 35°$ (20 min.)
Drift Speed	21 cm/s $\pm$ 1 cm/s	17 cm/s $\pm$ 1 cm/s
Drift Direction	$175° \pm 10°$	$324° \pm 5°$
Compass Heading	$18° \pm 4°$	$300° \pm 22°$
Wave Direction	~ 270°	~ 280°
Air Temperature	14.6 °C $\pm$ 0.0 °C	Steadily Decreasing 14.6 °C to 14.4 °C
Relative Humidity	Steadily Decreasing 90.2 % to 88.1 %	88.5 % $\pm$ 0.7 %
T @ 0.1 cm	Steadily Increasing 14.67 °C to 14.79 °C	14.30 °C $\pm$ 0.01 °C
T @ 0.5 cm	14.67 °C to 14.80 °C	14.31 °C $\pm$ 0.01 °C
T @ 1.0 m	14.66 °C to 14.78 °C	14.30 °C $\pm$ 0.01 °C
T @ 2.0 m	14.67 °C to 14.80 °C	14.31 °C $\pm$ 0.01 °C
T @ 5.0 m	14.67 °C to 14.80 °C	14.27 °C $\pm$ 0.01 °C

Recovery times of the magnitude for the low wind speed case (on the order of minutes) have not been observed or reported before in the literature. However, the disruption in this case was provided artificially by a surface-piercing cable. As described in Section 2.6, Ewing and McAlister (1960) also disturbed the skin layer artificially by using a pump. When the pump was turned off, the cool skin layer re-established within 5 seconds. They also reported an inability to measure the effects from less substantial disturbances. Again, a possible threshold may exist below which the skin layer remains unbroken. Ewing and McAlister (1960) also made measurements of actual breaking waves which agree with those of the impinging jet upon the surface. Contrary to the pump demonstration, though, the recovery of the cool skin layer took roughly 12 seconds. Other field investigators (e.g., Clauss *et al.*, 1970; Schluessel *et al.*, 1990) concur that the cool skin layer does re-establish within roughly 10 to 12 seconds. From the present study, we observed that not only was the strength of the disruption an important variable in the skin layer recovery, but also the initial state of the skin layer itself.

Late on the evening of January 26th, the wind speed died down to an almost undetectable level (< 1 m/s) which allowed for the development of what appeared to be free convection. As mentioned in Section 5.3, some authors (e.g., Grassl, 1976) believed free convection could not exist on the open ocean because the current shear would always engender enough turbulence to establish the molecular sublayer by forced convection. The "puffy" patchiness seen in Figure 5.24 shows the possibility of free convection under extremely low wind speeds found during Case 4 of Table 5.3. The puffy features appeared comparable in size and ΔT to the wake signatures. However, these features existed throughout the image as a background for the wake signatures. In fact, the turbulent wake patches continued to form as they did earlier in Case 1. However, we now observed that the disturbance needed to break the skin layer had been reduced as the instability of the cool skin layer above the warmer bulk water was sufficient resulting in the free convective patches with an apparent temperature
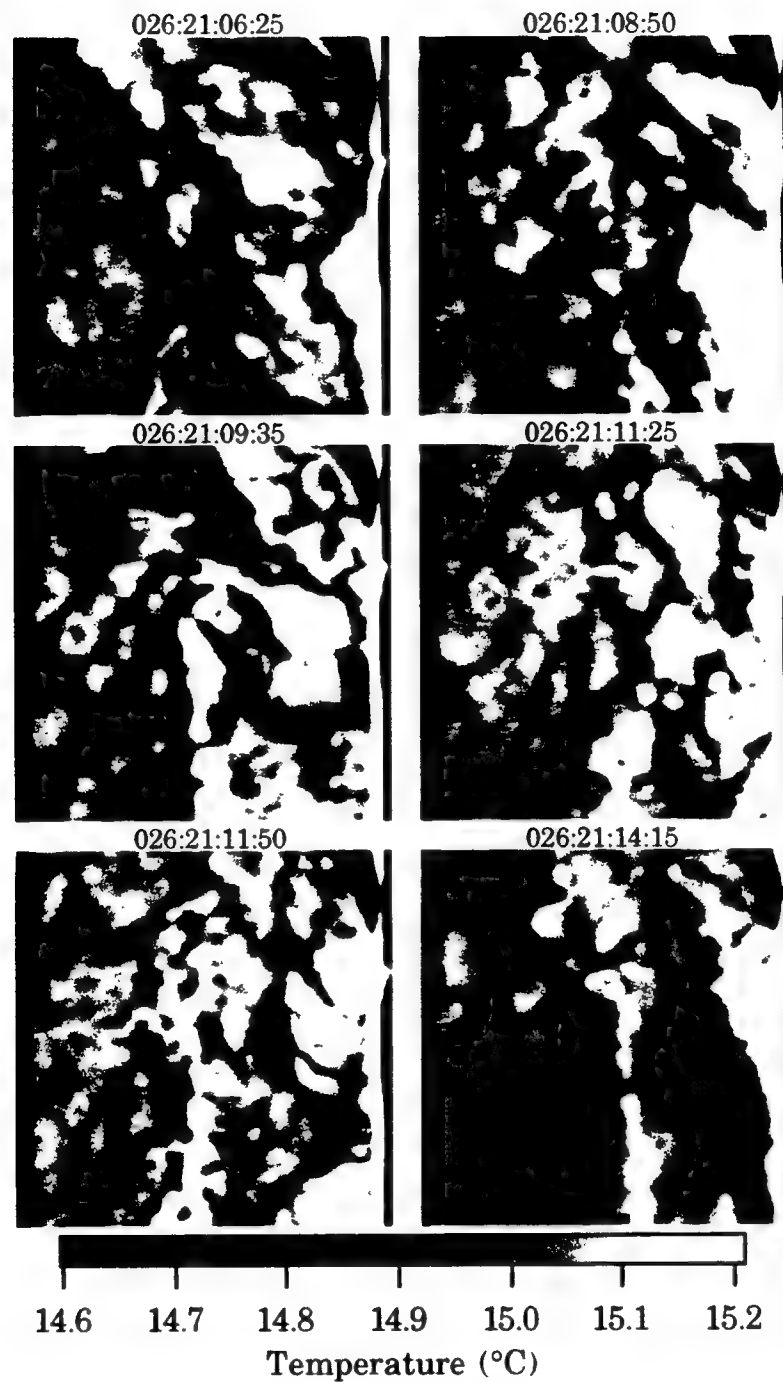
Figure 5.24 Puffy patchiness signifying the possibility of free convection under very low wind speed conditions (~ 0.7 m/s). Note the wire wakes continue to emanate from the cables. Environmental conditions shown in Table 5.3 under Case 4.

See Plate in Appendix.

difference ranging from 0.4 to 0.5 °C between the cool skin and the warmer bulk water mixed up from below. Verification of the temperature difference is provided in Section 5.6. From Cases 1, 3, and 4, we observed different turbulence thresholds at which the skin layer was destroyed. For the skin layer to recover, it must have overcome this threshold as the turbulence diminished enough for the skin layer to re-establish.

The recovery of the skin layer is a complicated process. The fact that the turbulent patch diminished in size as in Figure 5.16 for all wakes suggested that the skin layer fully recovered near the edges of the patch as it encroached toward the more turbulent center. The turbulence was weakest at the outskirts of the wake which allowed for the recovery, while the center of the patch remained disturbed. However, the turbulence which had continually enlarged the size of the patch was not enough to hinder the initiation of the skin layer recovery even at the center of the patch. Assuming the maximum ΔT_w was a measure of the cool skin ΔT, the skin layer was continually allowed to reach an equilibrium state as ΔT_w declined. The equilibrium state is defined as the point at which the skin layer has recovered to a thickness characterized by the level of turbulence in the water. According to the skin layer model,

$$\Delta T \sim -\frac{Q_{net}}{u_{*w}} \sim -\delta_v Q_{net} \tag{5.5}$$

the temperature difference across the skin layer supports the net heat flux. Since the net upward heat flux was constant in a global sense, the thickness of the molecular sublayer defined the temperature difference. The thickness of the molecular sublayer related directly to the turbulent intensity in the water. At each equilibrium state, the turbulence level at the interface diminished allowing the skin layer to become thicker and ΔT to increase ever closer to its initial value. The skin layer itself continually overcame successive turbulent "thresholds" as it recovered.

Liu and Businger (1975) explain how the layer can be randomly/intermittently destroyed resulting in the non-linear profiles

observed by investigators in the field and the laboratory (e.g., Khundzhua and Andreyev, 1974; Katsaros *et al.*, 1977). However, they did not suggest any rate of or time scale for the recovery of the skin layer. The results of our study suggest the direct relation between skin layer recovery rate and the level of turbulence or strength of disruption. At low Re_w, the peaks of ΔT_w and b occurred almost simultaneously resulting in the strong rates of recovery, $\partial(\Delta T_w)/\partial t$ and $\partial b/\partial t$, due to the low turbulent energy available.

The time at which the b maxima occurred increased with wave Reynolds number illustrating the leisurely continued spreading due to advection, diffusion, and the vortical/turbulent free-surface interaction process. At medium and high Re_w, the ΔT_w maximum preceded b_m leading to the very low $\partial(\Delta T_w)/\partial t$ as more turbulent energy was accessible to impede the skin layer's strong tendency to recover. Still, the turbulence at hand was not enough to suppress the genesis of recovery.

5.5 Calculation of the Skin Layer ΔT

The scanner provided an instantaneous measure of the temperature difference across the cool skin layer assuming the maximum ΔT_w occurred when the skin layer was completely destroyed. Conventionally, the skin layer temperature, T_{sst}, is found using Equation (3.32). To correct for reflection effects, the narrow field-of-view radiometers' temperature output needed to be converted to flux density for the range of 8 to 14 µm. Following from Equation (3.32), we considered the radiation balance

$$
\int_{8}^{14} M_{o\lambda}(\lambda, T_{IR})\partial\lambda = \int_{8}^{14} \varepsilon_{dw}(\lambda, \theta) M_{b\lambda}(\lambda, T_{sst})\partial\lambda \\
+ \int_{8}^{14} [1 - \varepsilon_{dw}(\lambda, \theta)] M_{r\lambda}(\lambda, T_{sky})\partial\lambda
$$

(5.6)

where T_{IR} is the temperature output from the PRT-5, T_{sst} is the actual sea surface temperature measured from the depths of 10 µm, T_{sky} is a measure of the sky temperature from the upward looking KT-19, and ε_{dw} is the

emissivity of water from Downing and Williams (1975). Even though the KT-19 instruments were shown to drift under intense heating, use of the upward-looking unit was appropriate for the correction of reflection. While the sky temperature varied by tens of degrees from clear to cloudy conditions, the drift of the KT-19 due to heating was only on the order of 0.1 °C. The temperature changes of the reflected source needed to cause a significant correction (~ 0.1 to 0.5 °C) were also on the order of tens of degrees. Therefore, the relative error of the KT-19 due to its drift was negligible for the sky reflection correction. In order to find T_{sst}, we initially evaluated the first term on the right-hand side of the equation as a function of temperature ranging from 275 to 300 °K and performed a 2nd order polynomial fit to the curve. For every timestep we evaluated the left-hand side and the second term on the right-hand side, grouped like terms and solved for the roots of a quadratic to arrive at the T_{sst}.

Before applying this algorithm to the data, we calibrated the PRT-5 to improve its accuracy. Two bucket calibration runs provided "bookends" for the measurement period. The so-called bucket calibration technique used a well-stirred bath produced by recirculating water from the bath through a tube with small holes creating jets of water skimming just below the surface and parallel to it. A thermistor measured the water temperature in the bath, T_{cal}, with the PRT-5 aimed at the surface. Assuming any skin layer was destroyed continuously, the PRT-5 measurement should have matched the T_{cal}. Correcting for the background sky reflection using the algorithm above, we found a value for the PRT-5. The difference between the corrected PRT-5 value, $T_{IR\text{-}c}$, and T_{cal} was the calibration constant, $C_{PRT\text{-}5}$, for the PRT-5. Therefore, $C_{PRT\text{-}5}$ was subtracted from all PRT-5 temperature readings before performing the sky correction algorithm. According to the calibration runs in Figures 5.25a and 5.25b on the evenings of January 26th and 29th, the average calibration constant $C_{PRT\text{-}5}$ was -0.12 °C ± 0.01 °C. The values for $C_{PRT\text{-}5}$ ranged from -0.10 °C to -0.15 °C. Therefore, we determined that the accuracy of the calibrated T_{sst} would be well within 0.1 °C.
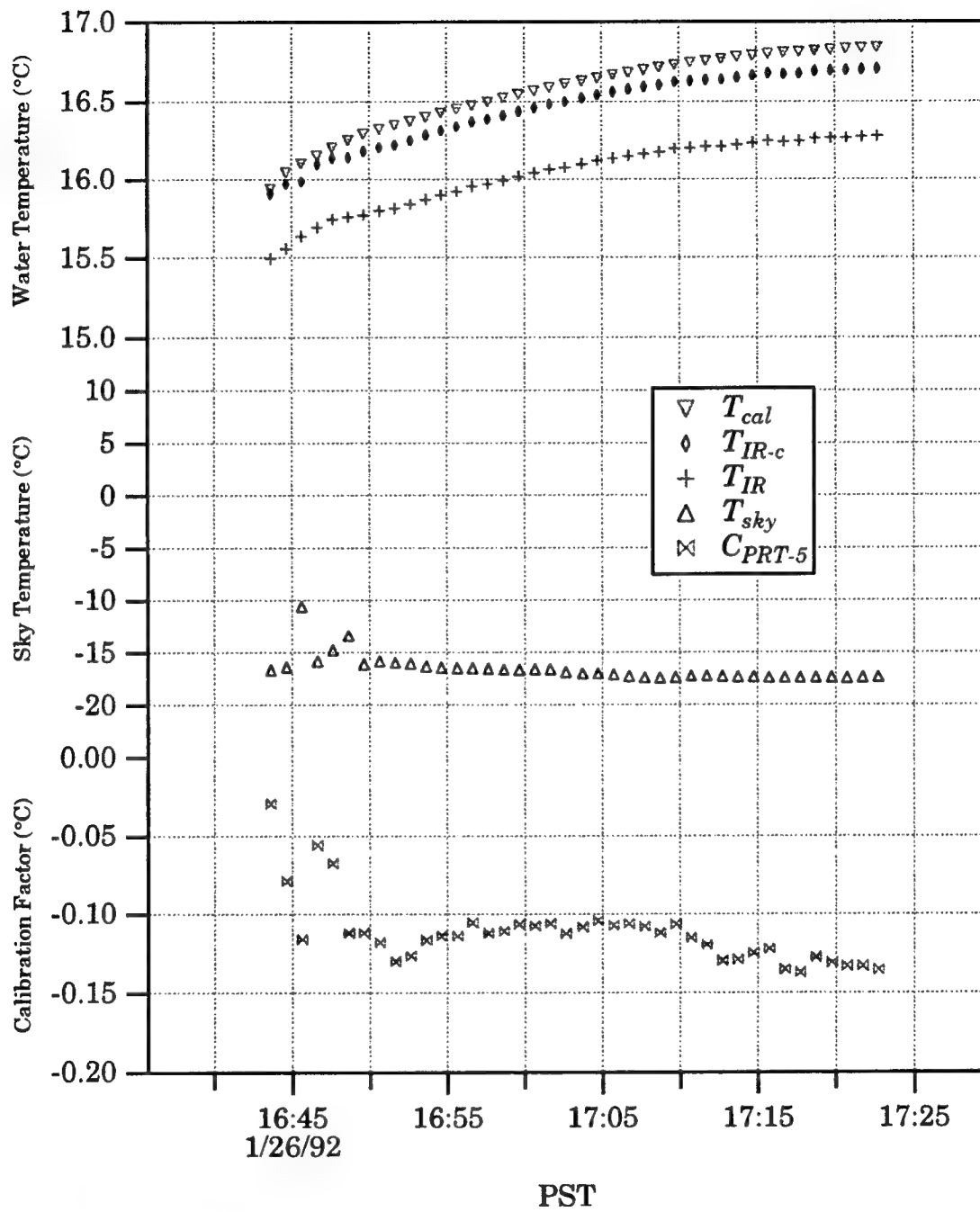
Figure 5.25a   Late afternoon calibration run for the PRT-5 on January 26, 1992.
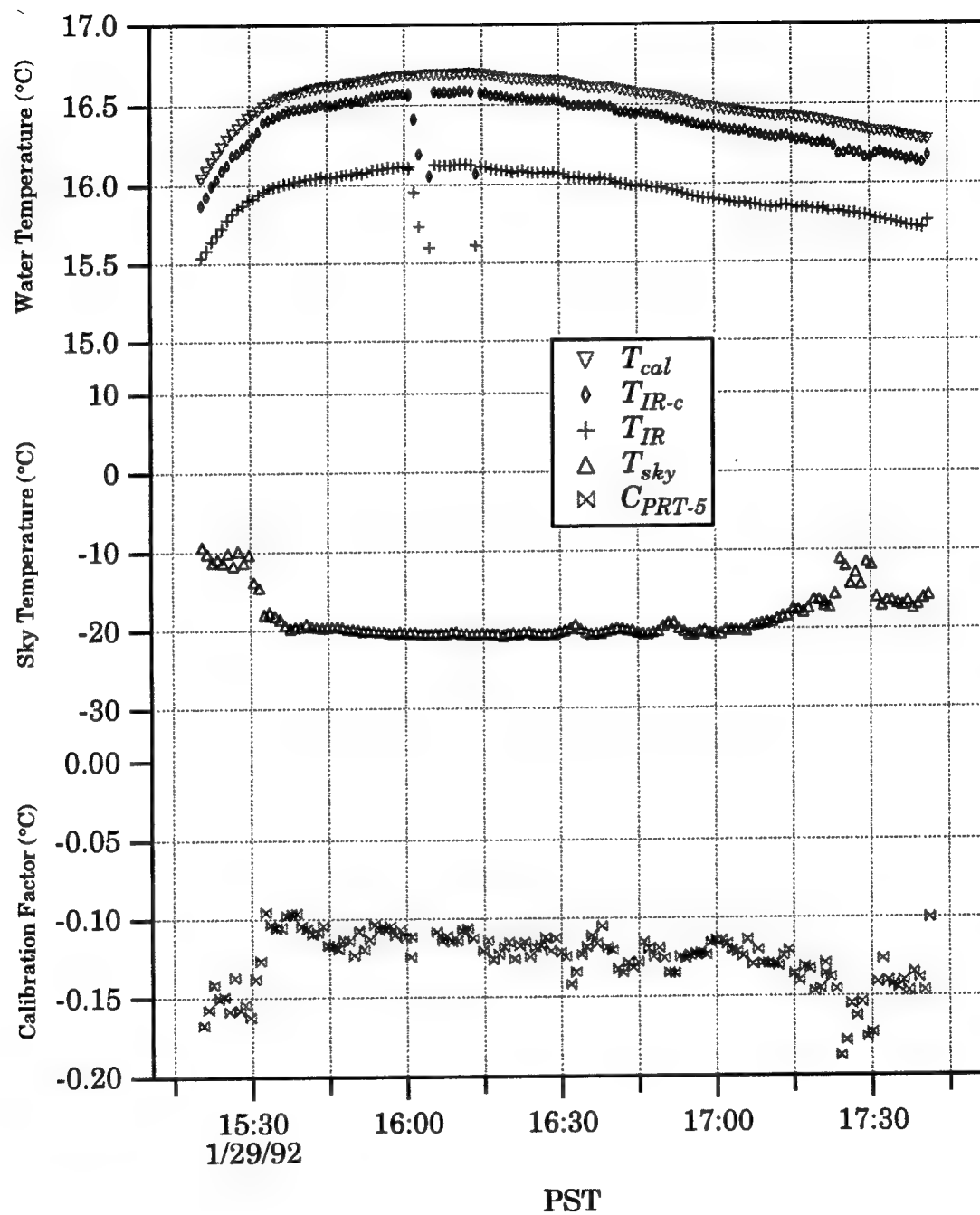
Figure 5.25b   Late afternoon calibration run for the PRT-5 on January 29, 1992.

Applying the calibration constant to the measured T_{IR} and correcting
for the sky reflection using the polynomial fit algorithm, one-minute
averages of the actual sea surface temperature, T_{sst}, along with T_{IR} and
T_{sky} are plotted in Figures 5.26a-d for January 25th through 28th. With a
clear sky (cold) the signal needed to be corrected more than for a cloudy sky
which was warmer. Under uniformly cloudy conditions, the sky was
roughly the same temperature as the sea surface and thus hardly any
correction was needed, since any deviation from blackness by the surface
was made up by the reflected sky radiation. From Figure 5.26, we see that
typically under clear skies the algorithm performed approximately a 0.4 to
0.5 °C correction for reflection. Under cloudy conditions the correction was
less, approaching the magnitude for C_{PRT-5} of 0.12 °C (calibration
constant's sign was negative). However, some slight errors might have
been induced by the procedure. The orientation of the up-looking KT-19 at a
zenith angle of 15° and the PRT-5 aimed at 15° incidence may have
produced one such inaccuracy primarily under partly cloudy conditions.
As the KT-19 received radiation from one part of the sky, the PRT-5
gathered reflected radiation from a slightly different part of the sky. The
distance between the parallel rays of radiation relative to the distance
traveled by the radiation depends upon the measurement height of the
instruments above the sea surface and the ceiling level of the sky. (The
ceiling level of the sky depends upon whether it is clear or cloudy and what
type of clouds exist.) At the edge of a cloud, one instrument may have
received radiation from the cloud and the other from the clear sky, thus
corrupting the correction. By using the measured value of the sky
irradiance from the KT-19, the effect of a cloud signal (warm) may have
forced an underestimated correction. Likewise, the measurement of an
apparently clear sky (cold) would tend to overestimate the correction.
Furthermore, as pointed out by Gasparovic *et al.* (1974) and Saunders
(1968), the surface roughness will diffuse the sky reflection out over an
extended area of the ocean. Nonetheless, the algorithm corrected for
reflection as expected considering these effects with possibly the only

Figure 5.26a   Time series for January 25, 1992 of the corrected and
calibrated IR SST, T_{sst}, along with the raw PRT-5
measurement, T_{IR}, and the radiometric sky
temperature, T_{sky}. Time series of thermistor
measurements at depth and ΔT's are included.

See Plate in Appendix.

Figure 5.26b   Time series for January 26, 1992 of the corrected and calibrated IR SST, T_{sst}, along with the raw PRT-5 measurement, T_{IR}, and the radiometric sky temperature, T_{sky}. Time series of thermistor measurements at depth and ΔT's are included. Large gap in the data of 6 hours corresponds to the time spent performing calibration runs and general maintenance.

See Plate in Appendix.

Figure 5.26c   Time series for January 27, 1992 of the corrected and calibrated IR SST, T_{sst}, along with the raw PRT-5 measurement, T_{IR}, and the radiometric sky temperature, T_{sky}. Time series of thermistor measurements at depth and ΔT's are included.

176

Figure 5.26d   Time series for January 28, 1992 of the corrected and calibrated IR SST, T_{sst}, along with the raw PRT-5 measurement, T_{IR}, and the radiometric sky temperature, T_{sky}. Time series of thermistor measurements at depth and ΔT's are included.

exception being the sharp changes in the measured sky temperature on January 27th and the early morning of January 28th.

The temperatures measured at different depths by the thermistor chain all provided a bulk temperature, T_b. According to our formulation for the bulk-skin temperature difference, $\Delta T = T_b - T_{sst}$, each bulk temperature at depth allowed for a different calculation of ΔT. The thermistor chain data along with the ΔT's calculated from these and the T_{sst} are also plotted in Figures 5.26a-d. At night when the temperature was usually uniform throughout the water column near the surface (< 5 m), any thermistor measurement provided a useful approximation for the bulk temperature leading to a valid ΔT. A notable exception to this occurred on the night of January 25th, when the temperature was only uniform with depth down to 1 meter. Note, the ΔT is a measure of the temperature difference across the skin layer which is usually less than a millimeter thick and always shallower than a few millimeters. However, during the day when solar irradiance was overbearing and volume absorption with depth occurred, the temperature profile within the first 5 meters varied significantly. Hence, the choice of measurement depth of bulk temperature from the thermistor chain was crucial since the ΔT changed considerably depending upon that choice.

5.6 Comparison of Calculated ΔT with Scanner Measurements: Results and Discussion

A comparison of the calculated ΔT with the maximum ΔT_w extracted from the scanner output of the wake patches was consistent. For Case 1, we have performed detailed time series of the wake signatures and determined the maximum ΔT_w's range from 0.4 °C to 0.5 °C as seen in Figure 5.19b. Similarly for Case 4, the free-convective patches produce ΔT's ranging from 0.4 to 0.5 °C. From the calculation of the temperature difference across the skin layer, we found ΔT to vary from 0.5 °C to 0.6 °C and remained constant over the 5 meter depth during these timespans shown in Figure 5.26b. One explanation of the 0.1 to 0.2 °C difference might

be that the skin layer was never completely broken by any disturbance as the net upward heat flux would have always generated some kind of recovery. For example, if the turbulent patch never totally disintegrated the skin layer, the maximum ΔT_w from the scanner underestimated the bulk-skin temperature difference. Likewise, if the jets did not fully disrupt the surface during the calibration run, the calibration would have underestimated C_{PRT-5}. The underestimation of the calibration constant may have resulted in the calculation of an overestimated ΔT. Regardless of whether or not the skin layer was completely destroyed, the combination of the experimentally determined error of the PRT-5 (0.1 °C), tape noise introduced during the digitizing of the scanner images, and the NET of the scanner ($\pm$ 0.05 °C) accounted for any discord between the measurements of ΔT and ΔT_w.

As mentioned in Section 2.5, the skin layer thins out considerably at higher wind speeds. The wispy wakes found in Case 3 provided a measure of the ΔT at these higher wind speeds. We estimated a ΔT_w of 0.1 °C with a nearly instantaneous recovery time. The disturbance from the cable was barely enough to disrupt the skin layer with the high level of turbulence already existing near the air-water interface. The calculated ΔT was uniform with depth and approximately equal to 0.2 °C as shown in Figure 5.26d. At these higher wind speeds, the skin layer re-established so quickly that the wakes probably did not provide an accurate measure of the magnitude of ΔT. During the same time period of Case 3, numerous breaking wave events appeared. Figure 5.27 represents a time series of one of these breaking events as a wave propagated from right to left in the image. The ΔT_w associated with the actively breaking crest was 0.3 to 0.4 °C, while the ΔT_w for the turbulent wake left behind was 0.15 to 0.20 °C. The turbulent wake, which was a much larger and stronger disturbance than the wispy wakes, likewise survived for less than 2 seconds indicating a very quick skin layer recovery rate. Jessup (1993) suggests that the ΔT_w for the actively breaking crest overestimates the skin layer temperature difference perhaps due to changes in the electromagnetic properties of the surface by increased surface roughness. However, the turbulent patch in the wake of
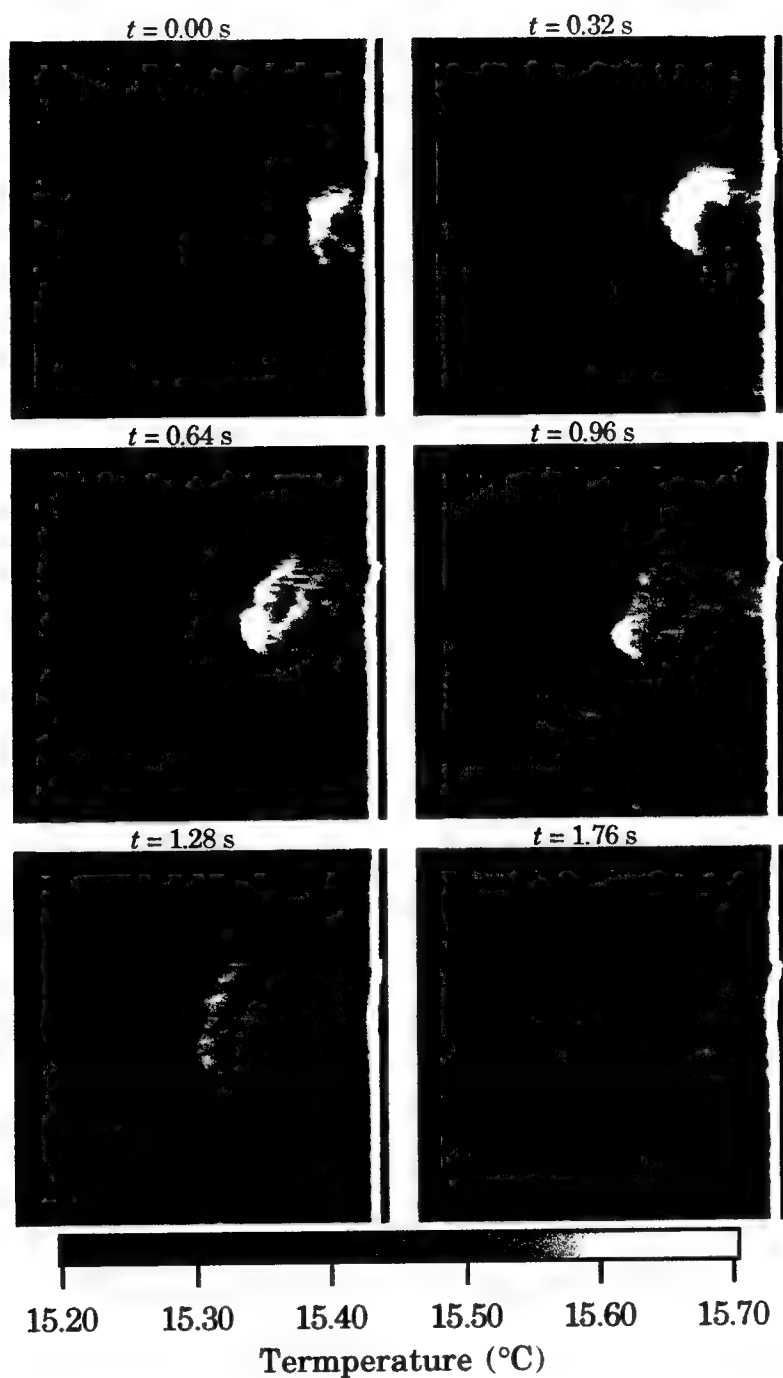
Figure 5.27 Nighttime sequence of the infrared signature of a breaking wave. The images show the apparent temperature change associated with the actively breaking crest and the turbulent wake. Environmental conditions shown in Table 5.3 under Case 3.

See Plate in Appendix.

the breaking wave produces a ΔT_w comparable to the calculated value for ΔT. The turbulence associated with the breaking process appeared to accomplish the total destruction of the skin layer. Nonetheless, the question remains as to whether the skin layer was destroyed completely by the crest, the turbulent patch, or both.

Assuming the electromagnetic properties of the actively breaking crest changed, most likely the reflectivity increased, more of the sky signal would have been reflected into the image. Not only would more of the sky be reflected, but also reflections from numerous zenith angles would have occurred. For this case, the sky was clear and thus colder than the sea surface, resulting in the underestimation of T_{sst}. Also, the actively breaking crest would have encapsulated or entrained air throughout the process. The air was warmer than the sea surface and thus would have increased the actual PRT-5 signal. Counteracting this was the overall accelerated heat flux (between -125 and -135 W/m^2) which tended to cool the surface. Combined with these effects, the bubbles associated with the actively breaking crest not only may have changed the electromagnetic properties of the surface but also altered the flux of heat across the air-sea interface. Bubbles, as an extremely thin surface, may have supported a weaker temperature gradient and therefore diminished the net upward heat flux. Furthermore, the wake of a breaking wave leaves behind an area of foam within the turbulent patch. The infrared characteristics of this foam have been known to appear cool as cited by Ewing and McAlister (1960). The appearance of cool foam, however, must depend upon the sky conditions. Quantifying the summation of these effects is beyond the scope of this discussion. Possibly, though, the turbulent wake left behind by the actively breaking crest did not totally destroy the skin layer.

Continuing our discussion of features and their effect on the ΔT, temperature fronts allowed us to check the response of the PRT-5 from the scanner image. At the tail end of Case 4, FLIP appeared to have crossed a temperature front as seen in Figure 5.28 where the imager was now pointed out perpendicular to the boom. (A monomolecular slick possibly

Figure 5.28 Nighttime sequence of infrared images depicting the FLIP crossing an apparent temperature front. The broad dark band across the image is a support cable for the instrument boom. The dark outline of the front possibly might be the aggregation of surfactant material and foam causing a change in the electromagnetic properties of the viewing area.
Environmental conditions shown in Table 5.3 under Case 4.

See Plate in Appendix.

could have changed the evaporation rate inhibiting the heat flux exiting the ocean and thus increasing the T_{sst}.) The change in temperature across the front was 0.34 °C from the scanner image. The T_{sst} from Figure 5.26b also followed the same trend warming up by 0.31 °C. The bulk temperatures remained relatively constant resulting in a decreased ΔT. Similarly on January 28th at noon, FLIP again crossed an apparent temperature front shown in Figure 5.29. Table 5.4 displays the environmental conditions related to this Case 5. Again, the scanner image showed a temperature difference across the front of 0.43 °C with the T_{sst} from Figure 5.26d warming up by 0.41 °C. As FLIP continued on farther into the "new" warm area, the imager was directed back parallel to the port boom and astonishingly cool wakes appeared in the scanner images of Figure 5.30. The ΔT_w was now -0.26 °C while the ΔT was -0.70 °C. This discrepancy may be related to the fact that ΔT was a direct measurement across a depth of 10 cm, while ΔT_w was a measure of the average temperature across the depth of mixing produced by the cable disturbance. Saunders (1967a) originally had suggested that the skin layer would remain cool no matter how intense the solar irradiance. Fedorov and Ginsburg (1992) concur that the heat flux at the interface will always be negative because the volume absorption of the ocean within the first few millimeters is less than 10 %. Evidently, the large-scale models appropriate for stable situations over longer periods of time need modification during the day, and possibly the nighttime, under conditions where spatial and temporal small-scale variability frequently exist.

One of the most interesting events observed during the FLIP experiment involved the rapid transition from a cool to warm skin layer which occurred on the morning of January 28th (designated as Case 6). The wakes from the wires remained warm during the mid-morning as shown in Figure 5.31a after a long night of ocean cooling. Suddenly, FLIP began to turn, aligning with the shifting wind direction. FLIP then crossed a surface temperature frontal feature which coincided directly with the change in wind direction from E to NNW. The wires appeared brighter suggesting the previously cloudy sky now had cleared and the sun was
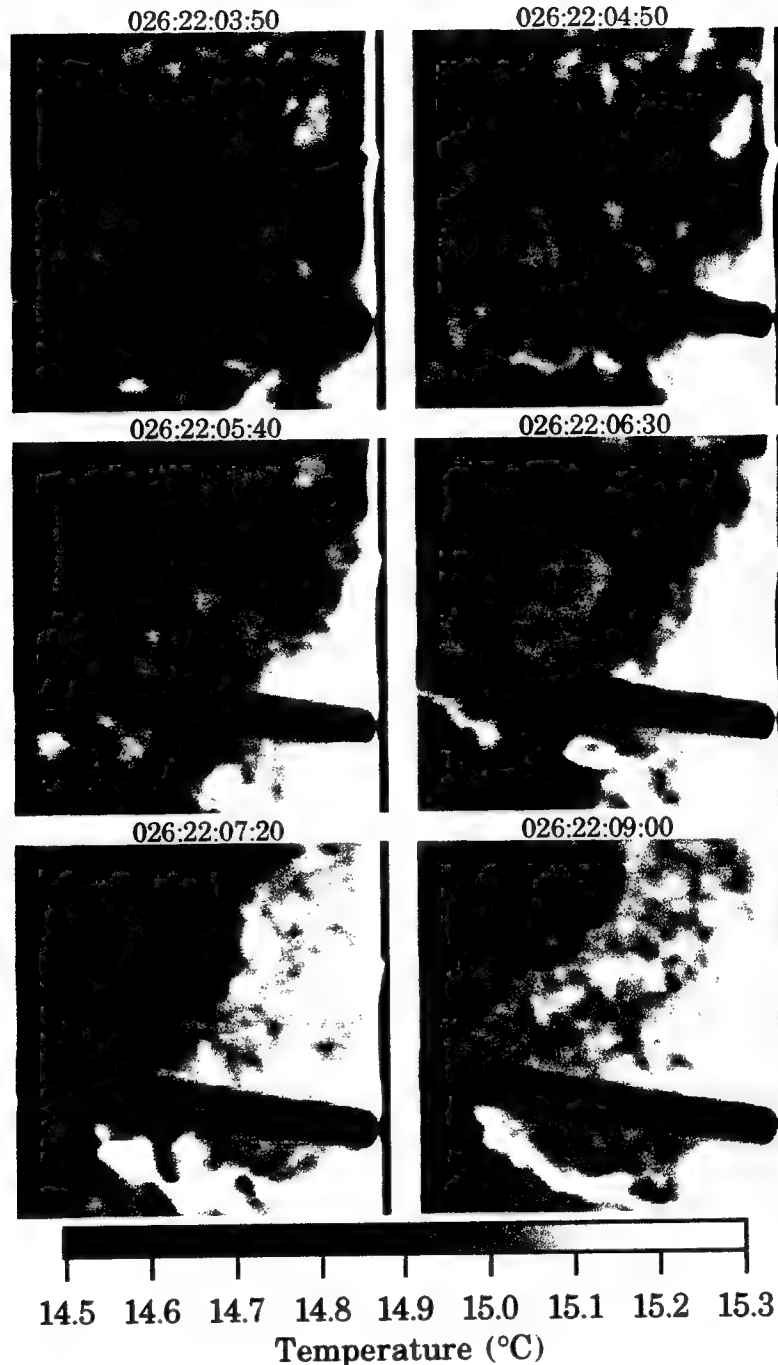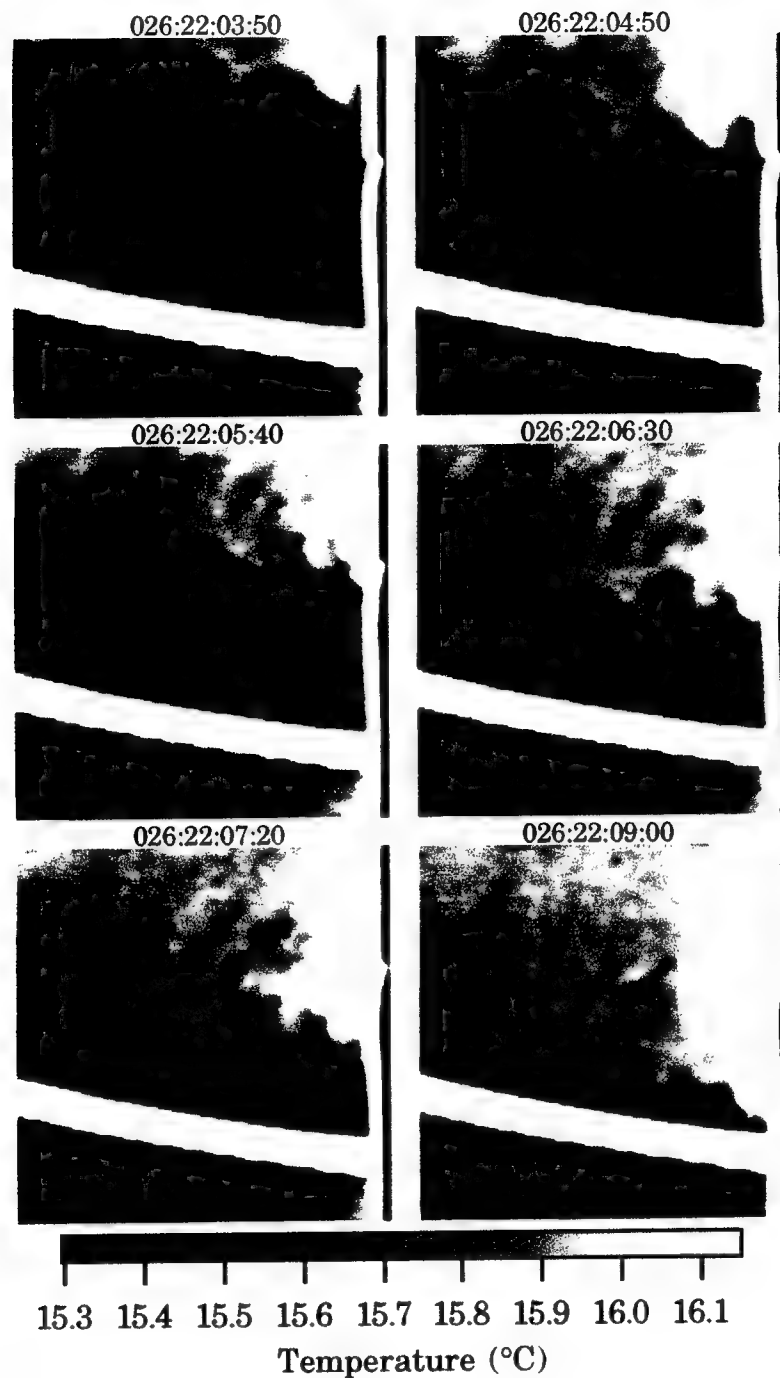
Figure 5.29 Midday sequence of infrared images depicting the FLIP crossing an apparent temperature front. The broad white band across the image is a support cable for the instrument boom. Environmental conditions shown in Table 5.4 under Case 5.

See Plate in Appendix.

Table 5.4   Environmental conditions for Cases 5 and 6.

Case	5 - Front/Cool Wakes	6 - Transition
Date	January 28, 1992	January 28, 1992
Time	11:55 —> 13:00 PST	10:15 —> 11:15 PST
Wind Speed	1.9 ± 0.3 m/s	0.9 ± 0.3 m/s
Wind Direction	334° ± 12°	94° ± 18° (40 min.) 334° ± 13° (20 min.)
Drift Speed	41 cm/s ± 4 cm/s	22 cm/s ± 2 cm/s
Drift Direction	164° ± 10°	156° ± 5°
Compass Heading	324° ± 15°	63° ± 10° (40 min.) 338° ± 17° (20 min.)
Wave Direction	~ 270°	~ 270°
Air Temperature	15.3 °C ± 0.1 °C	Steadily Increasing 15.0 °C to 15.2 °C
Relative Humidity	Steadily Decreasing 92.2 % to 89.2 %	92.6 % ± 0.2 %
T @ 0.1 cm	15.08 °C ± 0.16 °C	
T @ 0.5 cm	14.98 °C ± 0.07 °C	See Figure 5.32
T @ 1.0 m	14.85 °C ± 0.04 °C	
T @ 2.0 m	14.78 °C ± 0.01 °C	
T @ 5.0 m	14.71 °C ± 0.01 °C	
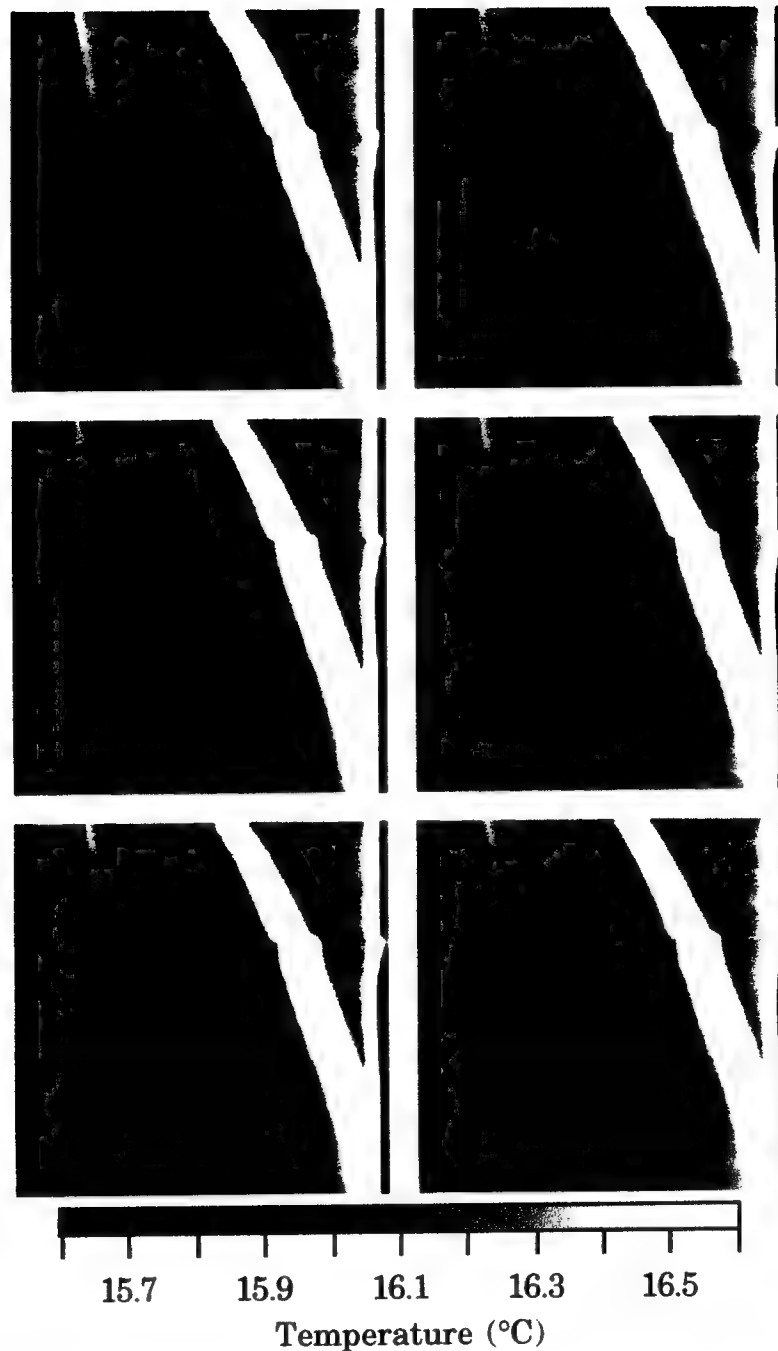
Figure 5.30 Cool wakes emanating from the surface-piercing cables
during Case 5 shown in Table 5.4. The images are spaced
roughly 10 to 20 seconds apart just prior to 12:05 PST. The
broad white band across the image is a support cable for the
instrument boom. The white lines in the upper left-hand
corner are the cables.

See Plate in Appendix.

028:10:12:30   **028:10:13:00**

028:10:13:10   **028:10:15:00**

028:10:46:35   **028:10:47:40**

15.1   15.3   15.5   15.7   15.9   16.1

Temperature (°C)

Figure 5.31a   Warm wakes emanating from the surface-piercing
cables during the late morning transition as discussed
in Case 6 of Table 5.4. FLIP begins to turn as suggested
by the change in direction of the wakes. Simultaneously,
the dark outline of the front appears.

See Plate in Appendix.
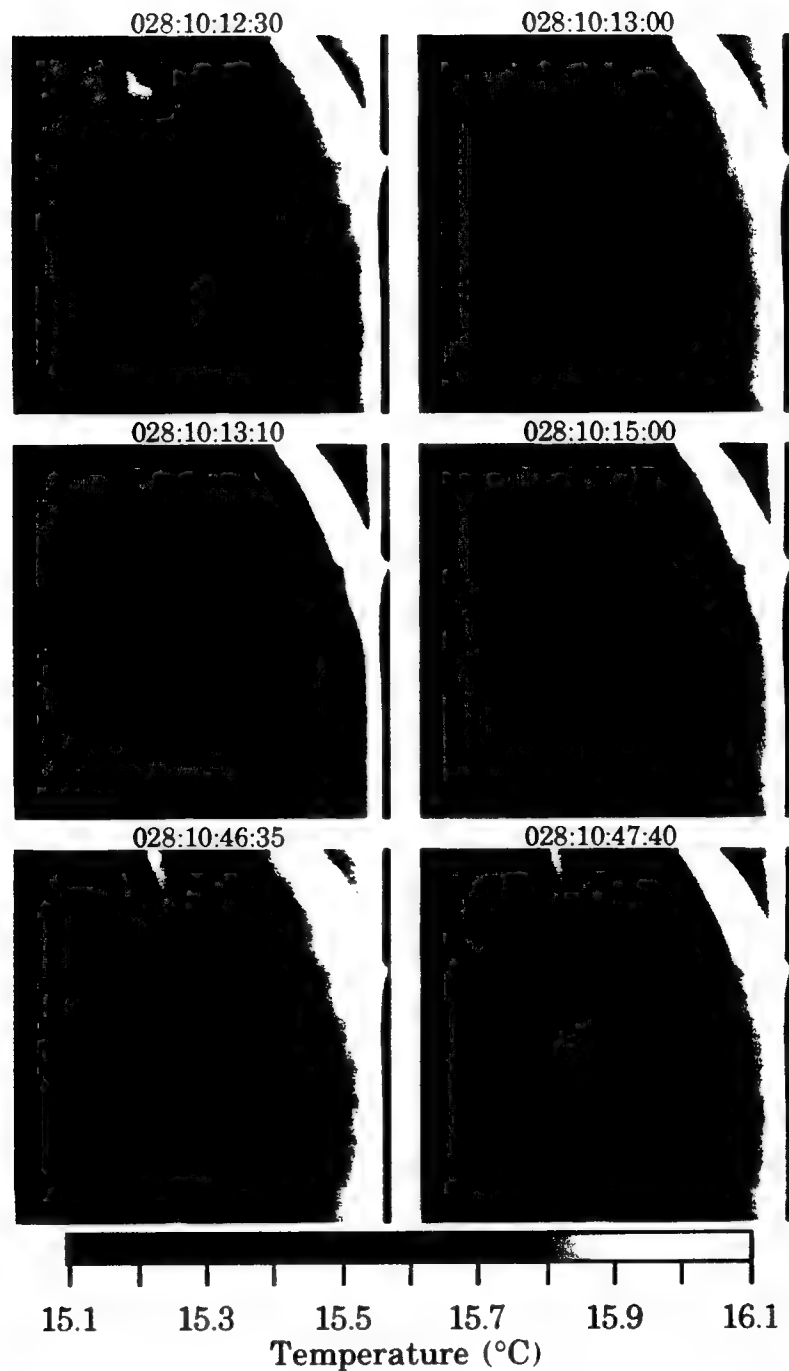
allowed to heat the wires and ocean. Initially the surface temperature appeared cooler corresponding to the change from a cloudy to a clear sky. However, the surface warmed up quickly. A few minutes later, the wakes emanating from the cables became cool as shown in Figure 5.31b. Table 5.4 displays the environmental conditions related to Case 6. Additionally, a time series of the temperature at constant depths in Figure 5.32 shows the effect of solar heating as the midday approached. The warm wakes with ΔT_w of 0.28 °C become cool wakes with ΔT_w of -0.25 °C in a matter of 15 minutes. However, throughout this time span the ΔT remained negative for all depths ranging from -0.88 °C to -0.09 °C which was found to be inconsistent with the occurrence of the transition. Why did we measure the transition in the scanner, but did not find the same behavior in the ΔT? As we discussed above, the temperature profile with depth during the day was strongly affected by the solar irradiance as evident from Figure 5.32. We have made measurements from the depths of 10 cm or greater where the water was cooler than at the surface resulting in negative ΔT's. At night, the temperature profile was basically uniform below the skin layer. Since the solar insolation was volume absorbed over a significant depth and time, however, the temperature profile from 10 cm up to the surface during the day coupled with the mixing depth (and volume) importance may have allowed for this transitional behavior. Again, the effect of a surfactant monolayer also may have assisted in the transitional process and bias the result as slicks may inhibit evaporation or possibly alter the electromagnetic properties of the surface. However, Garrett and Smith (1984) found that most environmental slicks do not inhibit evaporation.

5.7 Formulation and Calculation of the Net Heat Flux with Results

The discovery of the transition from the cool skin to a warm one necessitated discussion of the heat flux budget. In Chapter 2, we defined the heat flux budget as

$$Q_{net} = Q_{IR} + Q_G + Q_S + Q_H + Q_E. \tag{2.1}$$
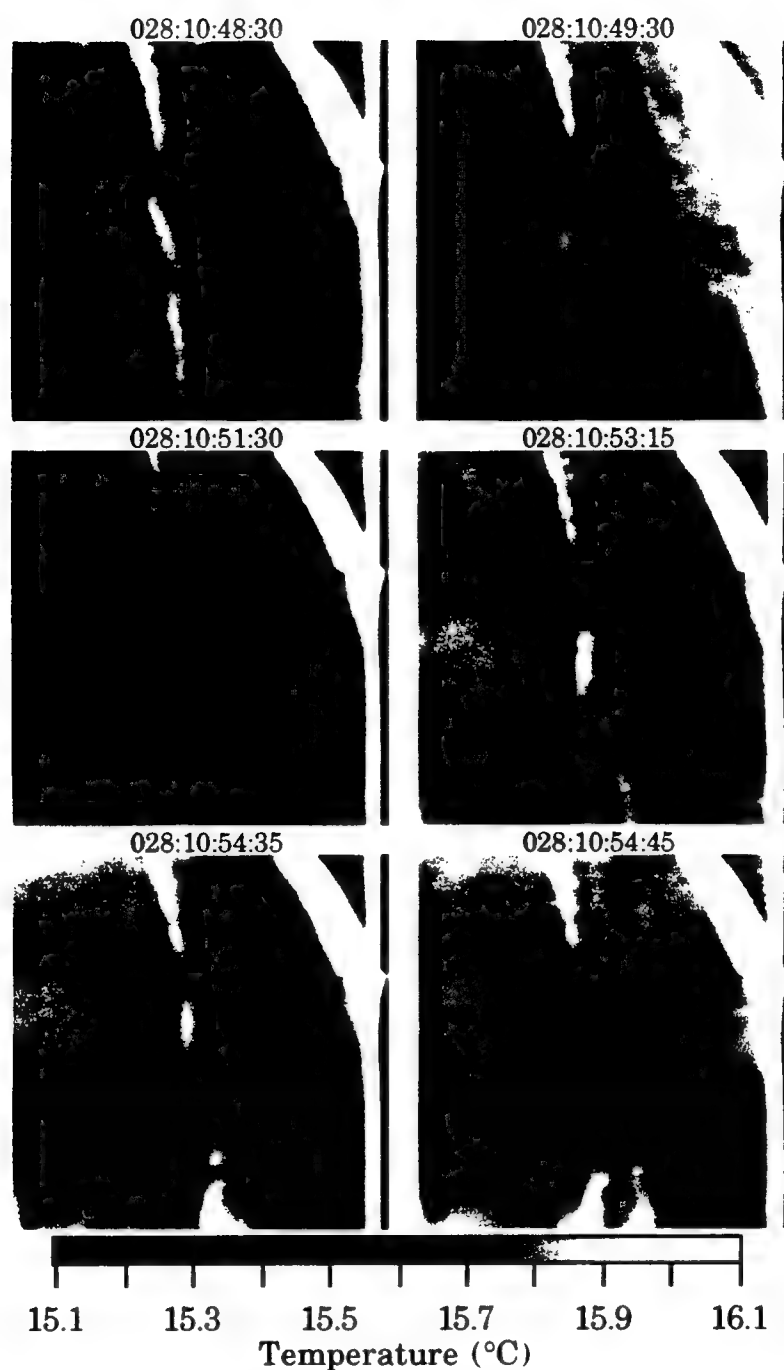
028:10:48:30   028:10:49:30

028:10:51:30   028:10:53:15

028:10:54:35   028:10:54:45

15.1   15.3   15.5   15.7   15.9   16.1

Temperature (°C)

Figure 5.31b   FLIP continues to turn, crossing an apparent temperature front. The wires appear brighter suggesting the previously cloudy sky is now clear and the sun is allowed to heat the wires and ocean. Initially the surface temperature appears cooler corresponding to the change from cloudy to clear sky. However, the surface warms up quickly. The final two images depict the cool wakes, thus completing the transition.

See Plate in Appendix.
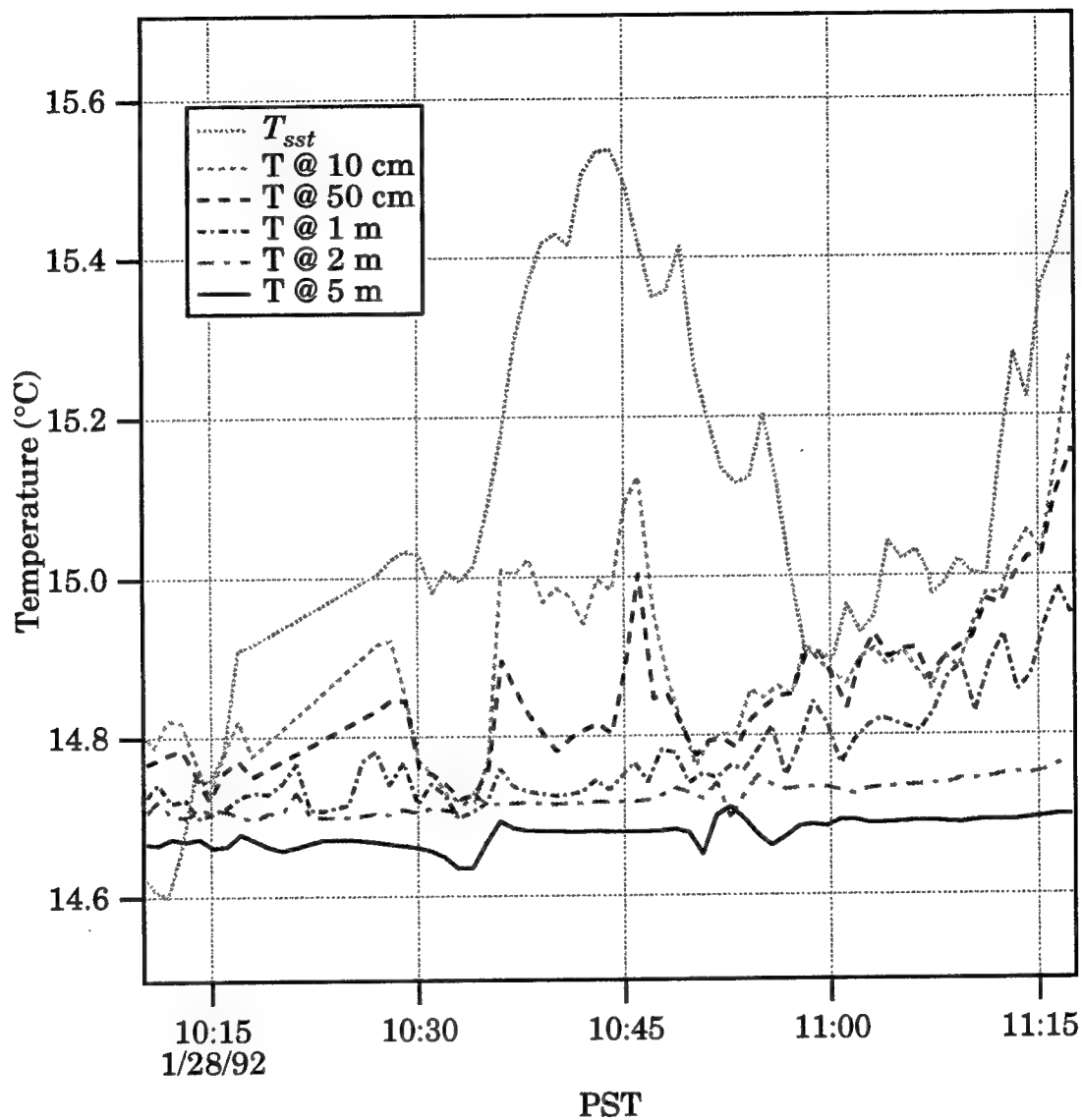
Figure 5.32 Blown-up time series of the third plot in Figure 5.26d depicting the effect of solar heating as midday approached during Case 6. The time series shows the bulk temperature measurements at constant depths along with T_{sst}.

More explicitly, the heat flux becomes

$$Q_{net} = -\varepsilon_{si}\sigma_b T_{sst}^4 + \varepsilon_{si}I_{LW} + [1 - a_s(\tau_{es})]I_{SW}$$
$$+ C_H \rho_a c_{pa}(T_a - T_{sst})U_{10} \tag{5.7}$$
$$+ C_E \rho_a L_e(q_a - q_s)U_{10}$$

with each term in (5.7) corresponding directly to the term in (2.1) where I_{LW} is the longwave irradiance measured by the pyrgeometer and I_{SW} is the shortwave irradiance measured by the pyranometer. For the longwave exitance, Q_{IR}, and longwave irradiance, Q_G, we needed to know the reflective properties of the ocean surface over a wide range of the electromagnetic spectrum. Downing and Williams (1975) have shown that the complex index of refraction varies notably in the region of 2 to 1000 μm. Consequently, the emissivity exceeds 99% at 10 to 12 μm but continues to decrease below 80% at much higher wavelengths (> 500 μm). The total emissivity of a body at a given temperature is given by the integral over all wavelengths of the product of the emissivity and Planck's law divided by the total blackbody radiation according to the Stefan-Boltzmann law resulting in

$$\varepsilon_{si} = \frac{\int_0^\infty \varepsilon_{dw}(\lambda)M_{b\lambda}(\lambda, T_{sst})d\lambda}{\sigma_b T_{sst}^4}. \tag{5.8}$$

The spectrally integrated emissivity, ε_{si}, is plotted as a function of temperature in Figure 5.33 for the range experienced on the ocean and used in the calculation of the infrared heat fluxes. Since the exiting radiation from the ocean peaks in the infrared, Stefan-Boltzmann's law defines the emittance while the measured downwelling radiation from the pyrgeometer, I_{LW}, defines the sky irradiance. The sum of these multiplied by the spectrally integrated emissivity results in the net longwave radiation.

$$\varepsilon_{si} = 0.879886 + 0.0004146 * T_{sst} - 4.7927 \times 10^{-7} * T_{sst}^{2}$$
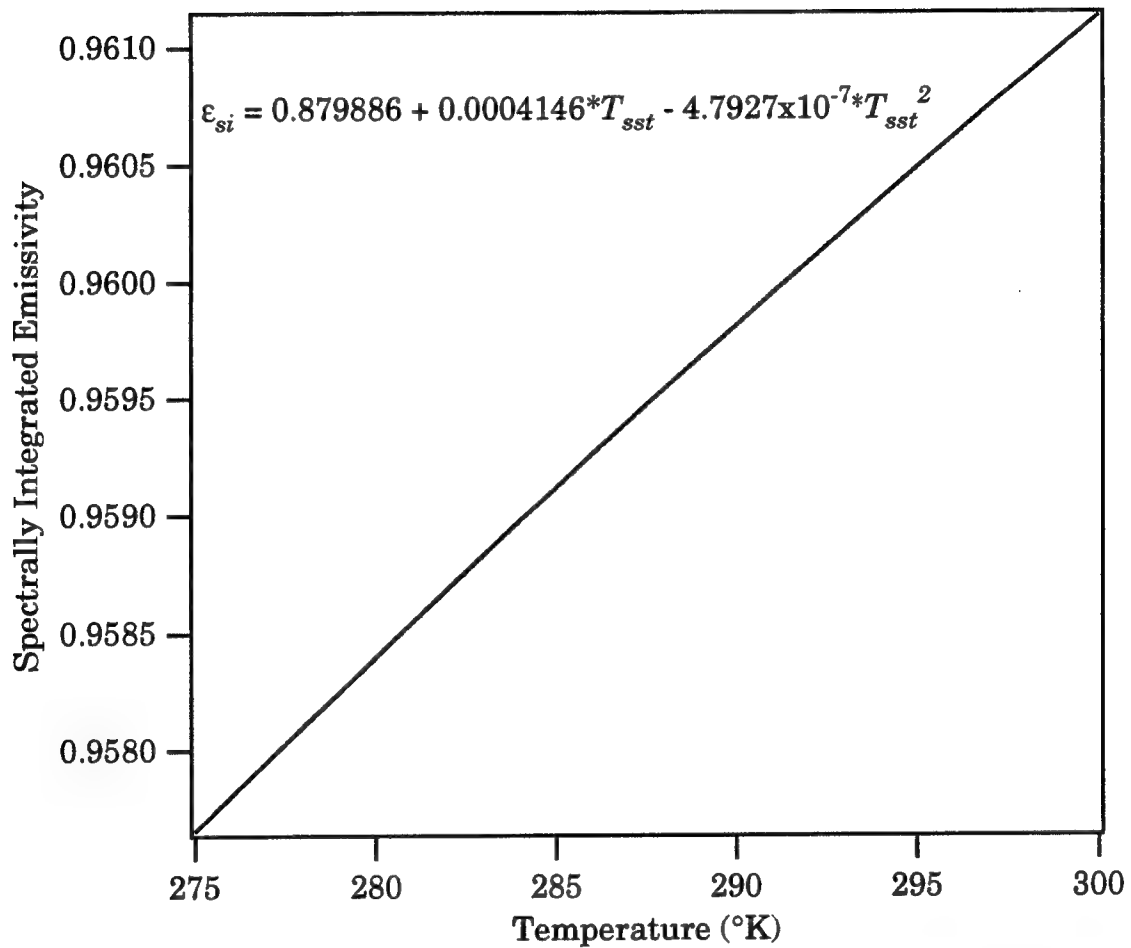
Figure 5.33 Spectrally integrated emissivity, ε_{si}, plotted from Equation (5.8) as a function of temperature for the typical range experienced on the ocean and used in the calculation of the infrared heat fluxes.

The net shortwave flux, Q_S, required a knowledge of the oceanic albedo, a_s. The ratio of the upwelling shortwave exitance to the shortwave irradiance defines the albedo of the sea surface. Payne (1972) directly measured the albedo from a research platform and related it to the transmittance, τ_{es}, of the atmosphere. The transmittance

$$\tau_{es} = \frac{I_{SW}}{I_{so}} \tag{5.9}$$

where I_{SW} is the solar insolation measured from the pyranometer and I_{so} is the solar radiation present at the top of the atmosphere simply calculated from a knowledge of time and location. The albedo was extracted from Payne's data using the transmittance and the elevation angle of the sun for a given local time of day. One minus the albedo times the pyranometer measured insolation results in the net solar flux, $[1 - a_s(\tau_{es})]I_{SW}$.

The sensible and latent heat fluxes, Q_H and Q_E, were derived from a model proposed by Liu *et al.* (1979). Applying the bulk formulations for the transfer constants according to Kondo (1975), Smith (1980), or Large and Pond (1981, 1982), we computed the turbulent fluxes. These fluxes along with the net solar and longwave fluxes displayed in Figures 5.34a-d for the same previous four days revealed the relative weakness of the latent and sensible fluxes. The downwelling sky radiation dictated the structure of the heat flux during the nighttime. Since Q_{net} controlled the temperature at the air-sea interface, the sky irradiance also significantly affected T_{sst}. For example, return to Figure 5.26d. In the early morning between 2 and 4 am, the up-looking KT-19 encountered radical changes in sky temperature from cloudy to clear and back to cloudy skies. Even after the correction of the PRT-5, though, T_{sst} continued to follow the structure of the sky. Therefore, cloudy or clear skies actually affect the surface temperature by altering the heat budget. The sky not only produced apparent changes due to deviations from unity of the sea surface emissivity, but also increased or decreased T_{sst} directly.

Figure 5.34a   Flux densities for January 25, 1992. The top plot shows
the latent, Q_E, and sensible, Q_H, fluxes. The middle plot
shows the solar, Q_S, and net longwave, $Q_G + Q_{IR}$, fluxes.
Finally, the bottom plot shows the total net heat flux,
Q_{net}, as a function of depth.
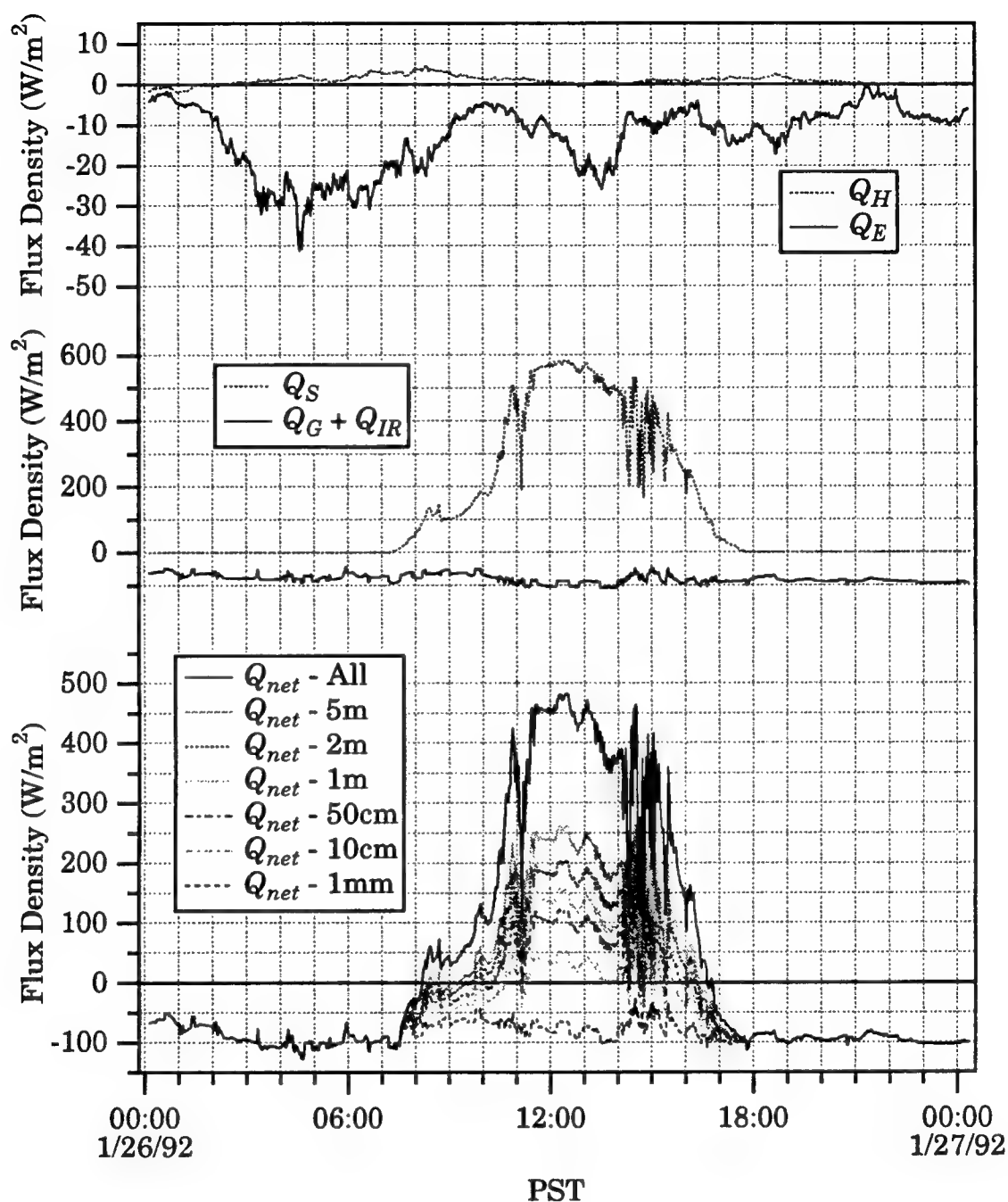
Figure 5.34b   Flux densities for January 26, 1992. The top plot shows the latent, Q_E, and sensible, Q_H, fluxes. The middle plot shows the solar, Q_S, and net longwave, $Q_G + Q_{IR}$, fluxes. Finally, the bottom plot shows the total net heat flux, Q_{net}, as a function of depth.
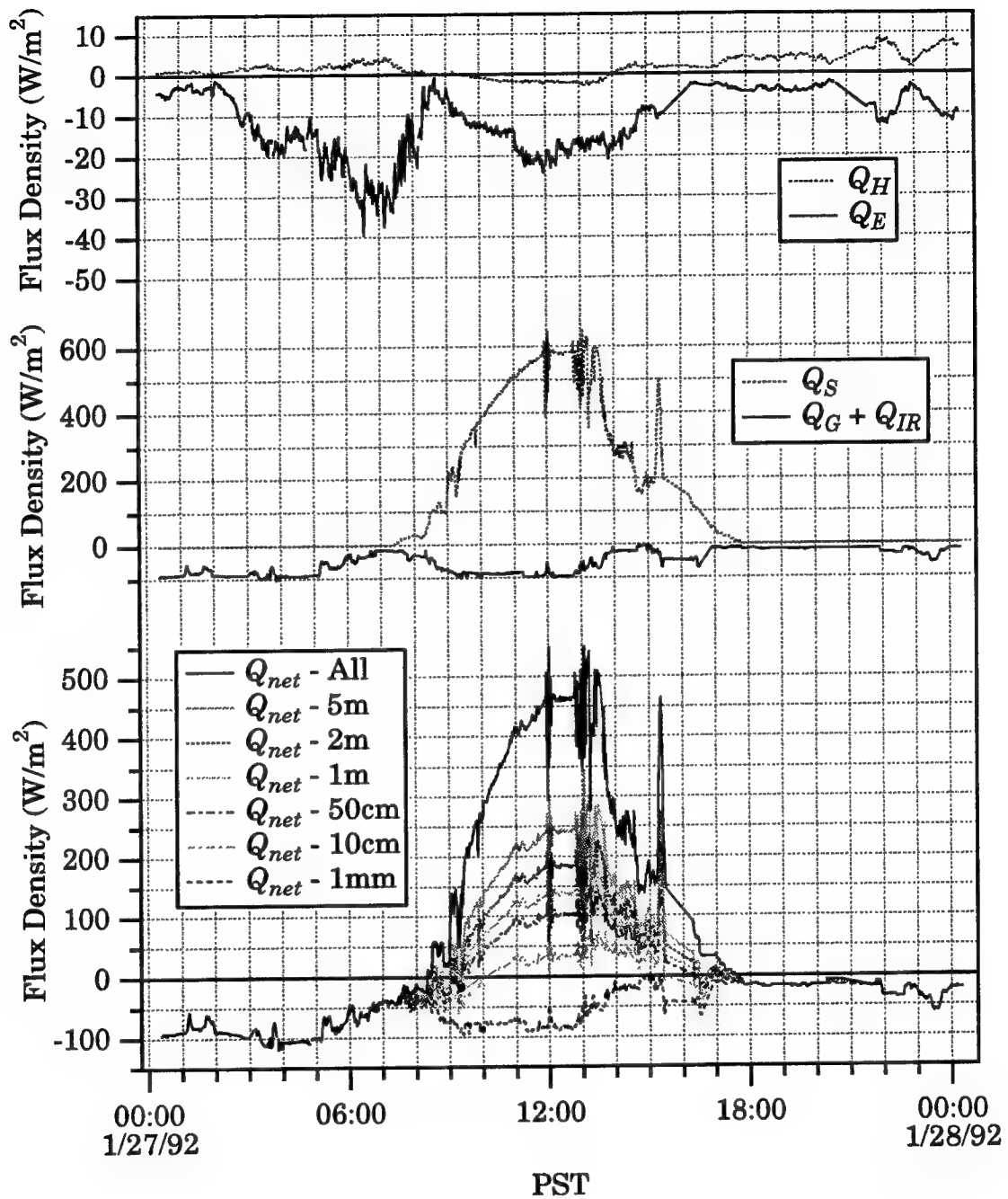
Figure 5.34c   Flux densities for January 27, 1992. The top plot shows the latent, Q_E, and sensible, Q_H, fluxes. The middle plot shows the solar, Q_S, and net longwave, $Q_G + Q_{IR}$, fluxes. Finally, the bottom plot shows the total net heat flux, Q_{net}, as a function of depth.
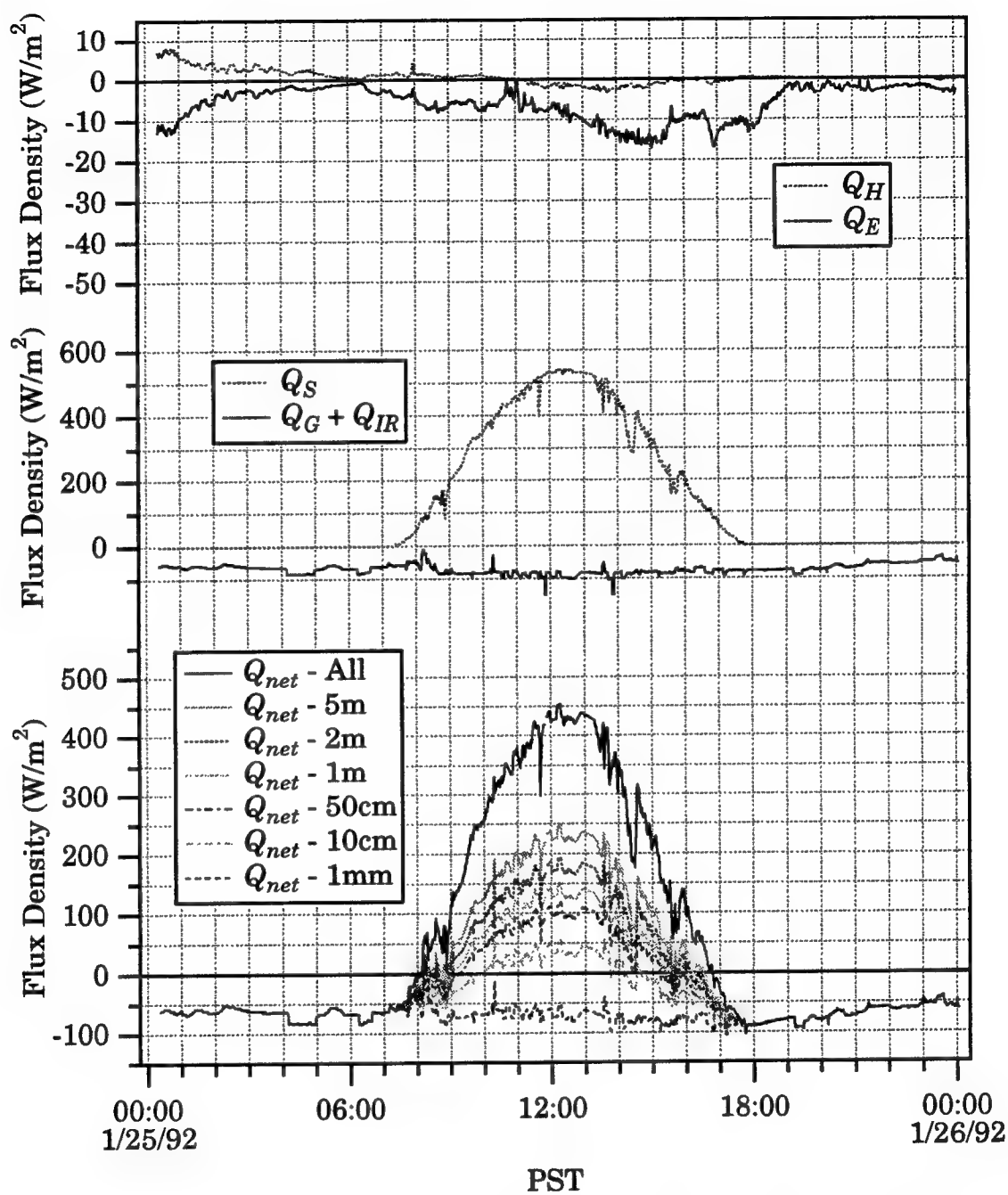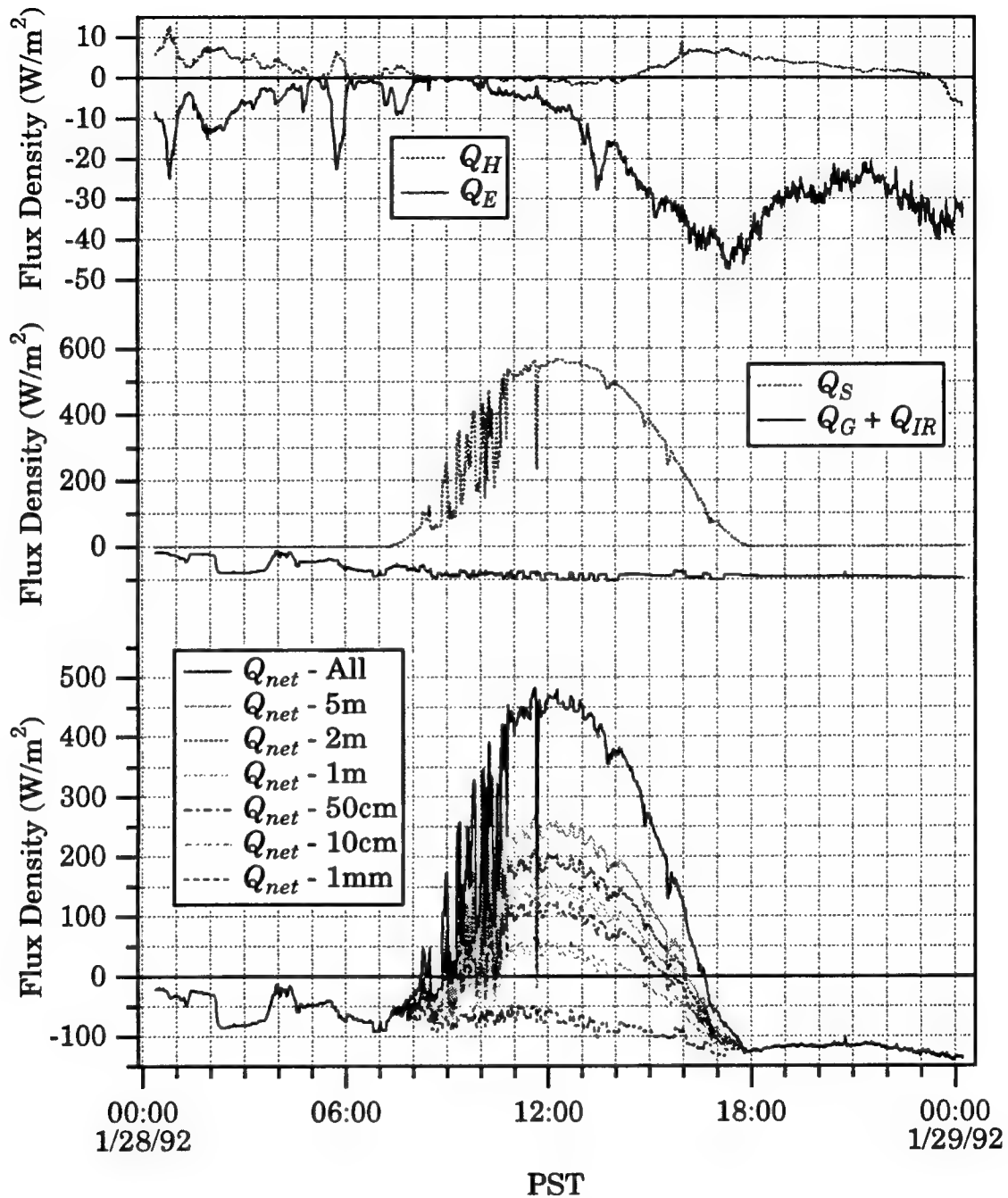
Figure 5.34d — Flux densities for January 28, 1992. The top plot shows the latent, Q_E, and sensible, Q_H, fluxes. The middle plot shows the solar, Q_S, and net longwave, $Q_G + Q_{IR}$, fluxes. Finally, the bottom plot shows the total net heat flux, Q_{net}, as a function of depth.

During the daytime the solar insolation dominated the radiation balance. At the bottom of Figure 5.34, the plot shows the total net heat flux. However, as Hasse (1971) and Fedorov and Ginsburg (1992) more recently point out, the solar insolation is absorbed over the depth of the surface layer. Fedorov and Ginsburg (1992) give updated measurements for the integral absorption of different layers near the surface used in the following analysis. Including these measurements into the net heat flux parameterization, Figure 5.34 shows the Q_{net} across surface layers of different depths according to the corrected term for solar radiation. Notice that the heat flux should not become positive right at the surface across the cool skin layer which is most often a millimeter thick. However, as the depth increased we find the heat flux became positive very quickly during the intense midday solar heating.

5.8 Models of ΔT from Q_{net} and Comparisons with Measured ΔT

Many previous investigators have proposed models of ΔT from a knowledge of the net heat flux. Saunders' (1967a) model of (2.14) is one of the major descriptions of the physics at the air-sea interface. Actually, considerable effort has been expended to determine the constant λ_o within his model. Fedorov and Ginsburg (1992) have compiled the results from field experimental data and estimate λ_o as a function of wind speed

$$\begin{aligned} \lambda_o &= 2+(5/7)U_{10} \quad for \ \ U_{10}<7 \ \ m/s \\ \lambda_o &= 7 \quad for \ \ 7<U_{10}<12 \ \ m/s \end{aligned} \tag{5.10}$$

Therefore, our presentation of Saunders' model is

$$\Delta T_s = -\lambda_o \frac{v Q_{net}}{k u_{*w}} \tag{5.11}$$

using Fedorov and Ginsburg's (1992) estimate for λ_o. Since the wind speed never exceeded 12 m/s during the time frame of the experimental data presented here, this parameterization was valid. Saunders assumed that during the day the net heat flux should account for the solar radiation absorbed within the thermal boundary layer at the interface. Hence, Q_{net} accounted for the amount of solar insolation absorbed within the first millimeter of water.

Fedorov and Ginsburg (1992) provided an alternative formulation including free convection. Following from (2.17)

$$\Delta T_{fg} = -2.83 \left(g C_{te} \rho_w k^2 / v \right)^{-\frac{1}{4}} Q_{net}^{\frac{3}{4}} \tag{5.12}$$

for $A = 0.25$ and $U_{10} < 5.5$ m/s, while

$$\Delta T_{fg} = -6.5 \frac{v Q_{net}}{k u_{*w}} \tag{5.13}$$

for $U_{10} > 5.5$ m/s. Likewise, Fedorov and Ginsburg also consider the solar irradiance absorbed within the molecular sublayer.

Both the Saunders (1967a) model and the Fedorov and Ginsburg (1992) scheme relate the theoretical temperature difference across the skin layer. Hasse (1971) devised a model to account for the difference in temperature between the measurement depth and the bottom of the skin layer. Considering both the molecular and turbulent diffusivities, α_m and α_t, across their respective depths, the temperature difference between the surface and the measurement depth, ΔT_{hd}, is

$$\Delta T_{hd} = -\frac{Q_{net}}{\rho c_p} \left\{ \int_0^\delta \frac{1}{\alpha_m} dz + \int_\delta^z \frac{1}{\alpha_t} dz \right\}. \tag{5.14}$$

Hasse realized the inverted wind speed dependence upon the viscous sublayer thickness, which defines the transition between the 2 layers. For

the molecular layer, the ΔT_{hd} is strictly a function of Q_{net}/U_{10}. However, the turbulent thermal diffusivity is both a function of wind speed and depth which forces ΔT_{hd} to be a function of $(Q_{net}/U_{10}) \bullet f\{z, \delta(U_{10})\}$ for the turbulent layer. When integrated over various depths, the two-layer model reduces to

$$\Delta T_{hd} = -C_1 \frac{Q_{IR} + Q_G + Q_H + Q_E}{U_{10}} - C_2 \frac{Q_S}{U_{10}} \qquad (5.15)$$

where C_1 and C_2 listed in Table 5.5 denote the coefficients which vary with depth and would be exact for 4 m/s winds. All the fluxes used by Hasse (1971) in his calculations of these coefficients have units of Langleys per minute (ly/min = 697.33 W/m²).

More recently, Schluessel *et al.* (1990) attempted to parameterize the bulk-skin temperature difference directly using

$$\Delta T_{sc} = j_0 + j_1 U_{10}(T_{sst} - T_a) \\ + j_2(q_s - q_a) + j_3(Q_{IR} + Q_G) \qquad (5.16)$$

during the nighttime and

$$\Delta T_{sc} = f_0 + f_1(Q_s/U_{10}) + f_2(q_s - q_a) \\ + f_3(Q_{IR} + Q_G) \qquad (5.17)$$

during the day where j_i and f_i for $i = 0$ to 3 listed in Table 5.6 constitute the optimized constants. Here, no consideration of solar absorption over depth is applied and the total net solar flux is used. Schluessel *et al.*'s (1990) parameterization, ΔT_{sc}, hardly ever correctly predicted the observed ΔT using the data presented here. For the present dataset, the sensible and latent fluxes were extremely low as seen in Figure 5.34 which was due to the small air-sea temperature difference and the high relative humidity throughout the experiment. However, during Schluessel *et al.*'s experiment near the North African coast in the Atlantic, the latent flux

Table 5.5   Constants for Hasse's model (from Hasse, 1971). * value
             obtained from fitted data.

Depth (m)	0.1	0.25	0.5	1.0	2.0	2.5	5.0	10.0
C_1	9.3*	9.4	9.6	9.9	10.2*	10.3	10.5	10.7
C_2	1.54*	1.61	1.75	1.90	2.09*	2.14	2.32	2.52

Table 5.6   Optimized coefficients for Schluessel *et al.*'s model (from
             Schluessel *et al.*, 1990).

Index	1	2	3	4
j_i	-0.285 °K	0.0115 s/m	37.255 °K	-0.00212 °K-m²/W
f_i	-0.415 °K	-0.00337 °K-m³/W-s	48.043 °K	-0.00355 °K-m²/W

often exceeded the negative net longwave flux unlike our data. This difference in latent heat flux alone resulted in the incorrect prediction of the actual ΔT. Therefore, the parameterization using their suggested optimized coefficients did not predict our data at all during the night. Furthermore, the optimized coefficients found during their study referenced the 2 m bulk temperature only. Any thermal stratification existing at any time would corrupt the comparison. Notwithstanding, sometimes during the day ΔT_{sc} approximated the measured ΔT's from deeper depths. At two meters, the solar absorption is nearly 50 %. Using the total net solar flux compensated for the fact our latent flux was much lower than that found by Schluessel et $al.$ (1990). Hence, the relatively close ΔT comparison during select parts of certain days was most likely coincidental.

For the FLIP data, the longwave flux dominated the Q_{net} and therefore ΔT. All of the present models, excluding Schluessel et $al.$'s (1990) parameterization, are displayed in Figures 5.35a-d corresponding to the same days previously discussed along with the measured ΔT. For each day, the plots show the comparison of the models (only 10 cm depth presented for Hasse's model) with the calculated ΔT using the temperature acquired from the 10 cm measurement depth. Accompanying each of these graphs is the wind speed and the net heat flux across a layer 1 mm, 10 cm, and 1 m thick. The graphs appear very disorganized at first glance, but many overall trends existed for the data. These three models generally followed the trends of the measured ΔT very well, especially at night when the temperature profile in the top 1 to 2 meters was relatively uniform. Also, the models performed much better at higher wind speeds (e.g., the night of January 28th) as opposed to the low wind speed cases scattered throughout the experiment. The Saunders (1967a) and Hasse (1971) models diverged sharply from the measured values when wind speeds drop below 1 or 2 m/s. The Fedorov and Ginsburg (1992) model, however, did not as it accounted for free convection which could have occurred at low wind speeds. Even so, their model assumed that free convection drove the heat flux up to higher wind speeds (< 5.5 m/s). Many times the Fedorov and

Figure 5.35a   Comparison of the ΔT models for January 25, 1992. The Q_{net} is plotted on the top of the graph with the wind speed in the middle. The bottom plot shows Saunders' model, ΔT_s, Fedorov and Ginsburg's model, ΔT_{fg}, and Hasses's model at 10 cm, ΔT_{hd}, all compared to the measured ΔT across the top 10 cm.

See Plate in Appendix.

Figure 5.35b   Comparison of the ΔT models for January 26, 1992. The Q_{net} is plotted on the top of the graph with the wind speed in the middle. The bottom plot shows Saunders' model, ΔT_s, Fedorov and Ginsburg's model, ΔT_{fg}, and Hasses's model at 10 cm, ΔT_{hd}, all compared to the measured ΔT across the top 10 cm.

See Plate in Appendix.

Figure 5.35c   Comparison of the ΔT models for January 27, 1992. The Q_{net} is plotted on the top of the graph with the wind speed in the middle. The bottom plot shows Saunders' model, ΔT_s, Fedorov and Ginsburg's model, ΔT_{fg}, and Hasses's model at 10 cm, ΔT_{hd}, all compared to the measured ΔT across the top 10 cm.
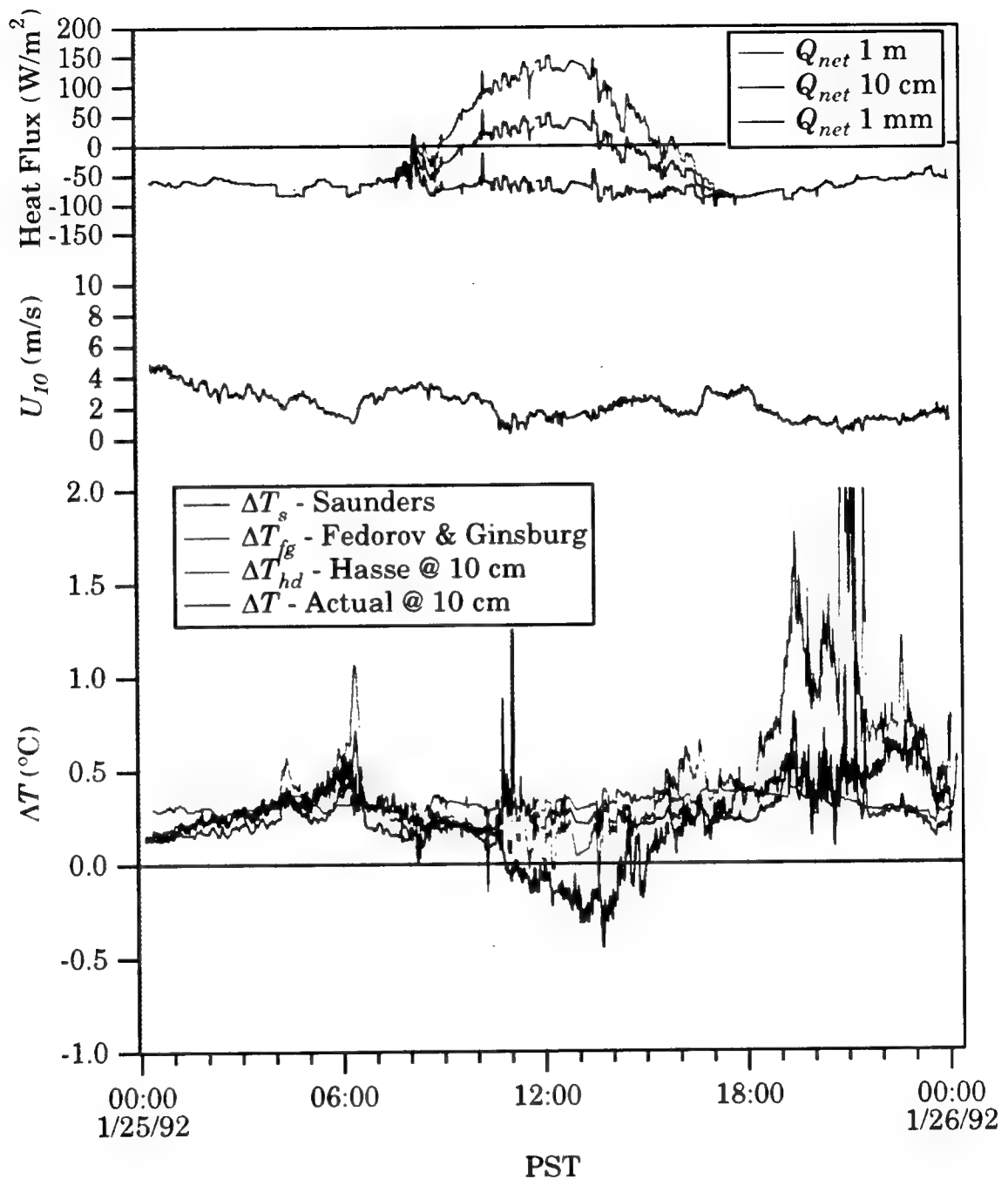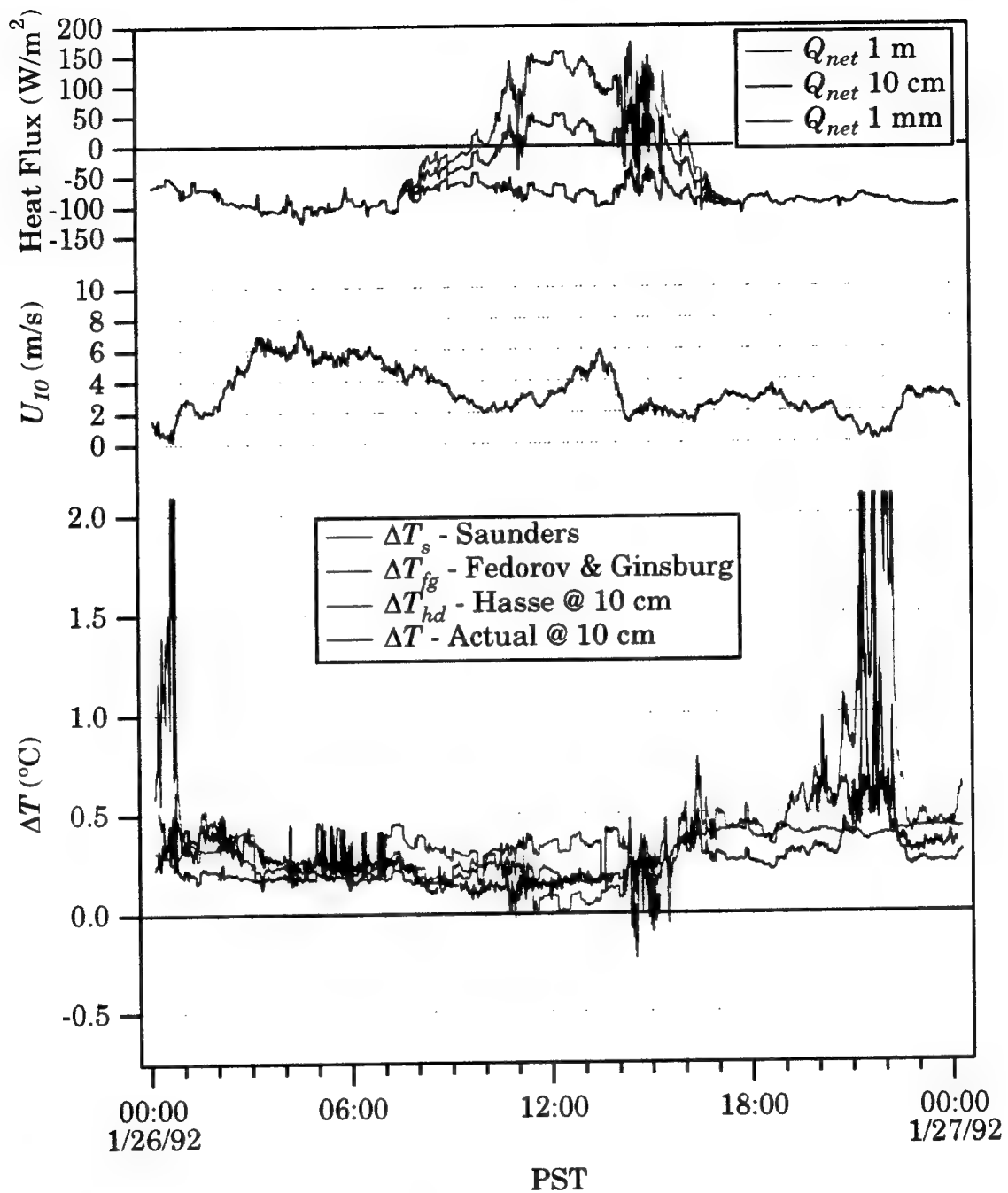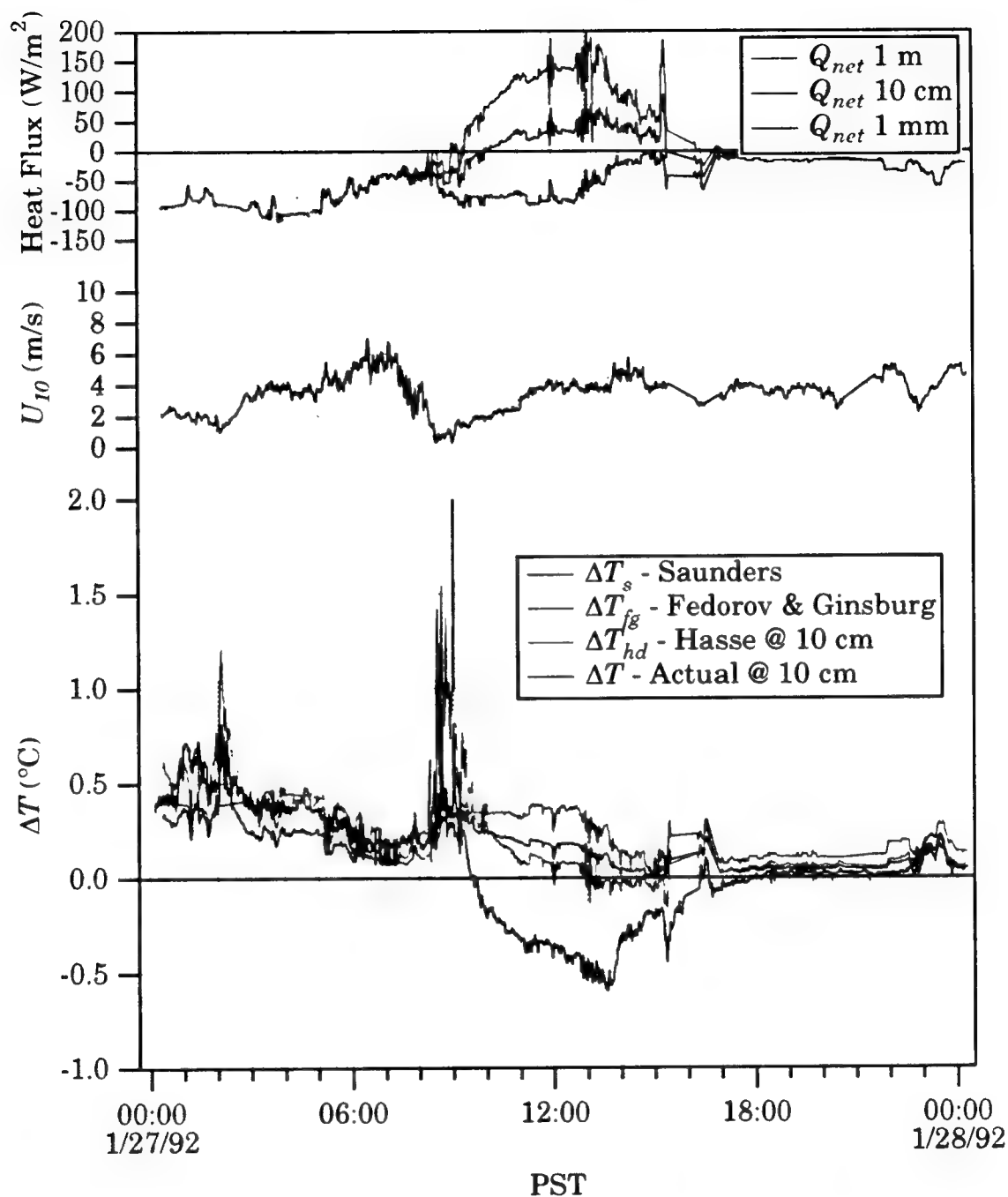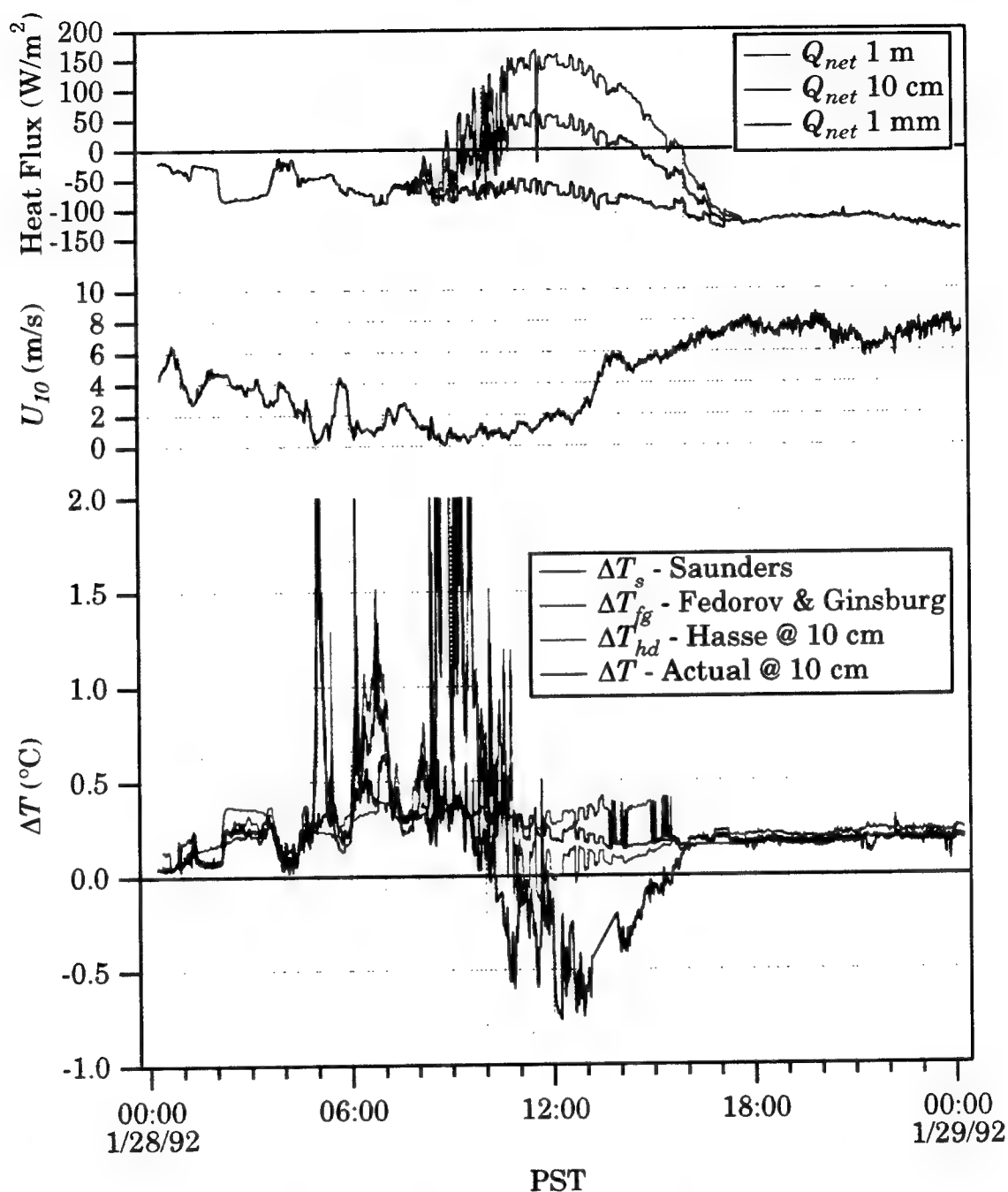
Figure 5.35d   Comparison of the ΔT models for January 28, 1992. The Q_{net} is plotted on the top of the graph with the wind speed in the middle. The bottom plot shows Saunders' model, ΔT_s, Fedorov and Ginsburg's model, ΔT_{fg}, and Hasses's model at 10 cm, ΔT_{hd}, all compared to the measured ΔT across the top 10 cm.

See Plate in Appendix.

Ginsburg model overpredicted the measured ΔT in the 2 to 5.5 m/s range where forced convection may have begun to dominate.

A comparison between January 26th and 27th provides an interesting observation of the possible difference between the effects of forced and free convection along with a look at the dependence of measurement depth. On January 26th, the wind speed remained moderate throughout the morning and midday, mixing the surface layer down to 5 m. This resulted in a positive ΔT throughout the day even under the midday insolation. However, on January 27th the wind speed declined sharply, coincident with the initiation of intense insolation, resulting in decreased mixing within the surface layer. This allowed for stratification within the top 10 cm and the measurement of a negative ΔT using a 10 cm bulk measurement. The time scales for the mixing of solar absorption with depth may depend directly upon the wind speed.

Saunders' (1967a) and the Fedorov and Ginsburg model predicted the ΔT only across the top millimeter while the closest measured value was for the top 10 centimeters. During the day when solar heating was prevalent, the Q_{net} remained negative or became positive depending upon the depth at which one performed the analysis. Therefore, the ΔT models of Saunders and Fedorov and Ginsburg usually remained positive while the measured values crossed over to the negative side as the net heat flux became positive. Hasse's (1971) model attempted to compensate for the depth of measurement as shown in Figure 5.35 where it most closely predicted the ΔT during the day when solar radiation intensified. Figures 5.36a-d show the difference between Hasse's models and the corresponding ΔT as depth increased. Accordingly, ΔT_{hd} decreased during the day following the zero-crossing of the actual measurement of ΔT. As Hasse's model tried to compensate for the depth of measurement, $\Delta T - \Delta T_{hd}$ decreased with increasing depth. This suggested that Hasse's model was less effective as depth increased. Even though the Hasse model frequently underestimated the decrease of ΔT, the concept of dependence upon measurement depth

Figure 5.36a   Comparison of the difference, $\Delta T - \Delta T_{hd}$, between the measured bulk-skin temperature difference and Hasse's model prediction of the same as a function of measurement depth. Comparison performed for data from January 25, 1992.
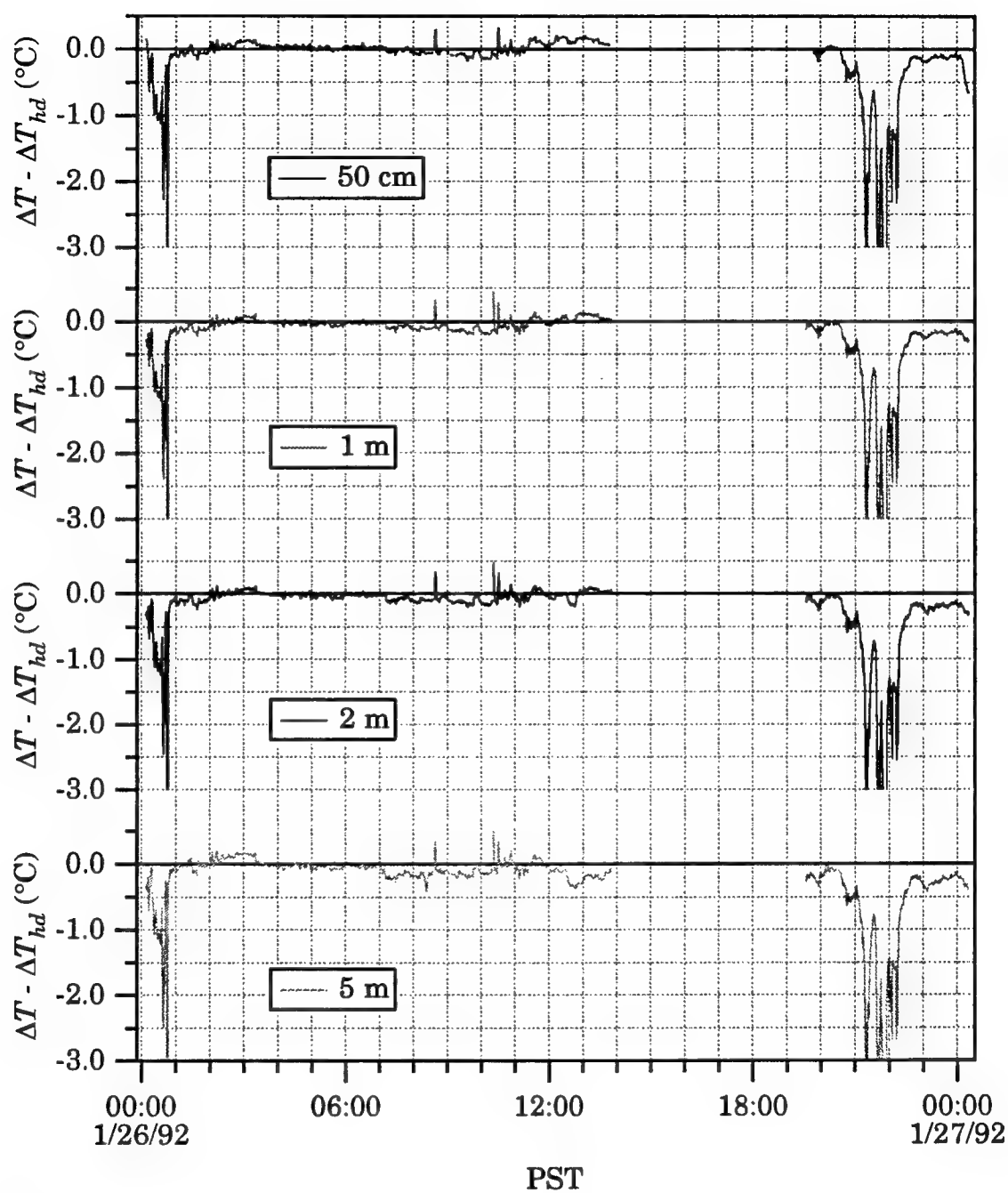
Figure 5.36b   Comparison of the difference, ΔT - ΔT_{hd}, between the measured bulk-skin temperature difference and Hasse's model prediction of the same as a function of measurement depth. Comparison performed for data from January 26, 1992.

Figure 5.36c   Comparison of the difference, ΔT - ΔT_{hd}, between the measured bulk-skin temperature difference and Hasse's model prediction of the same as a function of measurement depth. Comparison performed for data from January 27, 1992.

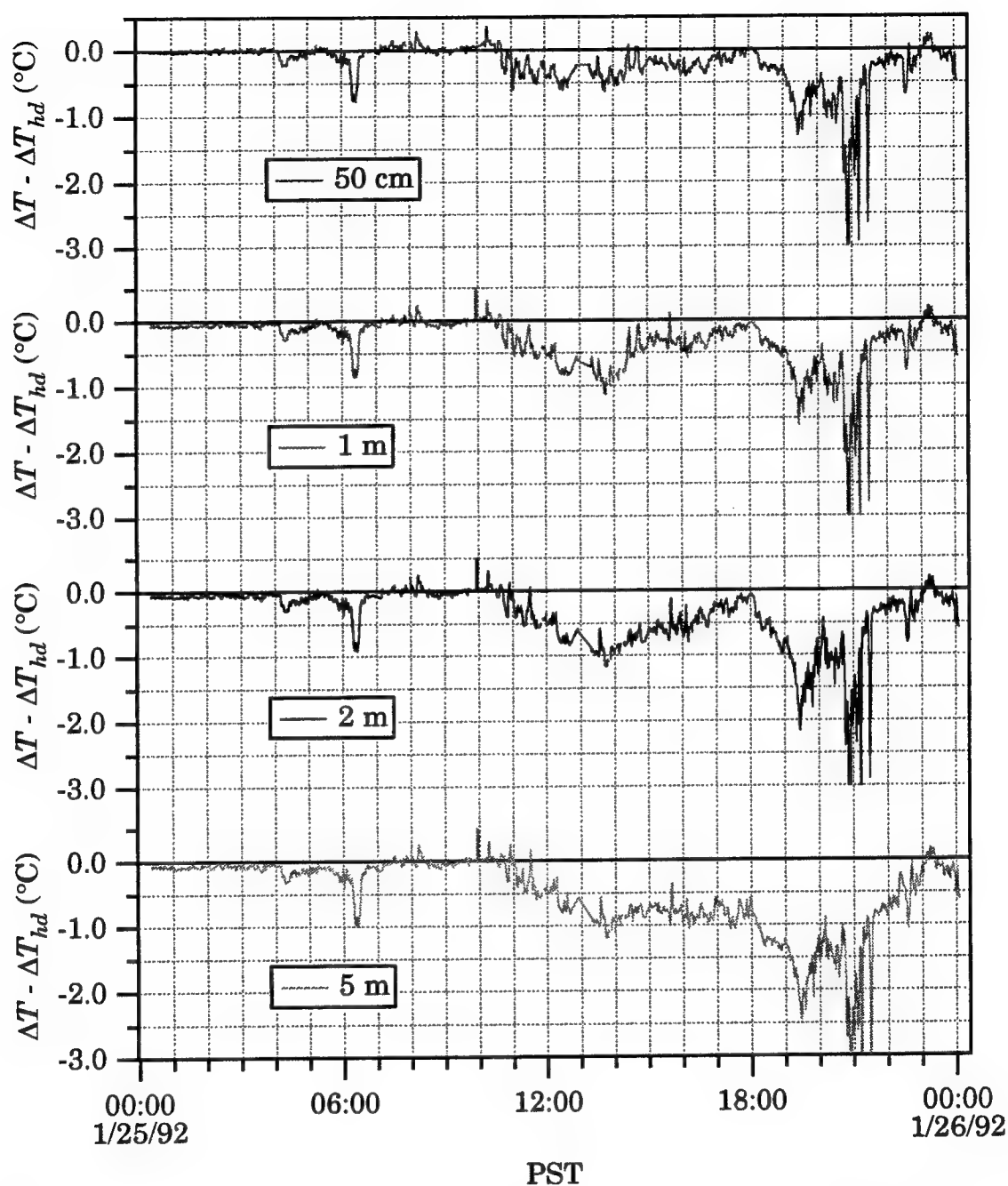Figure 5.36d Comparison of the difference, ΔT - ΔT_{hd}, between the measured bulk-skin temperature difference and Hasse's model prediction of the same as a function of measurement depth. Comparison performed for data from January 28, 1992.
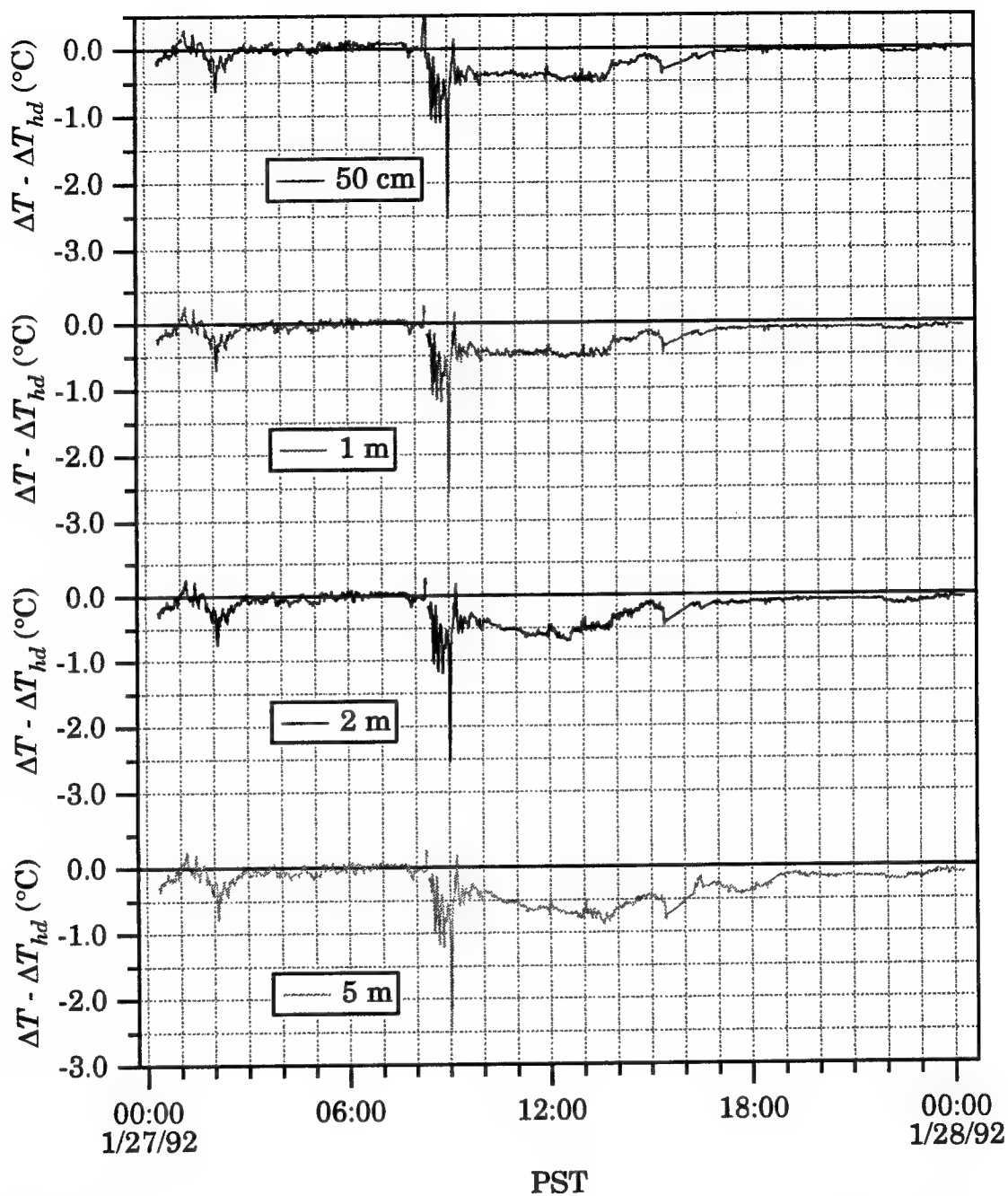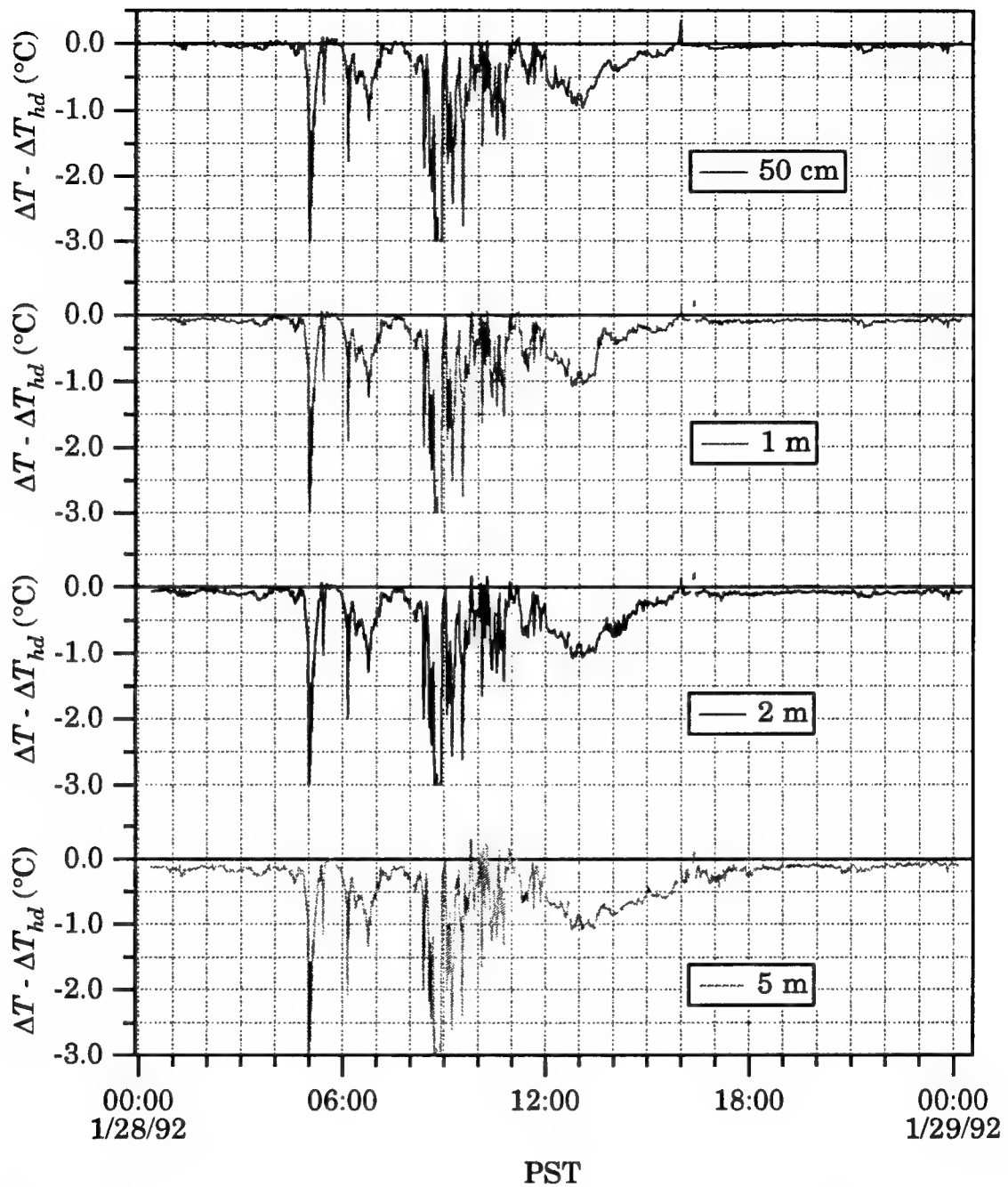
merits further research based upon these results and those of the scanner images which showed the importance of mixing depth (e.g., Cases 5 and 6).

CHAPTER 6

Summary and Conclusions

Measurements of skin temperature made aboard the R/P FLIP have been presented and show that infrared imagery is a useful tool to visualize and quantify turbulent disruptions of an air-water interface. Infrared imagery provides a non-intrusive 2-D measurement of temperature from the depths of 10 μm. Complementary point measurements were made with a narrow field-of-view radiometer, which when corrected for sky reflection and calibrated in-field was accurate to within 0.1 °C. With the cool skin layer as a background, a disturbance would mix the warmer water from below up to the surface. The infrared imager was be able to detect these disturbances. Under low wind speed conditions, the spatial size of the skin layer destruction was much larger than expected. An artificial disturbance of the skin layer by a cable 1 cm in diameter produced turbulent patches on the order of 1 meter in diameter which were observed to persist for up to 80 s before drifting out of the field-of-view of the imager. However, none of the disruptions under the low wind speed conditions recovered before drifting out of the field-of-view.

The size and shape of the disturbances produced by the cables were strongly dependent upon the characteristics of the flow (i.e., wave-current alignment). Therefore, a wave Reynolds number, Re_w, defined the strength of the each disturbance. The turbulent patches behaved differently both spatially and temporally for increasing Re_w. As Re_w increased, the patches increased in maximum size, persisted longer, and reached their peak size later. Not only did the patch width, b, experience a growth and decay, but the more relevant parameter, ΔT_w, did also. The disruption of the skin layer is a measure of the bulk-skin temperature difference, ΔT. Therefore, ΔT_w approximated the directly measured ΔT within the instruments' (e.g., infrared scanner, radiometers) capabilities. The slope of the decay of ΔT_w defined the skin layer recovery rate. Under low wind speed conditions, the skin layer recovered more rapidly for increasing Re_w. (The skin layer recovery rate increased according to the convention in Figure 5.21, but the

magnitude decreased.) Therefore, the recovery relates directly to the strength of disturbance.

However, the strength of skin layer disturbance had a diminishing effect with increasing wind speed. Turbulence on the water side of the air-sea interface and the net heat flux define the thickness of the skin layer. Under low wind speed conditions, low turbulence exists in the surface layer resulting in a thick conduction layer. Conversely, at high wind speeds a large amount of turbulence exists and the skin layer thins out. For the **same input** of an artificial disturbance, the skin layer behaved differently. In the low wind speed case, the disruption of the skin layer was extrapolated to last up to 120 s, while for the high wind speed case, the disruption lasted less than 2 s. The rates of recovery were responsible for the difference.

As the temperature within the patch decreased even as the wake continued to grow, the threshold for skin layer recovery at low wind speeds occurred earlier than that for wake dimension decay. We have shown that the skin layer began to recover very soon after the disturbance had passed. On the other hand, the wake width continued to grow signifying that the level of turbulence was still enough to rupture the skin layer but not totally destroy it as the skin layer recovery counteracted the turbulence. The thickness of the molecular sublayer relates directly to the turbulent intensity in the water. At each equilibrium state, the turbulence level at the interface diminished allowing the skin layer to become thicker and ΔT to increase toward its initial value. The skin layer itself continually overcame successive turbulent "thresholds" as it recovered. At higher wind speeds, the total recovery occurred 2 orders of magnitude more quickly, dominated by the increased heat flux and thinner conduction layer.

This thesis has shown that the skin layer recovery (rate) is a function of the strength of disturbance and also of the initial condition of the sea. (The sea condition depends upon the wind speed, friction velocity, background turbulence in the water, wave condition, etc.) We have found at

moderate wind speeds that the skin layer existed and recovered within 2 s
from both artificial (wire wakes) and natural (wave breaking) disturbances.
Other investigators have reported that the skin layer recovers within 10 s
following the disruption of a breaking wave and suggested that above wind
speeds of 10 m/s, the skin layer is never re-established (Ewing and
McAlister, 1960; Clauss *et al.*, 1970; Grassl, 1976).

Intriguing daytime signatures of cool wakes and a transition from
warm to cool wakes illustrated the importance of small-scale spatial
variability under low wind speed conditions and the non-uniform
temperature profiles existing during the day. At times of intense solar
heating and low wind speed, the measurements show that the skin layer
can appear warmer than the water below, using both the imager and the
narrow field-of-view radiometer. Furthermore, observations of a disturbed
skin layer in the images did not agree in magnitude, or in some cases sign,
with the direct measurements during the day of the bulk-skin temperature
difference, ΔT, which consistently showed the skin layer warmer than the
water below. Solar absorption with depth and the turbulent transport of
heat within the mixed layer presents a difficult problem when determining
the ΔT of the ocean skin layer. Saunders (1967a) and Fedorov and Ginsburg
(1992) both state that the skin layer should remain cool throughout the day
even under intense solar radiation. While these observations appeared to
contradict the beliefs of Saunders (1967a) and Fedorov and Ginsburg (1992),
the skin layer may in fact have remained cool. One reason is that the
measured ΔT was the temperature difference across at least the top 10 cm
while Saunders' and Fedorov and Ginsburg's model predict for only the
molecular layer, which is typically on the order of a millimeter thick.
Furthermore, the depth (and volume) of mixing produced by the cable
disturbance coupled with the non-uniform temperature profile existing
during the day may also account for this peculiar behavior.

The observations of cool wakes led to the comparison of ΔT models by
Saunders (1967a), Fedorov and Ginsburg (1992), and Hasse (1971) with the
actual measured bulk-skin temperature difference. The comparison

emphasized the inadequacy associated with the large-scale models appropriate for stable situations over longer periods of time. For the present dataset, longwave radiation dominated the regulation of the net heat flux at night while the solar insolation dominated during the daytime. We have seen that the sea surface temperature (IR SST) was strongly dependent upon the net heat flux during the nighttime, as the models imply. All of the ΔT models performed well at high wind speeds and at night. At low wind speeds (< 2 m/s), however, the Saunders and Hasse models diverged drastically from the actual ΔT. Fedorov and Ginsburg's model did not since it attempted to account for free convection. Nonetheless, their model often overpredicted the actual ΔT, assuming free convection occurred at higher wind speeds. During the day when solar absorption was important, Saunders' (1967a) and Fedorov and Ginsburg's (1992) models remained positive while the measured ΔT often became negative. Again, whereas their models predicted only the ΔT across the skin layer itself, the measured ΔT depicted the bulk-skin temperature difference to at least 10 cm. Hasse's model was the only one which attempted to compensate for the depth of measurement and allowed a direct comparison to the measured ΔT.

The ΔT models did not adequately predict the phenomenon of the daytime heat flux and skin layer development. Comparisons of the scanner observations of small-scale spatial variability with the measured ΔT from different depths leave many unanswered questions as to how the solar flux behaves near the surface (e.g., time and length scales for mixing) and affects the skin layer. The depth (and volume) of mixing is very important as shown by Cases 5 and 6 portrayed in Section 5.5, while more information about the temperature profile within the top 10 cm during the day is necessary. Compounding the problem is the fact that skin layer recovery time will bias the temperature estimate from the scanner images when determining the mixing depth once a more defined temperature profile is known. Notwithstanding, improved models similar in theory to Hasse's (1971) can be investigated and implemented for predictions of the skin layer

behavior and near-surface (< 5 m) temperature profiles, and compared with the small-scale spatial and temporal variability frequently observed.

In conclusion, this investigation has shown the feasibility of using an infrared scanner for detecting and quantifying disturbances at the air-water interface. As far as we know, these are the first published measurements of the skin layer recovery rates' dependence upon wind speed and strength of disturbance. The relation of skin layer recovery to gas exchange and to the air-sea fluxes merits additional research. Further work relating the skin layer recovery to surface renewal models and determining the feasibility of remotely measuring turbulence using infrared imagery is suggested. The model comparison established the need for modification of the models during the day, and possibly the nighttime, under conditions where spatial and temporal small-scale variability of the skin layer characteristics frequently exist. Furthermore, the observation of small-scale variability requires more detailed modeling of ΔT and the temperature profile in the near-surface layer, coupled with an understanding of its relevance to satellite remote sensing. Future laboratory studies of breaking wave and towed cylinder disruptors will provide the means to study the variation of skin layer recovery for a full range of wind speeds, heat fluxes, and turbulent intensities. Also, the spatial and temporal scales of depth (volume) of mixing and its relation to the stability of the skin layer and temperature profile warrant investigation. Possible field applications include the use of a surface-piercing cable to produce a continuous time series of instantaneous ΔT. The relation of these observations to the effects of Q_{net} and u_{*w} needs to be further explored. Finally, models of ΔT encompassing the complex mechanisms of formation and existence, along with models of remotely sensed free-surface turbulence, should be pursued.

LIST OF REFERENCES

Batchelor, G. K., An Introduction to Fluid Dynamics, Cambridge University Press, Cambridge, England, ©1967.

Bearman, P. W., On Vortex Shedding From a Circular Cylinder in the Critical Reynolds Number Régime, J. Fluid Mech., 37(3), pp. 577-585, ©1969.

Bearman, P. W., Vortex Shedding From Oscillating Bluff Bodies, Ann. Rev. Fluid Mech., 16, pp. 195-222, ©1984.

Bénard, H., Les Toubillons Cellulaires dans une Nappe Liquide Transportant de la Chaleur par Convection en Regime Permanent, Ann. Chim. Phys., 11, pp. 1261-1271, ©1901.

Berger, E., and R. Wille, Periodic Flow Phenomena, Ann. Rev. of Fluid Mech., 4, pp. 313-340, ©1972.

Bernal, L. P., and J. T. Kwon, Vortex Ring Dynamics at a Free Surface, Phys. Fluids A, 1(3), pp. 449-451, ©1989.

Bernal, L. P., A. Hirsa, J. T. Kwon, and W. W. Willmarth, On the Interaction of Vortex Rings and Pairs with a Free Surface for Varying Amounts of Surface Active Agent, Phys. Fluids A, 1(12), pp. 2001-2004, ©1989.

Birkhoff, G., and E. H. Zarantonello, Jets, Wakes, and Cavities, Academic Press Inc., New York, ©1957.

Cervenka, P. O., Remote Sensing the Thermal Macrowake, Opt. Eng., 28(7), pp. 819-827, ©1989.

Chu, T. Y., and R. J. Goldstein, Turbulent Convection in a Horizontal Layer of Water, J. Fluid Mech., 60, pp. 141-159, ©1973.

Clauss, E., H. Hinzpeter, and J. Müller-Glewe, Messungen zur Temperaturstruktur im Wasser an der Grenzfläche Ozean-Atmosphäre, Meteor-Forsch.-Ergebnisse, Reihe B, No. 5, pp. 90-94, ©1970.

Cox, C., and W. Munk, Measurements of the Roughness of the Sea Surface from Photographs of the Sun's Glitter, J. Opt. Soc. Am., 44(11), pp. 838-850, ©1954.

Dobson, F. W., Measurements of Atmospheric Pressure in Wind-Generated Sea Waves, J. Fluid Mech., 48(1), pp. 91-127, ©1971.

Downing, H. D., and D. Williams, Optical Constants of Water in the Infrared, J. Geophys. Res., 80(12), pp. 1656-1661, ©1975.

Ewing, G., and E. D. McAlister, On the Thermal Boundary Layer of the Ocean, Science, 131(3410), pp. 1374-1376, ©1960.

Fedorov, K. N., and A. I. Ginsburg, The Near-Surface Layer of the Ocean, VSP, Utrecht, Netherlands, ©1992.

Friedman, D., Infrared Characteristics of Ocean Water (1.5 - 15 µm), Appl. Opt., 8(10), pp. 2073-2078, ©1969.

Garber, D. H., R. J. Urick, and J. Cryden, Thermal Wake Detection, USNR&S Laboratory Report S-20, ©1945.

Garrett, W. D., and P. M. Smith, Physical and Chemical Factors Affecting the Thermal IR Imagery of Ship Wakes, NRL Report 5376, ©1984.

Gasparovic, R. F., G. H. Emmons, and L. D. Tubbs, Two-Wavelength Measurements of the Ocean Surface Radiometric Clutter, Proc. of IRIS, 19, pp. 85-100, ©1974.

Gasparovic, R. F., K. Peacock, and L. D. Tubbs, Airborne Radiometric Measurements of Sea Surface Temperature, Johns Hopkins APL Technical Digest, 3(1), pp. 4-11, ©1982.

Geernaert, G. L., Bulk Parameterizations for the Wind Stress and Heat Fluxes, Surface Waves and Fluxes: Volume I - Current Theory, Geernaert, G. L., and W. J. Plant, eds., Kluwer Academic Publishers, Dordrecht, ©1990.

Gemmrich, J., and L. Hasse, Small-Scale Surface Streaming Under Natural Conditions as Effective in Air-Sea Gas Exchange, Tellus, 44B, pp. 150-159, ©1992.

Grassl, H., The Dependence of the Measured Cool Skin of the Ocean on Wind Stress and Total Heat Flux, Boundary-Layer Meteor., 10(4), pp. 465-474, ©1976.

Halliday, D., and R. Resnick, Physics, John Wiley and Sons, New York, ©1978.

Hasselmann, K., T. P. Barnett, E. Buows, H. Carlson, D. E. Cartwright, K. Enke, J. A. Ewing, H. Gienapp, D. E. Hasselmann, P. Kruseman, A. Meerburg, P. Müller, D. J. Olbers, K. Richter, W. Sell, and H. Walden, Measurements of Wind-Wave Growth and Swell Decay during the Joint

219

North Sea Wave Project (JONSWAP), <u>Ergänzungsheft zur Deutschen Hydographischen Zeitschrift, Reihe A(8°), Nr. 12</u>, 95 pp., ©1973.

Hasse, L., The Sea Surface Temperature Deviation and the Heat Flow at the Sea-Air Interface, <u>Boundary-Layer Meteor., 1(3)</u>, pp. 368-379, ©1971.

Hasse, L., On the Mechanism of Gas Exchange at the Air-Sea Interface, <u>Tellus, 42B</u>, pp. 250-253, ©1990.

Hill, R. H., Laboratory Measurement of Heat Transfer, Wind Velocity Profiles, and Temperature Structure at an Air/Water Interface, <u>NRL Report 7212</u>, ©1970.

Hill, R. H., Laboratory Measurement of Heat Transfer and Thermal Structure Near an Air-Water Interface, <u>J. Phys. Ocean., 2</u>, pp. 190-198, ©1972.

Hirsa, A., G. Tryggvason, J. Abdollahi-Alibeik, and W. W. Willmarth, Measurement and Computations of Vortex Pair Interaction with a Clean or Contaminated Free Surface, <u>18th Symposium on Naval Hydrodynamics</u>, pp. 521-531, ©1991.

Hirsa, A., and L. M. Logory, Structure of Turbulence in the Surface Layer of a Flat-Plate Wake, <u>ONR Workshop on Free-Surface Turbulent Flows</u>, Pasadena, ©1994.

Hobson, D. E., and D. Williams, Infrared Spectral Reflectance of Sea Water, <u>Appl. Opt., 10(10)</u>, pp. 2372-2373, ©1971.

Holman, J. P., <u>Heat Transfer</u>, McGraw-Hill, New York, ©1990.

Jarvis, N. L., The Effect of Monomolecular Films on Surface Temperature and Convective Motion at the Water/Air Interface, <u>J. Colloid Sci., 17</u>, pp. 512-522, ©1962.

Jarvis, N. L., and R. E. Kagarise, Determination of the Surface Temperature of Water During Evaporation Studies. A Comparison of Thermistor With Infrared Radiometer Measurements, <u>J. Colloid Sci., 17</u>, pp. 501-511, ©1962.

Jessup, A. T., W. K. Melville, and W. C. Keller, Breaking Waves Affecting Microwave Backscatter, 2: Dependence on Wind and Wave Conditions, <u>J. Geophys. Res., 96(11)</u>, pp. 20561-20569, ©1991.

Jessup, A. T., The Infrared Signature of Breaking Waves, <u>A Symposium on the Air-Sea Interface</u>, Marseille, ©1993.

Kanwisher, J., On the Exchange of Gases Between the Atmosphere and the Sea, Deep-Sea Research, 10, pp. 195-207, ©1963.

von Kármán, T., Turbulence and Skin Friction, J. Aero. Sci., 1(1), pp. 1-20, ©1934.

Katsaros, K. B., The Sea Surface Temperature Deviation at Very Low Wind Speeds; Is There a Limit?, Tellus, 29, pp. 229-239, ©1977.

Katsaros, K. B., W. T. Liu, J. A. Businger, and J. E. Tillman, Heat Transport and Thermal Structure in the Interfacial Boundary Layer Measured in an Open Tank of Water in Turbulent Free Convection, J. Fluid Mech., 83(2), pp. 311-335, ©1977.

Katsaros, K. B., The Aqueous Thermal Boundary Layer, Boundary Layer Meteor., 18, pp. 107-127, ©1980a.

Katsaros, K. B., Radiative Sensing of Sea Surface Temperature, Air Sea Interaction: Instruments and Methods, Dobson, F., L. Hasse, and R. Davis, eds., Plenum Press, NY, pp. 293-317, ©1980b.

Keller, W. C., and W. J. Plant, Cross Sections and Modulation Transfer Functions at L and K_u Bands Measured During the Tower Ocean Wave and Radar Dependence Experiment, J. Geophys. Res., 95(C9), pp. 16277-16289, ©1990.

Khundzhua, G. G., and Ye. G. Andreyev, An Experimental Study of Heat Exchange Between the Ocean and the Atmosphere in Small-Scale Interaction, Izv., Atmospheric and Oceanic Physics, 10(10), pp. 685-687, ©1974.

Khundzhua, G. G., A. M. Gusev, Ye. G. Andreyev, V. V. Gurov, and N. A. Skorokhvatov, Structure of the Cold Surface Film of the Ocean and Heat Transfer Between the Ocean and the Atmosphere, Izv., Atmospheric and Oceanic Physics, 13(7), pp. 506-509, ©1977.

Kline, S. J., W. C. Reynolds, F. A. Schraub, and P. W. Runstadler, The Structure of Turbulent Boundary Layers, J. Fluid Mech., 30(4), pp. 741-773, ©1967.

Kondo, J., Air-Sea Bulk Transfer Coefficients in Diabatic Conditions, Boundary Layer Meteor., 9, pp. 91-112, ©1975.

Kreith, F., Principles of Heat Transfer, International Textbook Company, Scranton, ©1958.

Kreith, F., Radiation Heat Transfer, International Textbook Company, Scranton, ©1962.

Lamb, Sir H., Hydrodynamics, Dover Publications, New York, ©1945.

Large, W. G., and S. Pond, Sensible and Latent Heat Flux Measurements Over the Ocean, J. Phys. Ocean., 12(5), pp. 464-482, ©1981.

Large, W. G., and S. Pond, Open Ocean Momentum Flux Measurements in Moderate to Strong Winds, J. Phys. Ocean., 11(3), pp. 324-336, ©1982.

Levich, V. G., Physicochemical Hydrodynamics, Prentice-Hall, Englewood Cliffs, N. J., ©1962.

Lighthill, J., Waves in Fluids, Cambridge University Press, New York, ©1978.

Lighthill, J., An Informal Introduction to Theoretical Fluid Mechanics, Clarendon Press, Oxford, ©1986.

Lin, J.-T., and Y.-H. Pao, Wakes in Stratified Fluid, Ann. Rev. Fluid Mech., 11, pp. 317-338, ©1984.

Liu, W. T., and J. A. Businger, Temperature Profile in the Molecular Sublayer Near the Interface of Fluid in Turbulent Motion, Geophys. Res. Lett., 2(9), pp. 403-404, ©1975.

Liu, W. T., K. B. Katsaros, and J. A. Businger, Bulk Parameterizations of Air-Sea Exchanges of Heat and Water Vapor Including the Molecular Constraints at the Interface, J. Atmos. Sci., 36, pp. 1722-1735, ©1979.

Maul, G. A., Introduction to Satellite Oceanography, Martinus Nijhoff, Dordrecht, ©1985.

McAdams, W. H., Heat Transmission, McGraw-Hill, New York, ©1942.

McAlister, E. D., Infrared-Optical Techniques Applied to Oceanography I. Measurement of Total Heat Flow from the Sea Surface, Appl. Opt., 3(5), pp. 609-612, ©1964.

McAlister, E. D., and W. L. McLeish, Oceanographic Measurements with Airborne Infrared Equipment and Their Limitations, Oceanography From Space, Gifford C. Ewing, ed., Woods Hole Oceanogr. Inst., Ref. No. 65-10, pp. 189-215, ©1965.

McAlister, E. D., and W. McLeish, Heat Transfer in the Top Millimeter of the Ocean, J. Geophys. Res., 74(13), pp. 3408-3414, ©1969.

McAlister, E. D., and W. McLeish, A Radiometric System for Airborne Measurement of the Total Heat Flow from the Sea, Appl. Opt., 9(12), pp. 2697-2705, ©1970.

McKeown, W. J., Sensing Air/Water Interface Temperature Gradients With 2.0 - 5.0 Micron Interferometry, Ph.D. Dissertation, University of Wisconsin-Madison, 85 pp., ©1993.

McLeish, W., and G. E. Putland, Measurements of Wind-Driven Flow Profiles in the Top Millimeter of Water, J. Phys. Ocean., 5, pp. 516-518, ©1975.

Milgram, J. H., R. D. Peltzer, and O. M. Griffin, Suppression of Short Sea Waves in Ship Wakes: Measurements and Observations, J. Geophys. Res., 98(C4), p. 7103-7114, ©1993a.

Milgram, J. H., R. A. Skop, R. D. Peltzer, and O. M. Griffin, Modeling Short Sea Wave Energy Distributions in the Far Wakes of Ships, J. Geophys. Res., 98(C4), p. 7115-7124, ©1993b.

Miller Jr., A.W., and R. L. Street, On the Existence of Temperature Waves at a Wavy Air-Water Interface, J. Geophys. Res., 83(C3), pp. 1353-1365, ©1978.

Milne-Thomson, L. M., Theoretical Hydrodynamics, The MacMillan Company, New York, ©1950.

Omholt, T., Estimation of the Oceanic Momentum Sublayer Thickness, J. Phys. Ocean., 3, pp. 337-338, ©1973.

Panton, R. L., Incompressible Flow, John Wiley and Sons, New York, ©1984.

Paulson, C. A., and T. W. Parker, Cooling of a Water Surface by Evaporation, Radiation and Heat Transfer, J. Geophys., Res., 77, pp. 491-495, ©1972.

Paulson, C. A., and J. J. Simpson, The Temperature Difference Across the Cool Skin of the Ocean, J. Geophys. Res., 86(C11), pp. 11044-11054, ©1981.

Payne, R. E., Albedo of the Sea Surface, J. Atmos. Sci., 29, pp. 959-970, ©1972.

Peacock, K., R. F. Gasparovic, and L. D. Tubbs, High Precision Radiometric Temperature Measurements of the Ocean Surface, 15th Int. Symp. on Rem. Sens. of Env., pp. 1-10, ©1981.

Peltzer, R. D., W. D. Garrett, and P. M. Smith, A Remote Sensing Study of a Surface Ship Wake, Int. J. Remote Sensing, 8(5), pp. 689-704, ©1987.

Peltzer, R. D., J. H. Milgram, R. Skop, J. Kaiser, O. Griffin, and W. Barger, Hydrodynamics of Ship Wake Surfactant Films, 18th Symposium on Naval Hydrodynamics, pp. 533-552, ©1991.

Peltzer, R. D., O. M. Griffin, W. R. Barger, and J. A. C. Kaiser, High Resolution Measurement of Surface-Active Film Redistribution in Ship Wakes, J. Geophys. Res., 97(C4), p. 5231-5252, ©1992.

Robinson, I. S., N. C. Wells, and H. Charnock, The Sea Surface Thermal Boundary Layer and its Relevance to the Measurement of Sea Surface Temperature by Airborne and Spacebourne Radiometers, Int. J. Remote Sensing, 5(1), pp. 19-45, ©1984.

Robinson, I. S., Satellite Oceanography, Ellis Horwood Limited, Chichester, ©1985.

Rohsenow, W. M., and H. Choi, Heat, Mass, and Momentum Transfer, Prentice-Hall, Englewood Cliffs, N.J., ©1961.

Roshko, A., On the Drag and Shedding Frequency of Two-Dimensional Bluff Bodies, NACA Tech. Note No. 3169, ©1954.

Roshko, A., Experiments on the Flow Past a Cylinder at Very High Reynolds Numbers, J. Fluid Mech., 10, pp. 345-356, ©1961.

Rossby, H. T., A Study of Bénard Convection With and Without Rotation, J. Fluid Mech., 36, pp. 309-335, ©1969.

Sarpkaya, T., and M. Isaacson, Mechanics of Wave Forces on Offshore Structures, Van Nostrand Reinhold Company, New York, ©1981.

Sarpkaya, T., Energy Spectra for the Vortex/Free-Surface Interaction, ONR Workshop on Free-Surface Turbulent Flows, Pasadena, ©1994.

Saunders, P. M., The Temperature at the Ocean-Air Interface, J. Atmos. Sci., 24(3), pp. 269-273, ©1967a.

Saunders, P. M., Aerial Measurement of Sea Surface Temperature in the Infrared, J. Geophys. Res., 72(16), pp. 4109-4117, ©1967b.

Saunders, P. M., Radiance of Sea and Sky in the Infrared Window 800-1200 /cm, J. Opt. Soc. Am., 58(5), pp. 645-652, ©1968.

Saunders, P. M., Corrections for Airborne Radiation Thermometry, J. Geophys. Res., 75(36), pp. 7596-7601, ©1970.

Saunders, P. M., The Skin Temperature of the Ocean-A Review, Fifth Liege Colloquium on Ocean Hydrodynamics, 5, pp. 93-98, ©1973.

Schlichting, H., Boundary Layer Theory, McGraw-Hill, New York, ©1960.

Schluessel, P., W. J. Emery, H. Grassl, and T. Mammen, On The Bulk-Skin Temperature Difference and Its Impact on Satellite Remote Sensing of Sea Surface Temperature, J. Geophys. Res., 95(C8), pp. 13341-13356, ©1990.

Schmidt, W., Absorption der Sonnenstrahlung im Wasser, S. B. Akad. Wiss. Wien, 117, ©1908.

Schwartz, I. B., and R. G. Priest, Reflection Driven Ship Wake Contrasts in the Infrared, NRL Report 9144, ©1988.

Simpson, J. J., and C. A. Paulson, Small-Scale Sea Surface Temperature Structure, J. Phys. Ocean., 10, pp. 399-410, ©1980.

Slaouti, A., and J. H. Gerrard, An Experimental Investigation of the End Effects on the Wake of a Circular Cylinder Towed Through Water at Low Reynolds Numbers, J. Fluid Mech., 112, pp. 297-314, ©1981.

Smith, S. D., and E.G. Banke, Variation of the Sea Surface Drag Coefficient with Windspeed, Quart. J. Royal Met. Soc., 101, pp. 665-673, ©1975.

Smith, S. D., Wind Stress and Heat Flux Over the Ocean, J. Phys. Ocean., 10(5), pp. 709-726, ©1980.

Song, M., N. Kachman, J. Kwon, L. Bernal, and G. Tryggvason, Vortex Ring Interaction with a Free Surface, 18th Symposium on Naval Hydrodynamics, pp. 479-489, ©1991.

Spangenberg, W. G., and W. R. Rowland, Convective Circulation in Water Induced by Evaporative Cooling, Physics of Fluids, 4, pp. 743-750, ©1961.

Stewart, R. H., Methods of Satellite Oceanography, University of California Press, California, ©1985.

Tennekes, H., and J. L. Lumley, A First Course in Turbulence, MIT Press, Cambridge, MA, ©1972.

Townsend, A. A., Momentum and Energy Diffusion in the Turbulent Wake of a Cylinder, Proc. Roy. Soc. Lond., A190, pp. 551-561, ©1949.

Townsend, A. A., Temperature Fluctuation Over a Heated Horizontal Surface, J. Fluid Mech., 5, pp. 201-249, ©1959.

Weigand, A., and M. Gharib, The Interaction of Turbulent Vortex Rings with a Free Surface, ONR Workshop on Free-Surface Turbulent Flows, Pasadena, ©1994.

Wesely, M. L., Heat Transfer through the Thermal Skin of a Cooling Pond with Waves, J. Geophys. Res., 84(C7), pp. 3696-3700, ©1979.

Willert, C. E., and M. Gharib, The Interaction of Modulated Laminar and Turbulent Vortex Pairs with Free Surfaces, ONR Workshop on Free-Surface Turbulent Flows, Pasadena, ©1994.

Williamson, C. H. K., Oblique and Parallel Modes of Vortex Shedding in the Wake of a Circular Cylinder at Low Reynolds Numbers, J. Fluid Mech., 206, pp. 579-627, ©1989.

Witting, J., Effects of Plane Progressive Irrotational Waves on Thermal Boundary Layers, J. Fluid Mech., 50(2), pp. 321-334, ©1971.

Witting, J., Temperature Fluctuations at an Air-Water Interface Caused by Surface Waves, J. Geophys. Res., 77(18), pp. 3265-3269, ©1972.

Woodcock, A. H., Surface Cooling and Streaming in Shallow Fresh and Salt Waters, J. Mar. Res., 4, pp. 153-161, ©1941.

Woodcock, A. H., and H. Stommel, Temperatures Observed Near the Surface of a Fresh Water Pond at Night, J. Meteorol., 4, pp. 102-103, ©1947.

Wu, J., An Estimation of Oceanic Thermal-Sublayer Thickness, J. Phys. Ocean., 1, pp. 284-286, ©1971.

Yeh, H. H., Vorticity-Generation Mechanisms in Bores, Proc. Roy. Soc. Lond., A432, pp. 215-231, ©1991.

Yeh, H. H., Vorticity Generation at a Fluid Interface, Breaking Waves, Banner, M. L., and R. H. J. Grimshaw, eds., Springer-Verlag, Berlin, pp. 257-265, ©1992.

Appendix

a)

b) Meteorological
Sensors

IR Sensor

Surface-Piercing
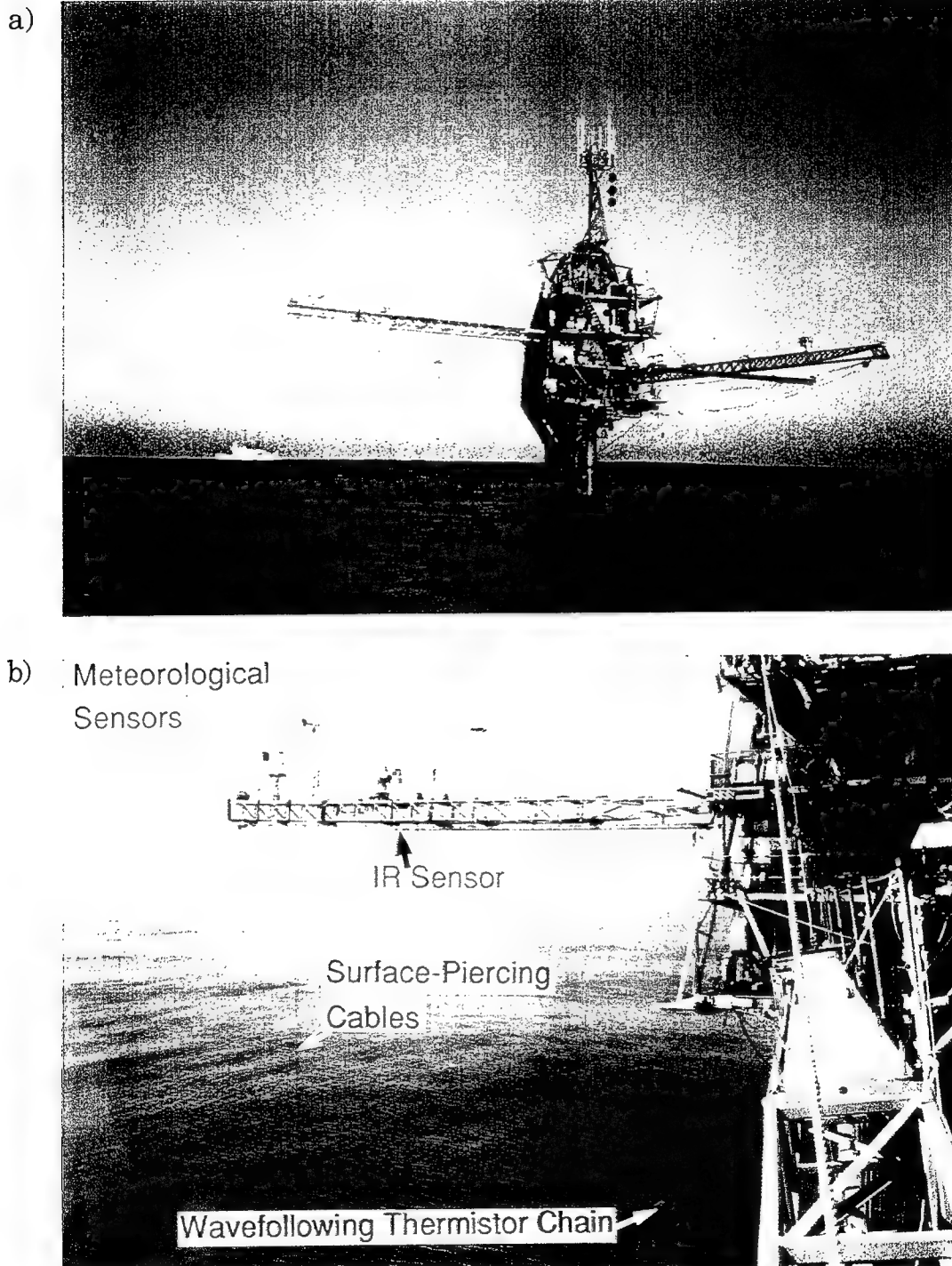Cables

Wavefollowing Thermistor Chain

Figure 5.5a-b   Photographs showing instrument deployment aboard
FLIP. In the bottom photograph (b), note the surface-
piercing cables at the end of the boom and the thermistor
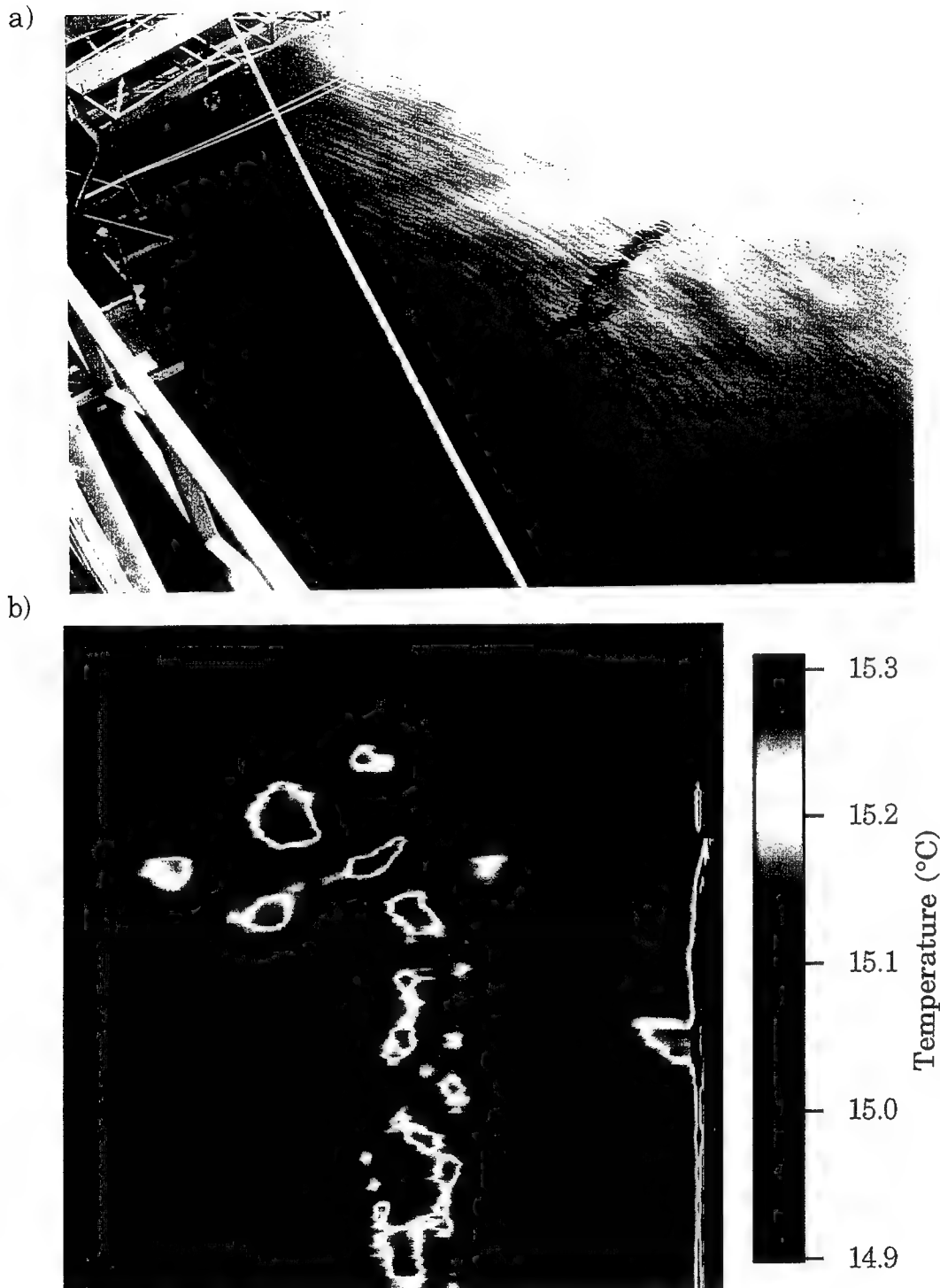chain buoy in the lower right corner.

Figure 5.7a-b   a) Photograph of the boom reflection on the sea surface.
b) Corresponding image of infrared reflection of the boom while looking down at the sea surface and oriented parallel to the boom.

Figure 5.8   Infrared image of the serpentine nature of the wakes
emanating from the instrument cables when the waves and
current are not aligned. The wakes are located in the upper
left corner. A guy wire runs diagonal through the image.
Hints of boom reflection appear below the wakes.

Figure 5.10 Time series of infrared images depicting the ordered wakes
emanating from the surface-piercing cables under low wind
conditions when the swell waves propagate in the direction of
the current. The long slender wakes develop by the
superposition of the crest of the swell and the current
velocities. The patches form when the velocity in the trough
counteracts the current. The cable diameter is 1 cm while the
patches are on the order of 1 m.

Figure 5.12 Time series of infrared images depicting the serpentine wakes emanating from the cables when the waves and current are not aligned.
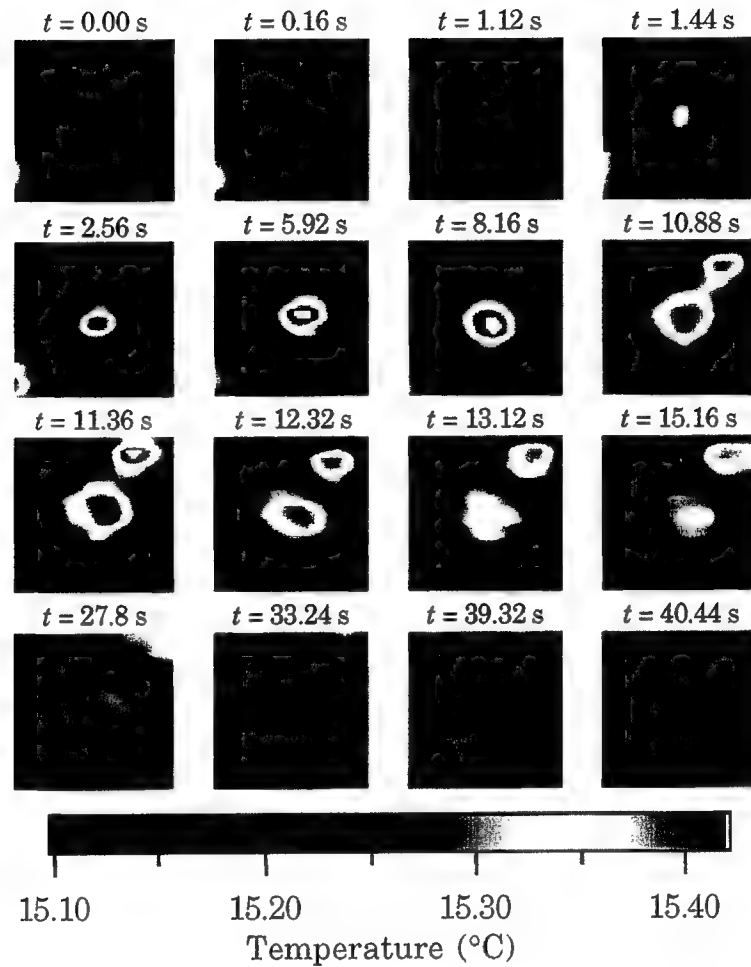
Figure 5.13 Time series of infrared images following one particular turbulent patch. The image size is roughly 1.5 m x 1.5 m. When the temperature within the patch reaches a maximum, the patch continues to grow in size. Upon maximum spatial growth, the wake recovers substantially as it propagates off the image after roughly 41 seconds.
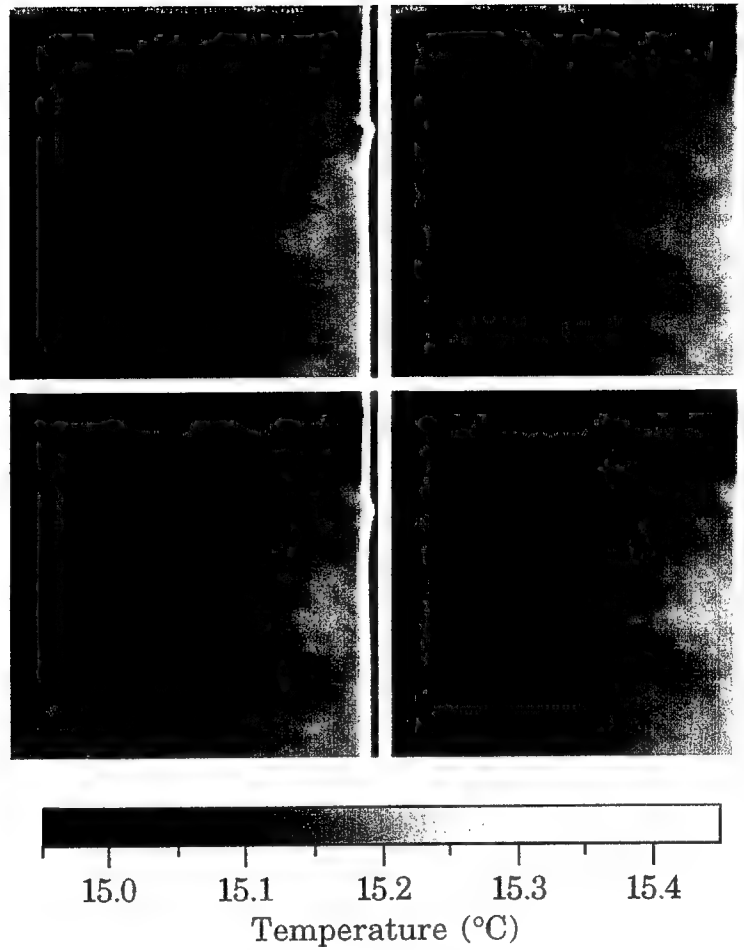
Figure 5.23 Snapshots of wispy wakes emanating from the surface-piercing cables. The dark vertical bands in the upper left corner are the cables while the faint white signatures at the bottom of the cables signify the wispy wakes. The wispy wakes last for less than a second.
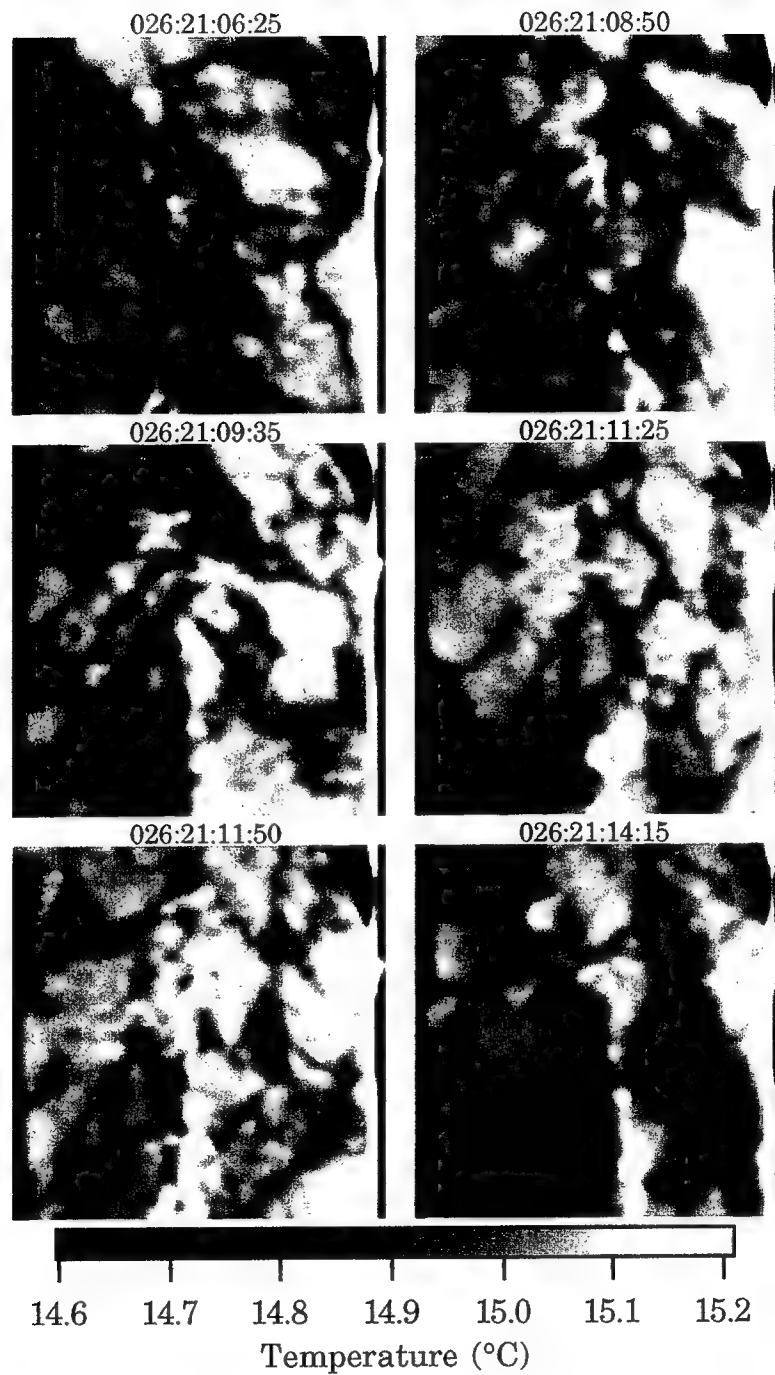
Figure 5.24 Puffy patchiness signifying the possibility of free convection under very low wind speed conditions (~ 0.7 m/s). Note the wire wakes continue to emanate from the cables. Environmental conditions shown in Table 5.3 under Case 4.
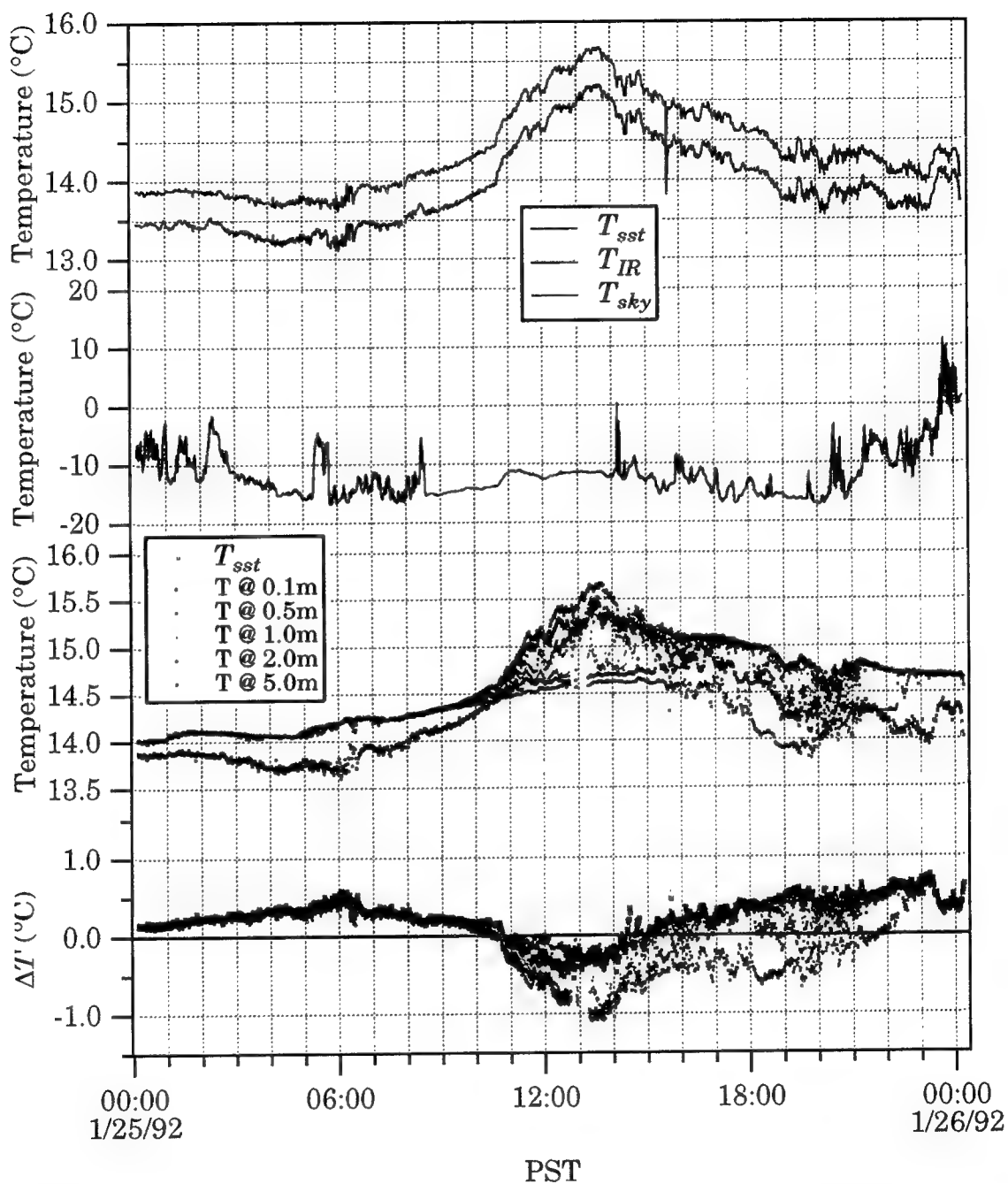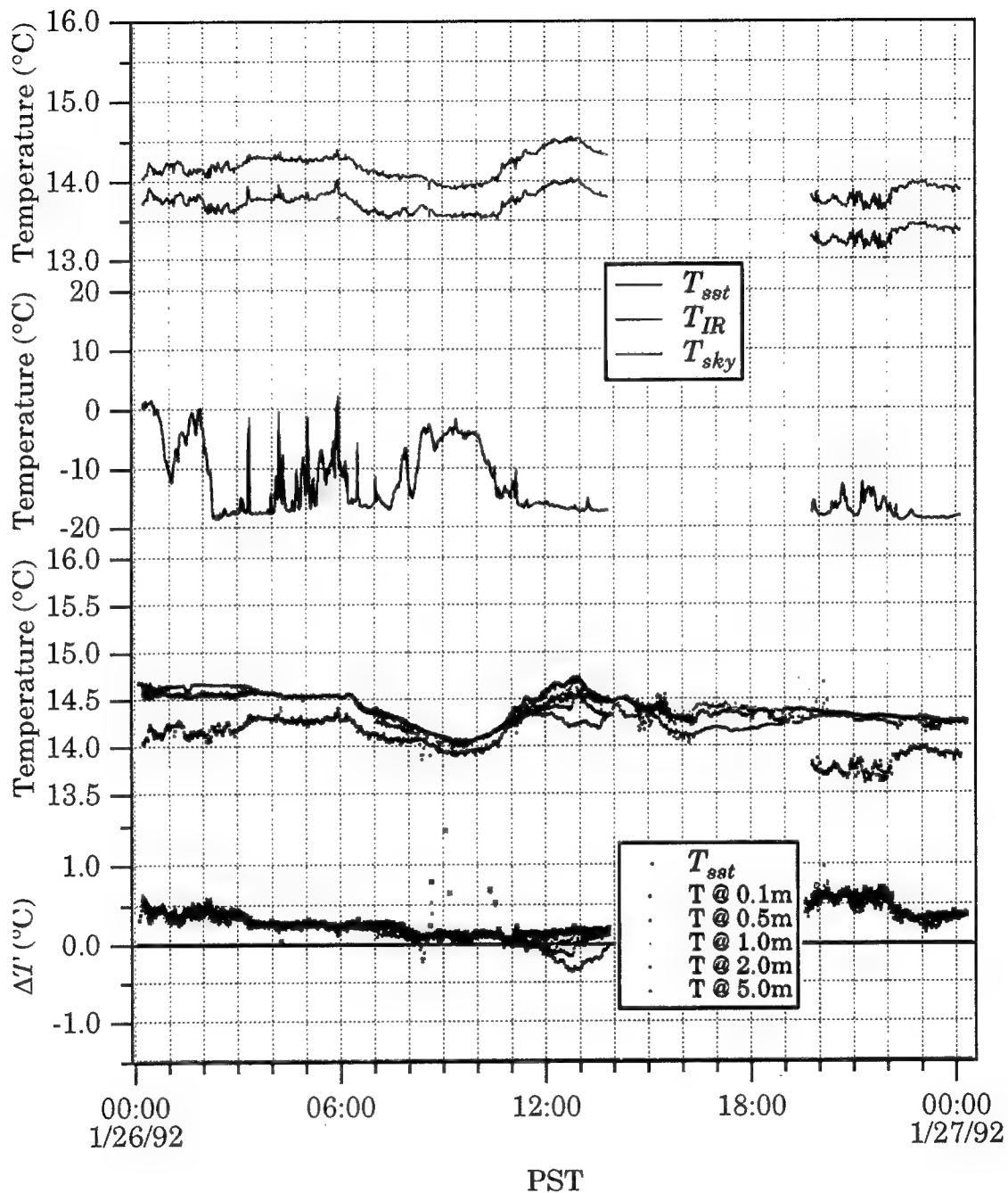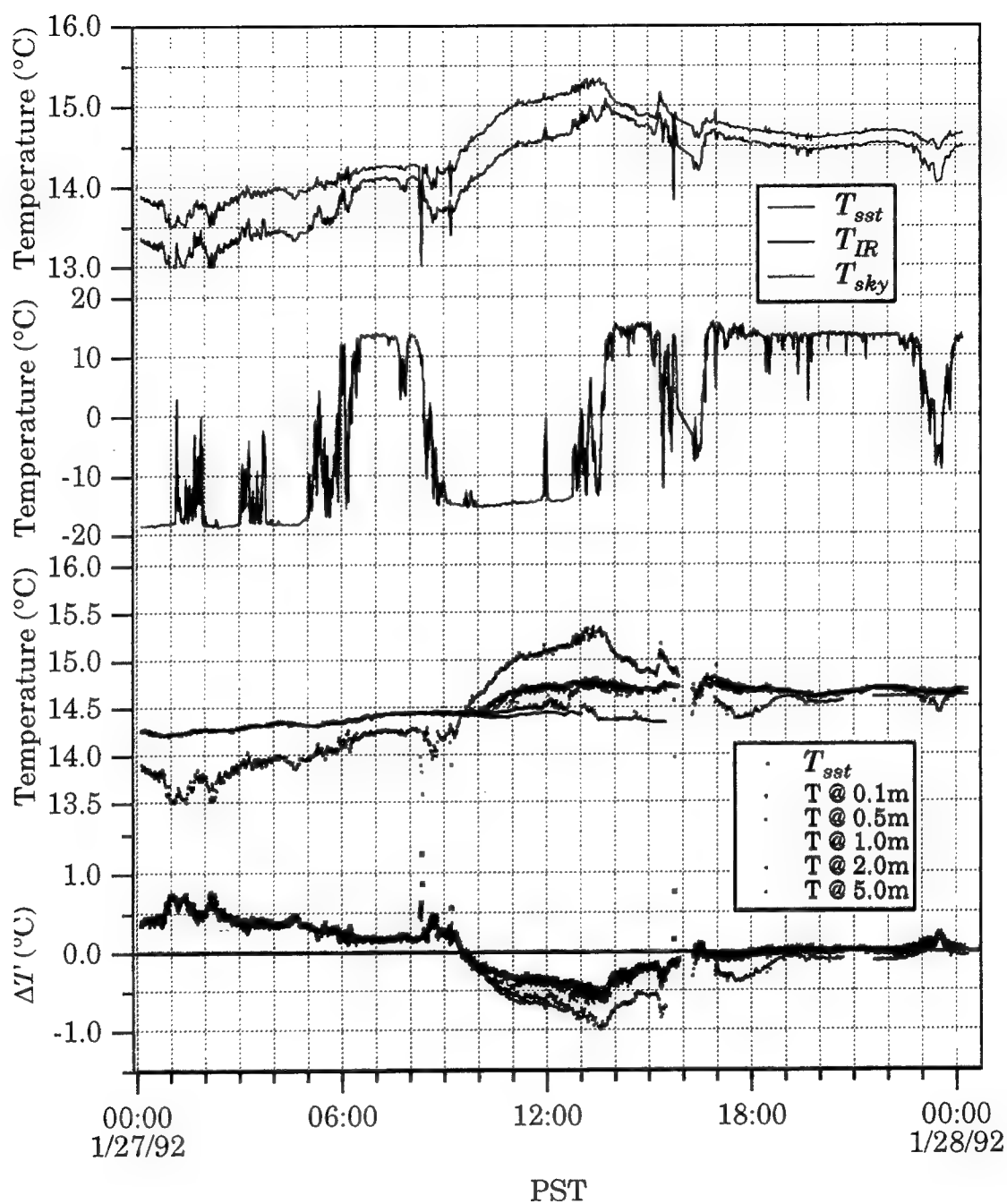
Figure 5.26a   Time series for January 25, 1992 of the corrected and calibrated IR SST, T_{sst}, along with the raw PRT-5 measurement, T_{IR}, and the radiometric sky temperature, T_{sky}. Time series of thermistor measurements at depth and ΔT's are included.

Figure 5.26b   Time series for January 26, 1992 of the corrected and calibrated IR SST, T_{sst}, along with the raw PRT-5 measurement, T_{IR}, and the radiometric sky temperature, T_{sky}. Time series of thermistor measur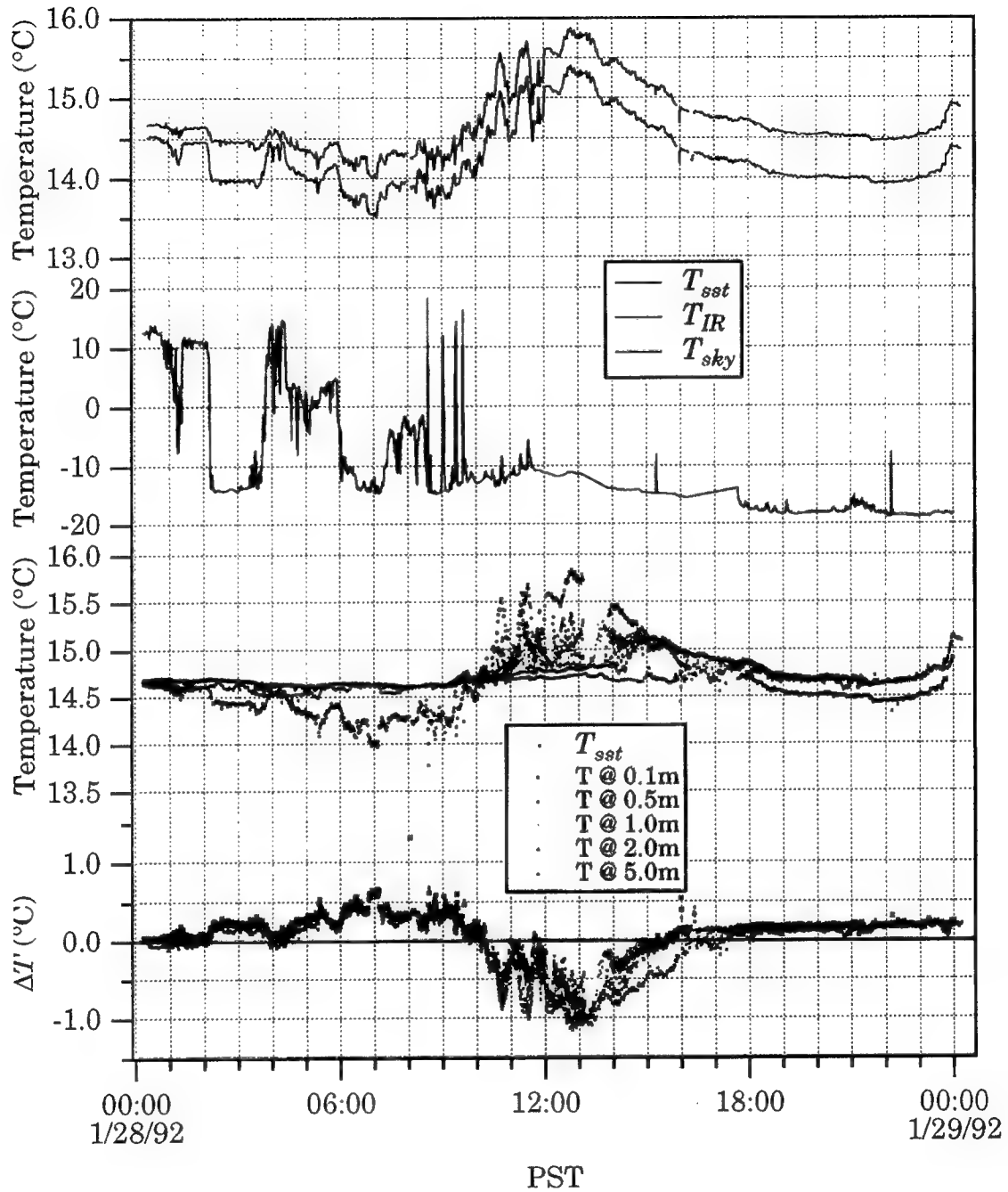ements at depth and ΔT's are included. Large gap in the data of 6 hours corresponds to the time spent performing calibration runs and general maintenance.

Figure 5.26c   Time series for January 27, 1992 of the corrected and calibrated IR SST, T_{sst}, along with the raw PRT-5 measurement, T_{IR}, and the radiometric sky temperature, T_{sky}. Time series of thermistor measurements at depth and ΔT's are included.

Figure 5.26d   Time series for January 28, 1992 of the corrected and calibrated IR SST, T_{sst}, along with the raw PRT-5 measurement, T_{IR}, and the radiometric sky temperature, T_{sky}. Time series of thermistor measurements at depth and ΔT's are included.
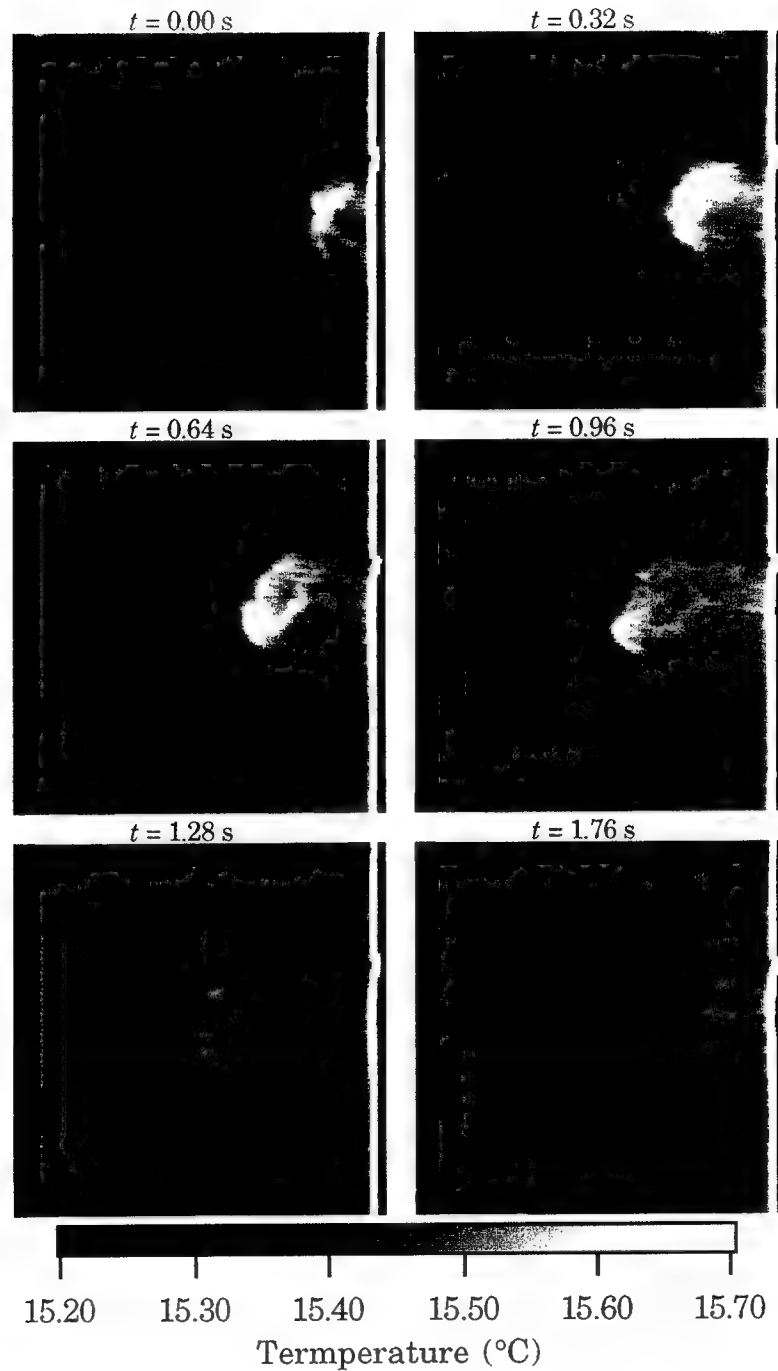
Figure 5.27 Nighttime sequence of the infrared signature of a breaking
wave. The images show the apparent temperature change
associated with the actively breaking crest and the turbulent
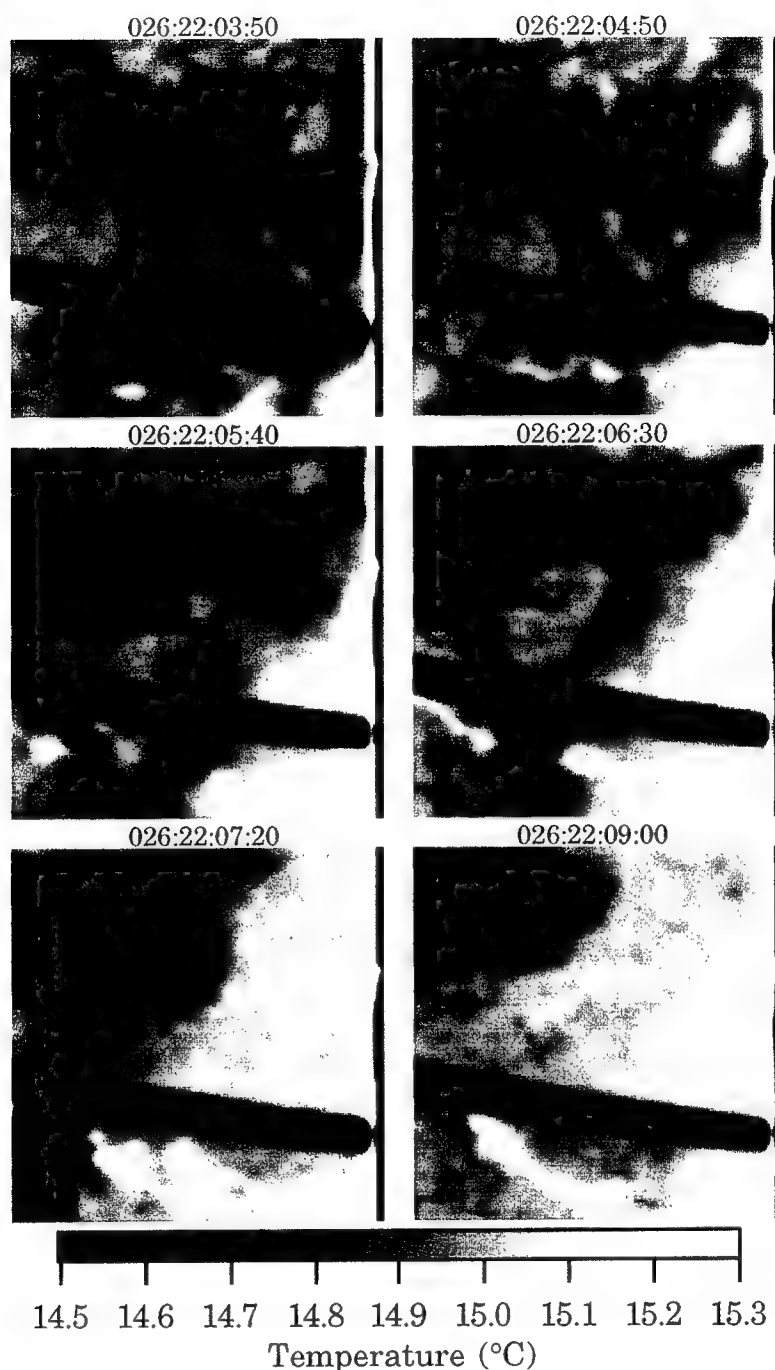wake. Environmental conditions shown in Table 5.3 under
Case 3.

Figure 5.28 Nighttime sequence of infrared images depicting the FLIP crossing an apparent temperature front. The broad dark band across the image is a support cable for the instrument boom. The dark outline of the front possibly might be the aggregation of surfactant material and foam causing a change in the electromagnetic properties of the viewing area.
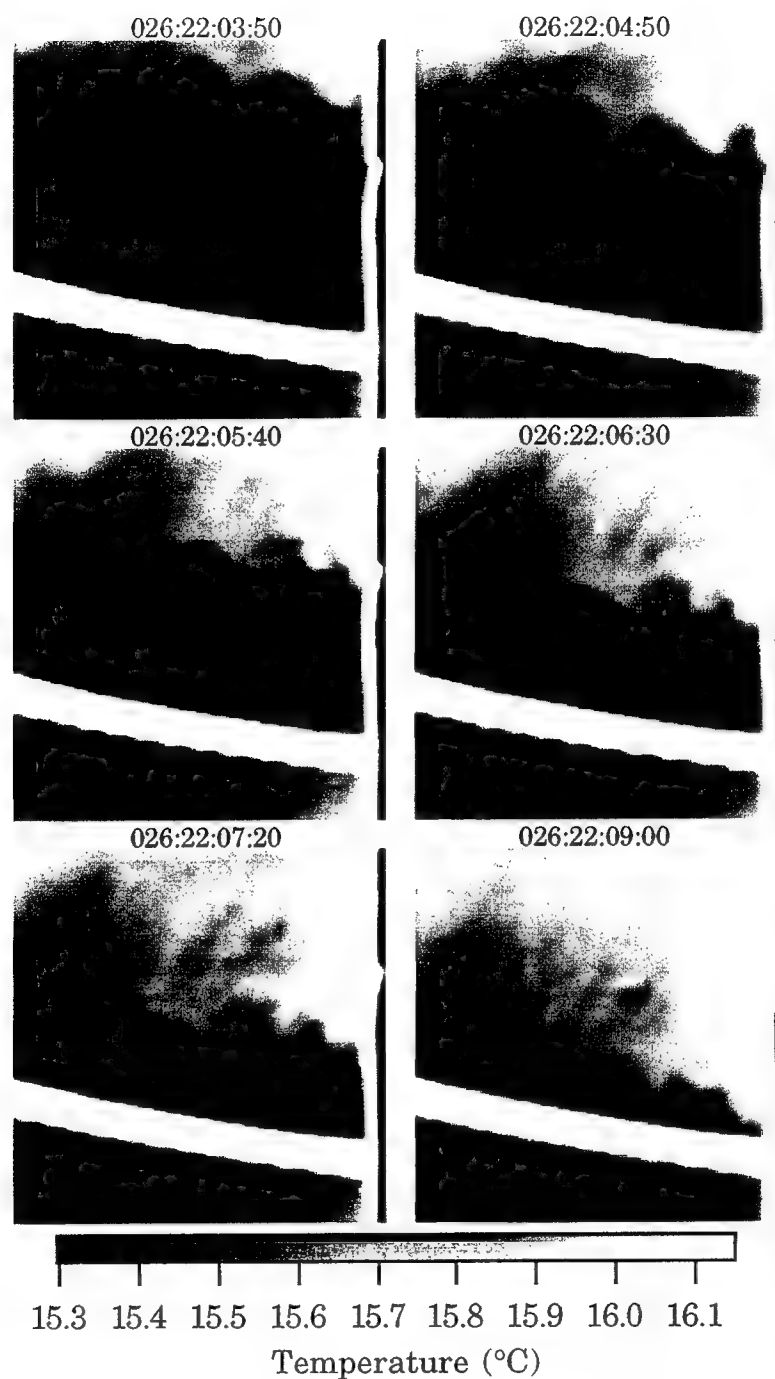Environmental conditions shown in Table 5.3 under Case 4.

Figure 5.29 Midday sequence of infrared images depicting the FLIP crossing an apparent temperature front. The broad white band across the image is a support cable for the instrument boom. Environmental conditions shown in Table 5.4 under Case 5.
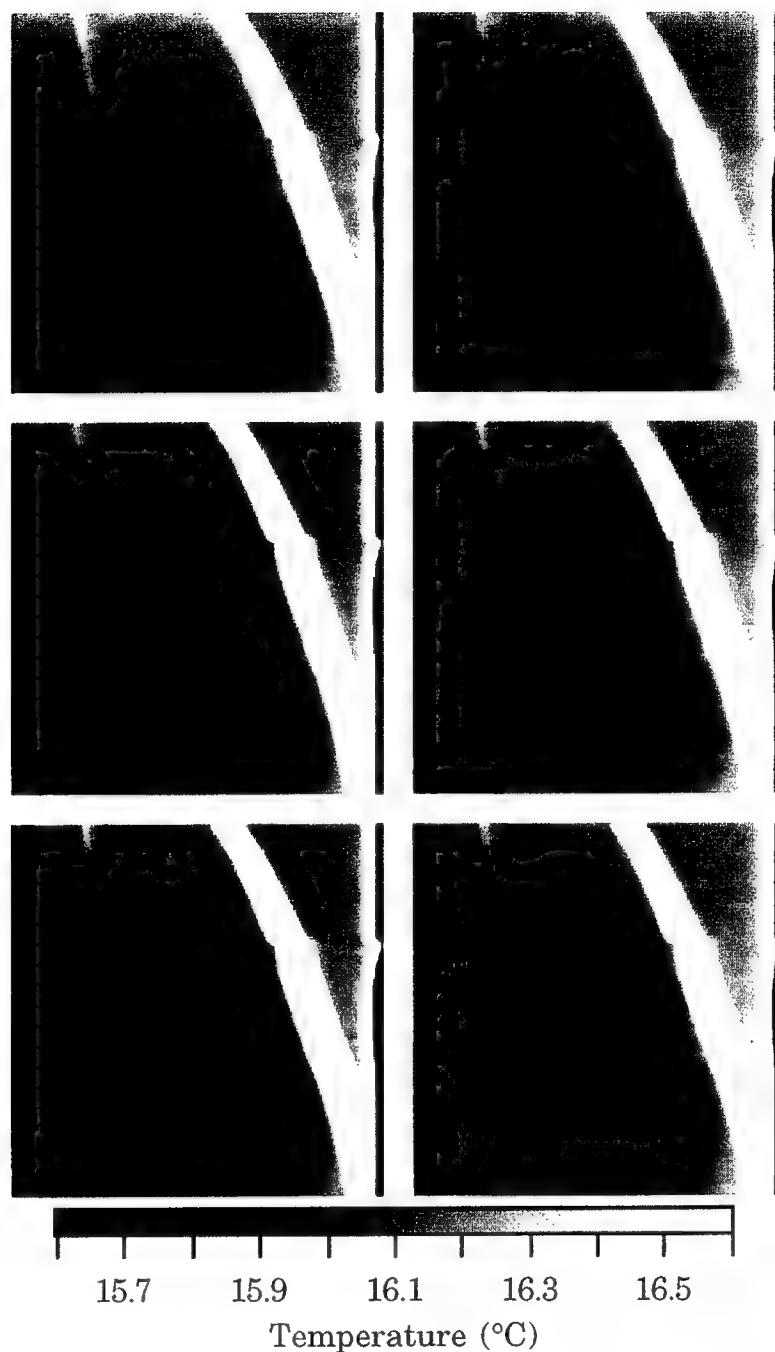
Figure 5.30 Cool wakes emanating from the surface-piercing cables during Case 5 shown in Table 5.4. The images are spaced roughly 10 to 20 seconds apart just prior to 12:05 PST. The broad white band across the image is a support cable for the instrument boom. The white lines in the upper left-hand corner are the cables.

028:10:12:30 028:10:13:00
028:10:13:10 028:10:15:00
028:10:46:35 028:10:47:40

15.1   15.3   15.5   15.7   15.9   16.1
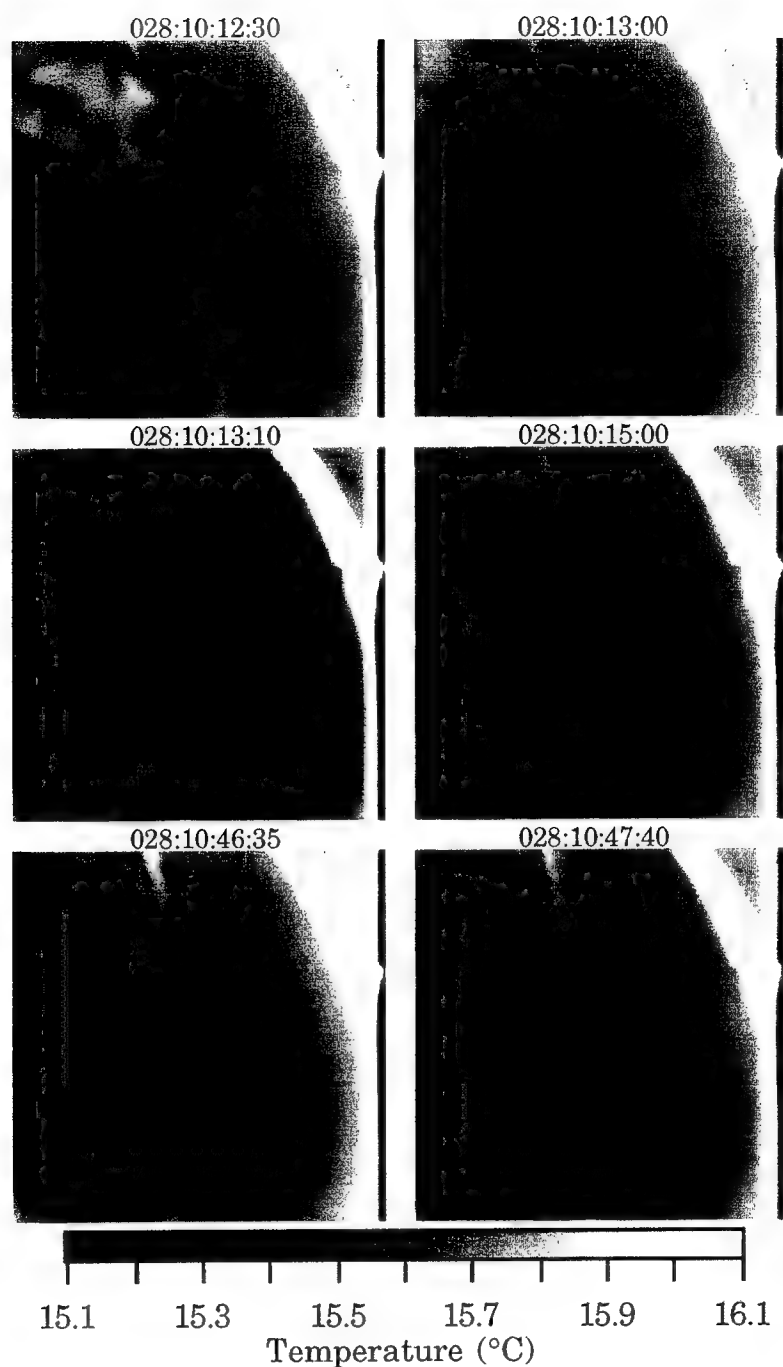Temperature (°C)

Figure 5.31a   Warm wakes emanating from the surface-piercing cables during the late morning transition as discussed in Case 6 of Table 5.4. FLIP begins to turn as suggested by the change in direction of the wakes. Simultaneously, the dark outline of the front appears.

028:10:48:30   028:10:49:30

028:10:51:30   028:10:53:15

028:10:54:35   028:10:54:45

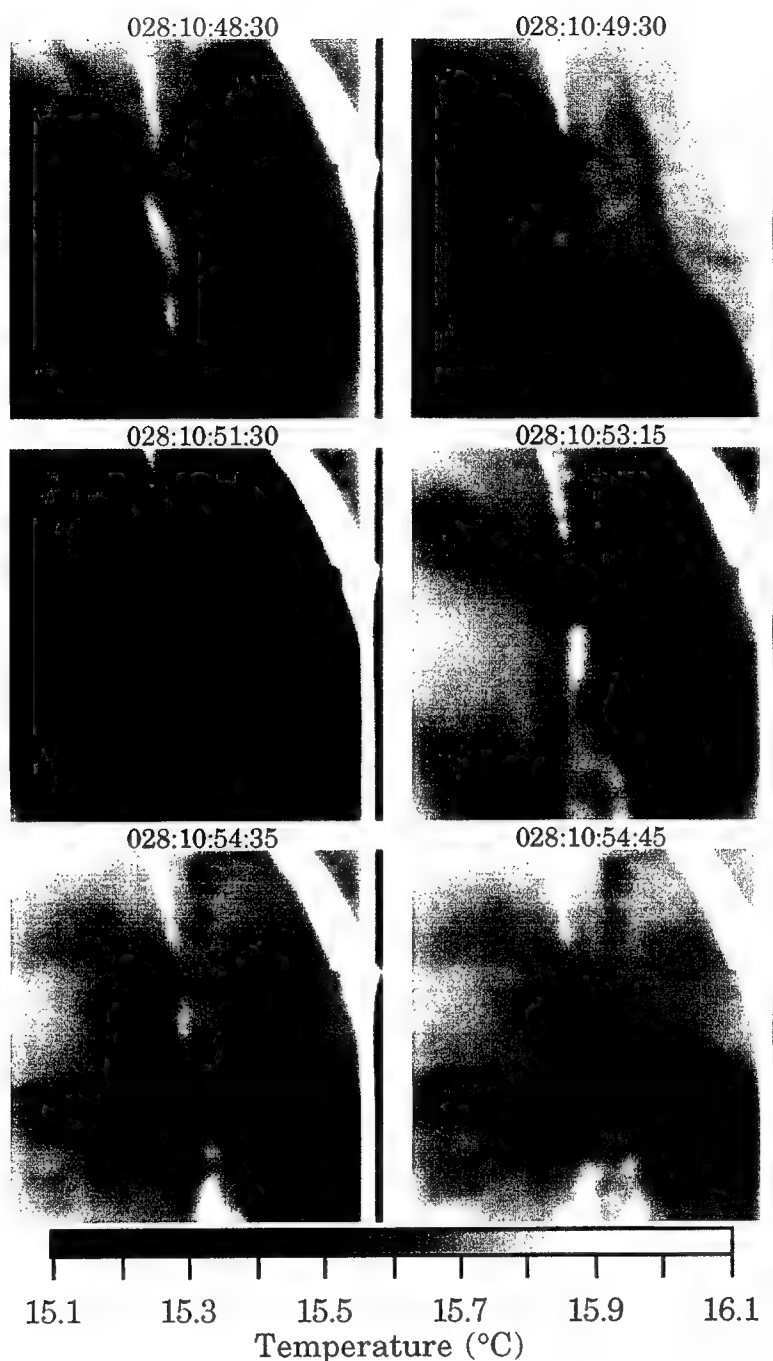15.1   15.3   15.5   15.7   15.9   16.1

Temperature (°C)

Figure 5.31b   FLIP continues to turn, crossing an apparent temperature front. The wires appear brighter suggesting the previously cloudy sky is now clear and the sun is allowed to heat the wires and ocean. Initially the surface temperature appears cooler corresponding to the change from cloudy to clear sky. However, the surface warms up quickly. The final two images depict the cool wakes, thus completing the transition.
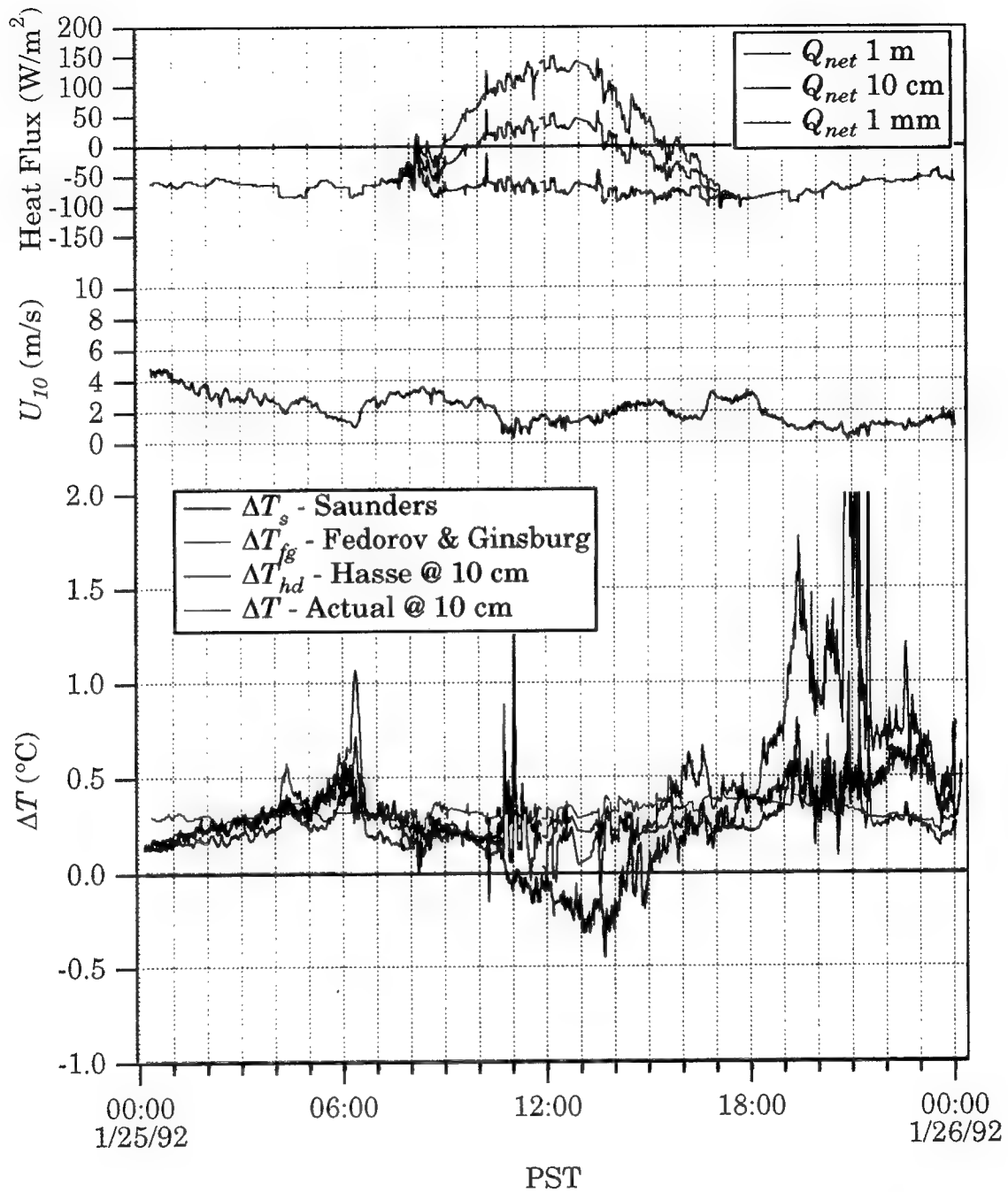
Figure 5.35a   Comparison of the ΔT models for January 25, 1992. The Q_{net} is plotted on the top of the graph with the wind speed in the middle. The bottom plot shows Saunders' model, ΔT_s, Fedorov and Ginsburg's model, ΔT_{fg}, and Hasses's model at 10 cm, ΔT_{hd}, all compared to the measured ΔT across the top 10 cm.
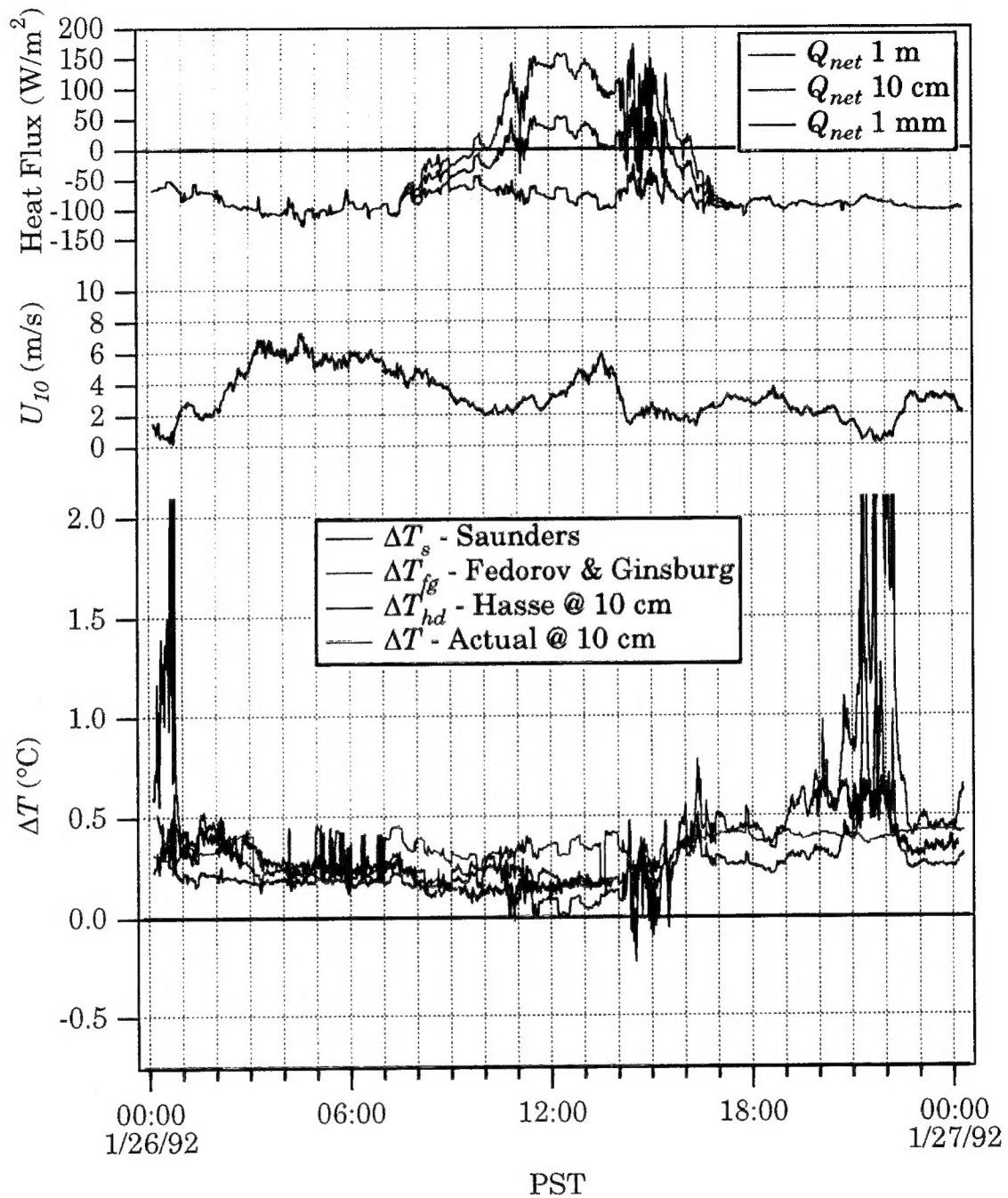
Figure 5.35b   Comparison of the ΔT models for January 26, 1992. The Q_{net} is plotted on the top of the graph with the wind speed in the middle. The bottom plot shows Saunders' model, ΔT_s, Fedorov and Ginsburg's model, ΔT_{fg}, and Hasses's model at 10 cm, ΔT_{hd}, all compared to the measured ΔT across the top 10 cm.
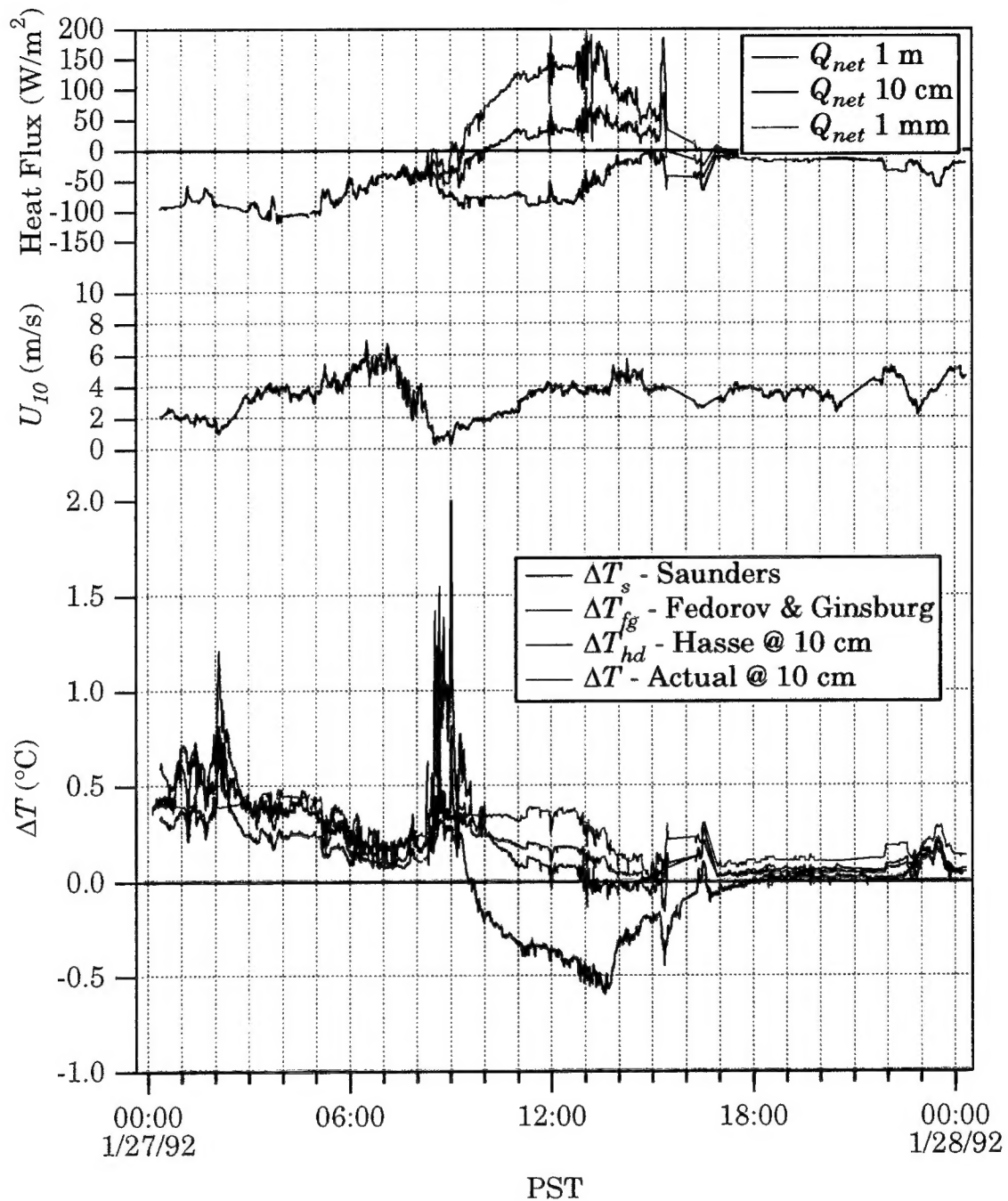
Figure 5.35c   Comparison of the ΔT models for January 27, 1992. The Q_{net} is plotted on the top of the graph with the wind speed in the middle. The bottom plot shows Saunders' model, ΔT_s, Fedorov and Ginsburg's model, ΔT_{fg}, and Hasses's model at 10 cm, ΔT_{hd}, all compared to the measured ΔT across the top 10 cm.
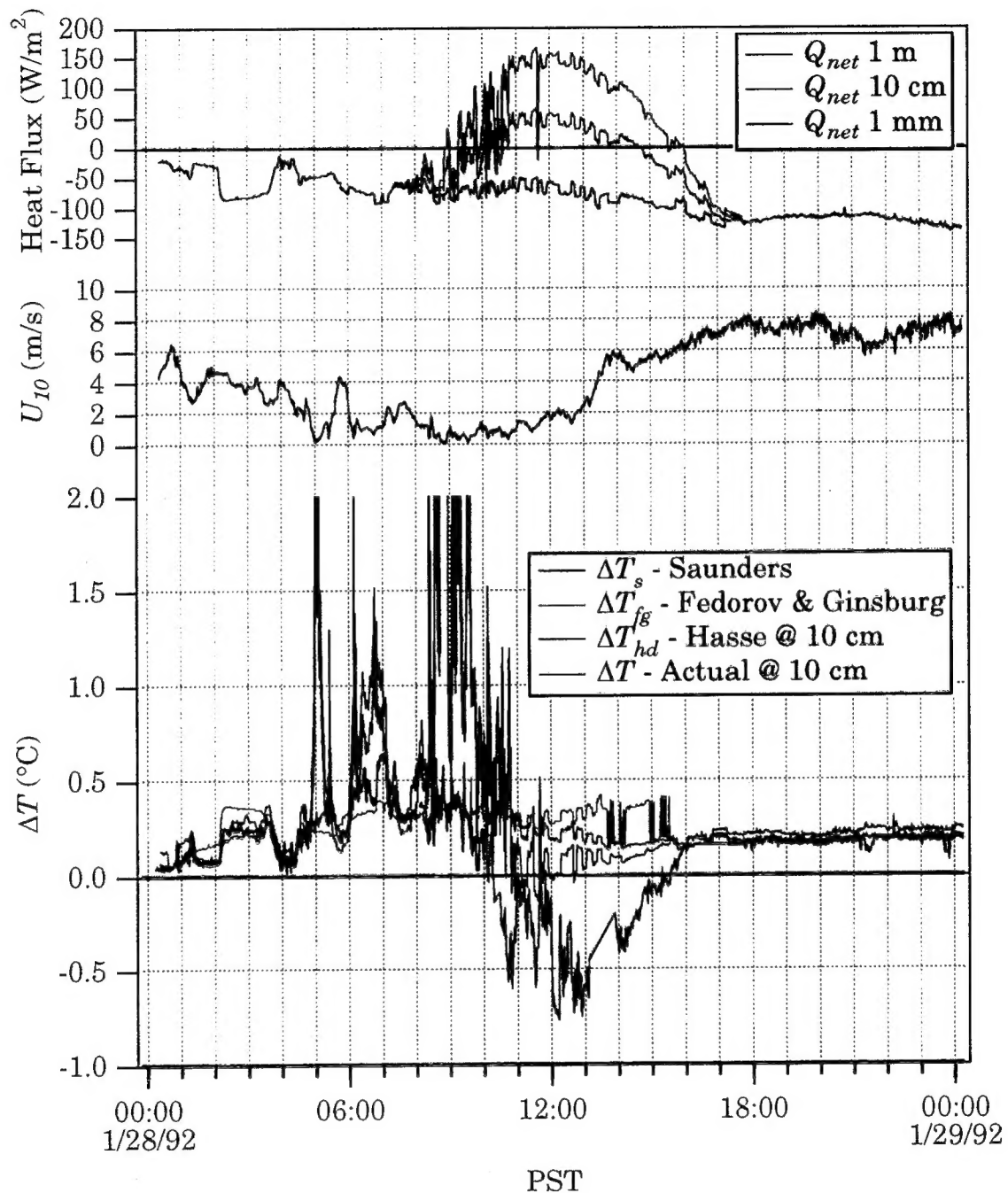
Figure 5.35d   Comparison of the ΔT models for January 28, 1992. The Q_{net} is plotted on the top of the graph with the wind speed in the middle. The bottom plot shows Saunders' model, ΔT_s, Fedorov and Ginsburg's model, ΔT_{fg}, and Hasses's model at 10 cm, ΔT_{hd}, all compared to the measured ΔT across the top 10 cm.

REPORT DOCUMENTATION PAGE

1. AGENCY USE ONLY (Leave blank)	2. REPORT DATE August 1994	3. REPORT TYPE AND DATES COVERED Technical

4. TITLE AND SUBTITLE

Infrared Field Measurements of Sea Surface Temperature: Analysis of Wake Signatures and Comparison of Skin Layer Models

5. FUNDING NUMBERS

N00014-91-J-1951
N00014-93-1-1326
NAWG-2888

6. AUTHOR(S)

Christopher J. Zappa

7. PERFORMING ORGANIZATION NAME(S) AND ADDRESS(ES)

Applied Physics Laboratory
University of Washington
1013 NE 40th Street
Seattle, WA 98105-6698

8. PERFORMING ORGANIZATION REPORT NUMBER

APL–UW TR 9412

9. SPONSORING / MONITORING AGENCY NAME(S) AND ADDRESS(ES)

Office of Naval Research
Remote Sensing and Space Program
Code 3215R
800 N. Quincy St.
Arlington, VA 22217-5660

National Aeronautics and Space Administration
Office of Mission to Planet Earth
NASA Headquarters
Washington, DC 20546

10. SPONSORING / MONITORING AGENCY REPORT NUMBER

11. SUPPLEMENTARY NOTES

12a. DISTRIBUTION / AVAILABILITY STATEMENT

Distribution Unlimited.

12b. DISTRIBUTION CODE

13. ABSTRACT (Maximum 200 words)

Infrared field measurements of ocean skin temperature made aboard the R/P FLIP in January of 1992 approximately 400 nautical miles off the coast of San Diego are presented. An extensive literature review accompanies these measurements probing the fundamentals of air-sea interaction, electromagnetics, and free-surface flows. A thin layer at the air-sea interface, known as the ocean skin layer, transfers heat by molecular conduction. The skin layer is on the order of a millimeter and typically 0.1 to 0.5 °C cooler than the water just below for conditions of net heat flux from the ocean to the atmosphere. Two surface-piercing cables hanging from FLIP's port boom, each 1 cm in diameter, provided a disturbance of the skin layer mixing the warmer water from below up to the surface. Employing an infrared imager, we detected the temperature variations, tracked the signatures and quantified the spatial and thermal changes in time of these artificial disturbances, which were on the order of a meter. This unique method of visualizing turbulence at an air-water interface provides a direct measurement of the bulk-skin temperature difference, ΔT. The recovery rate of the skin layer was found to be directly related to the level, or strength, of the disruption under low wind speed conditions (≈ 2 m/s). At moderate wind speeds (≈ 7 m/s), both the natural (breaking waves) and artificial (wakes) disturbances recovered within 2 s compared to an extrapolated recovery time of up to ≈ 120 s under low wind speeds for the wake signatures. The difference is primarily a function of the net heat flux and sublayer thickness, which relate directly to the existing environmental conditions (e.g., turbulence intensity, sea state, wind speed). Previous reports of ≈ 10 to 12 s skin layer recovery times emphasize the significance of our results. Signatures of cool wakes and a transitional sequence from warm to cool wakes over the course of 15 minutes highlighted the small-scale spatial variability and non-uniform temperature profile. Narrow field-of-view radiometers were used to compute calibrated and reflection corrected time series of ΔT (referenced to 10 cm depth) over a 4 day period. A comparison of the existing ΔT models is presented using measured values of the net heat flux, wind speed, and ΔT. For the present dataset, longwave radiation dominated the regulation of net heat flux at night while the solar insolation dominated during the day. The ΔT models did not adequately predict the phenomenon of the daytime heat flux and skin layer development under low wind conditions. Notwithstanding, the models agree well with the measured ΔT at night under high wind speeds.

14. SUBJECT TERMS

Ocean skin layer, skin layer recovery, free-surface wakes, free-surface turbulence, air-sea interaction, bulk-skin temperature difference, infrared sea-surface temperature (IR SST), infrared imagery

15. NUMBER OF PAGES

252

16. PRICE CODE

17. SECURITY CLASSIFICATION OF REPORT	18. SECURITY CLASSIFICATION OF THIS PAGE	19. SECURITY CLASSIFICATION OF ABSTRACT	20. LIMITATION OF ABSTRACT
Unclassified	Unclassified	Unclassified	SAR